PION PRODUCTION FROM FEW NUCLEON SYSTEMS IN THE REGION OF THE Δ_{1232} RESONANCE.

by

KEITH MICHAEL FURUTANI

A THESIS
SUBMITTED TO THE
FACULTY OF GRADUATE STUDIES AND RESEARCH
IN PARTIAL FULFILLMENT OF THE REQUIREMENTS
FOR THE DEGREE OF DOCTOR OF PHILOSOPHY

IN

NUCLEAR PHYSICS

DEPARTMENT OF PHYSICS
THE UNIVERSITY OF MANITOBA
WINNIPEG, MANITOBA
DECEMBER 1991

ISBN 0-315-77966-7

PION PRODUCTION FROM FEW NUCLEON SYSTEMS IN THE REGION OF THE Δ_{1232} RESONANCE

BY

KEITH MICHAEL FURUTANI

A thesis submitted to the Faculty of Graduate Studies of the University of Manitoba in partial fulfillment of the requirements for the degree of

DOCTOR OF PHILOSOPHY

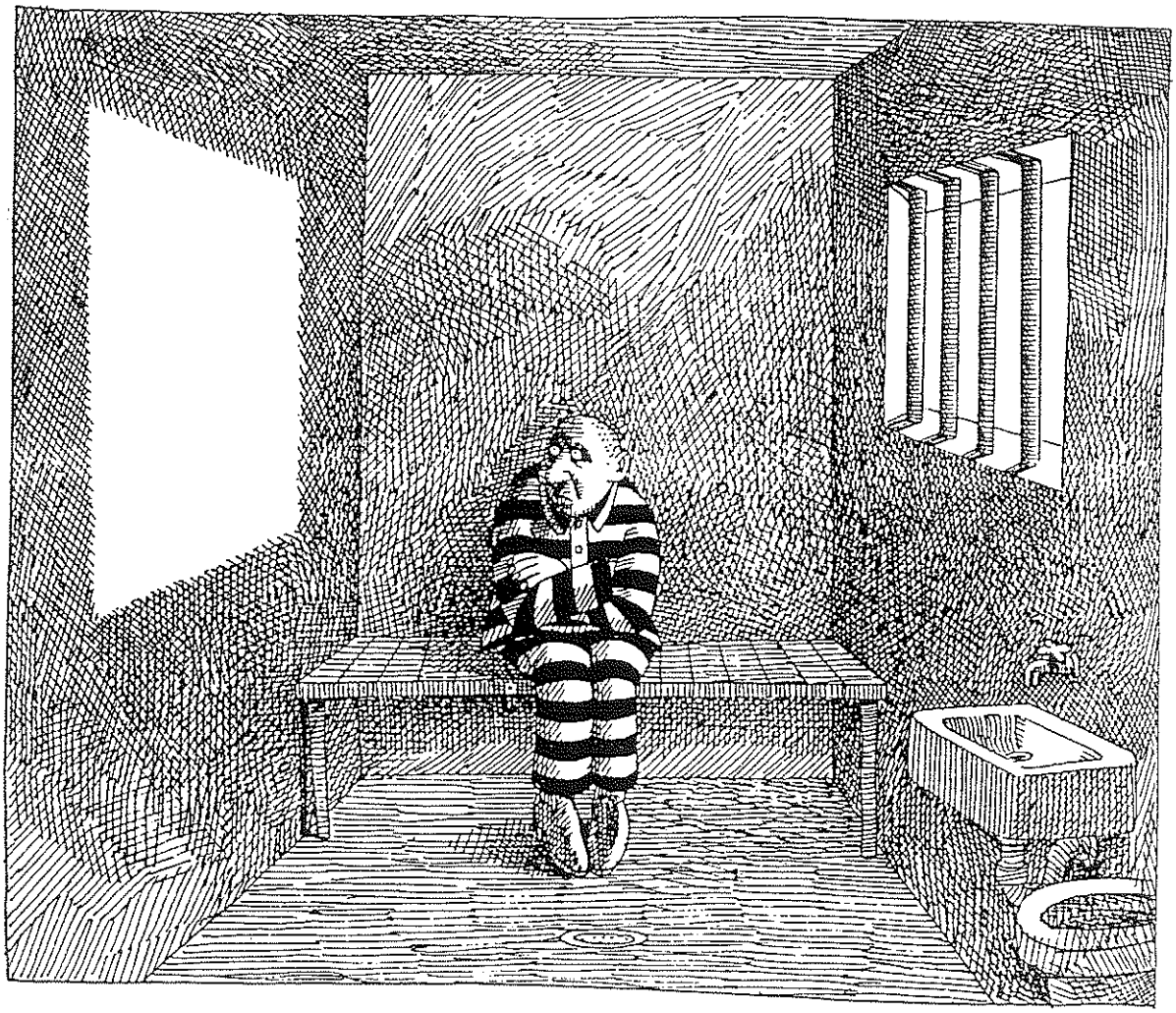

Dedication

To my family

for giving me the courage to strive for such a goal

and

to Sandra

for the love and support to achieve it.

Abstract

Angular distributions of the differential cross sections and analyzing powers have been measured for the ^{3}He($\vec{p}$,π^+)^{4}He and ^{4}He($\vec{p}$,π^+)^{5}He reactions at proton bombarding energies between 240 and 507 MeV providing a comprehensive set of data spanning the region of the Δ_{1232} resonance.

For these experiments, the University of Manitoba/TRIUMF liquid ^{3}He target was extensively refurbished and modified for provision of stable and reliable operation. A Monte Carlo study of the TRIUMF Medium Resolution Spectrometer for detecting pions was performed to investigate the acceptance, solid angle, and pion decay length of the spectrometer. Furthermore, for the ^{5}He spectra, a final state interaction calculation was carried out which uses information from the n + α elastic phase shifts.

The results obtained are of very high quality and are compared with a recent microscopic (p,π^+) calculation and a phenomenological study based upon the pp $\rightarrow$ dπ^+ amplitudes.

Acknowledgements

The content of this thesis is a refelection of the excellent guidance and supervision of a caring advisor, Dr. Willie Falk, whose attention to detail and insight into problems taught me more about physics than could be learned in any classroom or from any text. I am especially grateful that he had faith in an underdog student when others did not. I would also like to thank my committee for having the patience to hear all my questions and especially for their lucid answers.

There are three others whom also deserve special recognition. Two particularly close friends, Richard Y.H. Yeo and Alex Sekulovich, I would like to thank for the endless hours of discussion over many coffees and many beers of the salient points of getting through a graduate degree. My brother James, I must thank for having a generous heart to help me through the difficult times and for his bombastic nature to help me enjoy the good ones. Any accomplishments of mine are an influence of his positive spirit.

Acknowledgements are always very difficult to write since inevitably you leave someone out. That would be especially true in this case as I would never be able to acknowledge all the staff and friends that I have met and worked with over the past four years who had as much a part in my education as Dr. Bhakar's E & M course. I am indebted to them for their contributions to my outlook on physics and on life.

I would finally like to thank my high school physics teacher, Mr. K. Gerstmar, who possibly unknowingly, steered me into this crazy game which I have grown to love so much.

Contents

List of Figures

List of Tables

Chapter 1

Introduction.

It has been fifty six years since Yukawa proposed the existence of a nuclear force quantum, the pion [Yuk35], and forty four years since its discovery [Lat+47]. In the intervening period to the present day, our knowledge of the Nucleon-Nucleon (NN) interaction has evolved to a point where extremely sophisticated potentials describe a vast amount of data. The NN data are conventionally parameterized in terms of partial waves, and it is at this point that experiment is compared to theory. The NN interaction is contemporarily described by boson exchange potentials (in which the pion is just one possible boson) which quantitatively describe the NN elastic phase shifts [Mac89] very well.

While these potentials describe very well the on-shell amplitudes (elastic scattering phase shifts), it is the off-shell scattering which is the test of the validity of the potential. The success of the description of NN elastic scattering is therefore naturally extended to a description of the inelastic channel, NN $\rightarrow$ NNπ. These reactions are less understood and tested, primarily because now the pion is allowed to carry away some of the momentum and energy and hence one is probing a much more extensive region of phase space than in the elastic case. Furthermore, there are now three bodies in

Isospin of two nucleons		Total
T_i	T_f	cross section
1	0	σ_{10}
0	1	σ_{01}
1	1	σ_{11}
0	0	forbidden

Table 1.1: Isospin cross section notation.

the final state so that the theoretical computations are more difficult than for the two body case. The contemporary NN $\rightarrow$ NNπ theories are still in the spirit of the boson exchange potentials, but with diagrams which allow an inelastic pion production channel [DKS87]. Such theories are still in the early stages of testing and development.

1.1 Elementary Pion Production

The elementary NN $\rightarrow$ NNπ process is comprised of several possible reactions (for example: pp $\rightarrow$ npπ^+, pp $\rightarrow$ ppπ^0 and np $\rightarrow$ ppπ^-). A simple classification results by considering the isospin basis. In the isospin basis there are only four reactions. These are denoted by the isospin of the two nucleons in the incident channel, T_i, and the outgoing channel, T_f [GW54] (see Table 1.1). Note that of the four only three are allowed, since the isospin of the pion is one.

The possible elementary pion production reactions and their relation to the isospin cross sections are shown in Table 1.2. Note that for the case of pp $\rightarrow$ npπ^+ (σ_{10}) there is the possibility of the np system forming a bound

Reaction	Cross section
$pp \rightarrow d\pi^+$	σ_{10}^{d}
$pp \rightarrow np\pi^+$	σ_{10}^{np}
$pp \rightarrow pp\pi^0$	σ_{11}
$np \rightarrow d\pi^0$	$\frac{1}{2}\sigma_{10}^{d}$
$np \rightarrow np\pi^0$	$\frac{1}{2}\sigma_{10}^{np} + \frac{1}{2}\sigma_{01}$
$np \rightarrow nn\pi^+$	$\frac{1}{2}\sigma_{11} + \frac{1}{2}\sigma_{01}$
$np \rightarrow pp\pi^-$	$\frac{1}{2}\sigma_{11} + \frac{1}{2}\sigma_{01}$

Table 1.2: Isospin cross section reactions.

state deuteron. Therefore, one usually makes the further distinction between the bound and unbound case, σ_{10}^{d} and σ_{10}^{np} respectively.

Using the available data the isospin cross sections may be determined and these are shown in Fig. 1.1 (from Ref. [VA82]). Note that the low energy pion production cross section is described mostly by σ_{10}^{d} (that is the $pp \rightarrow d\pi^+$ reaction).

The description of elastic and inelastic processes from nuclei (both nucleon-nucleon scattering and pion production) is often formulated from the point of view of the elementary NN processes. However, one now must consider the field of the nucleus and this is most often described in an averaged way by an optical potential. The technique is usually performed by fitting the optical potential parameters to the case of elastic scattering at or near an equivalent energy for the process of interest. As an example, in the case of a stripping reaction, A(d,p)A+1, the analysis is usually done in a simple Born Approximation (with plane waves, a PWBA, where the field of the nucleus is ignored, or with distorted waves from an optical potential, a DWBA). A

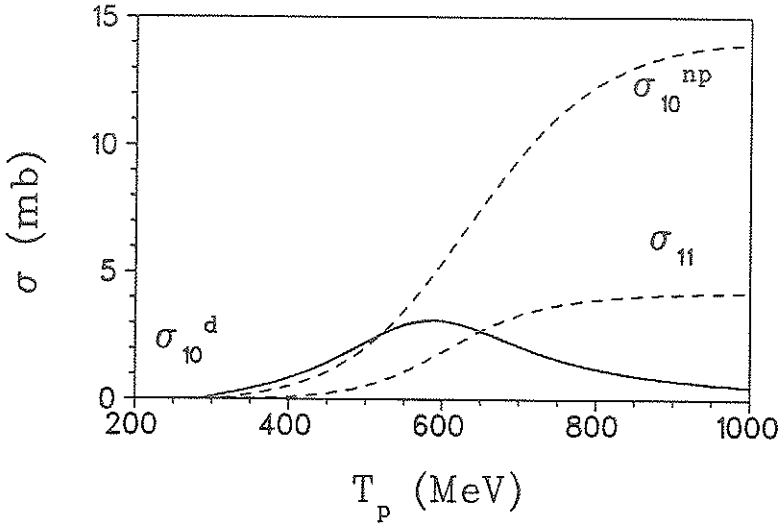

Figure 1.1: Elementary pion production cross sections.

method which is commonly used in the analysis of nucleon-nucleus elastic scattering is to include the information from the elementary processes (for example NN→NN) often obtained from the phase shifts. Such calculations are called Impulse Approximations (PWIA for plane waves and DWIA for distorted waves). A less common and much more difficult approach is to calculate the reaction mechanism using, for example, a boson exchange potential. The motivation for such calculations is to include the higher order processes explicitly rather than in an averaged way from an optical potential and in so doing investigate detailed points of the reaction mechanism. Such microscopic calculations are usually difficult and therefore are not as prevalent as the DWBA or DWIA calculations.

The reactions studied in this thesis are for few body nuclei (A=3,4) of the general A(p,π^+)A+1 reaction. These reactions may be studied theoretically in the context of a DWBA analysis (similar to those done for, say, (d,p)

stripping reactions) or with a full microscopic calculation. Examining these reactions from the point of view of the fundamental $NN \rightarrow NN\pi$ processes is also a useful approach, for example in a PWIA or DWIA calculation. These facets of A(p,π^+)A+1 reactions and the experiments performed to investigate them will now be discussed.

1.2 Nuclear Pion Production

Exclusive proton induced nuclear pion production is the study of reactions like A(p,π)A+1, where the residual A+1 nucleus is left in a well defined nuclear state. Due to the large mass difference between the incident proton and outgoing pion, there is a large momentum transfer imparted to the recoil nucleus. The momentum transfer (specifically the three momentum transfer) is defined in the following way.

$$\vec{q} = \vec{p}_f - \vec{p}_i \tag{1.1}$$

$$Q_{cm} = |\vec{q}| = \sqrt{p_i^2 + p_f^2 - 2p_i p_f \cos\theta_{cm}} \tag{1.2}$$

Even at threshold, the momentum transfer is large compared to the nuclear Fermi momentum (about 270 MeV/c). As an illustration, the momentum transfer versus the proton bombarding energy for the ^{3}He(p,π^+)^{4}He and the ^{40}Ca(p,π^+)^{41}Ca reactions is shown in Fig. 1.2.

It was this large momentum transfer which incited activity in the research of this reaction. It was hoped that using a simple reaction mechanism, similar to that for (d,p) stripping reactions studies, much could be learned about the high momentum components of nuclear wave functions. It was found, however, that such a simple picture did not explain the data adequately. Such ambiguities motivated detailed investigations of the reaction mechanism and also the limits of pion optical potentials. Continued uncertainty inspired

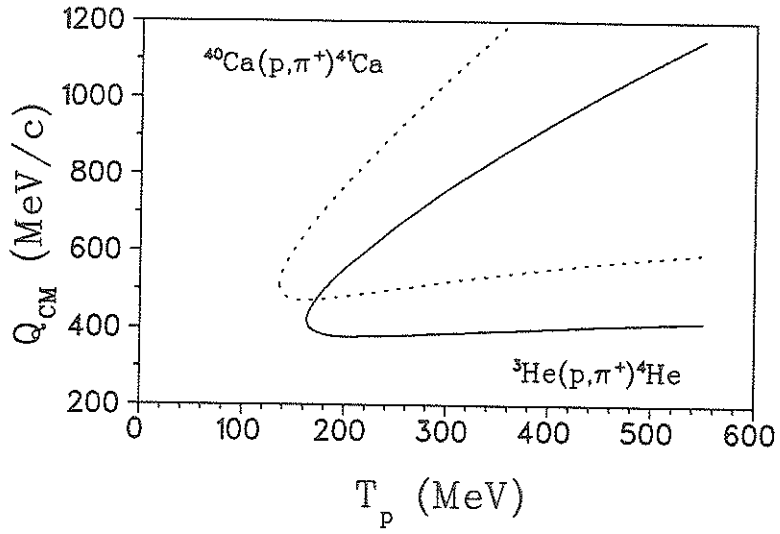

Figure 1.2: Momentum transfer for (p,π^+) reactions. The lower arm corresponds to Q_{cm} for 0° and the upper arm for 180°. (the solid line is for $^{3}He(p,\pi^+)^{4}He$ and the dotted line for $^{40}Ca(p,\pi^+)^{41}Ca$).

more effort in both theoretical and experimental investigations. While the A(p,π^+)A+1 reaction has been a very difficult reaction to study theoretically, it has also shown to be a very sensitive proving ground for current nuclear reaction theories.

1.2.1 Experimental

The early work of nuclear pion production was carried out at only selected energies and angles. An example is the study of the ^{12,13}C(p,π^+)^{13,14}C and ^{14}N(p,π^+)^{15}N reactions at $T_p = 600$ MeV and $\theta = 0°$ done at CERN [Dom+70] over 20 years ago. This work was followed shortly by work at Uppsala [DHG71] where both positive and negative pion production on a large variety of targets was extensively studied (see for example Refs. [Dah+73a], [Dah+73b] and [Dah+73c]). All the work was carried out near threshold (185 MeV) and with non-polarized beams but is generally considered to be the pioneering work on nuclear pion production. As an example of the quality of these early works, an energy spectrum for ^{12}C(p,π^+)^{13}C from Ref. [DHG71] is shown in Fig. 1.3.

The earliest work of nuclear pion production involving measurements of polarization as well as differential cross section is that of Heer *et al.* [HRT58]. They investigated pion production from C and Al at 209 MeV, but at only a few angles. The polarized beam was generated in the standard manner of that time, namely via a double scattering experiment. The authors noted that such a measurement is extremely time consuming and therefore similar measurements were not performed. With the advent of the intense polarized proton beams, spin observables (notably the analyzing powers) then became additional observables of investigation. In the Ann Arbor [KS78] convention

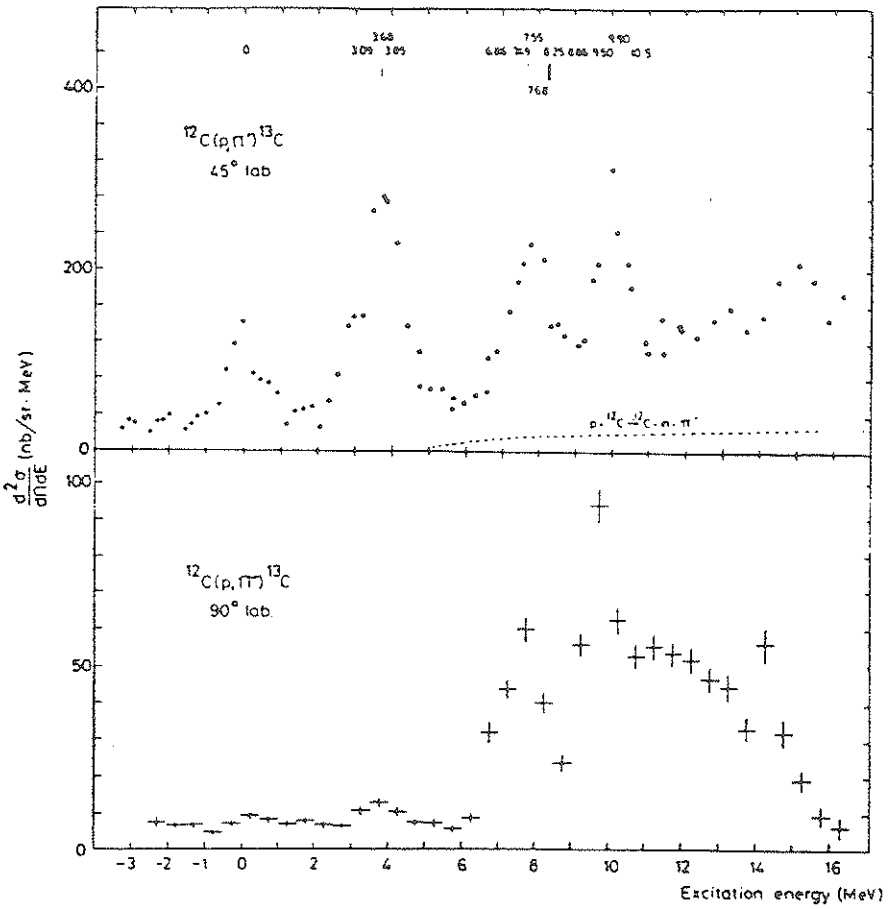

Figure 1.3: Energy spectrum from Dahlgren *et al.* showing quality of early pion production investigations.

the analyzing power is defined as

$$A_{N0} = \frac{1}{P} \frac{d\sigma(\uparrow)/d\Omega - d\sigma(\downarrow)/d\Omega}{d\sigma(\uparrow)/d\Omega + d\sigma(\downarrow)/d\Omega} \tag{1.3}$$

where P is the proton beam polarization. The subscript N indicates that the beam is polarized normal to the scattering plane and the subscript 0 indicates the target is unpolarized. The arrows indicate the direction of the polarization of the incident beam, i.e. up or down, with respect to the scattering plane (for example $d\sigma(\uparrow)/d\Omega$ is then the differential cross section for polarized-up protons). In the older Madison convention [BH71] the analyzing power is notated A_y. One should note that, by definition, the range of the analyzing power is between $+1$ and -1 and that it must be zero, by symmetry, for scattering angles of 0° and 180° .

Measurements of the analyzing power for a variety of nuclei near threshold were performed at the Indiana University Cyclotron Facility (IUCF) [Sjo+81] and at TRIUMF in Vancouver, Canada [Aul+78]. The analyzing power was found to be rich in structure and has, since then proven to be the point of greatest difficulty when comparing theory with data. In some nuclei, where the differential cross section may display only little variation with energy, the analyzing power may exhibit strong variation with energy. The analyzing power thus becomes a very important observable when studying (p,π^+) reactions.

As an indication of the amount of interest in these reactions generated by the research of the 1970's is the number of review articles of this field of research (see Refs. [Hoi79], [MM79] and [Fea81]). These reviews are excellent surveys of the data of that period and many of the conclusions and questions raised are still applicable today. Since the (p,π^+) conference in Indiana in 1981 [Ben82], many experiments have been performed and are usually of very high quality stressing the importance of polarization measurements.

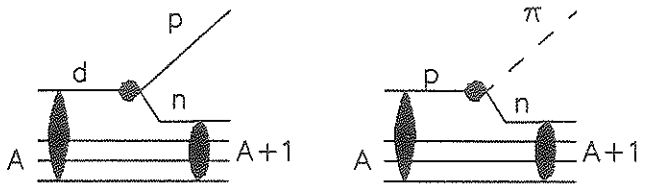

Figure 1.4: Comparison of (d, p) and (p,π^+) stripping reactions.

Such high quality data have inspired a great deal of theoretical activity as well, which will be presented in the following section.

1.2.2 Theory

In the initial investigations it was hoped that A(p,π^+)A+1 reactions would provide information about the high momentum components of nuclear wave functions. In the context of Direct Reaction theory one can make the obvious comparison between (d,p) and (p,π^+) reactions, as shown in Fig 1.4. It is therefore not difficult to see why these reactions were originally studied in the so called One Nucleon Model (ONM) or pionic stripping process analogous to a DWBA formalism used for (d,p) reaction studies.

As one might expect, the calculations were found to be very sensitive to optical model wave functions. Examples of DWBA calculations can be found in the work of Tsangarides [Tsa79]. His calculations were applied to many nuclei near threshold. In light of the comparison between (d,p) and (p,π^+) reactions, investigations of A(d,p)A+1 and A(p,π^+)A+1 were done at similar momentum transfers for several nuclei and the DWBA analyses per-

formed and compared (see for example [Ama+78] [Jac+80] and [And+81]). However, in all these DWBA studies only qualitative agreement with the data could be obtained. Indeed, it was concluded that a more comprehensive analysis was required beyond the simple DWBA formalism, specifically a microscopic calculation.

The analyzing power of a A(p,π^+)A+1 reaction is theoretically zero for all scattering angles in the PWBA (a ONM with no distortions). It was known that the analyzing power for the fundamental reaction, pp $\rightarrow$ dπ^+, is quite large (see Fig. 1.5). Therefore, when the measured analyzing power for nuclear pion production was experimentally found to be large, questions naturally arose as to the validity of the ONM picture. The analyzing powers were furthermore found to be *very* sensitive to the optical model wave functions. As an indication of this sensitivity the analyzing power for ^{12}C(p,π^+)^{13}C at approximately 200 MeV is shown for a variety of ONM calculations in Fig. 1.6 (from Ref. [Fea81]).

The need for more sophisticated calculations was very apparent. Indeed, with the evident failure of the ONM one proceeded naturally to higher order processes, the so called two nucleon models (TNM). The motivation for the TNM is twofold. Firstly, the nucleus can now share the momentum transfer over two nucleons, thereby decreasing the sensitivity to the distortions. Secondly, from π-Nucleus studies it has become evident that Δ isobar degrees of freedom play a fundamental role in describing pion processes. The Δ_{1232} (or simply Δ) is an isospin 3/2, spin 3/2 baryon resonance of mass 1232 MeV and width $\approx$ 115 MeV. It decays strongly to a pion and a nucleon, $\Delta \rightarrow \pi$N, with a nearly 100% branching ratio [Agu+90]. In a ONM, resonant rescattering through a Δ is not included explicitly. The ONM might therefore be missing a crucial piece of the (p,π^+) reaction mechanism. In Fig 1.7 two

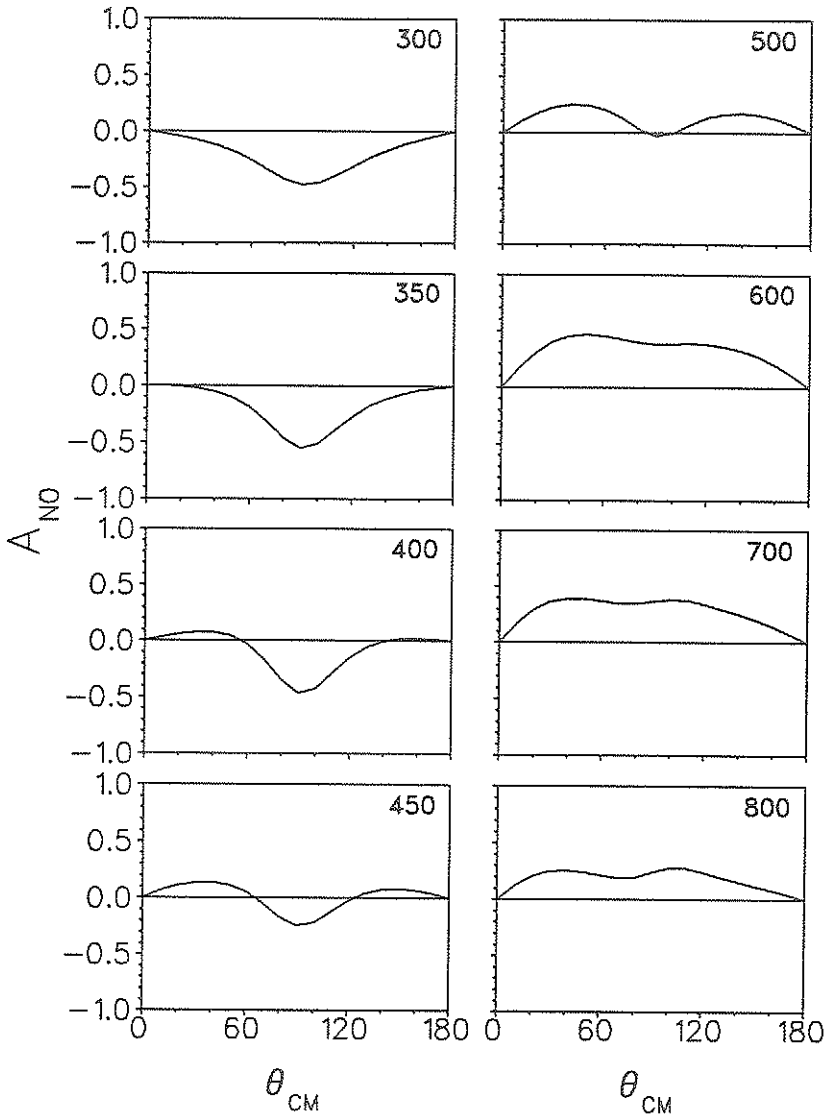

Figure 1.5: Analyzing powers for the pp $\rightarrow$ dπ^+ reaction at several proton energies. Curves are obtained using a smooth line through measured Legendre polynomial coefficients from fits to existing data.

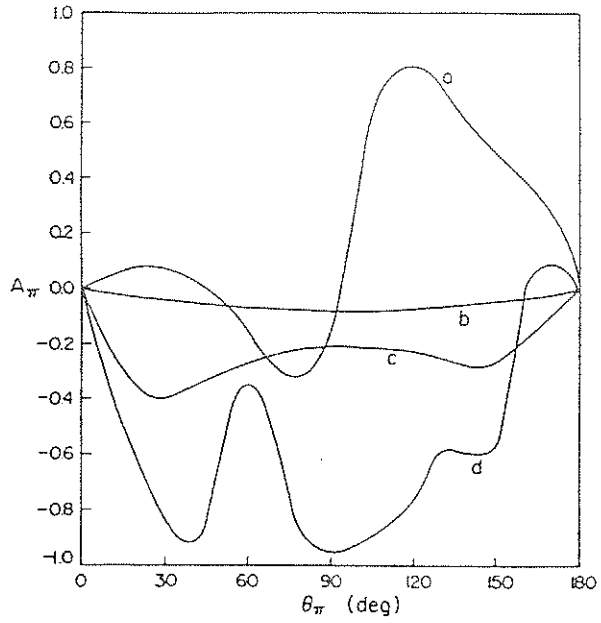

Figure 1.6: Analyzing power for $^{12}C(\vec{p},\pi^+)^{13}C$ from different ONM calculations at approximately 200 MeV.

typical diagrams of a TNM are shown, one with a nonresonant pion rescattering and one with a resonant pion rescattering through a Δ intermediate state. The term TNM is a generalization of models which includes higher order processes explicitly. However, one should note that each model may be slightly different due its assumptions and choice of reaction mechanism.

These microscopic calculations are very complicated and time consuming. As an example of a TNM calculation, Fig. 1.8 shows the result of a calculation by Iqbal and Walker [IW85] for $^{12}C(\vec{p},\pi^+)^{13}C^*_{9.50}$. The $C^*_{9.50}$ state is an almost pure 2p-1h state. A ONM is not able to populate such a state from the initial ^{12}C nucleus and hence, one would expect a dominant TNM contribution. For simplification, therefore, the Iqbal and Walker calculation does not include any ONM diagrams. Its treatment of the TNM however, is quite exhaustive and includes explicitly the Δ degree of freedom. In particular it does not make the approximation of a static intermediate Δ and

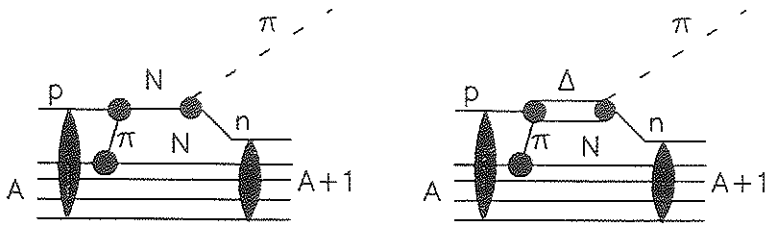

Figure 1.7: Two Nucleon Model.

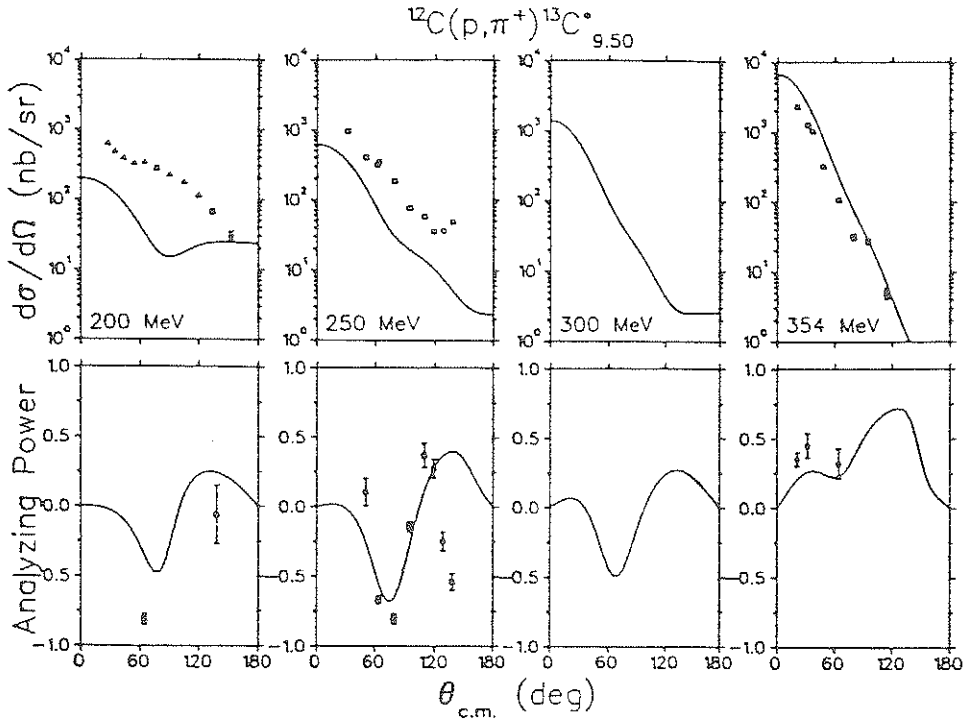

Figure 1.8: Two Nucleon Model calculation by Iqbal and Walker compared to data from [Hub+88].

is therefore expected to be valid in the region where the Δ_{1232} is dominant. Good agreement with the data is indeed observed in Fig. 1.8 at T_p= 354 MeV (the proton beam energy corresponding to that where a nucleon may be excited to a Δ in the nuclear frame). However, at energies away from the resonance energy, the calculation shows increasing disagreement. This result is typical of many TNM calculations. Agreement is quite fair where the assumptions used in the model are most valid, but poor where the validity of the assumptions are not as certain.

Special mention should be made of the relativistic ONM calculation by Cooper and Sherif [CS82]. Their calculation assumes a pionic stripping process and it is performed entirely in the framework of relativistic Quantum Mechanics, i.e. the Dirac Equation. Both pseudoscalar and pseudovector couplings for the πN vertex (which in the nonrelativistic limit are the same) were investigated. Since the momentum transfers are indeed large in A(p,π^+)A+1 reactions, calculations done in the nonrelativistic framework might not be valid. Certainly relativistic calculations appear to be a necessary part of the theoretical investigation of the (p,π^+) reaction mechanism. The results of Cooper *et al.* [CM86] agreed fairly well with data and indicate a great deal of promise. The calculation, however, only investigated pion production to single particle final states (for example ^{16}O(p,π^+)^{17}O and ^{40}Ca(p,π^+)^{41}Ca).

Finally a calculation which includes both the ONM and TNM and has been used to investigate specifically the ^{3}He($\vec{p}$,π^+)^{4}He reaction (studied in this thesis) is introduced. The model is called ORCHID and was developed at IUCF by P.W.F. Alons *et al.* [Alo+88]. Presently the code includes the ONM and the resonant part of the TNM with Delta propagation and distortions. Inherent in a TNM calculation, which includes the first order ONM as well, is the problem of double counting. The distorted waves used in the

ONM include higher order diagrams implicitly, including those described *explicitly* by the TNM diagrams! To circumvent this problem, the calculation uses plane waves for the ONM part and then uses distorted waves for the TNM part to include higher order effects. The model will be discussed more completely in Chapter 5 and compared with the data of this and previous work.

One may surmise that the present theoretical understanding of the proton induced nuclear pion production data is quite limited. Uncertainty with respect to the reaction mechanism and the sensitivity to distortions has made the study of these reactions frustrating but inspiring. It has prompted many new approaches and certainly tested many existing ones.

1.2.3 Negative Pion Production

One should also mention the A(p,π^-)A+1 reactions. The (p,π^-) reactions offer the unique feature that they cannot proceed via the ONM (shown in Fig. 1.4). They have been used to discover new nuclear excited states and studies have been performed comparing them with the (p,π^+) reaction to mirror final states (see [Thr84] [Kor87] [Hub88]). Since the (p,π^-) reaction is not studied in this work it will not be discussed further.

1.2.4 Systematics of Observables

Due to the lack of theoretical understanding and because of a large body of existing data, the problem of understanding (p,π^+) reactions has placed heavy emphasis on a search for systematics. Given the initial ideas of a DWBA approach, most of the initial works compared the angular distributions as functions of the momentum transfer Q_{cm}. Furthermore, with the large amount of data near threshold, many investigations were in terms of

the nuclear state dependence as a function of energy, examined over a relatively small energy region (from threshold to 200 MeV). Shortly thereafter and up to the present, studies were extended to include the analyzing power and energy dependence from threshold to above the Δ_{1232} resonance energy. Despite some exhaustive searches for systematics, only very broad general features of these (p,π^+) reactions have been noted.

A very detailed study of the systematics of these reactions was done by Couvert [Cou83] and the topic is also discussed in the several review articles of (p,π^+) research ([Hoi79] [MM79] and [Fea81]). For the states of a given nucleus the (p,π^+) reaction has been shown to be very selective and attempts were made early on to note any systematics in this selectivity. It is generally found that high angular momentum states are preferentially excited (beyond the (2J + 1) statistical factor), and specifically, stretched 2p-1h states.

Höistad [Hoi79] has noted the apparent correlation between the size or mass of a nucleus with the pion production cross section. He points out that in general the total pion production cross section decreases with increasing nuclear mass. A strong indication of this trend is shown in Fig. 1.9 (from Ref. [Hoi79]) where the approximate experimental cross sections are plotted for different target nuclei and final nuclear states. One might suspect that this trend may be due to the increase in pion multiple scattering in the final state. However, Höistad pointed out that this would imply an increase in the continuum cross sections with increasing nuclear target mass, which is not observed. He concludes, therefore, that the effect is a result of the (p,π^+) reaction mechanism itself. Couvert [Cou83] interpreted the trend to be due to increasing pion absorption with the increase in the amount of nuclear matter involved in the reaction.

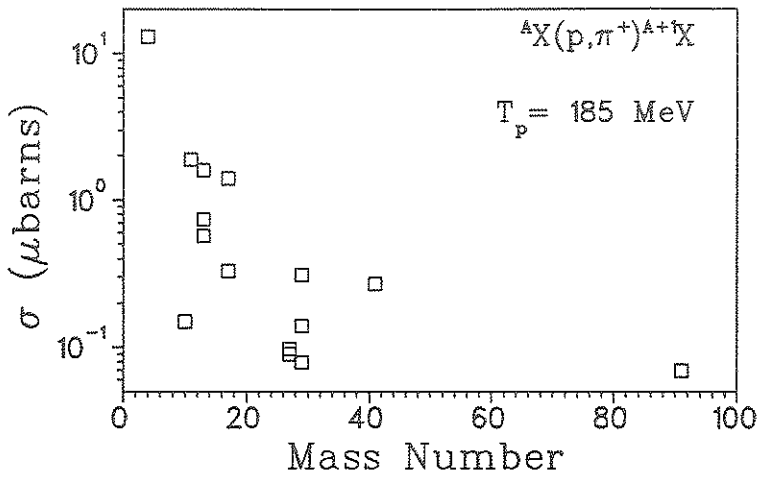

Figure 1.9: (p,π^+) total cross section dependence on target mass.

Couvert [Cou83] also discussed the importance of the role of kinematics in the interpretation of A(p,π^+)A+1 data. Specifically the four momentum transfer t, was suggested as the significant kinematic variable (as opposed to θ_{cm} or Q_{cm}). The four momentum transfer four vector may be defined as

$$q = q^{\mu} = p_i^{\mu} - p_f^{\mu} \tag{1.4}$$

in the usual relativistic notation. The four momentum transfer t is relativistically invariant and is defined as:

$$t = -q^{\mu}q_{\mu} \tag{1.5}$$

In terms of the cm energy and 3-momentum, t may be written as:

$$t = m_1^2 + m_3^2 - 2E_1E_3 + 2p_1p_3\cos\theta \tag{1.6}$$

It was also noted that total final kinetic energy in the cm frame ϵ_f^*, proved to be a useful *energy* variable when comparing different nuclei. Huber [Hub88] furthermore suggested that, rather than ϵ_f^*, one should consider $\sqrt{s} - M_A$ (where s is the Mandelstam variable corresponding to the total energy in the cm frame squared and M_A is the target mass) as the energy variable since

this corresponds to the energy available for a nucleon in the nuclear frame. In Fig. 1.10 kinematics for the same reactions as in Fig. 1.2 (^{3}He(p,π^+)^{4}He and ^{40}Ca(p,π^+)^{41}Ca) are shown, except now plotted versus relativistic invariants (the four momentum transfer $-$t and the energy variable suggested by Huber). For information, in Fig. 1.11 and 1.12 kinematics comparing the ^{1}H(p,π^+)^{2}H reaction and the ^{3}He(p,π^+)^{4}He reaction (studied in this thesis) are shown. The apparent discrepancy in kinematics between different nuclei is substantially reduced. One should note that the minimum value of $-$t for all (p,π^+) reactions is identical, namely,

$$-\,t_{min}(0^\circ) = (m_p - m_\pi)^2 \tag{1.7}$$

The proton bombarding energy at which this minimum occurs depends on the target mass but is approximately 30 MeV above threshold.

When the cross section for the pp $\rightarrow$ dπ^+ reaction is plotted versus proton bombarding energy a large bump at $T_p \approx 600$ MeV is observed and is attributed to the excitation of the proton to a Δ resonance [Bar73]. An energy dependent systematic that has been observed in (p,π^+) reactions is that the peak in the cross section (at a constant momentum transfer) appears near the energy where the proton may be excited to the Delta invariant mass, 1232 MeV [Hub88],

$$\sqrt{s} - M_A = M_\Delta = 1232\,\mathrm{MeV}. \tag{1.8}$$

In Fig. 1.13 the differential cross section for ^{12}C(p,π^+)^{13}C to the ^{13}C ground state and 9.50 MeV excited state are shown versus this energy variable and those for the pp $\rightarrow$ dπ^+ reaction versus the equivalent variable (from Ref. [Hub88]). The Δ_{1232} is a resonant intermediate state in pion-nucleon scattering, and therefore, strong implication of a two nucleon underlying mechanism is suggested.

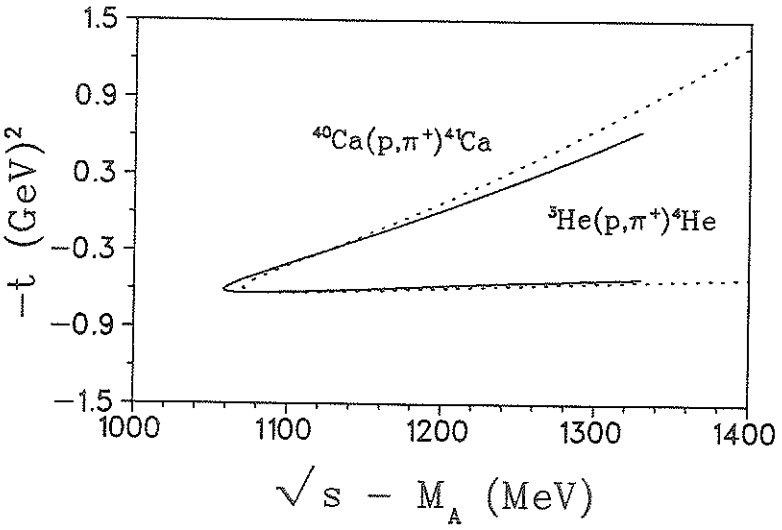

Figure 1.10: Kinematics for (p,π^+) reactions. The lower arm corresponds to $-$t for 0° and the upper arm for 180°. (the solid line is for ^{3}He(p,π^+)^{4}He and the dotted line for ^{40}Ca(p,π^+)^{41}Ca).

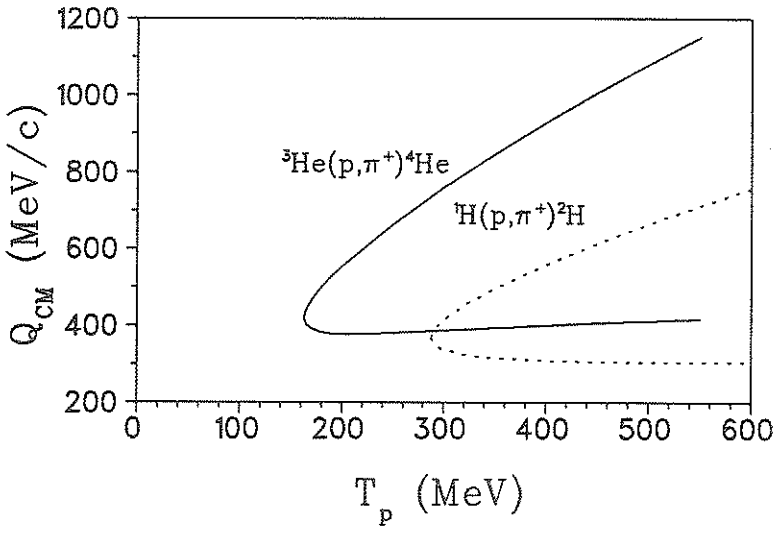

Figure 1.11: Momentum transfer for pp $\rightarrow$ dπ^+ and nuclear reactions. The lower arm corresponds to Q_{cm} for 0° and the upper arm for 180°. The solid line is for ^{3}He(p,π^+)^{4}He and the dotted line for ^{1}H(p,π^+)^{2}H.

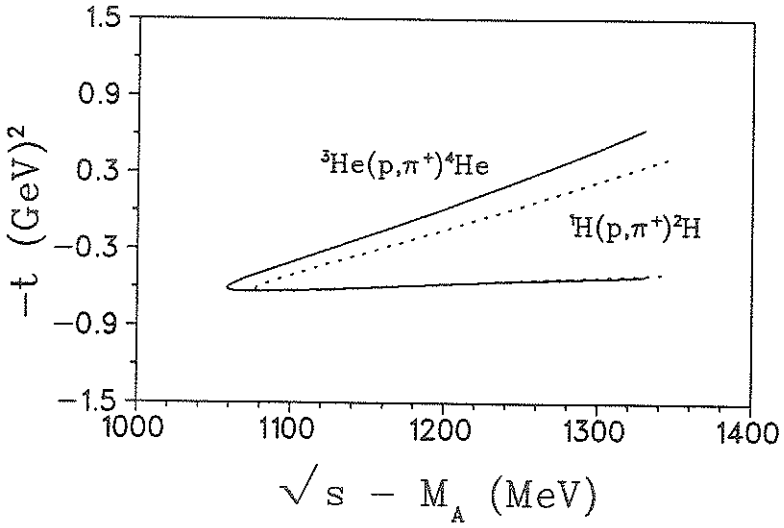

Figure 1.12: Kinematics for pp $\rightarrow$ dπ^+ and nuclear reactions. The lower arm corresponds to $-$t for 0° and the upper arm for 180°. The solid line is for ^{3}He(p,π^+)^{4}He and the dotted line for ^{1}H(p,π^+)^{2}H.

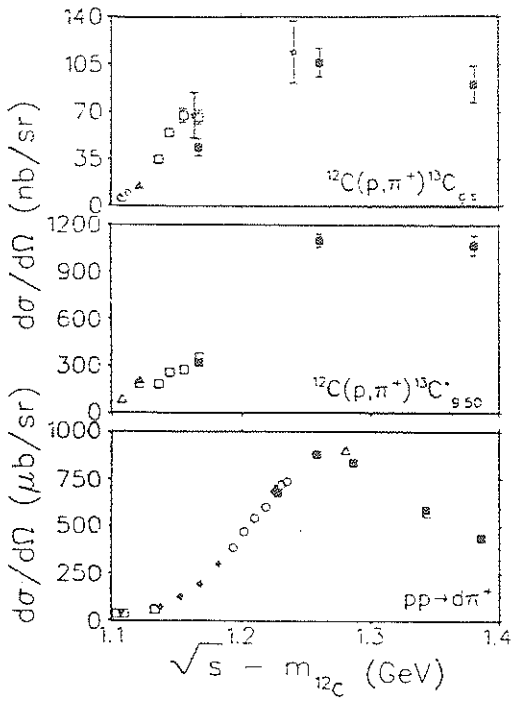

Figure 1.13: Differential cross section versus the *significant* energy variable for a constant four momentum transfer (t=0.50 GeV^2/c^2) for the ^{12}C(p,π^+)^{13}C reaction (ground state and 9.50 excited state) and the pp $\rightarrow$ dπ^+ reaction.

For certain A(p,π^+)A+1 reactions, and particularly close to threshold, the analyzing power has shown striking similarity to that of pp $\rightarrow$ dπ^+, especially when a kinematic transformation like that suggested by Couvert and Huber is performed (see Fig. 1.14 from Ref. [Jon79]). The peak in the cross sections at or near the energy where the Δ_{1232} may be excited and the similarity of the analyzing powers when comparisons are made on the basis of the significant kinematic variable provides strong evidence that the (p,π^+) mechanism in nuclei is very similar to that of the fundamental elementary process (that is, to pp $\rightarrow$ dπ^+).

Two recent works in pion production are those from Huber [Hub88] at TRIUMF and Korkmaz [Kor87] at IUCF. Korkmaz investigated the state

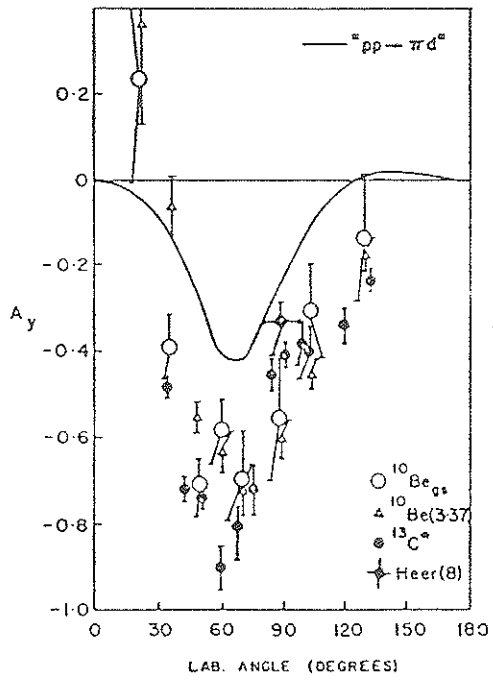

Figure 1.14: Analyzing powers for some (p,π^+) reactions around 200 MeV: ^{9}Be($\vec{p}$,π^+)^{10}Be$_{g.s.}$, ^{9}Be($\vec{p}$,π^+)^{10}Be$^*_{3.4}$ and ^{12}C($\vec{p}$,π^+)^{13}C* (average of three excited states) compared to the pp $\rightarrow$ dπ^+ reaction kinematically transformed.

dependence of $^{12,13}C(\vec{p},\pi^+)$ at 200 MeV. His work implied strong evidence for a $pp \rightarrow d\pi^+$ like underlying process. Huber's work was concentrated in the energy regime of the Δ_{1232}, and also showed evidence for an underlying $pp \rightarrow d\pi^+$ like mechanism.

This comparison to $pp \rightarrow d\pi^+$ is not a new idea. On the assumption that $pp \rightarrow d\pi^+$ is the dominating process, impulse type calculations (using $pp \rightarrow d\pi^+$ as the pion production mechanism) were developed by Ruderman [Rud52] and Kurath [Kur87]. The argument appears to be quite valid near threshold since the cross section for σ_{10}^{d} is much larger than σ_{10}^{np} or σ_{11}. This can be seen in Fig 1.1. The T matrix for the A(p,π^+)A+1 reaction is written as a sum over the possible nuclear pp interactions, described by the $pp \rightarrow d\pi^+$ differential cross section. The calculations require a kinematical transformation for the $pp \rightarrow d\pi^+$ data to obtain results for the nuclear reaction and the form of this transformation depends on the choice of how to deal with the offshell effects. Most calculations have been done with plane waves, but some authors have gone a little further and included distortions in the wave functions [Fea77]. Since these phenomenological calculations only used differential cross section data, no predictions of the analyzing powers could be made. Huber [Hub88] and Korkmaz [Kor87] have both used a kinematic transformation to compare the $pp \rightarrow d\pi^+$ reaction analyzing powers to their nuclear results and found qualitative agreement.

In this spirit a calculation which uses the $pp \rightarrow d\pi^+$ amplitudes is compared to the work of this thesis. The model uses the antisymmetrized nuclear wave function with the Pauli principle used explicitly. This calculation, along with others, will be more completely discussed in a later chapter.

1.3 Few Nucleon Exclusive Pion Production

A full microscopic calculation for pion production from complex nuclei is a formidable task. For this reason a profitable approach may be to consider pion production on few body nuclei. It is hoped that the task is simplified by decreasing the number of nucleons for a many body problem. Furthermore, the observables are not as sensitive to the nuclear structure details since the nucleons are mostly s-state and therefore the calculations are simplified in this respect as well.

There exists a substantial body of data for the ^{1}H($\vec{p}$,π^+)^{2}H and ^{2}H($\vec{p}$,π^+)^{3}H reactions. For the next s state nucleus, He, there are several measurements of the differential cross section. Data for the angular distributions are available close to threshold (Refs.[Wil+81], [Keh+86] and [LeB+85]), near the resonance energy, at 415 MeV, from Orsay [Tat+76] and at 800 MeV from Los Alamos National Laboratory[1] (LAMPF) [Hoi+84]. There is also a measurement from CERN at 600 MeV and 0° [Gab+72] and an old measurement from Dubna [ASS62]. Data from the time reversed charge symmetric reaction for energies across the Δ_{1232} resonance energy [Kal+78] may be transformed using charge symmetry and detailed balance to obtain data for the ^{3}He(p,π^+)^{4}He reaction.

Previous measurements have shown that the analyzing power is a very important observable of investigation, particularly when considering the energy dependence. Other spin observables have not been measured but could also prove to be equally or more useful than the analyzing power. Such analyzing power data for the ^{3}He($\vec{p}$,π^+)^{4}He reaction exists near threshold from IUCF [Keh+86] and at 800 MeV from LAMPF [Hoi+84]. In Fig. 1.15 the data of Kehayias *et al.* are shown with an ORCHID calculation [BAD90a]

[1] also known as the Clinton P. Anderson Meson Physics Facility

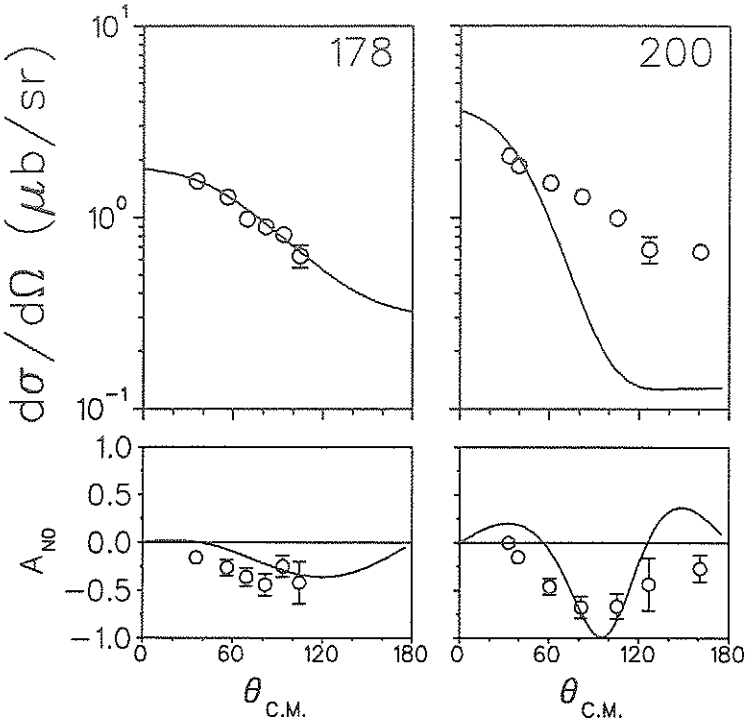

Figure 1.15: ORCHID calculation for ^{3}He($\vec{p}$,π^+)^{4}He at 178 and 198 MeV compared to the data of Kehayias *et al.* from IUCF.

for the reaction. It is observed that the calculation agrees quite well with the data near threshold. However, little more may be learned without other measurements at higher energies. For the ^{4}He($\vec{p}$,π^+)^{5}He reaction there is only polarization data from LAMPF at 800 MeV [Hoi+84]. The ^{3,4}He($\vec{p}$,π^+)^{4,5}He reactions data from Höistad *et al.* are shown in Fig. 1.16. The analyzing powers for the ^{3}He($\vec{p}$,π^+)^{4}He reaction are observed to have a large oscillatory behaviour, distinctly different from the results near threshold. The data near threshold are quite similar to those of low energy pp $\rightarrow$ dπ^+ (see Fig. 1.5) and this is similar to that found for other nuclei as well (see Ref. [Fea81] for example). By studying the analyzing power for these reactions as the proton bombarding energy increases, one may hope to achieve some understanding of the (p,π^+) reaction in few body nuclei.

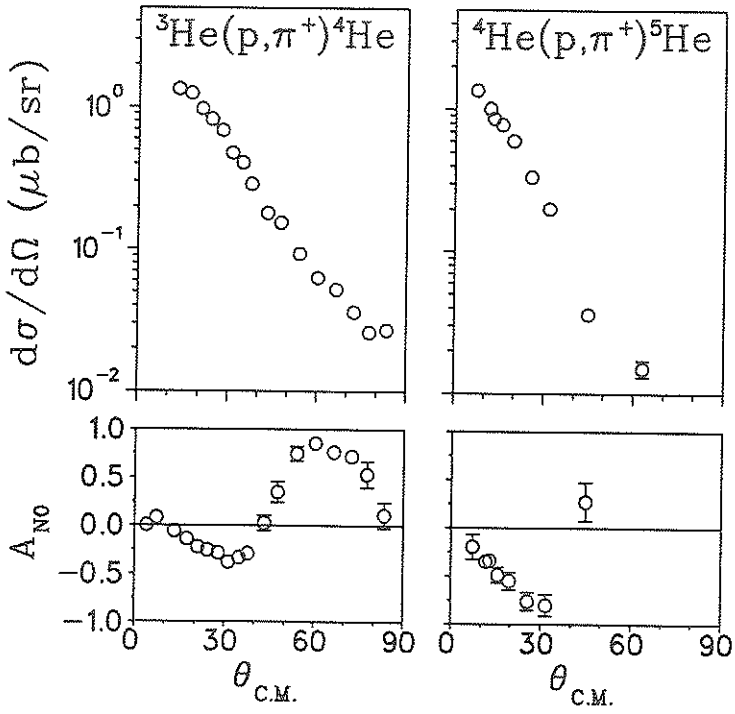

Figure 1.16: Differential cross sections and analyzing powers for the ^{3,4}He($\vec{p}$,π^+)^{4,5}He reactions at T_p = 800 MeV from Höistad *et al.*

An obvious void of analyzing power data for ^{3}He($\vec{p}$,π^+)^{4}He and ^{4}He($\vec{p}$,π^+)^{5}He exists in the region between threshold and 800 MeV. In light of the importance of the Δ_{1232} in these reactions the present study investigated the differential cross sections and analyzing powers in the region between threshold and 800 MeV, the energy region spanning the Δ_{1232} resonance.

1.4 Summary

The subject of this thesis then, is to examine (p,π^+) reactions in few body systems. In so doing, one hopes to achieve an understanding of the (p,π^+) reaction mechanism where the system is relatively simple. The observable which has proven to be most useful for understanding pion production is the analyzing power. Therefore, measurements of the differential cross section and analyzing powers for the ^{3}He($\vec{p}$,π^+)^{4}He ($J^\pi = 0^+$) and ^{4}He($\vec{p}$,π^+)^{5}He ($J^\pi = \frac{3}{2}^-$) reactions were performed. These experiments were carried out at TRIUMF using a cryogenic liquid helium target and a magnetic spectrometer. The outline of these experiments is discussed in Chapter 2. The data were analyzed and the methods used are discussed in Chapter 3. Results are presented and are compared to existing data and data from other reactions in Chapter 4. In Chapter 5 early theoretical calculations are discussed as well as the comparison of the data with two recent calculations, a pp $\rightarrow$ dπ^+ IMPULSE model, and a microscopic ONM/TNM model (ORCHID). The conclusions drawn from the work of this thesis are then summarized in Chapter 6.

Chapter 2

Experiments

The experiments for the work described in this thesis were performed at the TRIUMF cyclotron laboratory in Vancouver, CANADA. There were two experiments performed and these are summarized in Table 2.1.

Expt	Reaction studied	Dates of running experiment
E413	^{3}He($\vec{p}$,π^+)^{4}He	Sept 30-October 9, 1988
E564	^{4}He($\vec{p}$,π^+)^{5}He	May 1-11, 1990

Table 2.1: Experiments of this work.

Polarized protons from a polarized ion source were accelerated by the TRIUMF cyclotron and extracted down the proton hall beam line 4B (BL4B). The proton beam was incident on the University of Manitoba/TRIUMF liquid ^{3,4}He target mounted on the 4BT2 scattering chamber. Scattered pions were detected by the Medium Resolution Spectrometer (MRS), and the recoil nucleus was left undetected. Each of these facets of the experiment will be discussed in detail in the following sections.

2.1 Proton Beam

The ion source (POLISIS) is a Lamb shift polarized proton ion source [BMS82] which produces H^- ions with polarizations of typically 70%. These polarized H^- ions are then accelerated by the TRIUMF cyclotron [CES77]. The TRIUMF cyclotron is a sector focussed isochronous cyclotron and accelerates H^- ions to energies between 180 and 520 MeV. To select the beam energy a stripping foil is placed in the circulating beam at a chosen cyclotron radius. The foil strips off the two electrons and the resultant H^+ ion, the proton, is then bent out of the cyclotron tank by the cyclotron magnetic field. The beam is subsequently transported down beam line 4B (BL4B), shown in Fig 2.1, by a series of bending and quadrapole magnets to the MRS scattering chamber (4BT2), and then onto the proton hall beam dump.

Along the beam line there are various beam property monitors. At the 4BT1 position (see Fig.2.1), there is the In-Beam-Polarimeter (IBP) which monitors the beam polarization and intensity via proton elastic scattering [Abe+85]. A schematic of the electronic logic of the IBP is shown in Fig. 2.2. A Secondary Emission Monitor (SEM) also monitors the beam current at a position down stream of the 4BT2 target (4BM8 in Fig. 2.1) via secondary electron emission from the proton energy deposited in Aluminum. The IBP and SEM provide independent measures of the number of beam protons, at positions upstream and downstream of the target. The method of extracting number of beam protons and their polarization from these monitors is discussed in the Analysis Chapter.

Other monitors along the beam line measure the beam profile as, for example, 4BM7 in Fig. 2.1, just upstream of the MRS scattering chamber. These monitors serve to aid in tuning the beam line transport and provide data for beam profiles for the purpose of Monte Carlo modelling of the ex-

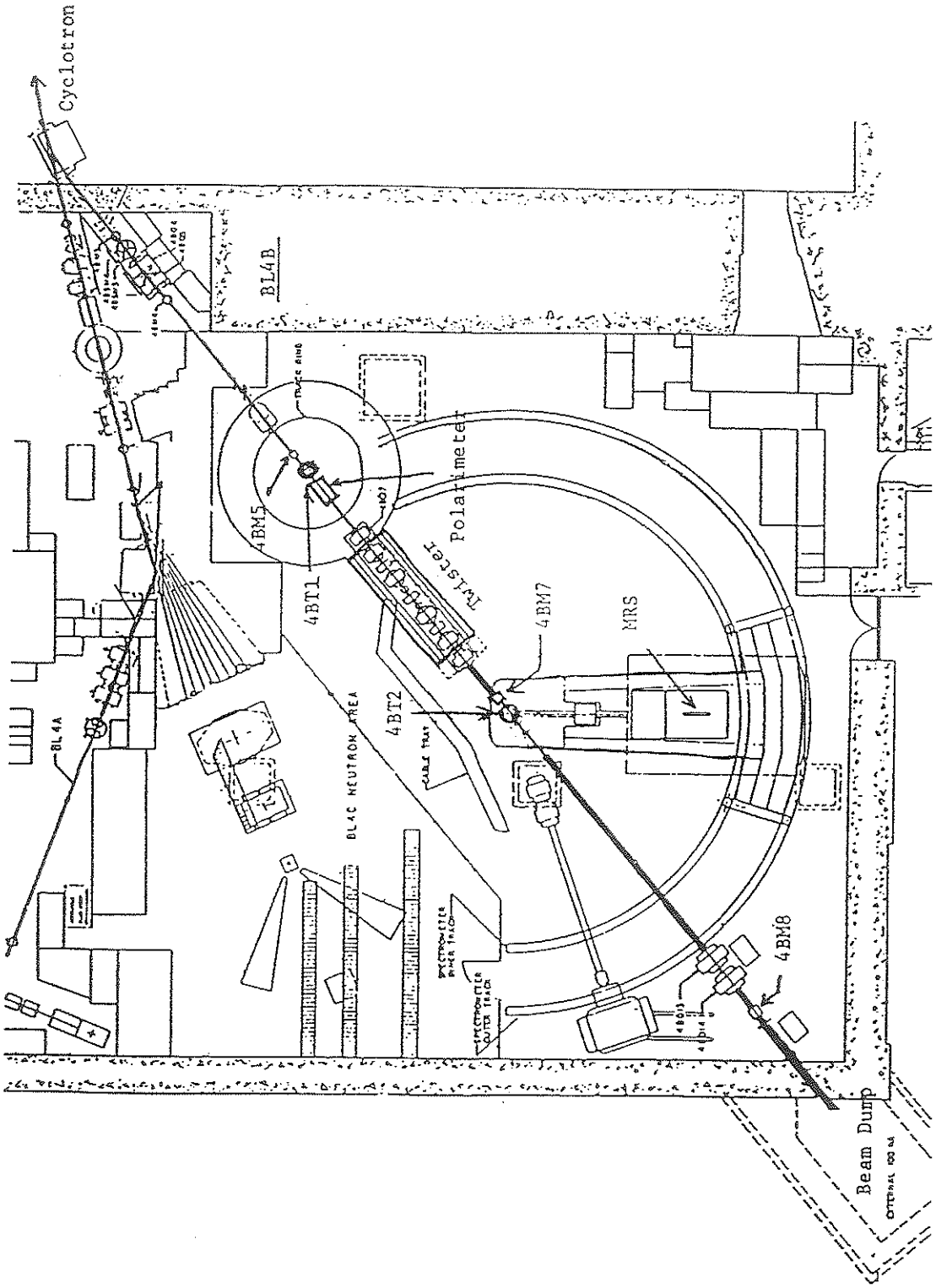

Figure 2.1: TRIUMF beam line 4B.

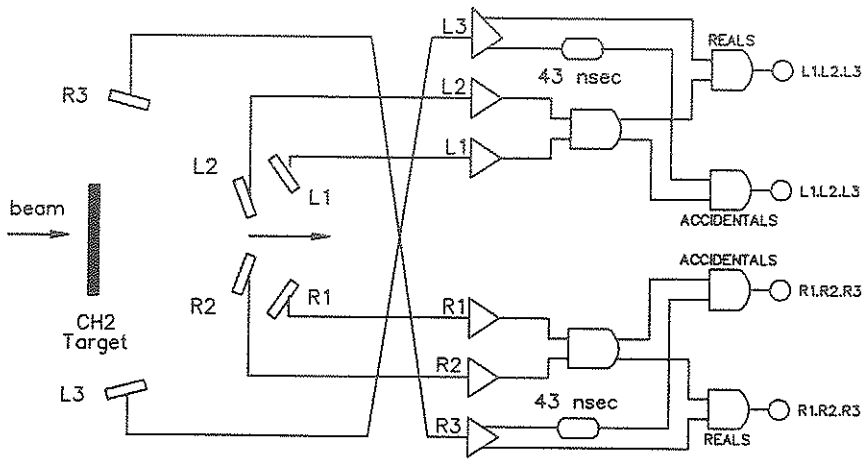

Figure 2.2: Schematic of the electronic logic of the BL4B In Beam Polarimeter.

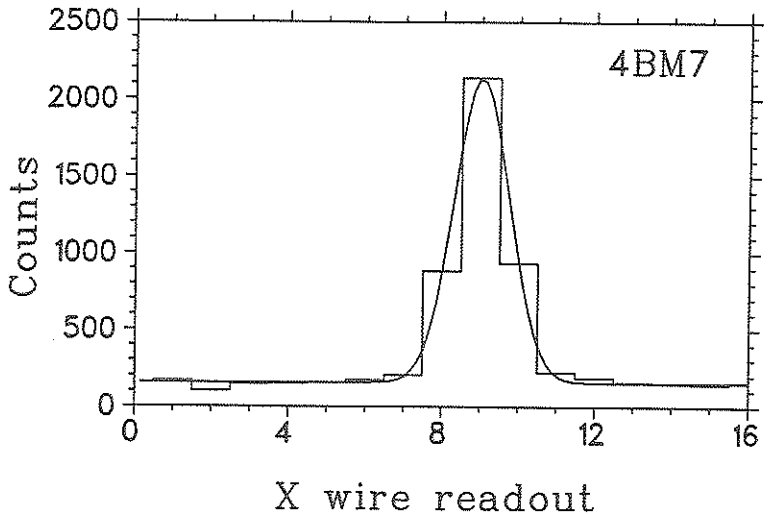

Figure 2.3: Beam profile monitor 4BM7 showing Gaussian fit.

periment. A sample output is shown in Fig. 2.3 along with a Gaussian fit where the horizontal scale represents 3 mm/wire.

2.2 Target

The ^{3}He and ^{4}He targets used in this study utilized the same cryostat, the University of Manitoba/TRIUMF liquid ^{3}He cryostat. The cryostat was originally built for p +^{3}He elastic scattering measurements for the MRS at TRIUMF [Has+81] more than ten years ago. Since the present experiments were also done on the MRS the target was ideal for these measurements. The cryostat had not been used for several years and required much refurbishing to make the target stable and reliable for the present experiments. The cryostat is shown diagrammatically in Fig. 2.4. In this section the cryostat design, instrumentation and operation and the various tests and calibration measurements of the target will be discussed.

2.2.1 Cryostat Design and Modifications

The cryostat was initially intended to operate as it did for the ^{3}He($\vec{p}$,p)^{3}He experiments. This was not found to be possible, and several major modifications were done to the cryostat design.

Helium Gas Handling System

The cryostat originally had its own gas handling system [Has+81] and this was removed for a more modern and reliable system. The system was replaced with the *Helium Gas Handling Cart* from the TRIUMF Cryogenic Targets Group (CTG). A manifold was constructed to interface between the

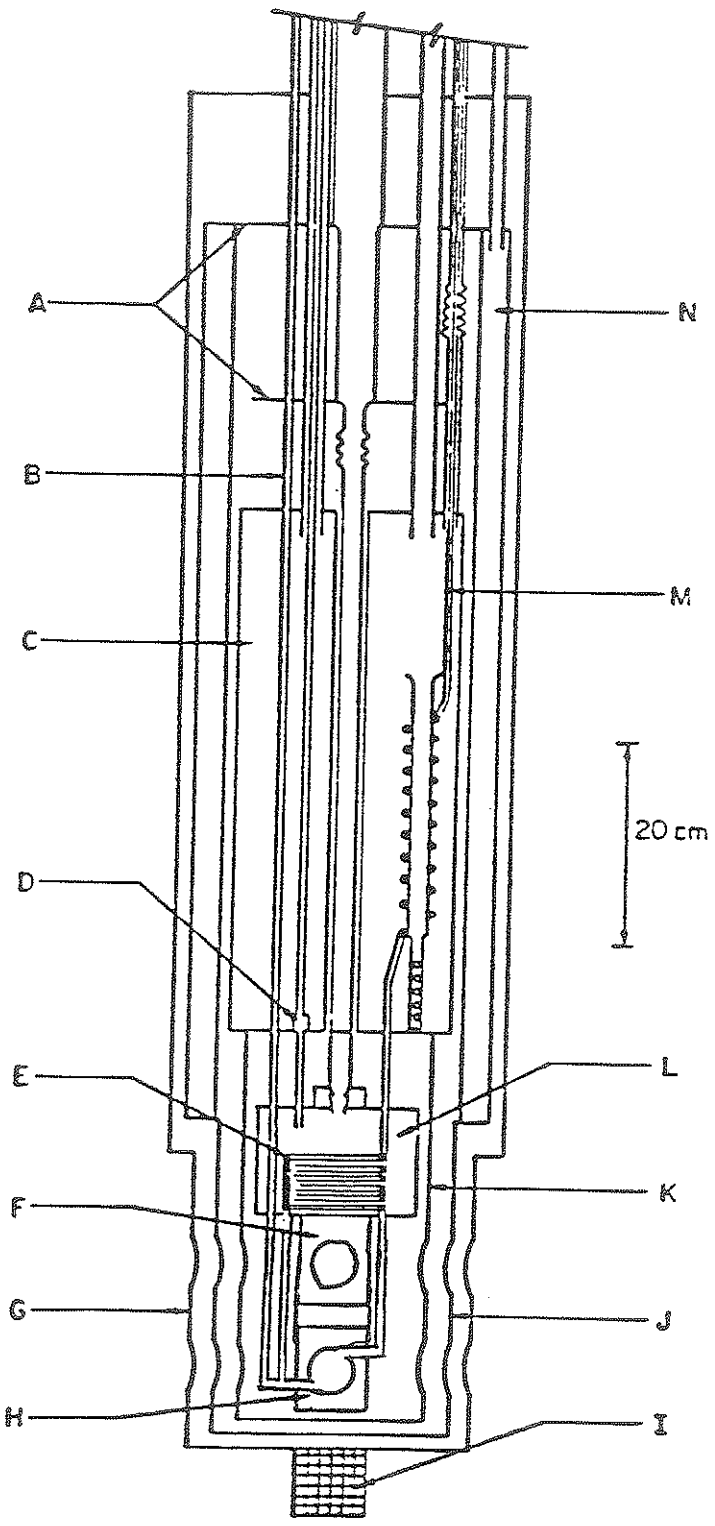

Label	Definition
A	Copper radiation shield
B	^{3,4}He gas outlet
C	Liquid ^{4}He reservoir
D	Needle valve
E	^{3,4}He condensing coil
F	Dummy target cell
G	Tail section
H	Target cell
I	Scintillating screen
J	Liquid nitrogen shield
K	Liquid helium radiation shield
L	Pumped liquid helium bath
M	^{3,4}He gas inlet
N	Liquid nitrogen jacket

Figure 2.4: University of Manitoba/TRIUMF liquid ^{3}He cryostat.

CTG Gas Cart and the cryostat. A schematic of the gas handling system is shown in Fig. 2.5. The black circles, unless otherwise indicated, are manually operated valves. The liquid N_2 (LN2) cold traps serve to trap out any moisture which would cause blockages in the target gas feed and return lines inside the cryostat. The manifold was designed with extra ports for the purpose of connecting to a leak detector and/or a helium bottle during test runs. The SCRAM valve[1] is a valve which opens when the pressure, monitored by a pressure transducer, exceeds some preset point. In this way the pressure is not allowed to rise above a certain value avoiding possible line ruptures or explosions. PT1 and PT2 are the pressure monitoring devices discussed in the Instrumentation Section (Section 2.2.2) below.

Target Cell

The target design originally used nickel windows soldered to the target and dummy cell. This method was found to be very unreliable, developing vacuum leaks after a few cyclings to LN2 temperature. A new design was therefore implemented for the target cell but the dummy cell was left in the original design since its vacuum integrity was not crucial. The design used Indium sealed flanges for the windows and the couplings for the cell to the cryostat feed and return lines. In Fig. 2.6 the general design of the target cell is shown illustrating how the connections to the *feed* and *return* lines are made. The details of the dimensions and geometry are shown in Fig. 2.7. This new design produced vacuum integrity with relatively simple installation procedures. The system was tested by subjecting the cell to cryogenic temperature cycling with liquid Nitrogen and Helium, and was found to be very reliable.

[1]Nupro Co., Willoughby, Ohio, USA.

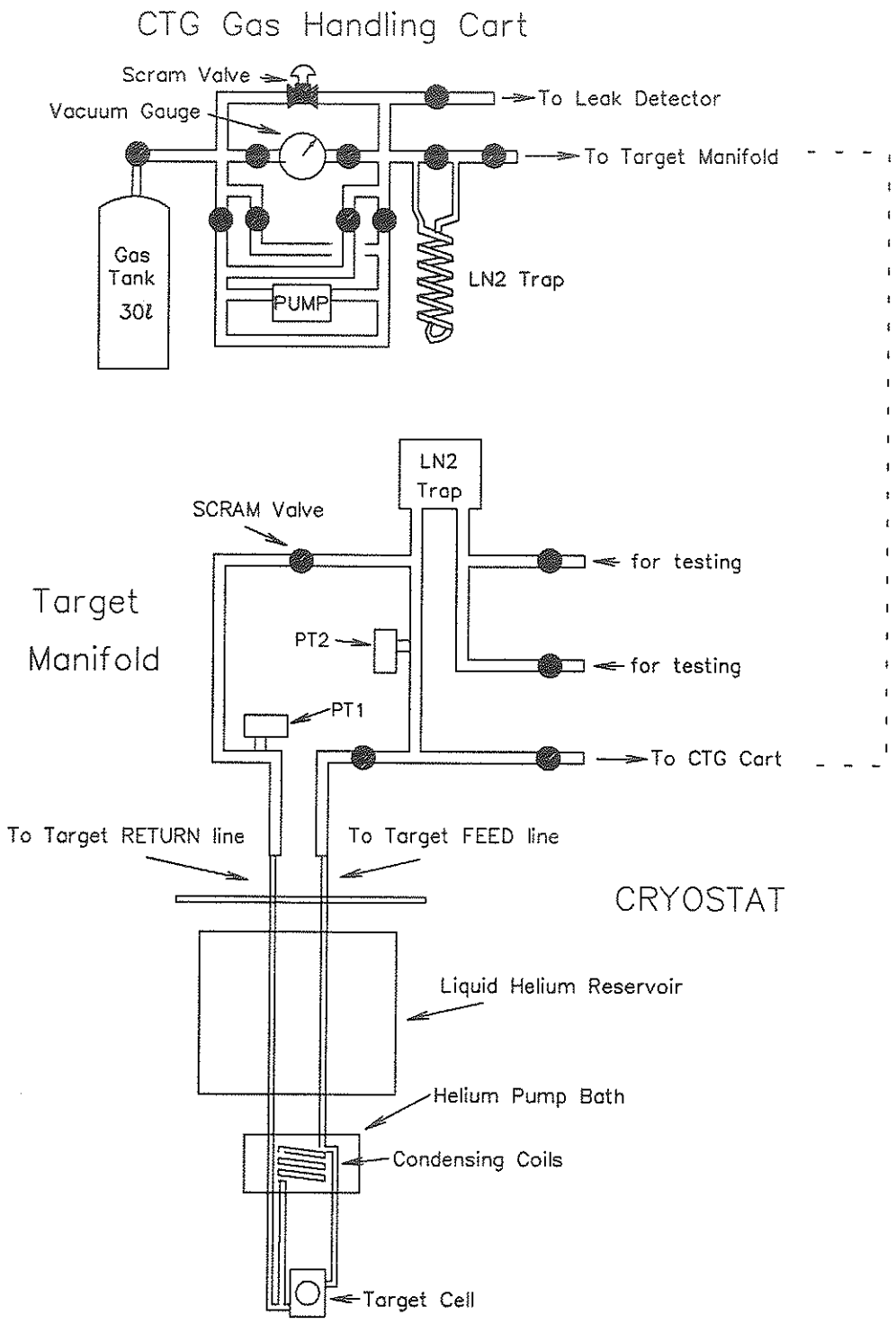

Figure 2.5: Schematic of helium gas handling system.

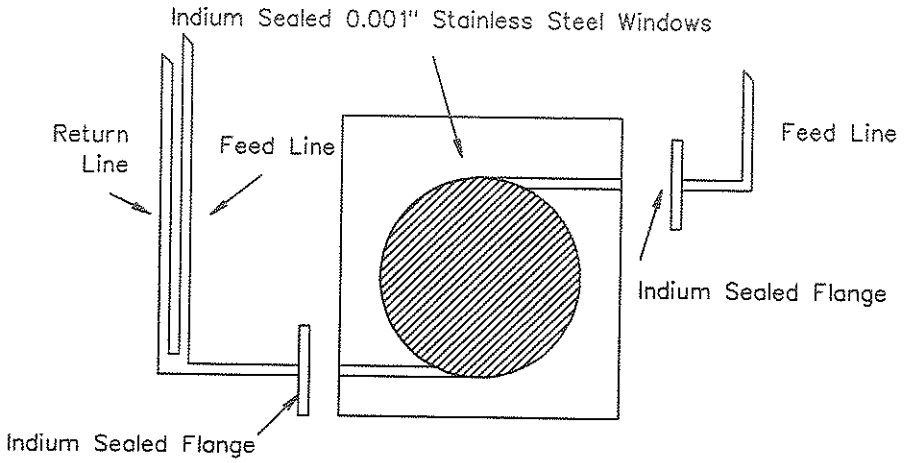

Figure 2.6: Target cell general design showing the connections to the *feed* and *return* lines with Indium sealed flanges.

In the original design, the target cell was above the dummy cell. That is, the target cell was nearest to the Pumped Bath. Working in the area of the target cell beneath the Pumped Bath with this design proved very painstaking. By switching the positions of the target and dummy cell, placing the dummy cell above the target cell, provided much more room in which to work, and simplified the procedure of changing windows or target cells. In this new position the target cell is substantially farther from the cold sink, the Pumped Bath, and there was some initial concern if this design would jeopardize condensation of the helium gas to liquid. Tests showed that the cell would approach only 3K when under vacuum. However with helium in the cell, the liquid itself provided ample cooling of the cell and temperatures around 2K were reached.

2.2.2 Instrumentation

The cryostat is comprised of many devices for the purpose of monitoring the performance of the target. The device controllers and outputs were contained

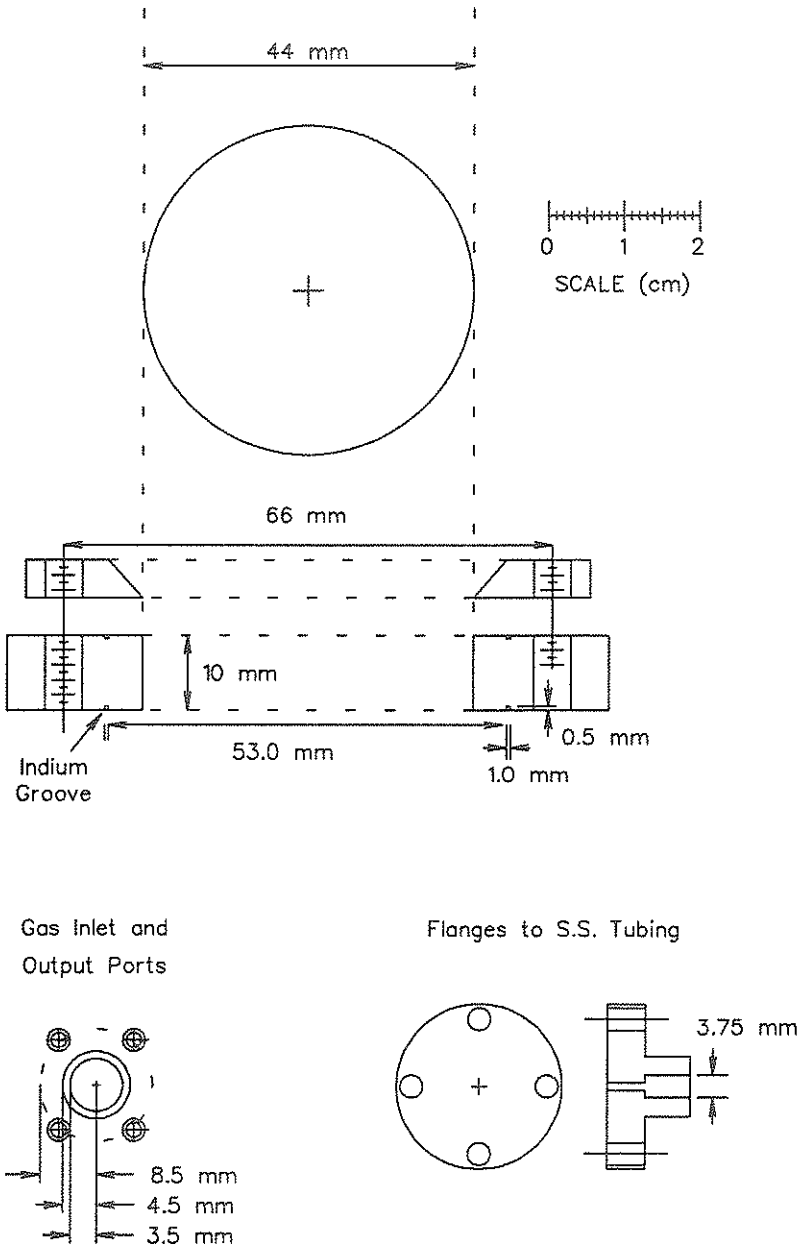

Figure 2.7: Schematic of target cell indicating the dimensions and geometry.

in two racks, *Local* and *Remote*. The Local rack contained all the monitoring device controllers and outputs and was situated by the cryostat. The *Remote* rack contained only some of the important ones, and was situated in the Counting Room during the experiment. The devices used to monitor the cryostat performance are now discussed.

Vacuum

The vacuum measurement ranges from 10^{+3} to 10^{-7} Torr and to cover such a broad range in pressure several devices were used. The vacuum system is shown schematically in Fig. 2.8. G type gauges are mechanical differential vacuum gauges used for monitoring the vacuum from atmosphere down to around 50 Torr. The TC type gauges are Thermo-Couple Gauges[2] whose sensitivity is from around 1 to 10^{-3} Torr. From there down to the level of 10^{-7} Torr Ion Gauges[3] (IG) are used. For historic reasons, the vacuum region is separated into two regions, VAC1 and VAC2. VAC2 refers to the area around the target cell, and VAC1 is everywhere else. Originally these areas were to be separated by a Kapton window so that in the event of a target cell window rupture the costly ^{3}He could be recovered. It is not known whether such a window was ever implemented and tested. The cryostat in its present state does not have a physical separation and so VAC1 and VAC2 are always at the same vacuum.

Initial rough pumping from atmospheric pressure was done with a mechanical oil pump[4]. After the system is roughed down to $\approx 10^{-4}$ Torr further pumping down was done by two water cooled diffusion pumps[5], DP1 and

[2]Varian, Vacuum Division, Lexington, Mass., USA.

[3]Granville-Phillips Company, Boulder, Colorado, USA.

[4]Sargent-Welch Scientific Co., Skokie, Illinois, USA

[5]Varian, Vacuum Division, Lexington, Mass., USA.

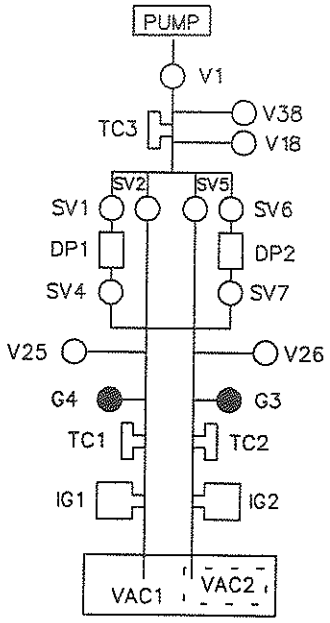

Figure 2.8: Schematic of vacuum system.

DP2. The vacuum system also contains many types of valves where the V type are mechanically controlled valves, and the SV type are electrically controlled air powered Solenoid Valves. The SV's are used with the TC gauges in a vacuum interlock system in the event of a vacuum failure.

Helium Monitoring

The cryostat has two liquid Helium regions used to cool the cryostat, the *Reservoir* and the *Pumped Bath*. The reservoir is filled about once per day and the bath is filled from the reservoir using the Needle Valve about once every four hours. This is shown in Fig. 2.4. Self regulating control of the needle valve via a motor formed part of the original design. It was found however that the torque required to turn the needle valve when the cryostat was at Helium temperature was quite substantial and therefore the present design was not functional.

The level of liquid helium in the reservoir is monitored using an Superconducting level probe[6]. The level of liquid helium in the bath is monitored using a chain of seven carbon resistors. The difference in the resistance when the superconducting wire (or a carbon resistor) is in an atmosphere of saturated helium vapour and when it is submersed in liquid helium, is used to determine the helium level.

The cell is cooled by pumping on the helium in the pump bath with a mechanical oil pump[7]. The pump reduces the vapour pressure of the liquid helium in the bath to $\approx$ 1 Torr which corresponds to a bath temperature of $\approx$ 1.5 K. The bath pressure is monitored with a mechanical differential vacuum gauge and a thermocouple gauge.

Target Cell Monitoring

Mounted on the target cell are two calibrated Germanium resistors[8]. One is mounted on the top and the other mounted on the bottom, denoted RT1 and RT2 respectively. By performing four wire resistance measurements the resistance of RT1 and RT2 can be accurately obtained. From the calibration provided by the manufacturer the temperature of the target cell is then deduced (see Fig. 2.9). The temperatures RT1 and RT2 did not always agree. When the cell is under vacuum it was found that the bottom resistor read a slightly higher temperature than the top. One possibility for this discrepancy is that the cooling is mainly by conduction when the cell is under vacuum, and since the bottom is farther from the cold sink its temperature is higher. When the cell is filled with liquid helium the top is found to be slightly

[6]Oxford Instruments, Oxford, England

[7]Sargent-Welch Scientific Co., Skokie, Illinois, USA

[8]Lake Shore Cryotronics, Inc. Westerville, Ohio, USA.

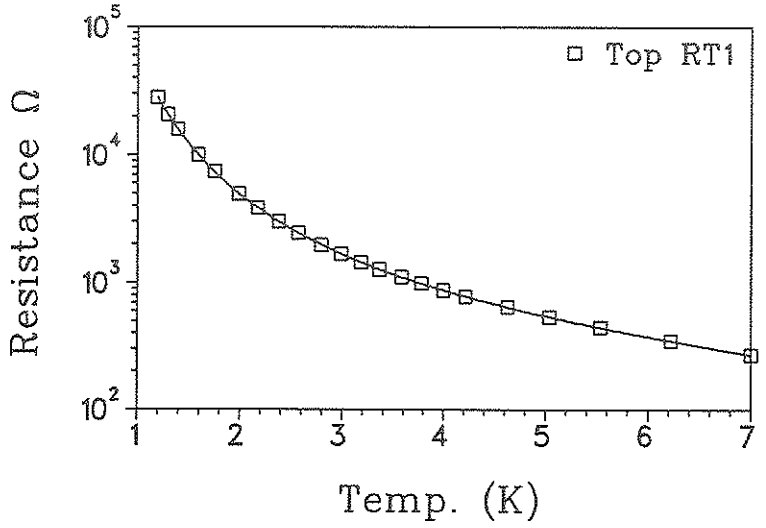

Figure 2.9: Calibration of Top resistor.

higher. Again, a plausible explanation is that it is a result of the mechanism of the cell cooling, which in this case is the liquid helium. The feed line *from* the condensing coil is connected to the bottom of the cell and the boil off return *to* the condensing coil is connected to the top of the cell. Therefore the lower portion of the cell is slightly cooler than the top of the cell since it is closer to the source of cooled helium. The discrepancy is about 0.2 K and therefore the uncertainty in the temperature is estimated to be 0.2 K.

For the purposes of studying the cell's response to a heat load, a heater was mounted on the target cell. The heater is comprised of a length of Manganin wire which has a resistance of 200 Ω. By using a constant current supply, the power dissipated in the heater may be controlled.

The pressure of the target gas lines are monitored via pressure transducers[9],

[9]National Semiconductor Corp., Sunnyvale, Calif. USA.

PT1 and PT2. These are mounted on the target manifold, see Fig. 2.5, and provide a voltage which is linearly dependent on pressure. The zero point is determined by measuring the output voltage when the transducers are at vacuum, and the slope determined by combining this measurement with one at another known pressure, usually atmospheric. The linearity is very stable for these devices but the offset must be checked often[10].

Computer

Most of the signals from the cryostat are sent to an ADC card mounted on an IBM PC computer allowing online monitoring and storage of data. The TRIUMF written software program TICS [Kei89] was used[11]. The program is widely used at TRIUMF and has the capability of generating time line curves for the monitoring devices. An example of these is shown in Fig. 2.10. This figure was produced by a *screen dump* on the IBM PC and so what is seen in Fig. 2.10 is what is seen on the IBM PC screen. The example shows four devices: RT1, RT2, PT1 and PT2 each represented by a graph in a box. In each box is shown the *y-range* and the *time-range*. The numbers in the top right hand corner of each box is the time and the average readout for the device sampled at the time indicated by the vertical line in the box. For example for RT1, a time of 0:12:20 was selected and the average value of RT1 was 3.217 K at that time. The time in top left corner of the page is the absolute time and date of the screen dump, 14:09:55, Sept 15. Note that one may look back at the data previously logged as well as at data currently logged.

The information is logged to hard disk at a preset frequency. For the

[10]Private communication with TRIUMF CTG technicians.

[11]TICS was implemented on the target's IBM PC by G. Waters and F. Duncan

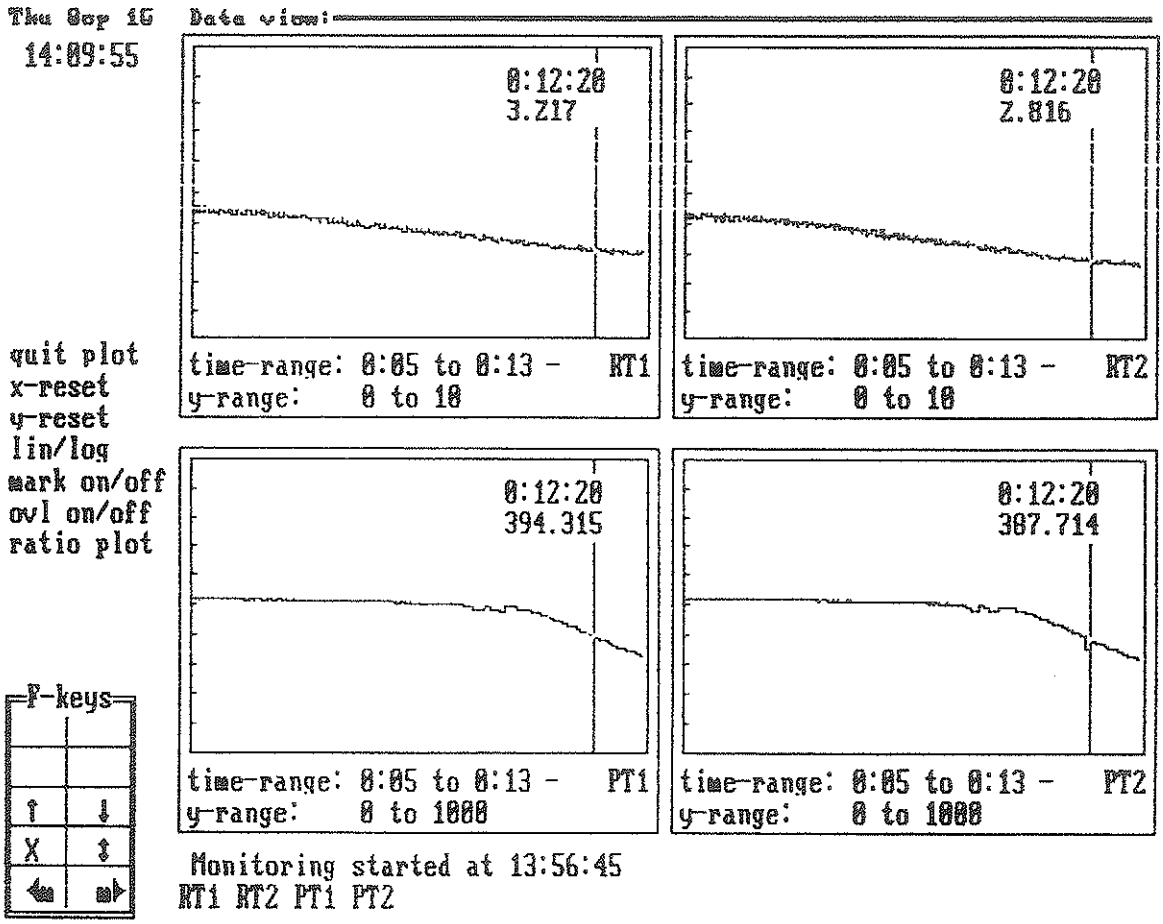

Figure 2.10: Computer information page.

experiment the time bins were usually five minutes and for the test runs, usually on the order of seconds. For a particular device the computer logs the average, maximum and minimum value recorded in the time bin. The sampling resolution is on the order of several msec so that any bursts from the average in the time bin will appear in the maximum and minimum values. In the plots shown in Fig. 2.10 the points are the average and the error bars are the maximum and minimum values, *not* the average deviation.

The log files on the IBM hard disk were transferred onto VCR Exabyte tapes for permanent storage. This stored information was then transferred to a VAX computer to study the stability of the target operation during the experiment.

2.2.3 Operation

It was intended to make the operation of the target as simple as possible in order to minimize effort and of course minimize mistakes during the course of an experiment. It was found that one experienced person with the help of another was required to operate and maintain the target.

Cool Down

The cryostat cool down from dormant state at room temperature to operational state at 2K requires a minimum of two days. The cryostat is first evacuated in all regions, except the LN2 jacket. Depending on the amount of humidity and how long the cryostat has been dormant, this rough down to 10^{-4} Torr takes approximately 8 to 24 hours.

Following this rough down the Helium Pump Bath and Reservoir are flushed with high purity N_2 gas several times to prevent moisture blockages

in later stages of the cool down. Subsequently the LN2 jacket is filled and after an intial cryo pumping period, usually half an hour, the Helium Bath and Reservoir are filled with LN2 to allow precooling. This period takes approximately 8 hours. The vacuum at this point has improved from that at room temperature and is around 10^{-5} to 10^{-6} Torr.

Once the cryostat is precooled to LN2, the LN2 is blown off from the Reservoir and Bath and the latter purged several times using high purity Helium gas. This step is crucial as any residual LN2 may cause blockages when the cryostat is cooled to 4K. After one is confident that all the LN2 is removed and the Reservoir and Bath only contain helium gas, one then introduces liquid ^{4}He to the reservoir. During the Reservoir filling stage the Needle Valve between the Bath and Reservoir is opened to allow filling of the Bath. To avoid possible seizing of the Needle Valve, the Needle Valve is opened and closed periodically. During and following the filling stage the vacuum has improved to typically 10^{-6} or 10^{-7} Torr.

Once the ^{4}He bath level indicators show the Bath is full, the Helium Bath roughing pump is started, and the Bath temperature gradually drops to about 1.6 K in approximately one hour. At this point the ^{3}He (or ^{4}He) gas is introduced to the target cell (which has been under vacuum this entire time). The Helium gas condenses and the target cell now contains liquid ^{3}He (or ^{4}He). The system stabilizes in about an hour to a temperature of about 2K and a vacuum of typically 10^{-7} Torr.

Maintenance

Once the system stabilizes only periodic maintenance is required. The Needle Valve is opened periodically during the experiment to fill the bath, usually

every four hours, and then requires about 15 minutes to restabilize to operational state. The Helium Reservoir used $\approx 25l$ of liquid helium for a fill and along with the Helium Reservoir, the LN2 jacket and the LN2 trap of the CTG Helium Cart, required filling typically once per day.

2.2.4 Tests for Liquid Helium Condensation

Before using the target in the experiment, it was subjected to several tests. One test was to confirm the condensation of liquid helium in the target cell. To test this, the heater installed on the target cell was used and the temperature response of the cell, as measured by RT1 and RT2, studied. When the cell is under vacuum, and the target cell is cooled down to approximately 2 to 4 K, the target cell heater was set to various power levels, from 5-80 mW. The rapid temperature change shown in Fig. 2.11 was observed. The explanation of these graphs was discussed in Section 2.2.2 above. The same procedure is repeated when the cell is filled with liquid helium. The temperature does not change significantly until approximately 200 mW of power is delivered into the target by the target heater. This is shown in Fig. 2.12. It is this drastic difference in response to heat load that is taken to be a clear indication of liquid condensation in the cell.

Independent evidence for the condensation of helium in the cell can also be obtained from the pressure transducer readings, PT1 and PT2. Assuming an ideal gas law for the helium one may determine the amount of helium condensed in the cell provided the volume of the gas cell and of the condensing coils is known. The volume determinations are discussed in the Calibration Section and the results are shown in that section in Table 2.2 on page 55.

For this calculation ^{3}He is assumed (a similar type of calculation is done

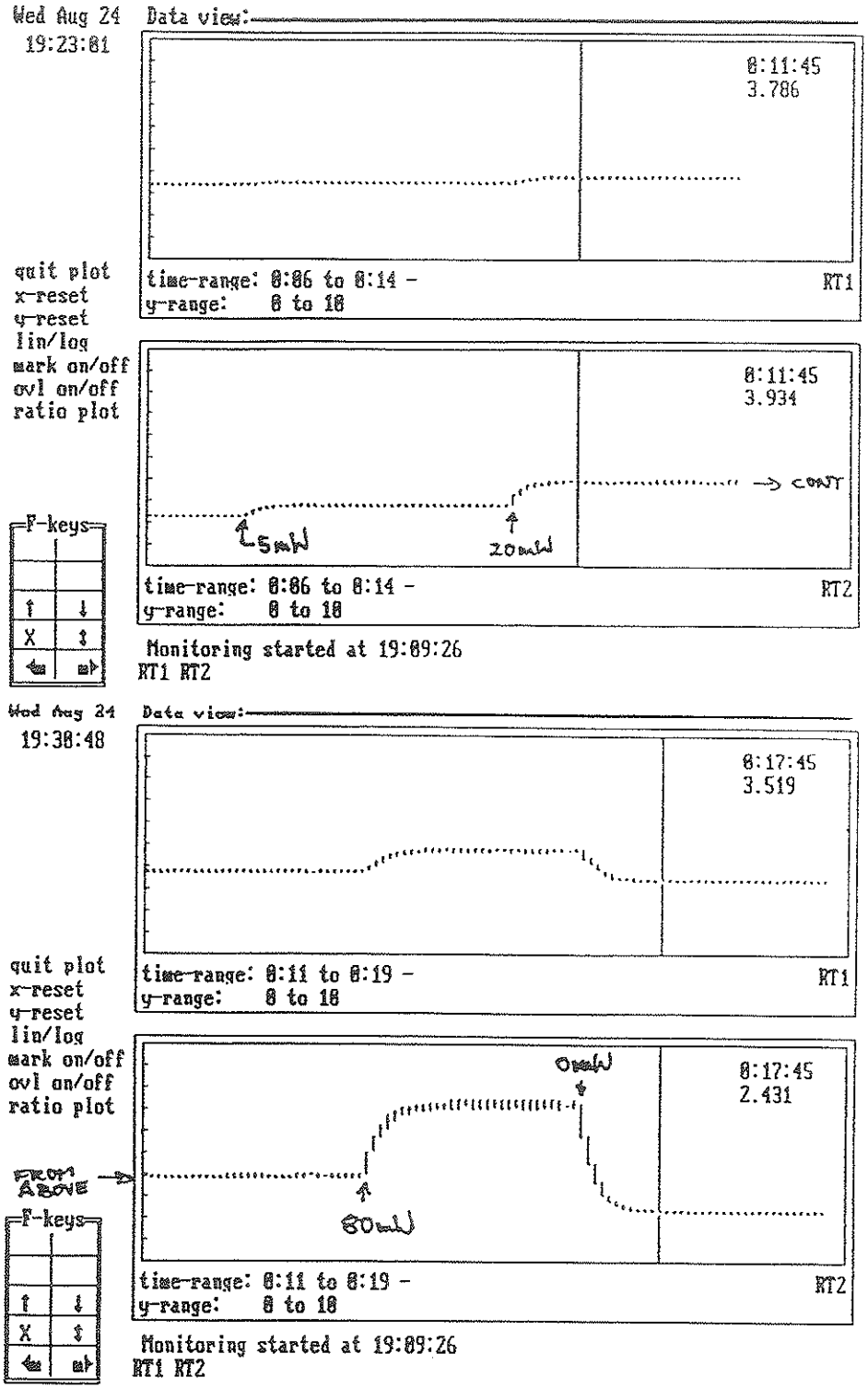

Figure 2.11: Target cell temperature response for cell under vacuum.

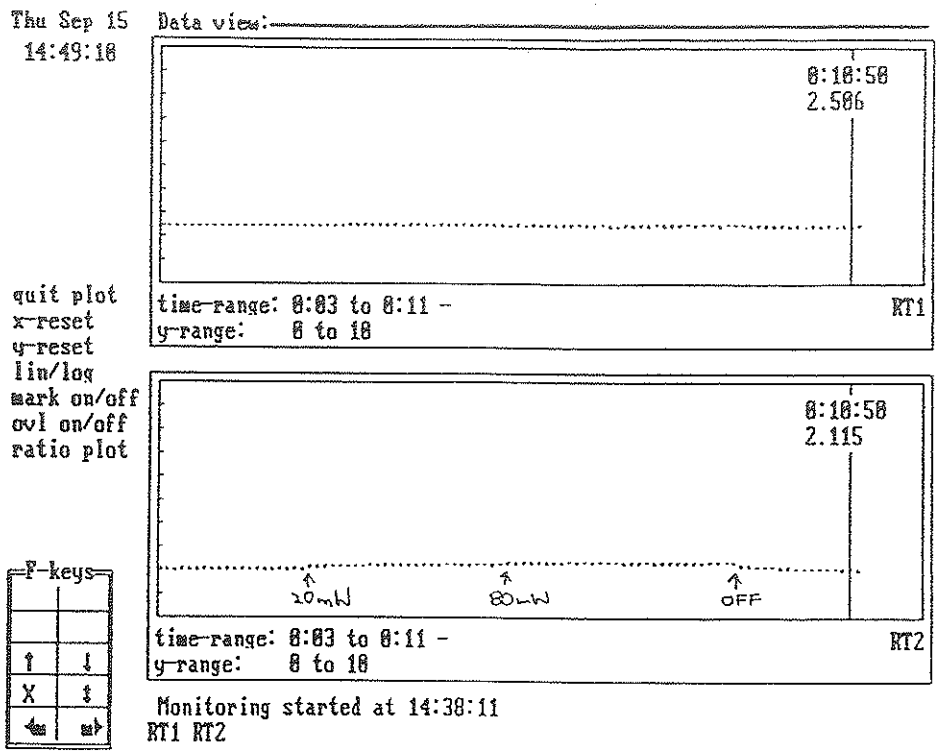

Figure 2.12: Target cell temperature response for cell filled with liquid helium.

for ^{4}He). Initially the helium gas is in a storage tank volume V_1=30l at temperature T_1=293K with some initial pressure, P_i. When the valve between the tank and the target cell is opened, the gas fills the entire system. The entire system is presumed to be at the same pressure, P_f. The notation of the volumes are shown schematically in Fig. 2.13. The gas inside the target gas lines, V_3 is at 4 K and has not condensed. This gas will therefore have a different density than that in the storage tank, V_1. The residual volume is the condensed liquid, V_2.

To calculate the relationship between the final and initial pressure and the volume of condensed liquid the calculation is performed by assuming some final volume of condensed liquid. The final tank pressure, P_f, is the same throughout the system so the final pressure must be the vapour pressure of the liquid helium at the cooled temperature. The vapour pressure tempera-

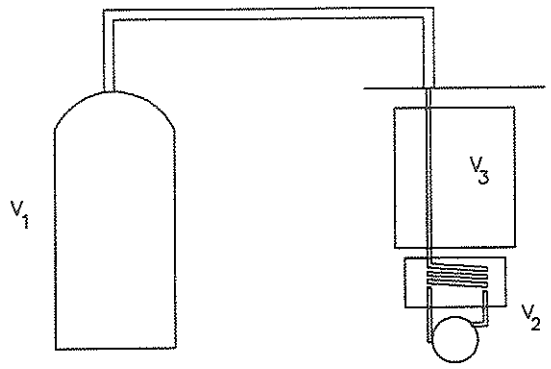

Figure 2.13: Schematic of the volumes for helium gas system.

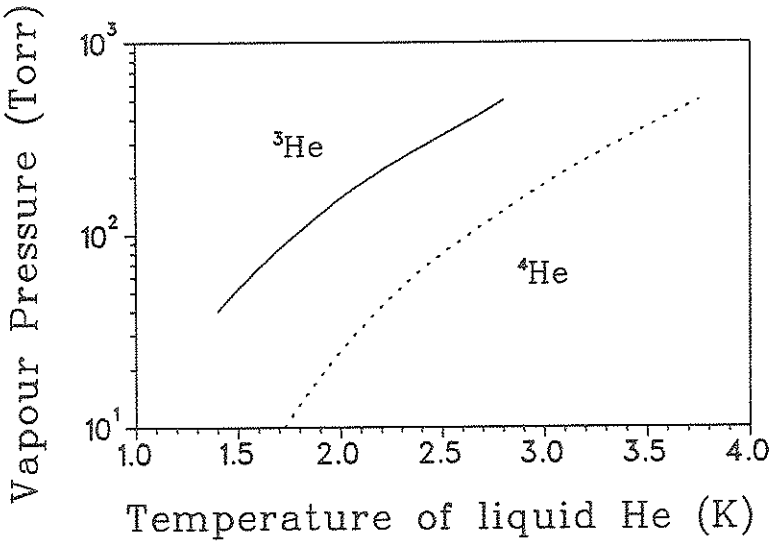

Figure 2.14: Vapour pressure-temperature curves for ^{3,4}He.

ture dependence for ^{3}He may be obtained from references [Coy66] and this is shown in Fig. 2.14. The liquid helium has a different density for different final pressures (temperatures) and this may be obtained from the density curves shown in Fig. 2.16 in the Target Density Section, on page 56. From the known molarity of ^{3}He, 3.0162 $\frac{g}{mole}$, the total number of moles of helium that are condensed, n_2 is obtained. The number of moles in the volume V_1 and V_3 may be evaluated assuming an ideal gas law.

$$n_1 = \frac{P_f V_1}{RT_1} \tag{2.1}$$

$$n_3 = \frac{P_f V_3}{RT_3}. \tag{2.2}$$

where $T_3 = 4\,K$

Now the number of moles of helium in the final system is known, and since the system is closed this must also be the number in the initial system, n_0.

$$n_0 = n_1 + n_2 + n_3 \tag{2.3}$$

Since all the helium was initially in the storage tank, the initial pressure P_i, is related to n_0 via the equation:

$$P_i = \frac{n_0 R T_1}{V_1}. \tag{2.4}$$

The results are shown in Fig. 2.15. The different lines correspond to different final condensation volumes.

Experimentally the initial pressure was 560 Torr and the final pressure was approximately 90 Torr (for the ^{3}He experiment). By interpolation of Fig. 2.15, one observes that a volume of about 30 cm^3 liquid ^{3}He did indeed condense and this corresponds to filling the target cell and condensing coil. This implies then that the target is full and ^{3}He was successfully condensed to a temperature of approximately 2K!

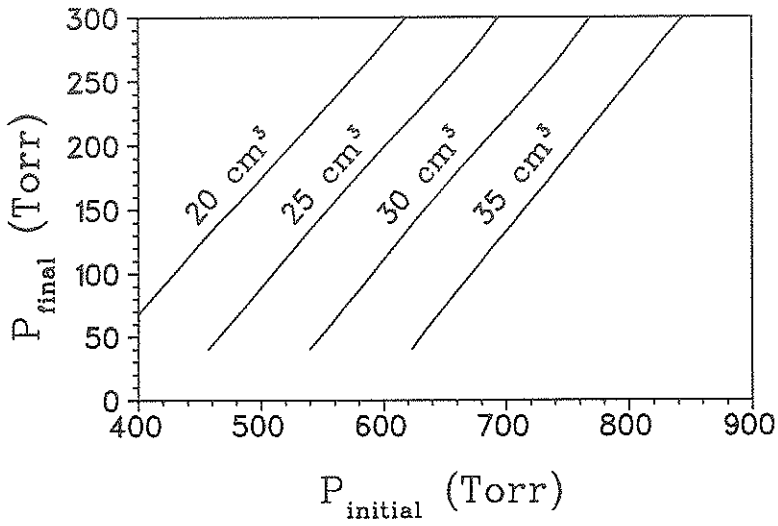

Figure 2.15: Pressure-condensed volume calculation for ^{3}He.

A similar procedure was used for the evidence of ^{4}He condensation.

2.2.5 Beam Power Dissipation

From Fig. 2.12 it is observed that the target can handle loads of 100 mW. For experiment E413 and E564 the beam energies ranged from 240 to 507 MeV and currents were as high as 30 nA for back angle measurements. The power dissipated in the target by the proton beam may be estimated by using the Bethe-Bloche equation for energy loss or from Tables [Gre87]. For 10 nA of current a 240 MeV proton beam dissipates about 6mW of power in the target cell (approximately 20% from the stainless steel windows and approximately 80% from the liquid Helium). Measurements of cross section were also performed for a specific angle but with different beam currents to investigate possible density fluctuations due to local boiling. However, to within errors, no effect was observed.

2.2.6 Calibration

Here the various calibration measurements of the cryostat and target are discussed. To determine the condensed volume of helium in the cell the volumes of the cell and associated gas lines were required. To determine the differential cross section one requires the effective target thickness which may be written as:

$$\text{Effective Target Thickness} = \rho_T(\text{He}) \times L_t \times Q \tag{2.5}$$

The absolute target density, $\rho_T(\text{He})$, was determined by examining the target temperature, T, and then obtaining the density from density versus temperature curves. The calculation of the correction factor Q and the target length L_t are discussed in the Analysis Chapter, however they are mentioned here since their calculation requires knowledge of the position of the cryostat with respect to the MRS scattering chamber. These were determined using precise instrumentation and compared with experimental results and these measurements are discussed below.

Volumes of Gas Handling System

The volumes of the helium gas handling system were determined by assuming the validity of Boyle's Law,

$$V_x = \frac{P_0}{P_x} \times V_0. \tag{2.6}$$

Using a known volume V_0 and the pressure readings from the pressure transducers, the unknown volumes V_x were obtained. The known volume was a machined brass cylinder with a total volume, including connections, of 77.3 cm^3. Using this volume for V_0 the volumes of the rest of the gas handling system were determined as presented in Table 2.2. The Method column

Gas System Volumes		
Volume	Method	Result
4K gas lines	R	20 ± 3 cm^3
Condensing coils	Hasell	≈ 12 cm^3
Target cell	R	14 ± 5 cm^3
Target cell	G	18.2 cm^3
Condensing volume		≈ 30 cm^3

R: *measured with Reference volume.*

G: *determined volume Geometrically.*

Table 2.2: Volumes of Helium gas handling system.

indicates how the measurements were made, either by *Geometry* (G) or with respect to the *Reference* volume (R). The volume of the condensing coils was obtained from measurements made by *Hasell* [Has84].

Target Density

A graph of the density dependence of ^{3}He [Coy66] is shown in Fig 2.16, and for ^{4}He [Coy66] in Fig 2.17. The temperatures obtained from the Germanium resistors during the experiment were approximately: RT1 = 1.9 K and RT2 = 2.1 K. These temperatures are in the nearly constant density region of the liquid ^{4}He curves, shown in Fig. 2.17, so that the uncertainties are small, $\approx$ 1%. For the liquid ^{3}He curves of Fig. 2.16, the temperature is in the non zero slope region. However, the effect is still less than 3%.

For both experiments measurements of proton elastic scattering were also carried out to verify the target density. The analysis procedure for obtaining the differential cross sections is discussed in the following Chapter. The re-

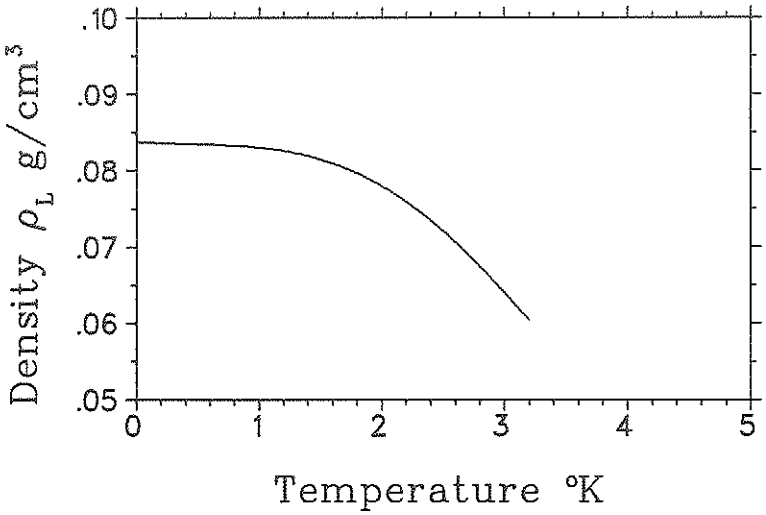

Figure 2.16: Density of liquid ^{3}He at saturation.

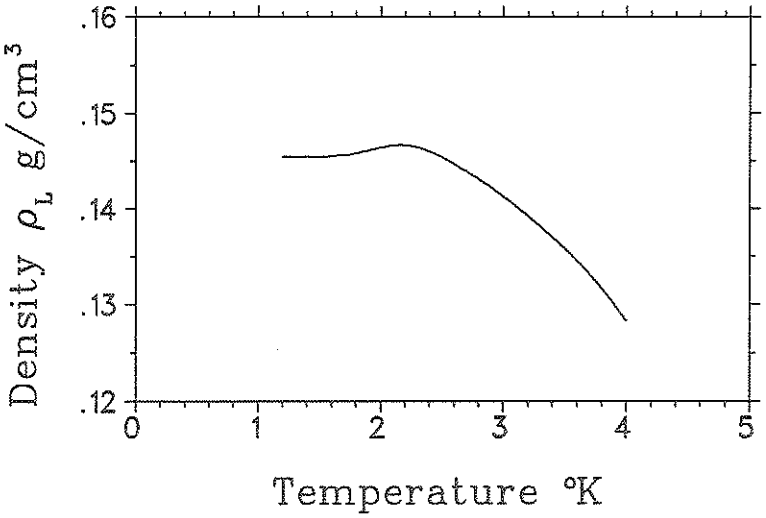

Figure 2.17: Density of liquid ^{4}He at saturation.

^{3}He(p,p)^{3}He at $\theta_{lab} = 40.0°$			
T_p (MeV)	$d\sigma/d\Omega_{lab}$ ($\frac{\mu b}{sr}$) $\pm$ relative ($\pm$ sys)	Difference†	Source
416	60.0±2.1 (±6.0)		E413 Run#133
415	84.1±3.3 (±3.3)	+28.6 %	[Beu+74]
415	52.7±1.8 (±2.8)	−13.8 %	[Has+86]
^{4}He(p,p)^{4}He at $\theta_{lab} = 33.0°$			
T_p (MeV)	$d\sigma/d\Omega_{lab}$ ($\frac{\mu b}{sr}$) $\pm$ relative ($\pm$ sys)	Difference†	Source
500	297.0±14.8 (±29.7)		E564 Run#11
500	351.0±3.5 (±17.6)	+15.3 %	[Mos+80]

† *Difference between previous data and present measurement.*

Table 2.3: Comparison of elastic cross sections.

sults obtained in the present measurement and those obtained previously are shown in Table 2.3. For ^{3}He, the measurements are higher by approximately 14% in comparison to the data (taken with the same target) from Hasell *et al.* [Has+86]. The systematic error for the Hasell measurement is ≈6%. Hasell also noted however, that their data were 20-30% lower than other unpublished data [Beu+74] at forward angles while in good agreement with previous measurements at back angles [Fra+77]. The elastic measurement performed during E413 was found to be 29% smaller than that measured by Beurtey *et al* [Beu+74].

For ^{4}He the result is 15% lower than that from Moss *et al.* [Mos+80]. The Moss data were obtained from normalization to another measurement [Ste+77] and the systematic error is ≈5%. The Moss data were found to be in good agreement with previous data from Klem *et al.* [Kle+77] to within about 7%.

The systematic uncertainties of the ^{3}He and ^{4}He elastic scattering measurements of this thesis are about 10% (errors in the elastic differential cross sections are the same as for ^{3}He(p,π^+)^{4}He data, discussed in Section 3.6.1, however without the uncertainty due to the pion decay fraction). The proton elastic measurements of the present experiment are therefore in agreement with previously published data to within the systematic errors.

Target Planar Position

To determine the planar position of the target cell, precision measurements using a theodolite were performed. In Fig. 2.18 the coordinate system of the target cell with respect to the MRS scattering chamber is defined. O′ defines the centre of the target and O the centre of the MRS scattering chamber. The transverse offset from the axis of rotation of the cryostat was found to be quite large. Referring to the X-Y coordinate system shown in Fig. 2.18 the transverse offset was found to be

$$X_{\text{offset}} = 10.5\,\text{mm}.$$

The longitudinal offset in the beam direction from cryostat axis was

$$Y_{\text{offset}} = 1.0\,\text{mm}.$$

These offsets were attributed to an accident when the cryostat was being first commissioned[12]. Thus, as illustrated in Fig. 2.18, the geometric centre of the cell is 10.5 mm to the left of the incoming beam and 1.0 mm downstream from the axis of rotation.

The vertical offset depends on whether the cryostat is cooled or not. At room temperature the difference between the dummy and target cell centres

[12]R. Abegg, private communication (TRIUMF).

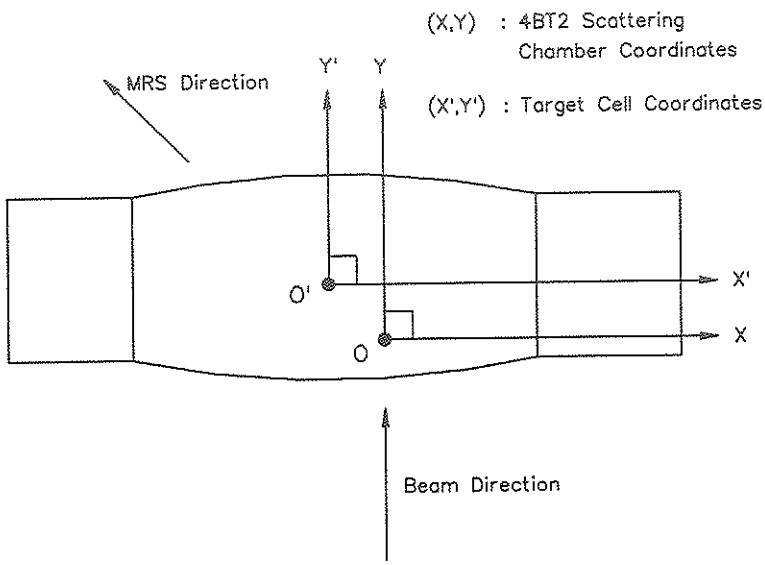

Figure 2.18: Coordinates of target cell in 4BT2 scattering chamber. O represents the axis of rotation of the scattering chamber and cryostat.

was 101.6 mm. The difference between the target cell and the centre of the CH2/ZnS screen mounted on the bottom of the cryostat (see Fig. 2.4) was 102.7 mm. When the target cools, it contracts. Most of the contraction is from the material above the cells, and is estimated to be 3 mm. The difference between the cell centres is assumed to not change but the difference between the target cell and CH2/ZnS screen centres has increased to 105.7 mm. The vertical motion of the lifting mechanism is 98.4 mm from the dummy cell to target cell position, and 104.8 mm from the target cell to screen position. In Table 2.4 are the positions of the centres with respect to the normal axis of the beam.

Note that different screens were used and a 6.35 mm spacer was added between experiments E413 and E564. The error in the vertical offsets due to the uncertainty in the measurements and the uncertainty in the contraction calculation is estimated to be 0.5 mm.

Z Offsets of Cryostat†			
Expt	Target Cell	Dummy Cell	CH2/ZnS Screen
E413	−5.1 mm	−1.9 mm	−6 mm
E564	+1.3 mm	+5.5 mm	+1 mm

†*Error in offsets estimated at 0.5 mm.*

Table 2.4: Position centres with respect to normal beam axis.

Target Rotation Position

By using a mirror and telescope sighting down the beamline the absolute zero angle was determined. The error in this zero measurement was estimated by considering the subtended angle due to the uncertainty in placing the mirror parallel to the plane of the target.

$$\delta\theta = \frac{\delta \mathrm{r}}{\mathrm{r}} \approx \frac{0.5\,\mathrm{mm}}{60\,\mathrm{mm}} \times \frac{360^\circ}{2\pi} = 0.5^\circ \tag{2.7}$$

The uncertainty in the zero due to the telescope measurement itself is negligible due to the long distance (about 10 m) over which the measurement was made.

The target rotation angle calibration was determined when the cryostat was mounted on the MRS scattering chamber. By counting the teeth on the rotation drive gear an average of

$$\frac{360^\circ}{111\,\mathrm{teeth}} = 3.24\,\frac{\mathrm{deg}}{\mathrm{tooth}} \tag{2.8}$$

was determined. The rotation angle as a function of pot voltage was determined by measuring the voltage of the resistor pot mounted on the rotation mechanism. In Fig. 2.19 the calibration of the target angle with resistor pot voltage is shown. The line is a linear fit for purposes of interpolation and extrapolation. A reasonable estimation of the relative error of the rotation

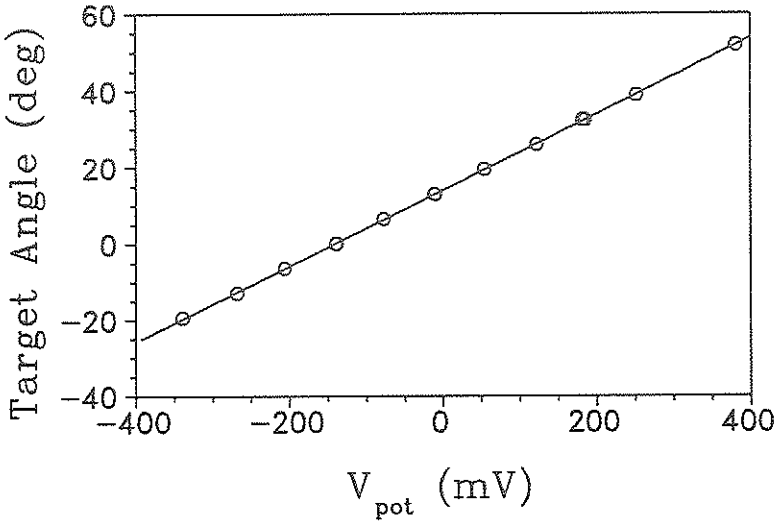

Figure 2.19: Calibration of rotation angle of cryostat.

angle may be estimated from the linear fit variance. This was determined to be $\pm 0.4°$.

The target worked nearly flawlessly for the duration of the two experiments. The task of recommissioning the target and getting it on the beam floor running smoothly was completed thanks to the support of D.C. Healey and the Cryogenic Targets Group at Triumf and in particular fellow graduate student F.A. Duncan.

2.3 Medium Resolution Spectrometer

The scattered pions were measured by the Medium Resolution Spectrometer (MRS). The MRS is shown in Fig. 2.20 illustrating the respective positions of the various detectors comprised of wire chambers and scintillators. The

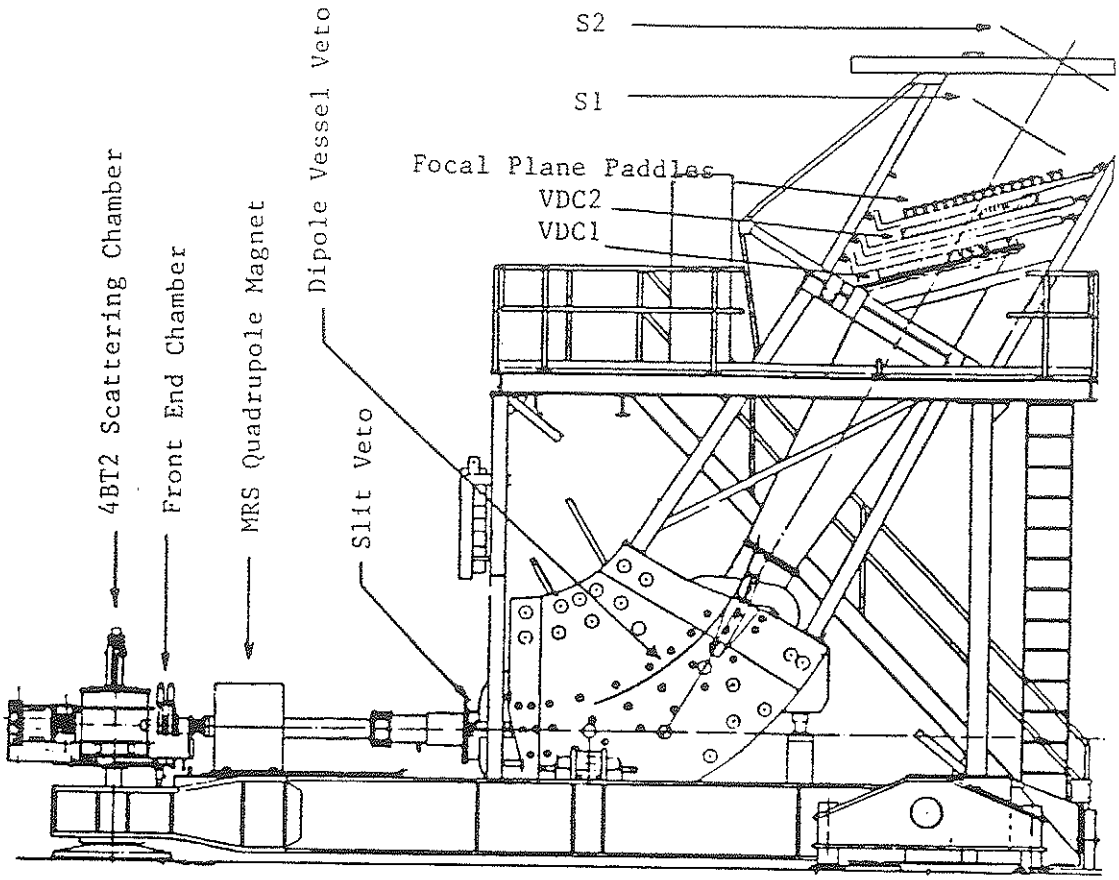

Figure 2.20: Medium Resolution Spectrometer.

electronics and trigger of the MRS is controlled by the *ECL*[13] computer program. A Quadrapole-Dipole 1.6 GeV/c proton spectrometer [Mil83], the MRS is usually tuned for a *point to point* focus for proton scattering experiments [Hic88]. The wire chambers provide the coordinate information for event recontruction using the information from a beam optics, *Transport* [Bro+77], calculation of the MRS. To study the MRS as a pion spectrometer a Monte Carlo calculation was performed. All these facets will be discussed in greater detail in the following subsections.

[13]written by Peter Green, TRIUMF.

2.3.1 Detectors and Coordinate Determination

The MRS is comprised of a variety of detectors shown in Fig. 2.20. These are the Front End Chamber (FEC), the two Vertical Drift Chambers (VDC1 and VDC2), the scintillator hodoscope- Focal Plane Paddles (FPP's), and the trigger scintillators S1 and S2. S1 was not used in either of the two experiments.

Front End Chamber.

The Front End Chamber (FEC) is comprised of four wire planes each consisting of 16 pairs of alternating anode and cathode wires. Two of the planes are horizontal (X0 and X0′ for the bend plane) and two of the planes are vertical (Y0 and Y0′ for the non bend plane). The primed and unprimed planes are offset from one another by half an interanode spacing and therefore facilitate the determination of whether the particle passed to the left or right of a *struck* wire. (See Fig. 2.21). The interpolated positions are called X0 and Y0, and the FEC has a resolution of typically 0.7 mm.

Drift Chambers.

The Vertical Drift Chambers (VDC1 and VDC2, or VDC's) are positioned at the top end of the MRS at a 45° angle to the central trajectory of the spectrometer (see Fig. 2.20). Each VDC is comprised of two wire planes, X and U, which give positions in the bend plane (X wire plane) and 30° to the bend plane (U wire plane). Together the X and U planes provide information for the calculation of the non bend plane coordinate Y. The VDC's planes have 176 wires each with an inter-wire separation of 6 mm. By examining the drift time to the wires one is able to determine the position and trajectory of the particle. See Fig. 2.22. The resolution of the VDC's is typically 150

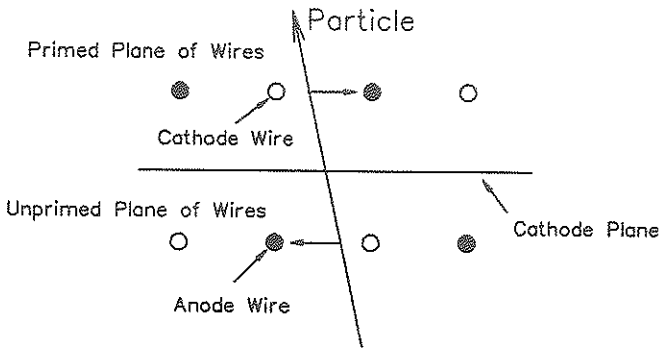

Figure 2.21: Cross sectional view of FEC showing position interpolation.

μm in the X direction. The combination of the two VDCs makes it possible to determine the focal plane intersection of the particle trajectories.

2.3.2 Trigger and Data Acquisition

The MRS electronics is comprised of CAMAC type modules which are mounted in racks on the MRS platform and in the 4B counting room. The electronics setup is reasonably standardized but is in constant evolution to improve the system[14].

Trigger

An event was defined by a hit in one of the FEC planes, a hit in the VDC X1 plane, a signal in S2, a signal in the FPP within a preset hardware cut, and a time of flight between the FEC and the FPP within another preset hardware cut. The logical AND of all these signals formed a MASTER trigger and subsequently the system was frozen while all the ADC's and TDC's

[14]The trigger was assembled by C.A. Miller, TRIUMF.

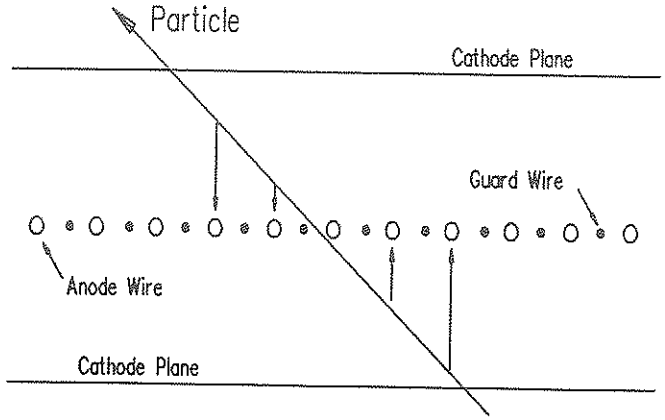

Figure 2.22: Cross sectional view of VDC showing position interpolation.

were read. The MRS trigger system is shown schematically in Fig. 2.23.

Data Acquisition

The Vax Data ACquisition System (VDACS) consisted of a TWOTRAN compiled and linked program running on a front-end processor[15]. The program is listed in Appendix A. Upon generation of a flag by a Master Trigger, the program would write the ADC's and the DRIFT chamber data (comprising a composite event word) to tape. These events are written in the order shown in Table 3.1 in Section 3.1.1. A sample of the events is routed to an online chamber decoding routine for monitoring the performance of the experiment via on-line displays. For online monitoring of the Scalers, the TWOTRAN program was written such that the Scalers were read every five minutes (and in addition at the flag of an END-OF-RUN) and subsequently written to tape.

The online decoding routine for these experiments was a LISA subroutine,

[15]J-11 Starburst CES model 2180.

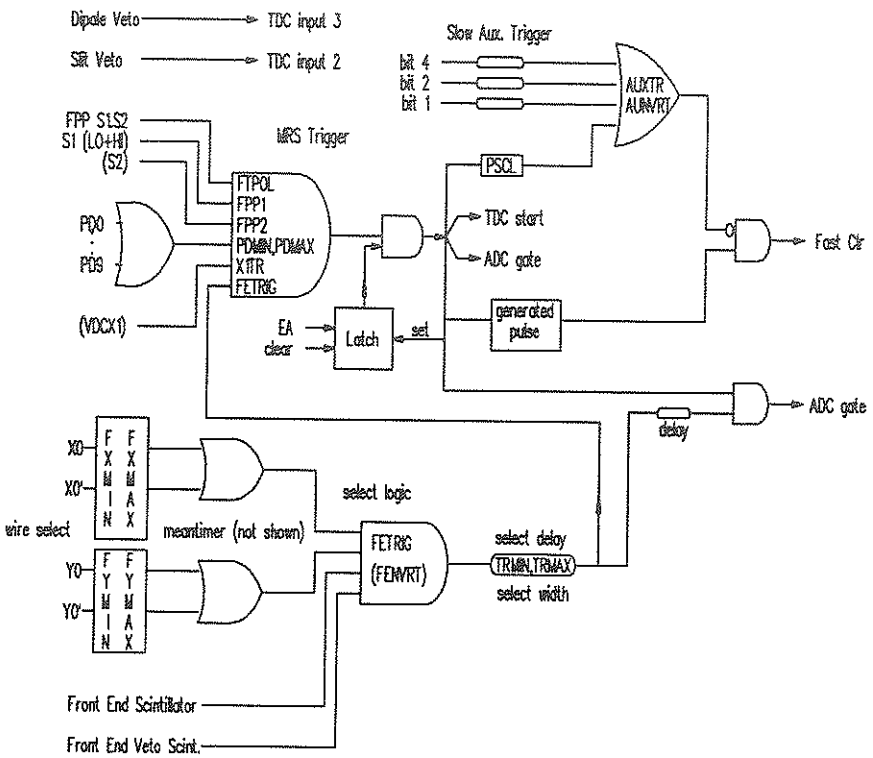

Figure 2.23: MRS trigger.

(see Analysis Chapter, Section 3.1.1) and calculated first order reconstruction of the focal plane, target and other coordinate spectra. Furthermore, a program for observing the scaler rates was available to monitor efficiency sensitive Front End Chamber (FEC) rates.

2.3.3 MRS Transport

The coordinate system of the MRS and that defined for Beam Transport [Bro+77] is shown in Fig. 2.24. Also shown for comparison is the usual definition for the beam coordinates. In order to avoid any ambiguity the coordinates will be specified within the context of discussion. In the beam coordinate system the z-axis is in the direction of the incoming beam and the y-axis perpendicular to the scattering plane formed by the x-z axes. For the MRS/LISA and Transport frames the z-axis is parallel to the (curved)

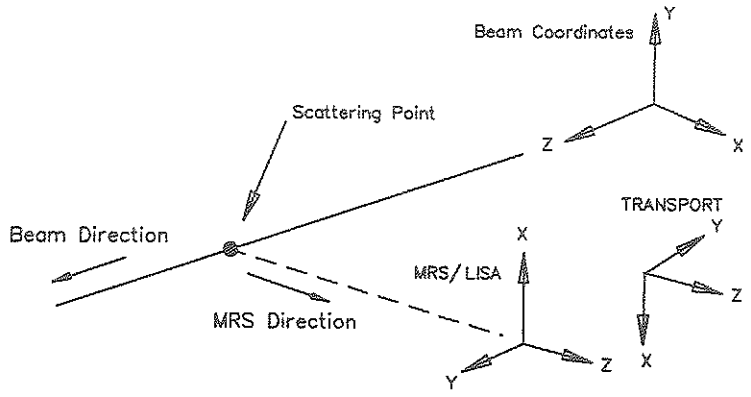

Figure 2.24: Scattering plane coordinate systems.

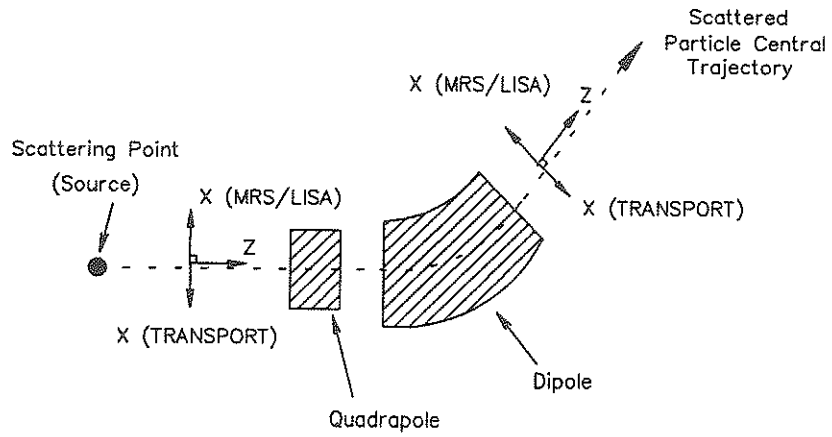

Figure 2.25: Coordinate systems of MRS.

central trajectory through the spectrometer system. The plane formed by this curved z-axis is called the *bend plane*. The y-axes are perpendicular to this plane, but point in opposite directions in the MRS/LISA and Transport coordinate systems. The y-direction is referred to as the *non-bend plane* direction. Both of the latter frames are right handed systems (i.e. $\hat{x} = \hat{y} \times \hat{z}$).

A vector is used to describe the trajectory and position of the ray of the

scattered particle passing through the MRS.

$$X_i = (X, \theta, Y, \phi, Z, \delta) \tag{2.9}$$

X and Y describe the position of the ray with respect to the central ray and are in units of cm. θ and ϕ describe the slope with respect to the central trajectory and are in units of mrad. The position measured along the central trajectory with respect to the source (target) is Z and is in units of m. δ is the momentum deviation of the ray from the central momentum, p_o, and is defined as

$$\delta = \frac{p - p_o}{p_o}. \tag{2.10}$$

Note that it is dimensionless. The central momentum, p_o, is the momentum corresponding to the central ray.

To first order the relation between the target coordinates, $\vec{X}_t$ and the focal plane coordinates, $\vec{X}_f$ can be described by a matrix, where the individual elements depend on field settings, and physical factors of the system.

$$X_i = R_{ij} X_j \tag{2.11}$$

Transport calculations are discussed in many texts, see for example [Hum86].

To understand the MRS optics a second order calculation was performed using typical parameters for the MRS[16]. This is shown in Fig. 2.26. The dashed lines represent important positions in the MRS, i.e. the detectors and the magnets. The rays are a sample of different initial momenta, position and angle to illustrate the optics of the MRS. Note that the MRS quadrapole is focussing in the non-bend plane and defocussing in the bend plane. The position of the quad (with respect to the target and the dipole) and the ratio of the quad field to the dipole field (Q/D ratio) are such that the R_{ij} matrix

[16]Obtained from C.A. Miller, TRIUMF

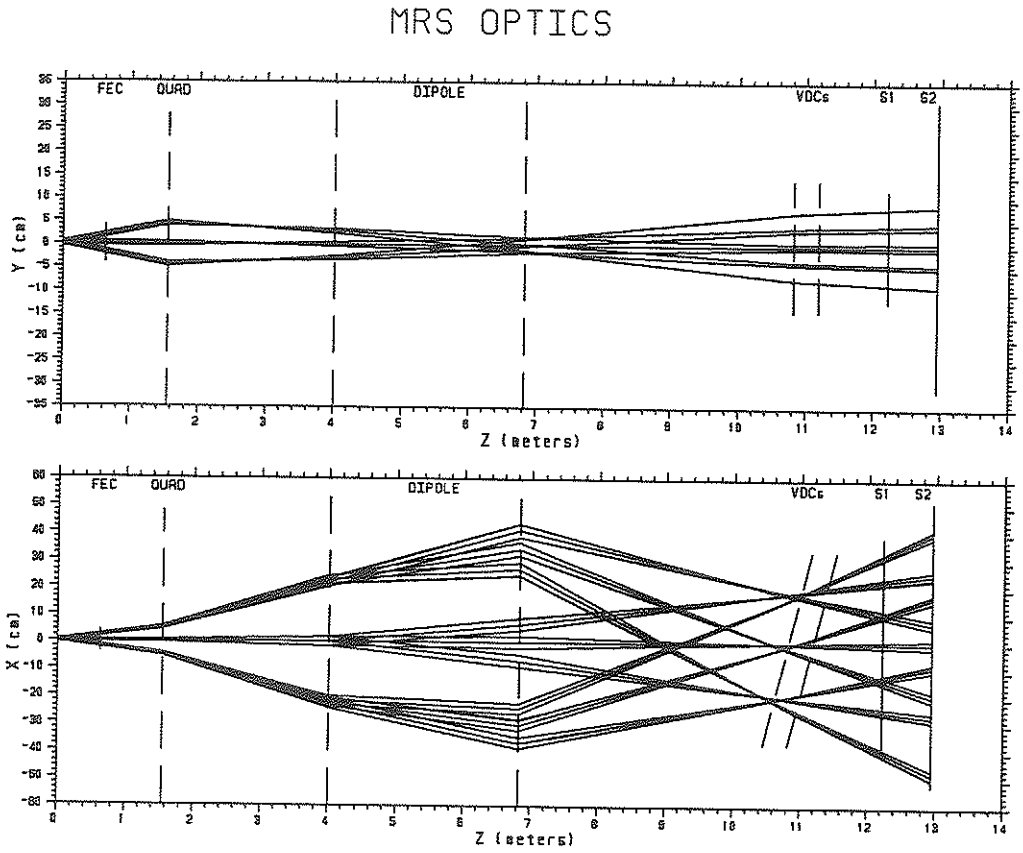

Figure 2.26: Calculation of MRS optics to second order.

simplifies to the following form:

$$\begin{pmatrix} X_f \\ \theta_f \\ Y_f \\ \phi_f \\ L_f \\ \delta_f \end{pmatrix} = \begin{pmatrix} R_{11} & R_{12} & 0 & 0 & 0 & R_{16} \\ R_{21} & R_{22} & 0 & 0 & 0 & R_{26} \\ 0 & 0 & R_{33} & R_{34} & 0 & 0 \\ 0 & 0 & R_{43} & R_{44} & 0 & 0 \\ 0 & 0 & 0 & 0 & 0 & 0 \\ 0 & 0 & 0 & 0 & 0 & 1 \end{pmatrix} \begin{pmatrix} X_t \\ \theta_t \\ Y_t \\ \phi_t \\ L_t \\ \delta_t \end{pmatrix} \tag{2.12}$$

A calculation of the parameters using the INTRAN [Kos88] code from TRIUMF for typical settings of the MRS gives the following typical values, (note the values are meant only as indicative of sign and magnitude):

$$R_{ij} = \begin{pmatrix} -0.37 & 0 & 0 & 0 & 0 & 3.8 \\ -12 & -2.7 & 0 & 0 & 0 & 6.3 \\ 0 & 0 & -7 & -0.1 & 0 & 0 \\ 0 & 0 & -12 & -0.2 & 0 & 0 \\ 0 & 0 & 0 & 0 & 0 & 0 \\ 0 & 0 & 0 & 0 & 0 & 1 \end{pmatrix} \tag{2.13}$$

From these values one can make various observations about the MRS transport. Firstly notice the R_{12} element is zero, which implies point to point focussing in X. Secondly notice from the R_{11} and R_{33} elements that the focal plane image is inverted and has a large Y magnification. Lastly note that R_{26} is rather large which implies that θ_f must have a large momentum dependence. This momentum dependence was corrected for and is discussed in a section below.

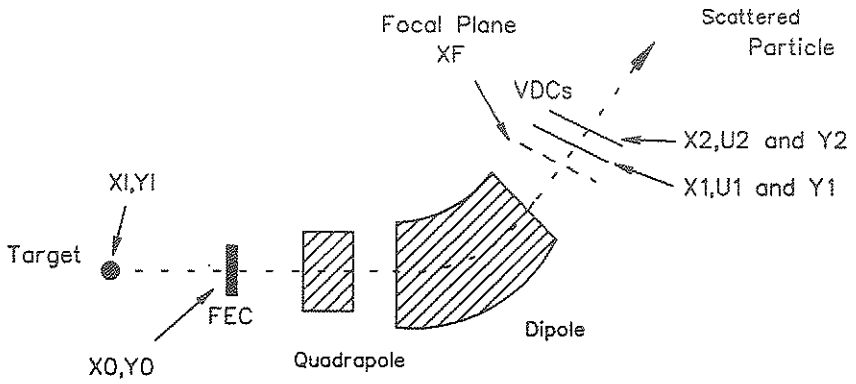

Figure 2.27: Coordinate systems of event reconstruction.

2.3.4 Event Reconstruction

To trace the event through the system, the information from the various wire chambers coordinates is used. The various coordinates calculated in this section for the event reconstruction are shown in Fig. 2.27 and refer to the MRS/LISA coordinate system of Fig. 2.24.

To distinguish from transport coordinates, defined in Eqn. 2.9, the LISA/MRS coordinates are notated as:

$$\begin{pmatrix} \mathrm{XF} \\ \mathrm{THETA} \\ \mathrm{Y} \\ \mathrm{PHI} \\ \mathrm{LF} \\ \mathrm{DELTAF} \end{pmatrix} = \mathrm{R}'_{\mathrm{ij}} \begin{pmatrix} \mathrm{XI} \\ \mathrm{THETAI} \\ \mathrm{YI} \\ \mathrm{PHII} \\ \mathrm{LT} \\ \mathrm{DELTAT} \end{pmatrix} \tag{2.14}$$

The coordinates are similar as explained above except that the units are not necessarily the same (for example the MRS/LISA target coordinates XI and YI, are in 50μm units whereas the transport target coordinates $\mathrm{X_t}$ and $\mathrm{Y_t}$, are in units of cm) . Therefore, the values of the non zero elements of the

matrix R'_{ij} are not quite the same as R_{ij} in Eqn. 2.12.

The discussion will be broken into three parts, the bend plane coordinates (XF, XFK, THETA and THETAPC), the non bend plane coordinates (Y1, Y2 and PHI) and the target coordinates (XI and YI).

Bend Plane Coordinates

From the VDC's X plane wires the bend plane coordinates X1 and X2 are obtained. From X1 and X2 the focal plane coordinate, XF is determined. The calculation of XF (shown in Fig. 2.28) is as follows:

$$\mathrm{XF} = \frac{(\mathrm{VDCDIST} \times \mathrm{X1C0}) - (\mathrm{FOCALF} \times \mathrm{DX12})}{\mathrm{VDCDIST} - (\mathrm{DX12} \times \mathrm{TANDELTA})} \tag{2.15}$$

where

$$\mathrm{DX12} = \mathrm{X1} - \mathrm{X2} + \mathrm{X1C0} \tag{2.16}$$

and VDCDIST and X1C0 are geometrical factors of the VDC's. FOCALF and TANDELTA are adjustable parameters representing the distance of the focal plane from the X1 plane and the tilt of the focal plane with respect to the plane defined by the VDC's respectively. Nominal values for these parameters are known from considering the second order Transport of the MRS and are given in Table 2.5.

The bend plane angle THETA (i.e. the deviation from the central ray inclined at 45° with respect to the VDCs), is determined from the difference of the two VDC coordinates (see Fig. 2.28). For THETA in mrad:

$$\mathrm{THETA} = \frac{\frac{\mathrm{VDCDIST}}{\mathrm{DX12}} - 1}{\frac{\mathrm{VDCDIST}}{\mathrm{DX12}} + 1} \times 1000. \tag{2.17}$$

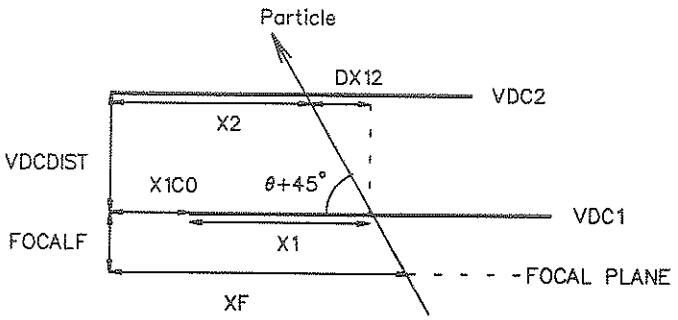

Figure 2.28: Focal Plane reconstruction from the VDC coordinates X1 and X2.

MRS VDC's Geometrical Factors†	
VDCDIST	5472
X1C0	5472
XUSEP	525
Nominal Focal Plane Parameters†	
FOCALF	−1000
TANDELTA	0

†*in 50 μm units*

Table 2.5: VDC's geometrical factors and nominal parameters for focal plane.

The raw focal plane coordinate, XF, may be further modified to improve resolution by taking into account the finite acceptance of the MRS. For different scattering angles the scattered particles have different momenta. Suppose the central lab scattering angle is ϑ. Then for a given central angle one can calculate the momentum slope, $dp/d\vartheta$ from kinematics. If m_A is the target mass and ϑ is the central (MRS) angle, then the momentum slope may be calculated as follows (all quantities in the lab frame):

$$\frac{dp_\pi}{d\vartheta} = -p_\pi \times \frac{\sin\vartheta}{\frac{p_\pi(E_p+m_A)}{p_p E_\pi} - \cos\vartheta} \tag{2.18}$$

If the difference of the scattering angle from the central angle, $\Delta\vartheta = \vartheta - \vartheta_{\text{central}}$, is known, then a correction for this kinematical effect may be made. (Note $\Delta\vartheta$ is the same as the Transport coordinate ϕ_t in Eqn. 2.12 above).

$$XF = XFK + \frac{dXF}{d\vartheta} \times \Delta\vartheta \tag{2.19}$$

$$XF = XFK + \frac{dXF}{dp_\pi}\frac{dp_\pi}{d\vartheta} \times \Delta\vartheta \tag{2.20}$$

The dXF/dp_π dependence may be determined from the first order transport matrix (from R_{16} in Eqn. 2.12) or it may also be readily obtained from experiment.

Using the $pp \rightarrow d\pi^+$ reaction with its relatively high cross section, the pion peak is placed at different points across the focal plane by varying the MRS dipole field. The result is shown in Fig. 2.29. From this graph one observes that the relation between p_π/B and XF is well parameterized by a straight line.

$$\frac{p_\pi}{B} = \alpha + \beta XF + \ldots \tag{2.21}$$

α and β are obtained from a fit to the *Focal Plane Scan.* By differentiating this equation and after some algebraic manipulation the desired slope, dXF/dp_π is obtained.

$$\frac{dXF}{dp_\pi} = \frac{1}{p_\pi}\frac{(\alpha + \beta XF)}{\beta} \tag{2.22}$$

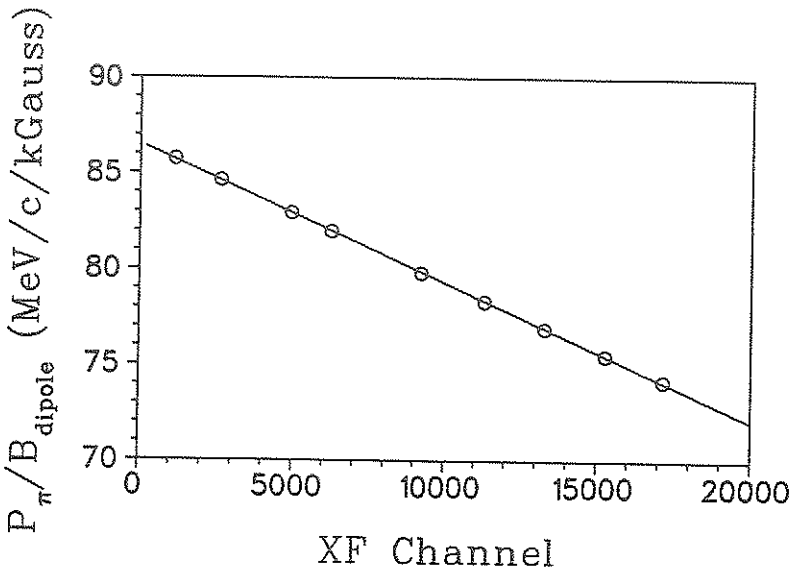

Figure 2.29: p_π/B versus XF from $pp \rightarrow d\pi^+$ scan.

The slope was obtained both from the transport calculation and from experiment and the results agreed well.

If a point target is assumed then a measure of $\Delta\vartheta$ from the non-bend plane coordinate of the FEC may be extracted.

$$\Delta\vartheta = (\mathrm{Y0} - \mathrm{Y0_{cntr}}) \times \frac{\mathrm{d}\vartheta}{\mathrm{dY0}}. \tag{2.23}$$

$\mathrm{d}\vartheta/\mathrm{dY0}$ is simply a transformation from the units of ϑ to those of MRS/LISA coordinate Y0. Using this expression:

$$\mathrm{XFK} = \mathrm{XF} + \frac{\mathrm{dX_f}}{\mathrm{dp_\pi}} \frac{\mathrm{dp_\pi}}{\mathrm{d}\vartheta} \frac{\mathrm{d}\vartheta}{\mathrm{dY0}} \times (\mathrm{Y0} - \mathrm{Y0_{cntr}}) \tag{2.24}$$

$$\mathrm{XFK} = \mathrm{XF} + \mathrm{FKIN} \times (\mathrm{Y0} - \mathrm{Y0_{cntr}}) \tag{2.25}$$

where

$$\mathrm{FKIN} = \frac{\mathrm{dXF}}{\mathrm{dp_\pi}} \frac{\mathrm{dp_\pi}}{\mathrm{d}\vartheta} \frac{\mathrm{d}\vartheta}{\mathrm{dY0}} \tag{2.26}$$

FKIN is often referred to as the *kinematic correction*. Its magnitude changes substantially depending on the magnitude of $\mathrm{dp_\pi}/\mathrm{d}\vartheta$ which is large for $pp \rightarrow$

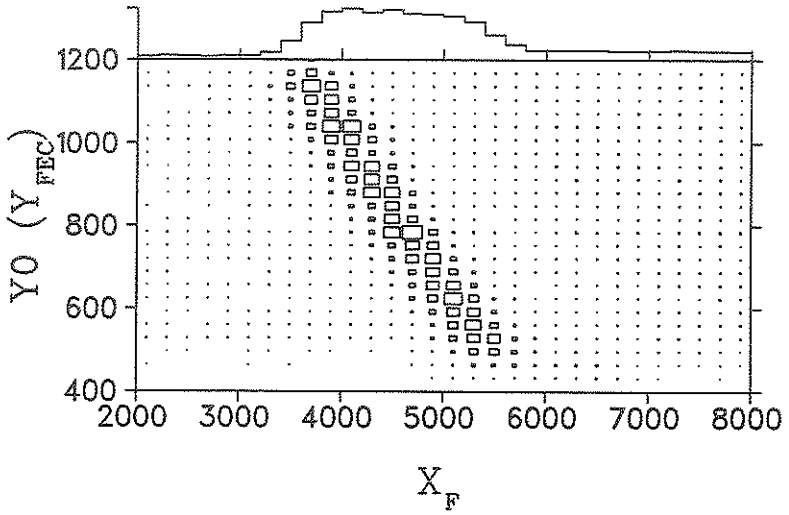

Figure 2.30: Effect of kinematics on the focal plane resolution for the $pp \rightarrow d\pi^+$ reaction.

$d\pi^+$ but smaller for heavier target nuclei like ^{3}He and ^{4}He. This effect is shown in Fig. 2.30, where the graph indicates the dependence on Y_{FEC}, (i.e. Y0 or $\Delta\vartheta$), when the kinematic correction has been set to zero. When the correction is in place and the dependence corrected, the pion peak sharpens in the *corrected* XF spectrum XFK. See Fig. 2.31. Note that a large amount of the momentum dependence (arising from the correlation with the pion scattering angle) in the XF coordinate has been eliminated (or the R_{16} momentum spread dependence in Eqn. eq:matrix has been eliminated).

However, Eqn. 2.12 shows that the bend plane angle at the focal plane THETA, still has a momentum spread dependence. From the R_{26} element in the typical first order transport matrix, Eqn. 2.13, it can be seen that this momentum dependence is large. The momentum spread at the focal plane is related to the focal plane coordinate XFK, and so the momentum

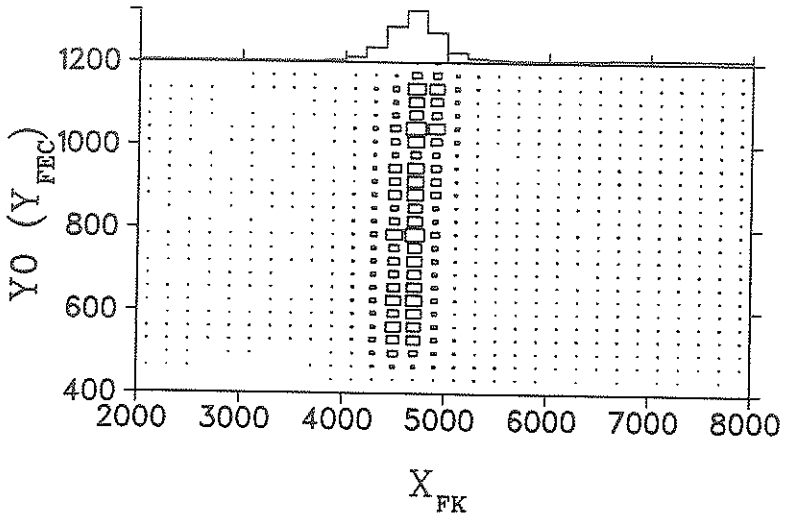

Figure 2.31: Same as in Fig. 2.30 but with kinematic correction included.

spread dependence in THETA may be corrected for by eliminating the XFK dependence in THETA.

$$\mathrm{THETAPC} = \mathrm{THETA} + \mathrm{TCXF} * \mathrm{XFK} + \mathrm{TPC0} \tag{2.27}$$

The parameters TCXF and TPC0 are obtained from the first order transport matrix and then fine tuned during the analysis. Their nominal values may be calculated as follows:

$$\mathrm{TCXF} = -\frac{\alpha}{\beta} \tag{2.28}$$

$$\mathrm{TPC0} = -\mathrm{TCXF} \times \mathrm{XF_{cntr}} \tag{2.29}$$

where the parameters α and β are defined as,

$$\alpha = \frac{\mathrm{R_{26}}}{\mathrm{R_{16}} \times \sqrt{2}} \tag{2.30}$$

$$\beta = 200 + \alpha \times \frac{\mathrm{XF_{cntr}}}{1000} \tag{2.31}$$

and XF_{cntr} is the center of the focal plane coordinate, 17032.

Using XFK and THETAPC instead of XF and THETA, the first order transport matrix has been decoupled to eliminate the dependence on the momentum spread δ.

Non Bend Plane Coordinates

From the combination of the U and X wire plane coordinates the non bend plane Y coordinates, Y1 and Y2 are obtained. This is shown in Fig. 2.32 where the VDC is shown from a top view and the X coordinate is increasing in the direction of decreasing momentum. Note that the coordinate axes are in the same plane as, and perpendicular to, the chamber wires. The U coordinate may be written in terms of (X,Y) coordinates as follows:

$$U = X \cos 30° - Y \sin 30° \tag{2.32}$$

This may be rewritten as:

$$Y = \sqrt{3}X - 2U \tag{2.33}$$

Finally one obtains:

$$Y1 = \sqrt{3}(X1 - X_{corr}) - 2U1 + Y_{cntr} \tag{2.34}$$

and similarly for Y2. X_{corr} is a correction for the finite separation in the X and U planes and given by:

$$X_{corr} = \frac{XUSEP \times DX12}{VDCDIST} \tag{2.35}$$

where XUSEP is given in Table 2.5. Y_{cntr} is the center of the Y coordinate and is 4901. From Y1 and Y2 the non-bend plane angle coordinate PHI in mrad is obtained.

$$PHI = \frac{Y2 - Y1}{\sqrt{VDCDIST^2 + DX12^2}} \times 1000. \tag{2.36}$$

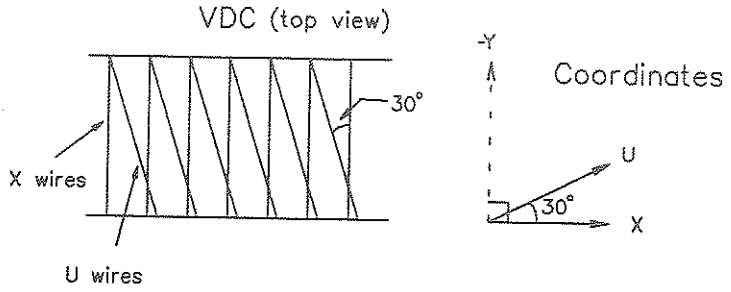

Figure 2.32: (X,U) and (X,Y) coordinate systems of VDCs.

Target Coordinates

From the FEC the two coordinates, X0 and Y0, are extracted. The coordinate information from the VDC's provides a vector ((X, θ, Y, ϕ) or (XFK, THETAPC, Y, PHI) in MRS/LISA coordinates) which when drawn back to the FEC using the first order transport matrix, R_{ij}, provides the target coordinates X_t and Y_t (or XI and YI in MRS/LISA coordinates). This is obviously for the ideal case, and subject to multiple scattering and higher order optical effects. The equations for drawing back to the target are reasonably simple to derive.

The bend-plane target coordinate reconstruction is written as:

$$XI - XI_{cntr} = XITH \times THETAPC + XIX0 \times (X0 - X0_{cntr}) \qquad (2.37)$$

where XITH and XIX0 are given as :

$$XITH = -\frac{\beta}{\gamma} \qquad (2.38)$$

$$XIX0 = -\frac{R_{22}}{\gamma \times L} \qquad (2.39)$$

β was defined in Eq. 2.31 and γ is defined as:

$$\gamma = R_{21} - \frac{R_{22}}{L} - \frac{R_{11} \times R_{26}}{R_{16}}. \tag{2.40}$$

$XI_{cntr} = X0_{cntr} = 800$ are the centres of the target and FEC coordinate respectively. L is the distance from the target to the FEC which is 63 cm for the ^{3}He experiment.

One may also calculate the non-bend plane target coordinate YI from the Transport matrix elements as follows.

$$YI - YI_{cntr} = YIY1 \times (Y1 - Y_{cntr}) + YIY0 \times (Y0 - Y0_{cntr}) \tag{2.41}$$

where

$$YIY1 = \frac{L}{\lambda} \tag{2.42}$$

$$YIY0 = \frac{R_{34}}{\lambda} \tag{2.43}$$

and

$$\lambda = L \times R_{33} - R_{34}. \tag{2.44}$$

Again $YI_{cntr} = Y0_{cntr} = 800$ are the centres of the respective coordinates.

These are the first order transport coordinates relevant to the MRS. For online monitoring and offline analysis the coordinates were calculated from the wire chamber coordinates. During the experiment they were used initially to tune and then to monitor the performance of the MRS. They are also used in the offline analysis to define an event in conjunction with other results and this is discussed in the Analysis Chapter.

2.3.5 Monte Carlo

Since the MRS was to be used as a pion spectrometer, a Monte Carlo study was performed to obtain the effective length and the acceptance of the MRS

and to gain general insight into its performance and dependence on various parameters. For the purpose of these studies the $pp \rightarrow d\pi^+$ reaction was used as a calibration reaction due its relatively high cross section (typically millibarns) and its cleanly resolved pion peak (corresponding to the recoil deuteron). The Monte Carlo study incorporated most of the effects that are important in the actual experiment, namely energy loss, straggling, multiple scattering, pion decay and finite geometry. The Monte Carlo starts from the core source code of REVMOC [KR89], a TRIUMF based program written for the study of beam lines. The output is written in VDACS type format (see Section 2.3.2) and so can be analyzed exactly the same as the raw experimental data files. A table of the Monte Carlo elements and a sample REVMOC input file are shown in Appendix C.

Solid Angle

It is known that the solid angle of the MRS is dependent on the ratio of the Quadrapole to Dipole field (Q/D ratio) and this parameter was therefore kept as nearly constant as possible during the experiment. In the past experimental running of the MRS it was assumed that the slope $d\Delta\Omega/d(Q/D)$ was small. However it was found that this is indeed not true at all for the small fields involved when running the MRS as a pion spectrometer (but approximately valid for the larger fields involved in running it as a proton spectrometer). Indeed, from the Monte Carlo study it was found that a 3% change in the Quad field resulted in a 4% change in the solid angle. That is

$$\frac{d\Delta\Omega}{\Delta\Omega} \approx 1.33 \times \frac{d(Q/D)}{Q/D} \tag{2.45}$$

This is also found experimentally (see Appendix F). Therefore, if the Q/D ratio is not known very accurately or if it is known to vary substantially, then a reasonably large error should be used when one uses a constant value of the solid angle in the analysis. This is discussed further in the Analysis

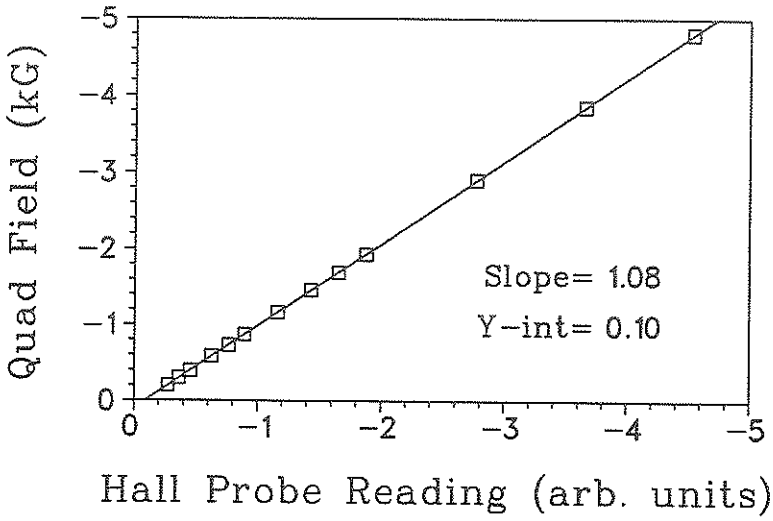

Figure 2.33: Calibration of the MRS quadrapole Hall probe.

Chapter and in Appendix F.

It was discovered, unexpectedly, that the Hall probe used to measure the field of the quadrapole had never been calibrated before the experiments; consequently this was done later[17]. The comparison between the Quad Field (measured with a Gaussmeter) and the output reading in the MRS counting room (related to the Hall probe current) are shown in Fig. 2.33. The result is fit very well with a straight line with a slope of nearly unity. The error of the calibration was estimated at 5%[18]. This is very important as this implies an uncertainty in the Q/D ratio of 5%. This therefore implies that a solid angle determination by the Monte Carlo would contain an intrinsic systematic error of about 7% (from Eqn. 2.45).

[17]Calibration performed on Dec. 4, 1990 by S. Yen, TRIUMF.

[18]S. Yen, TRIUMF, private communication, 1990.

Not unexpectedly, it was found that the solid angle is very sensitive to Quad position. The error in the Quad position was estimated at $\approx$ 1cm and, for E413, even larger since the Quad position was not recorded. It should also be noted that REVMOC [KR89] uses approximations for the quadrapole field distributions which have effects at the few percent level [Doo91].

Since the input into the Monte Carlo is not known accurately enough one cannot compare the Monte Carlo and experimental results *absolutely*. Apart from a solid angle normalization factor one may still however make *relative* comparisons between the experimental and Monte Carlo data.

Pion Survival Fraction

The pion decays to a muon and a muon anti-neutrino.

$$\pi \rightarrow \mu + \bar{\nu}_{\mu}$$

Since the pion has zero spin the decay is isotropic in the pion rest frame. The muon maximum decay angle and decay probability distribution in the lab depends on the pion kinetic energy. In Fig. 2.34 one sees that the muon maximum decay angle is less than 20° for the pion kinetic energies of the reactions studied in this work. For pion kinetic energies greater than 50 MeV a large fraction of these decay at the maximum decay angle. The distribution of the decay probability with angle in the lab frame is shown in Fig. 2.35. This is due to the large Lorentz boost for kinetic energies of around 50 MeV and higher. Because of this substantial change in direction, most of the pions which decay before and inside the dipole are lost to the detector system. Those which decay after the dipole are often detected in the following detectors. The pion survival fraction may be written as an intrinsic efficiency. The fraction that do survive in a given length L is given by the equation 2.46 where τ is the mean life, m_{π} is the mass (in MeV/c^2) and p_{π}

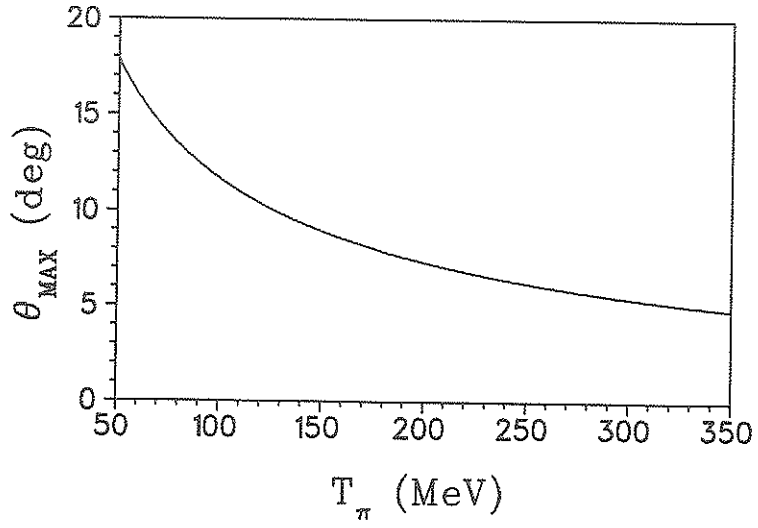

Figure 2.34: Maximum muon lab angle for $\pi \rightarrow \mu\bar{\nu}_\mu$ decay.

the momentum (in MeV/c) of the charged pion.

$$\frac{N_\pi}{N_{\pi 0}} = \exp\{-\frac{m_\pi L}{p_\pi c\tau}\} \tag{2.46}$$

Since the muons from pions that decay after the dipole are often detected in the detector stack following the dipole, the effective length is possibly less than the actual total flight path (the distance from the target to the S2 scintillator is 12.9 m). Huber [Hub88] estimated a value of 11 m for the pion effective survival length but did not determine whether such a description was adequate. He noted that this would require a Monte Carlo investigation. From the Monte Carlo studies of this work it was found that the pion survival fraction is well described by such a parameterization (see Eqn. 2.47) and that the value of the length changed only slightly with variation in the Q/D ratio,

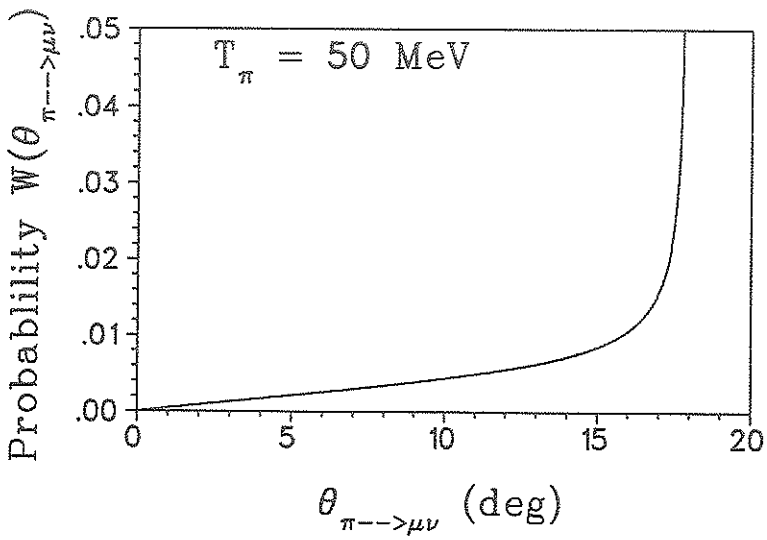

Figure 2.35: $\pi \rightarrow \mu\bar{\nu}_\mu$ decay probability as a function of muon angle.

Quad position and pion momentum.

$$\eta_\pi = \exp\{-\frac{m_\pi L}{p_\pi c\tau}\} \tag{2.47}$$

An estimate for the pion decay length was obtained in these Monte Carlo studies, and its error determined from the small variation for different pion momenta and Q/D ratio.

$$L_\pi = 11.10 \pm 0.03\text{m} \tag{2.48}$$

The error in the pion decay correction is dependent on the pion momentum.

$$\frac{\delta\eta_\pi}{\eta_\pi} = \frac{m}{pc\tau} \times \delta L \tag{2.49}$$

For a pion of momentum 400 MeV/c, $\delta\eta_\pi/\eta_\pi = 0.1\%$ and for a pion of momentum 100 MeV/c, $\delta\eta_\pi/\eta_\pi = 0.5\%$.

Losses

Due to multiple scattering some of the pions will be scattered in and out of the detector. This effect was measured using the Monte Carlo, and compared with the pp $\rightarrow$ dπ^+ calibration measurements. The losses due to multiple scattering and to pion absorption were only a few percent and varied with pion momentum. Typical values that were obtained from the Monte Carlo for different momenta are shown in Table. 2.6. It was found that the losses due to the target multiple scattering were very small and that most were from the detectors farther up the MRS. The values which are greater than unity indicate that at the higher pion momenta, in-scattering is occurring. The uncertainty in the losses shown in Table. 2.6 is that due to statistics alone and it should be noted that the uncertainty in η_{loss} does not include the uncertainty in the absorption cross sections. A reasonably large uncertainty should therefore be associated to this correction. Within these uncertainties an average value of η_{loss} was used which encompassed the observed range of losses and this was estimated to be:

$$\eta_{\text{loss}} = 0.97 \pm 0.03 \tag{2.50}$$

Acceptances

Using the Monte Carlo a focal plane scan and target scan was performed and compared with the results with experiment. Both scans used the pp $\rightarrow$ dπ^+ reaction with the MRS at a fixed scattering angle. For the focal plane scans the dipole field was varied and therefore sampled the MRS acceptance at different focal plane positions. For the target scans the dipole field was fixed and the proton beam was swept horizontally across the CH_2 target thereby sampling the MRS non-bend plane acceptance at the target. The implication

Losses				
Reaction	T_p (MeV)	θ_{lab} (deg)	p_π (MeV/c)	η_{loss}
p(p,π^+)d	507	28.1	291.2	1.021 ± 0.020
	507	91.0	147.7	0.972 ± 0.026
^{3}He(p,π^+)^{4}He	416	18.4	352.0	1.014 ± 0.023
	300	122.1	159.0	0.968 ± 0.027
	240	115.0	115.1	0.957 ± 0.029

Table 2.6: Typical losses due to absorption and multiple scattering determined by Monte Carlo.

of the scans on the data analysis is discussed in Chapter 3, however here their comparison with the Monte Carlo is discussed.

The comparisons with the experimental pp $\rightarrow$ dπ^+ scan and the Monte Carlo for the focal plane acceptance is shown in Fig. 2.36. The statistical uncertainties in the data are $\approx$2%. In the central region of the focal plane the agreement is quite excellent however, there is some disagreement in the tails of the acceptance distribution.

In Fig. 2.37 the comparison between the target acceptance for experimental pp $\rightarrow$ dπ^+ scan and the Monte Carlo is shown. For the result taken during E413 the agreement is good for the left side but not for the right side. The target acceptance scan for the E564 pp $\rightarrow$ dπ^+ scan is also shown in Fig. 2.37. There the distribution is much more symmetric, but agreement with the Monte Carlo result is about the same as E413. Since there is no difference between the E564 and E413 setup (as far as the pp $\rightarrow$ dπ^+ scans are concerned), the two scans merit equal weight. For the determination of the effective active target length the MRS acceptance is required. The effect

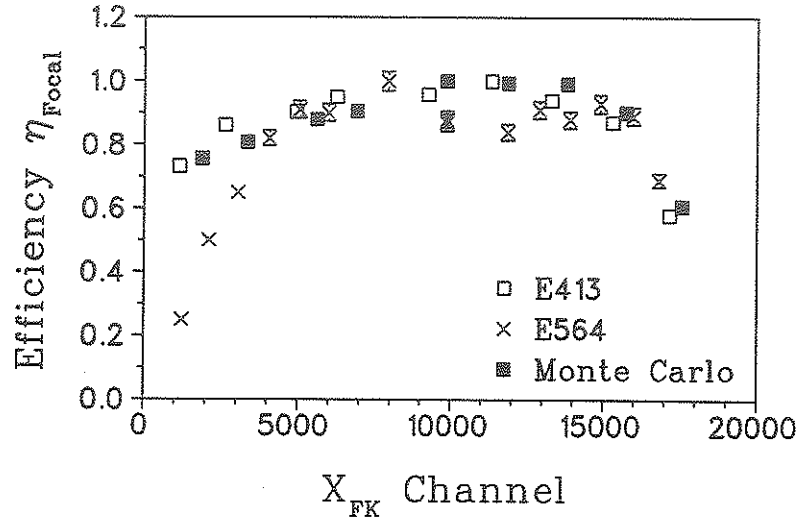

Figure 2.36: Comparison of E413 and E564 pp $\rightarrow$ dπ^+ MRS focal plane acceptance scan with Monte Carlo results.

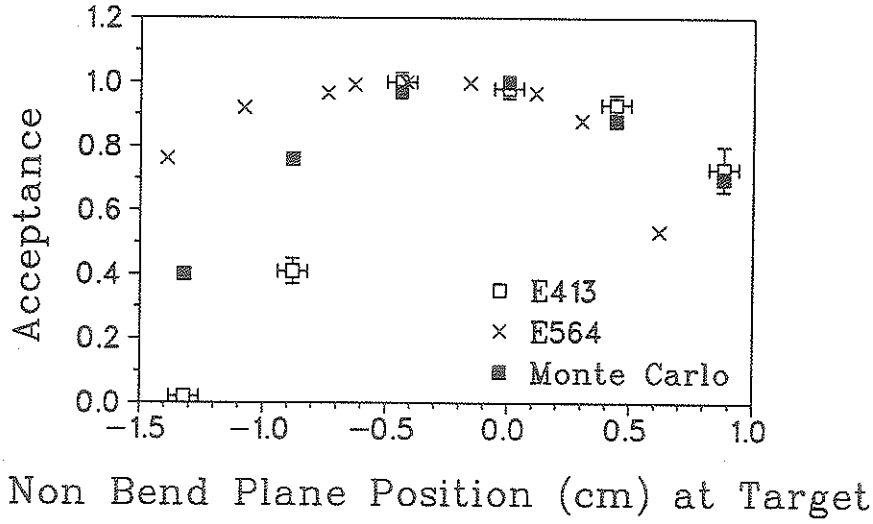

Figure 2.37: Comparison of E413 and E564 pp $\rightarrow$ dπ^+ MRS non bend plane acceptance scan with Monte Carlo results.

of this variation in the E413 and E564 target scans turns out to be minimal and is discussed in the Analysis Chapter.

2.4 Summary

The experiments were each performed in about 100 hours of beam on target. The MRS required initial diagnostic tuning, and the target required several days for set up and cooling. Following this preparation step, the experiments ran rather smoothly owing in large part to an excellent staff in a collaborative effort.

Chapter 3

Analysis

The offline analysis was carried out at the University of Manitoba using the Physics Vax Cluster and a TRIUMF-supplied software package, LISA. Data tape files were copied to disk allowing for easy replaying of data. Data files were then processed by LISA into histogrammed spectra of the appropriately calculated variables. The peak in the pion momentum spectrum was integrated above the background to obtain the area. The area and number of beam protons were then used to calculate the yield, correcting for the rate-dependent efficiencies of the apparatus. The cross section is obtained by normalizing the yield to the target density, the pion survival fraction and the rate-independent acceptances. Each of these facets of the analysis is described in greater detail in the following sections.

3.1 Data Extraction

3.1.1 Event Processing - LISA

LISA [Fre88] is a TRIUMF-supplied software package which is by no means standardized and shall therefore be summarized here. The LISA program is a FORTRAN written program which usually runs as a SUBPROCESS. The

program is as follows:

```
      PROGRAM LISA
      include 'lisa$dir:flacom'
      include 'lisa$dir:concom'
      integer*2 iether_data (32768)
      common/ether/iether_data
      CALL INITS
1     CONTINUE
      CALL CHKFLA (&1)
      CALL GETEVT
      CALL INSERT (&1)
      CALL CONTST (&1)
      CALL EVBEV (&1)
      CALL CONSPE
      CALL DISP
      GOTO 1
      END
```

The GETEVT routine obtains the EVENT from the disk file. There are two types of EVENTs, *Scalers* and triggers referred to as *Events*. Each event was comprised of the ADC and TDC data and the Drift Chamber data. In the GETEVT routine the processing of the Drift Chamber data in SUBROUTINE DRIFT was carried out to give the drift chamber wire coordinates X0, Y0, X1, X2, U1 and U2. The event data word stream is shown in Table 3.1.

This event data word is processed in the INSERT routine (shown in Appendix B). In the INSERT routine the coordinates discussed in Section 2.3 are calculated including the non bend plane coordinates Y1 and Y2, the reconstructed target coordinates XI and YI, and the focal plane coordinates, XF and XFK. Apart from these coordinates the coordinate ESUM, which is the maximum ADC signal from the Trigger paddles (FPP0 $\rightarrow$ FPP9), is also calculated. The plot of this coordinate versus TTB (the Time of Flight from Top to Bottom) is called SPID (Spectrum Particle IDentification). In this spectrum the pions are selected via software cuts and this is shown in Fig. 3.1.

Events which pass this cut are then subjected to further cuts on all the calculated coordinates:

MRS Event Data Word									
1	DCR	2	DCR2	3	HDR0	4	TTB	5	TRF
6	TSLT	7	TDIP	8	TS1	9	TS2	10	TREC
11	TVET	12	HDR1	13	ESL1	14	EDIP	15	FPP0
16	FPP1	17	FPP2	18	FPP3	19	FPP4	20	FPP5
21	FPP6	22	FPP7	23	FPP8	24	FPP9	25	HDR2
26	ES1H	27	ES1L	28	ES2	29	HDR3	30	EREC
31	EVET	32	SPAR	33	HDRV	34	U1	35	X2
36	U2	37	X1	38	X0	39	Y0		

Table 3.1: Data word stream for MRS event.

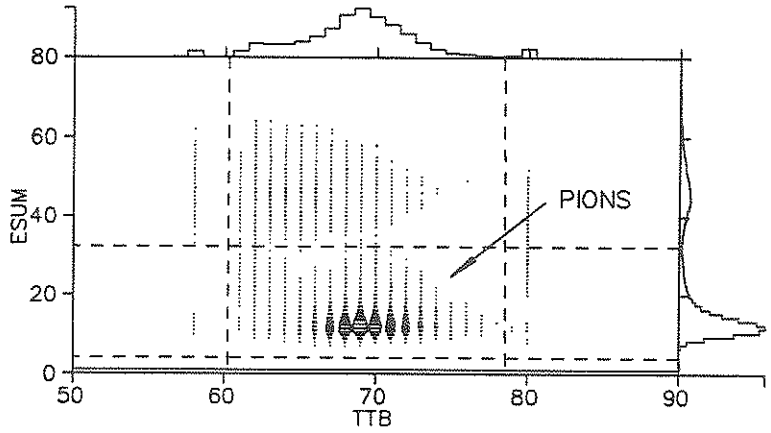

Figure 3.1: SPID spectrum, ESUM versus TTB.

target cuts	XI and YI
acceptance cuts	X0 and Y0
angle cuts	THETAPC and PHI

Typical spectra of these coordinates are shown in Fig. 3.2. To determine where to place the cuts with confidence, insight from the Monte Carlo was used, i.e. the distribution of pion events as compared to muon events. One then considered the final focal plane spectra with only those events which pass all these cuts. The errors in the judgement of these coordinate cuts was estimated by *analyzing the data* several times and examining the variance of the extracted peak area. The error was found to be typically 3%.

3.1.2 Extraction of Peak Area for ^{4}He

A sample focal plane spectrum for p ^{3}He $\rightarrow$ ^{4}He π^+ which passed all the cuts is shown in Fig. 3.3. From kinematics the peak at channel $\approx$ 5000 corresponds to the recoil ^{4}He nucleus in its ground state. To obtain the peak area the background around the peak is fitted assuming a linear dependence on the coordinate XFK and the peak area then extracted. Error in this extraction is dependent on the resolution of the system and on the reaction being studied. For reactions like pp $\rightarrow$ dπ^+ and p ^{3}He $\rightarrow$ ^{4}He π^+, the final state is cleanly resolved and so the errors are very small, typically 2%.

3.1.3 Extraction of Peak Area for ^{5}He

^{5}He is not a bound state nucleus, but rather a resonance observed in low energy n + α scattering. The ground state is attributed to the $p_{\frac{3}{2}}$ part of the interaction with a Q value and FWHM of approximately 0.9 MeV and 0.6 MeV respectively. There is also a first excited state at 4 MeV due to the $p_{\frac{1}{2}}$ part of the interaction with a FWHM of about 5 MeV. The energy level

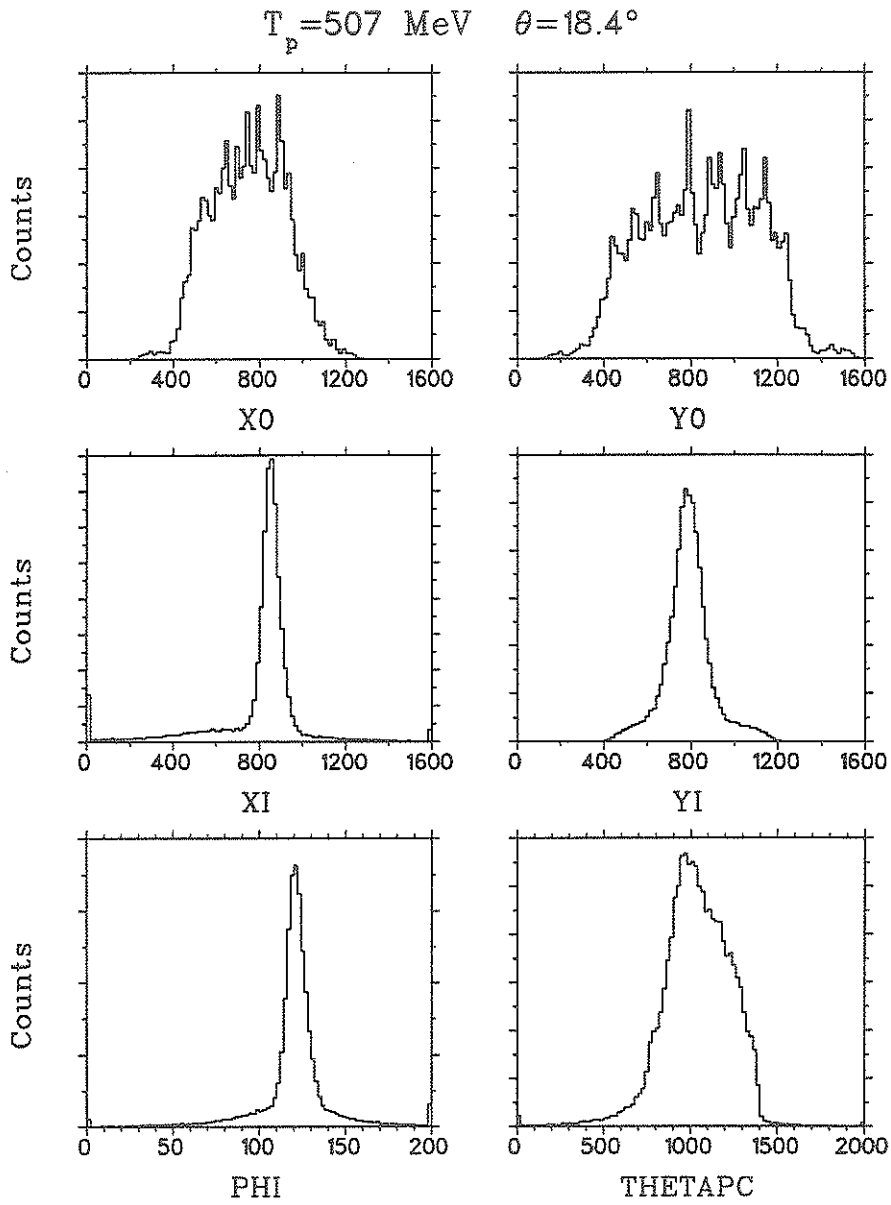

Figure 3.2: Typical coordinate spectra for p ^{3}He $\rightarrow$ ^{4}He π^+.

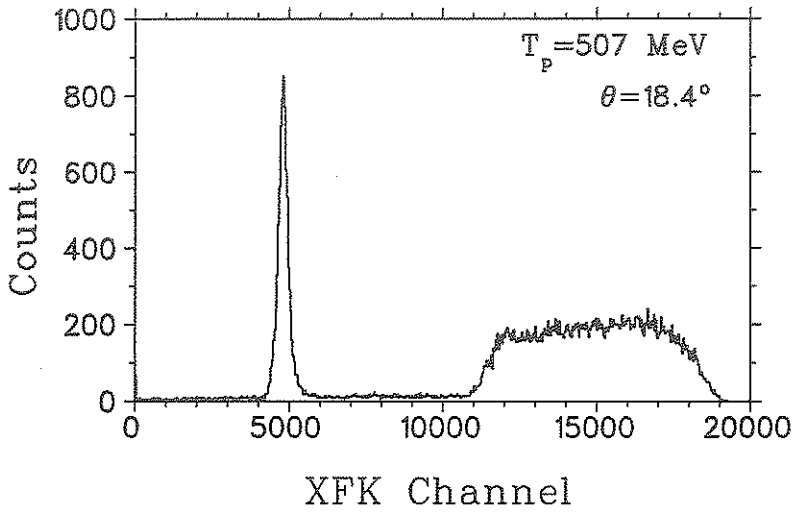

Figure 3.3: Focal plane spectrum for p ^{3}He $\rightarrow$ ^{4}He π^+.

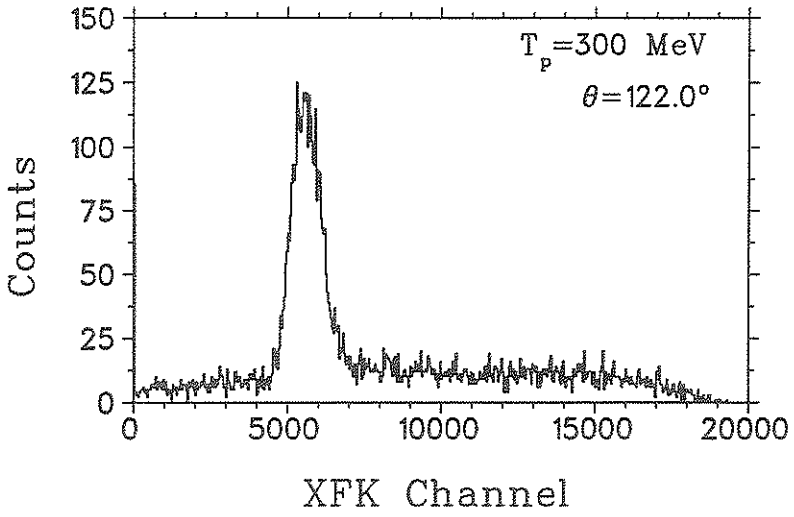

Figure 3.4: Focal plane spectrum for p ^{3}He $\rightarrow$ ^{4}He π^+ at back angles.

diagram for ^{5}He is shown in Fig. 3.5. A sample focal plane spectrum for p ^{4}He $\rightarrow$ ^{5}He π^+ which passed all the cuts is shown in Fig. 3.6.

Background Subtraction

Since the ^{5}He is a broad resonance, one has first to understand the background in order to subtract it, to obtain the pions resulting from ^{4}He(p,π^+). During the experiment, background measurements with the dummy target cell were made at several angles for each proton bombarding energy. Pions that originate from the iron and nickel (stainless steel) in the cell windows with energies corresponding to the ^{4}He(p,π^+)^{5}He reaction are very high in the continuum. It is known from published measurements ([Cra+80] and [Kra+82]) that in such situations the pion momentum spectrum is nearly constant over a large momentum range and also changes only slowly with angle. Furthermore, the slope changes only gradually, increasing with increasing proton bombarding energy. For the background measurements of this experiment, the pion momentum spectra were also found to be reasonably linear which is therefore consistent with the observations of Ref. [Cra+80] and Ref. [Kra+82]. In Fig. 3.7 the background spectra are shown versus pion momentum for T_p = 400 MeV (only the momentum range where the focal plane acceptance is nearly unity is shown). It is observed that the slope is nearly independent with angle and this observation is also supported in the literature [DiG+85].

Since the shape of the background spectra for each proton bombarding energy were found to be nearly independent of angle, an average background spectrum was used for each proton energy. For a given proton energy, the background spectrum for each angle was parameterized with a fit to Legendre polynomials. For T_p = 400 MeV the Legendre polynomial fits to the

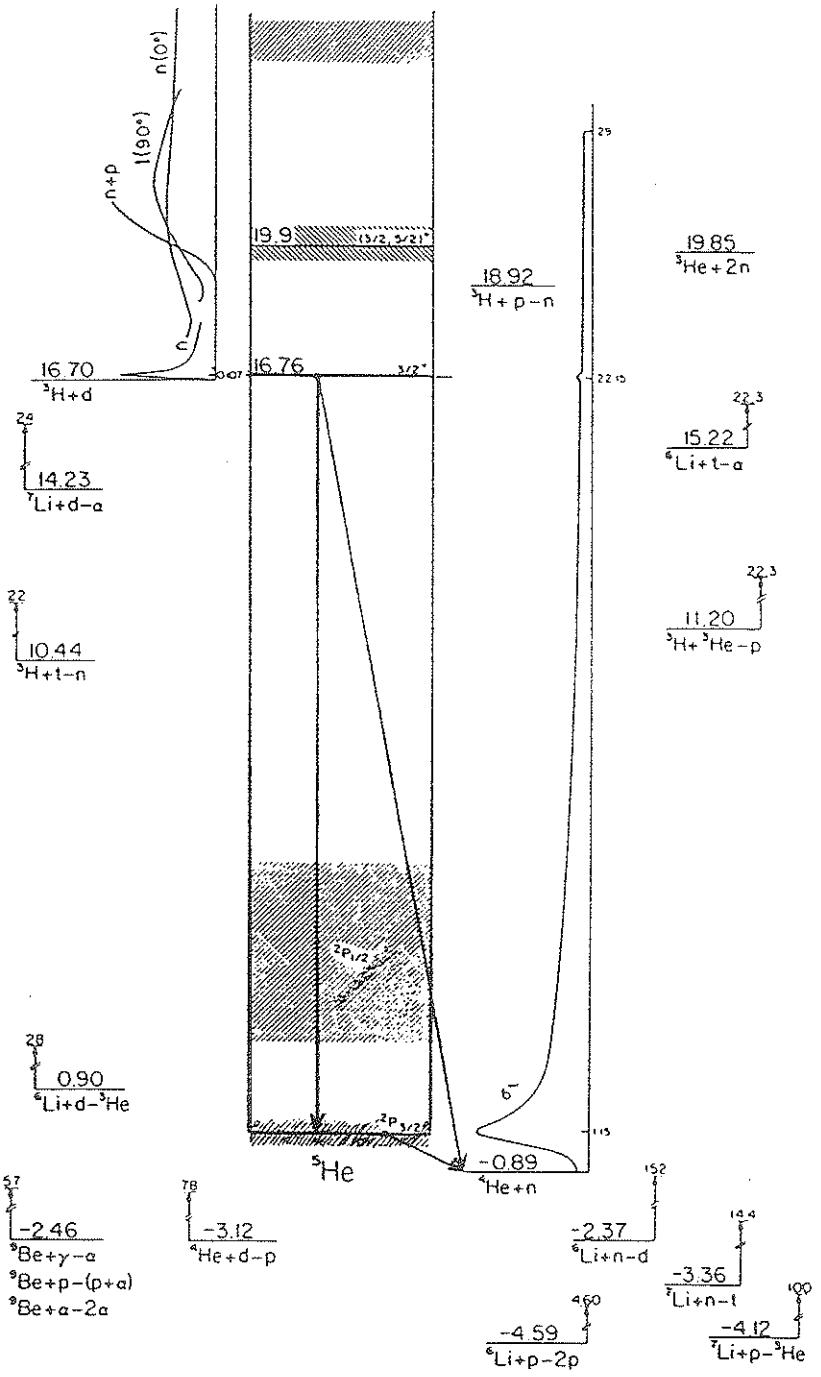

Figure 3.5: Energy level diagram for ^{5}He.

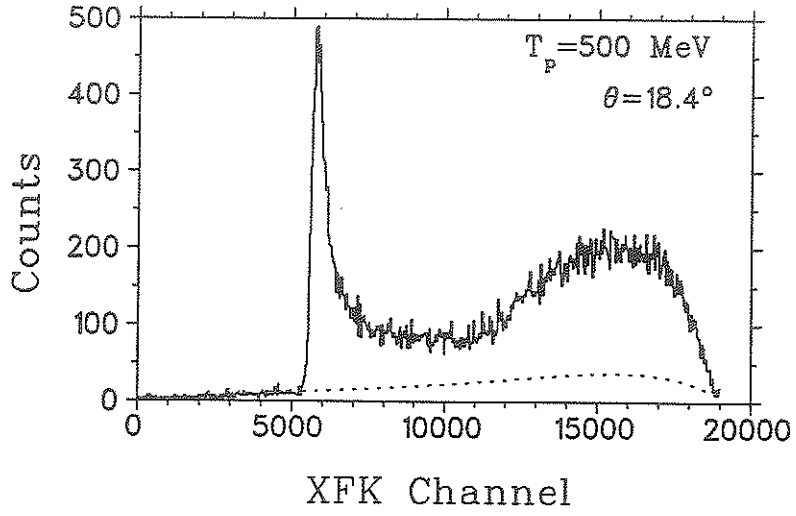

Figure 3.6: Focal plane spectrum for p ^{4}He $\rightarrow$ ^{5}He π^+. The dotted line is the background contribution.

background spectra for several angles are shown in Fig. 3.8. For a given energy, the Legendre polynomial coefficients were then averaged for all the angles. This fit was then compared to each of the angles again to verify the observation of angle-independence of the background. A typical background spectrum is shown in Fig. 3.9 with the solid line being that obtained from the averaged fit.

To obtain the background contribution to a ^{4}He(p,π^+) spectrum the averaged background spectrum for the same proton bombarding energy was renormalized using the high energy side (low XFK channel) of the ^{5}He pion spectrum. A typical example is shown in Fig. 3.6 where the dotted line is the background contribution to the XFK spectrum. The error in this method was determined by considering the variance in the fitting coefficients and observing the variance in the peak area with the sensitivity of normalization of

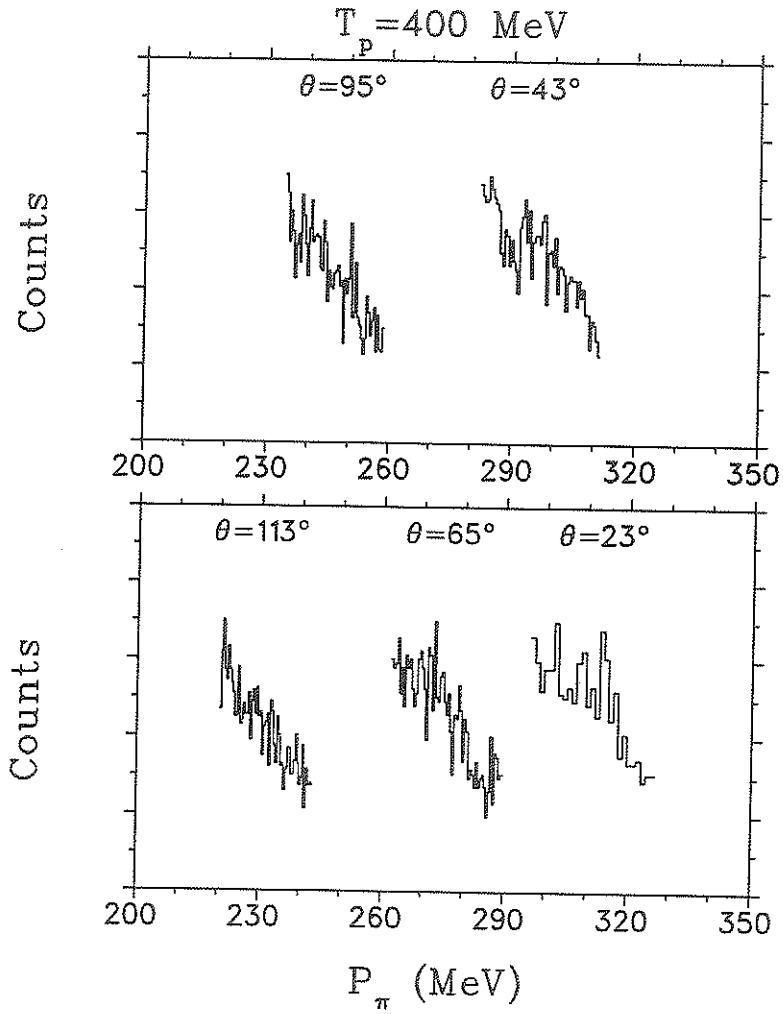

Figure 3.7: Background pion momentum spectra for several angles at T_p = 400 MeV.

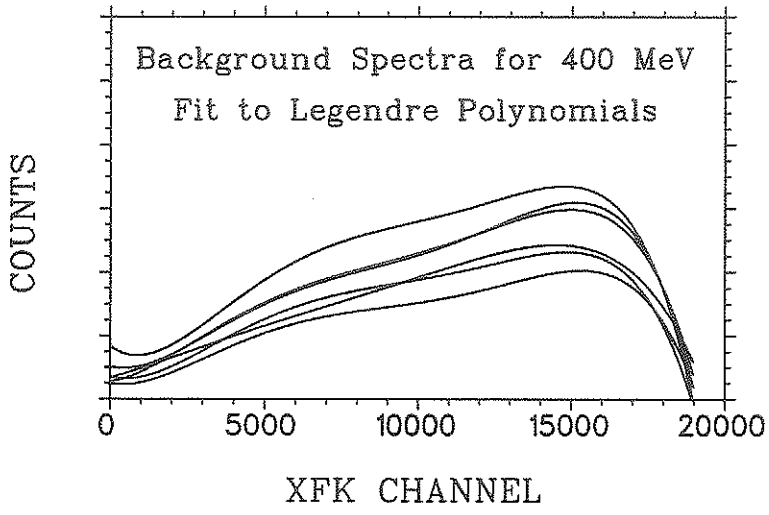

Figure 3.8: Background pion spectra for several angles at $T_p = 400$ MeV fit to Legendre polynomials.

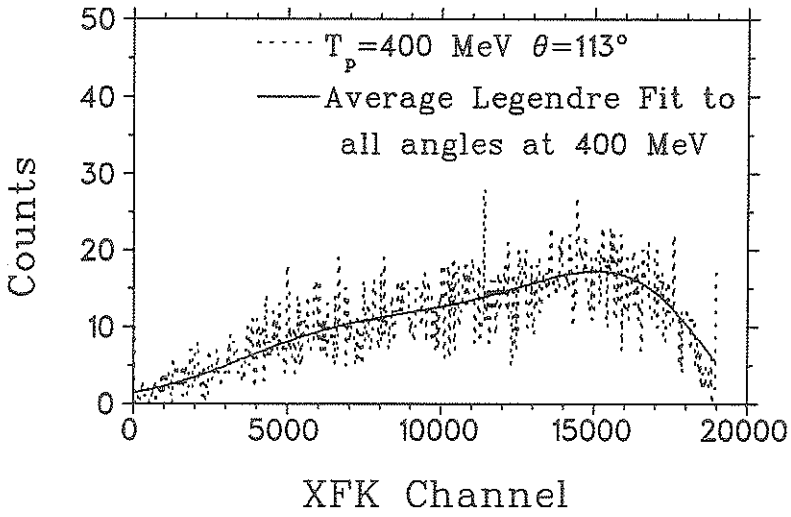

Figure 3.9: Comparison of background pion spectrum with averaged fit to Legendre polynomials for $\theta_{cm} = 113°$ at $T_p = 400$ MeV.

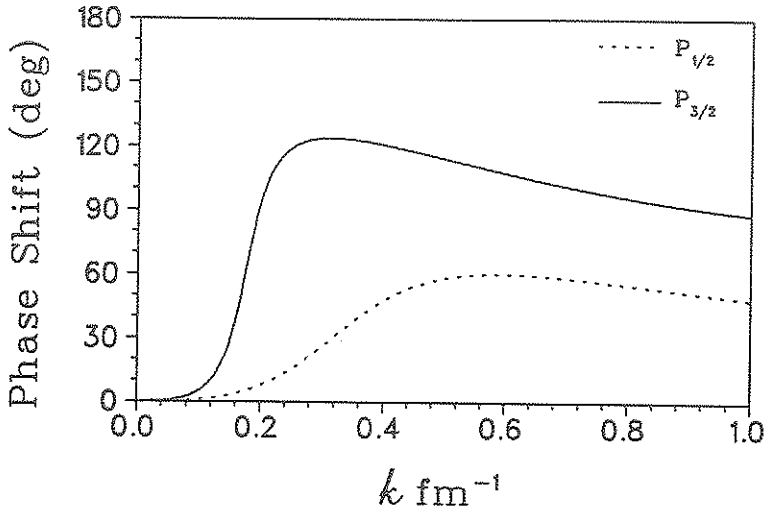

Figure 3.10: p-wave phase shifts for α + n scattering.

the background. For the lowest energy, $T_p = 240$ MeV, background measurements at only two angles were made and so the error was rather large, ≈6%. For the three higher energies, 300, 400 and 500 MeV, typically 6 angles each were done, and the error was much smaller, ≈3%.

Final State Interaction

In order to try and understand the pion spectra, an example of which is shown in Fig. 3.6, a final state interaction (FSI) calculation was performed based upon the low energy n + α elastic scattering phase shifts. A calculation for the ^{5}He FSI for this reaction was performed by Germond and Wilkin [GW85] where the FSI was momentum-transfer dependent in their model. The calculation presented here is model independent but uses Germond and Wilkin's development to obtain the ^{5}He wave function from n+α phase shifts.

The n + α elastic scattering data were fitted to a phase shift analysis by Bond and Firk [BF77]. The p-wave phase shifts of their fit are shown in Fig. 3.10. These phase shifts were then parameterized in terms of a separable

	β_l (fm^{-1})	λ_l (fm^{-2l-3})
$s_{\frac{1}{2}}$	1.101	0.5412
$p_{\frac{3}{2}}$	1.489	5.5111
$p_{\frac{1}{2}}$	1.241	1.544

Table 3.2: Values for the potential for n + α scattering data.

potential of the generalized Yamaguchi form by Germond and Wilkin. The functional form is as follows:

$$v_l(p) = \frac{p^l}{(p^2+\beta_l^2)^{l+1}} \tag{3.1}$$

This leads to a parameterization of the phase shifts which for the p-wave part of the interaction is

$$k^3 \cot\delta_1 = \frac{(k^2+\beta_1^2)^4}{2\pi^2\lambda_1} + \frac{(k^2-\beta_1^2)(\beta_1^4+10\beta_1^2k^2+k^4)}{16\beta_1^3}. \tag{3.2}$$

The parameters β and λ are shown in Table. 3.2 for the s and p wave parts of the interaction. Only the p-wave was considered since the s-wave part was shown to be negligible by Germond and Wilkin.

The ^{5}He wave function was written in terms of the separable potential parameters and the n + α phase shifts. For the p-wave part the radial wave function is given by

$$\begin{aligned}\psi_{k,l}^{(-)}(r) &= e^{-i\delta_1}\{\cos\delta_1 j_1(kr) - \sin\delta_1[y_1(kr) - i\frac{\beta_1^2}{k^2}h_1^{(1)}(i\beta_1 r) \\ &\quad -\frac{1}{2}(1+\frac{\beta_1^2}{k^2})\beta_1 r h_0^{(1)}(i\beta_1 r)]\}.\end{aligned} \tag{3.3}$$

The functions $j(x)$, $y(x)$ and $h^{(1)}(x)$ are the spherical Bessel, Neumann and Hankel functions respectively. The $p_{\frac{3}{2}}$ wave function is shown in Fig. 3.11 and the $p_{\frac{1}{2}}$ wave function is shown in Fig. 3.12 for momenta k = 0.2 and 0.4 fm^{-1} (corresponding to excitation energies of 1.04 MeV and 4.15 MeV

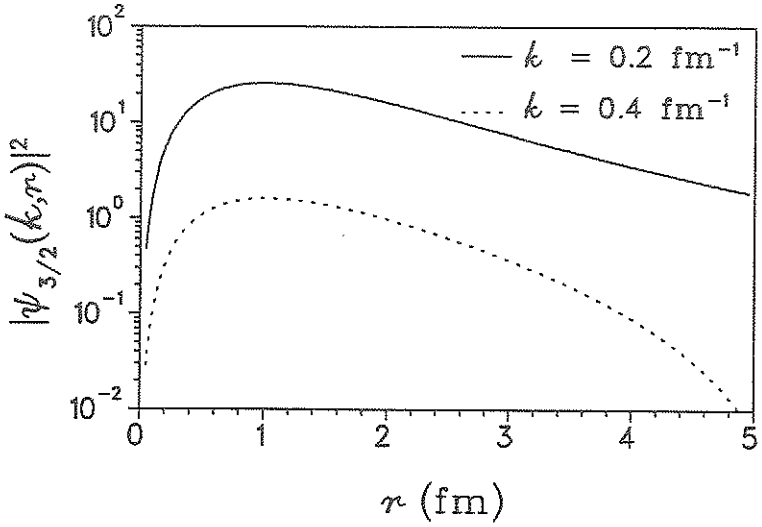

Figure 3.11: The $p_{\frac{3}{2}}$ state $n + \alpha$ wave function.

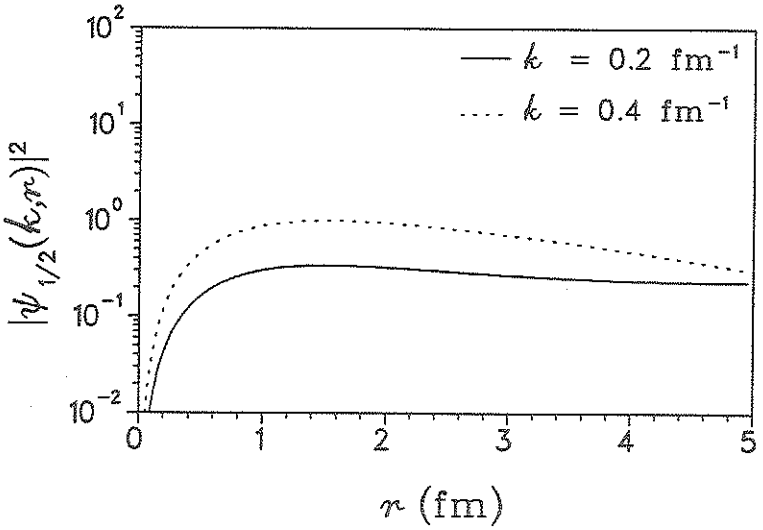

Figure 3.12: The $p_{\frac{1}{2}}$ state $n + \alpha$ wave function.

respectively in the $n + \alpha$ system).

The final state interaction is usually calculated as an enhancement of the phase space. Consider the case of

$$1 + 2 \rightarrow 3 + 4 + 5 \tag{3.4}$$

where specifically we wish to consider the reaction

$$p + \alpha \rightarrow \pi^+ + n + \alpha \tag{3.5}$$

The cross section is proportional to a matrix element squared and a phase space factor.

$$\frac{d\sigma}{d\Omega_3 dp_3} = |\langle 345|M|12\rangle|^2 \times \text{Phase Space} \tag{3.6}$$

The phase space factor $(dR_3/d\Omega_3 dp_3)$ may be calculated from relativistic kinematics [Hag63] and is shown in Appendix D to be:

$$\frac{dR_3}{d\Omega_3 dp_3} = \frac{\pi p_3^2}{2E_3} \times \frac{\sqrt{(E_{45}^2 - (m_4 + m_5)^2)(E_{45}^2 - (m_4 - m_5)^2)}}{2E_{45}^2} \tag{3.7}$$

where

$$E_{45} = m_4 + m_5 + E_x, \tag{3.8}$$

and E_x is the internal excitation energy of 4 and 5. The cm momentum k for the $n + \alpha$ system is a function of the excitation energy of the ^{5}He system, E_x.

$$k = \frac{\sqrt{2\mu E_x}}{\hbar c} \tag{3.9}$$

where k is expressed in units of fm^{-1} and μ is the reduced mass of the $n + \alpha$ system.

$$\mu = \frac{m_4 m_5}{m_4 + m_5} = 750.42\,\text{MeV} \tag{3.10}$$

A sample calculation of the phase space for $T_p = 300$ MeV and $\theta_{lab} = 95°$ is shown in Fig. 3.13.

The thrust of a final state interaction calculation is summarized very well by G.F. Wolters:

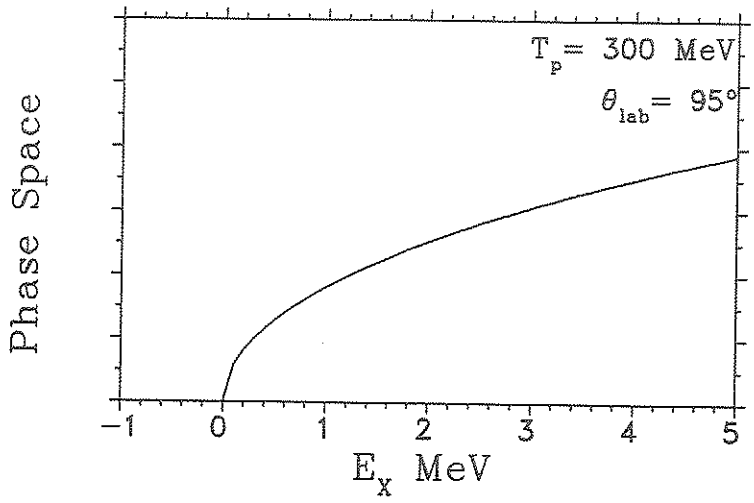

Figure 3.13: The relativistic three particle phase space for $p+\alpha \rightarrow \pi^+ + n + \alpha$ at $T_p = 300$ MeV and $\theta_\pi^{lab} = 95°$.

> "The main idea how to take into account the effect of final state interactions is to multiply the transition amplitude, which one would have in the absence of final state interactions, by the wave function describing the particular state in which the interactions between particles in the final state takes place." [1]

In this case the state wave function $|45\rangle$ is the ^{5}He wave function $\psi(k,r)$ and is written as a function of the $n+\alpha$ relative coordinates r and k. In Figures 3.11 and 3.12 it is observed that the shape of the wavefunction does not change significantly for the range of momentum k corresponding to low values of the excitation energy E_x. Thus it is justifiable to write the wave function in factorized form

$$|45\rangle \sim \psi_j(k,r) \sim \zeta_j(k)\phi_j(r). \tag{3.11}$$

[1] G.F. Wolters, *Final State Interactions* in Kinematics and Multiparticle Systems edited by M. Nikolić for the Proceedings of the International School of Elementary Particle Physics, Gordon and Breach Science Publishers Ltd., New York, p.278 (1968).

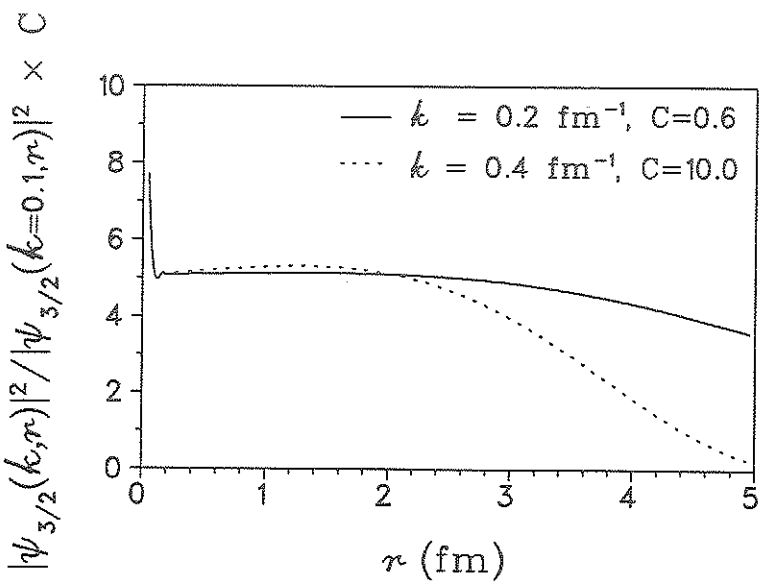

Figure 3.14: Comparison of $\psi(k = 0.2\,\mathrm{fm}^{-1}, r)$ and $\psi(k = 0.4\,\mathrm{fm}^{-1}, r)$ to $\psi(k = 0.1\,\mathrm{fm}^{-1}, r)$ for $p_{\frac{3}{2}}$ state. Note that the ratio is nearly constant for $r \leq 2$ fm.

The FSI enhancement factor, generally expressed as

$$|\psi(k, r = r_0)|^2 \propto |\zeta(k)|^2, \tag{3.12}$$

is then relatively independent of the particular choice of the radius parameter r_0. This was indeed found to be the case for the $p_{\frac{3}{2}}$ and $p_{\frac{1}{2}}$ states individually, as the details given in Figs. 3.14 and 3.15 verify.

However, comparison of the shape of the wavefunction for $p_{\frac{3}{2}}$ with that for $p_{\frac{1}{2}}$ illustrated in Fig. 3.16, show them to be quite different. Consequently, the relative strength of the $p_{\frac{1}{2}}$ contribution to that of the $p_{\frac{3}{2}}$ contribution will depend on the choice of radius parameter r_0. In order to make the calculation less dependent on the specific value of r_0 the following definition was adopted

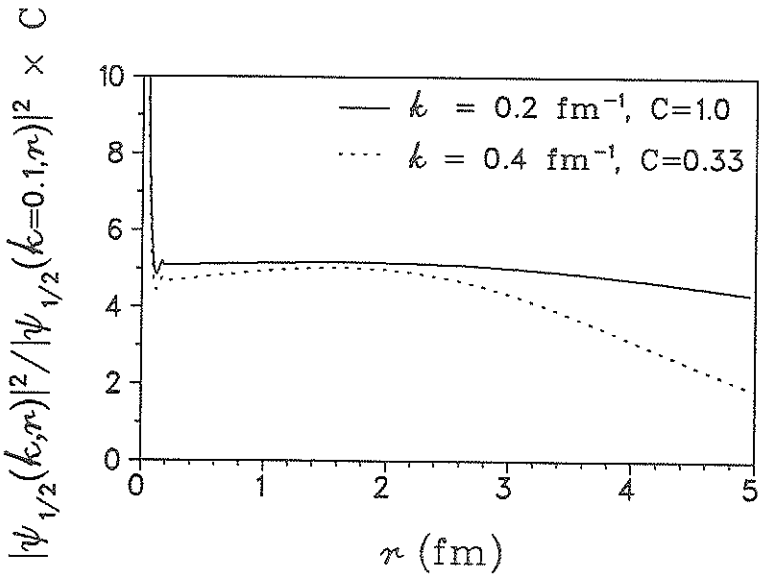

Figure 3.15: Comparison of $\psi(k = 0.2\,\mathrm{fm}^{-1}, r)$ and $\psi(k = 0.4\,\mathrm{fm}^{-1}, r)$ to $\psi(k = 0.1\,\mathrm{fm}^{-1}, r)$ for $p_{\frac{1}{2}}$ state. Note that the ratio is nearly constant for $r \leq 2$ fm.

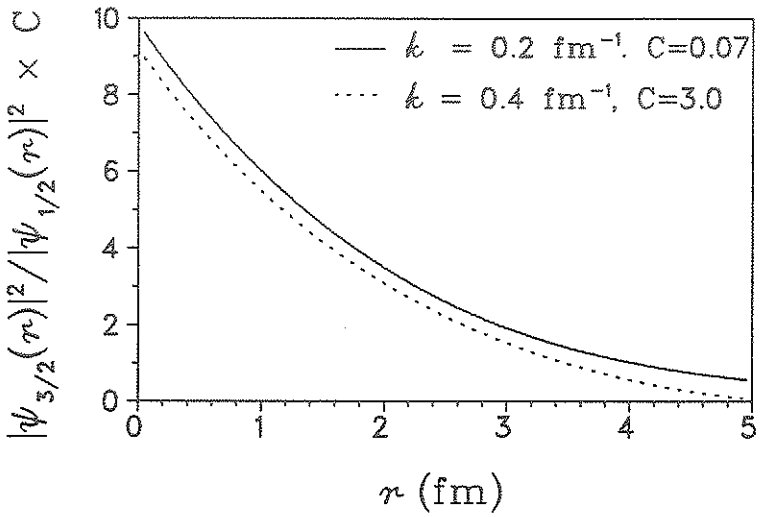

Figure 3.16: Comparison of $\psi_{3/2}(k,r)$ to $\psi_{1/2}(k,r)$ for $k = 0.2$ and 0.4 fm^{-1}.

for the FSI enhancement factor

$$|\zeta_j(k)|^2 = (2j+1)\int_{r_1}^{r_2} |\psi_j(k,r)|^2 r^2\, dr \tag{3.13}$$

where $r_1 = 0$ and $r_2 = 2$ fm.

Now Eqn. 3.6 may be written as

$$\frac{d\sigma}{d\Omega_3 dp_3} = |\langle 3(45)|M|12\rangle|^2 \times |\zeta_{total}(k)|^2 \times \frac{dR_3}{d\Omega_3 dp_3} \tag{3.14}$$

where

$$|\zeta_{total}(k)|^2 = |\zeta_{p_{1/2}}(k)|^2 + |\zeta_{p_{3/2}}(k)|^2 \tag{3.15}$$

The enhancement, $|\zeta(k)|^2$, is shown in Fig. 3.17 where the dotted line is the contribution of the $p_{\frac{3}{2}}$ state only, the dot-dash line is the contribution of the $p_{\frac{1}{2}}$ state only and the solid line is the total enhancement.

The dependence of the enhancement on the integration limits (r_1 and r_2 in Eqn. 3.13) was investigated. The enhancements calculated with different integration limits are shown in Fig. 3.18. Around the peak there is very little change, however at higher excitation one notices a difference in the relative

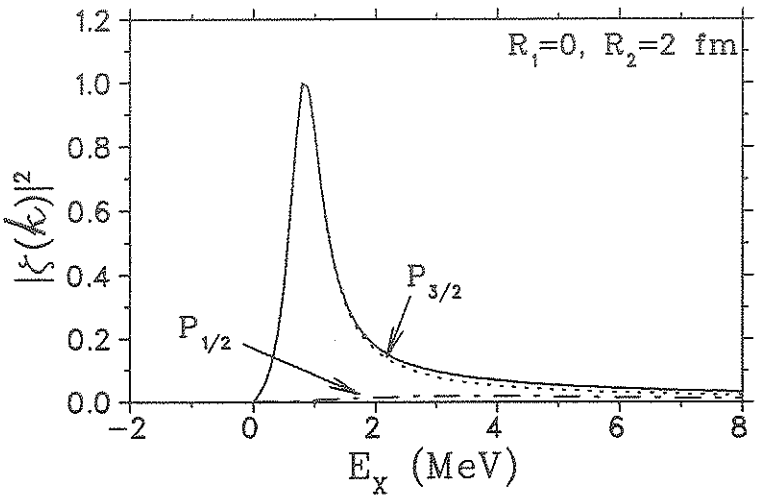

Figure 3.17: Enhancement, $|\zeta(k)|^2$, for $\pi^+ + \mathrm{n} + \alpha$. The dotted line corresponds to the contribution from the $p_{\frac{3}{2}}$ state only and the dot-dash line corresponds to the contribution from the $p_{\frac{1}{2}}$ state only. The curve has been normalized so that maximum is unity.

contribution from the $p_{\frac{3}{2}}$ and $p_{\frac{1}{2}}$ states. This is reflected in the fraction of the $p_{\frac{3}{2}}$ and $p_{\frac{1}{2}}$ states' contribution to the total final state interaction spectrum. In Table. 3.3 the contributions of the states from zero to 4.44 MeV excitation for different integration limits are presented. The calculation was performed for $T_p = 500$ MeV and $\theta_{lab} = 18°$ however the results are quite insensitive to pion angle and beam proton energy as will be discussed below. One observes that up to 4.44 MeV the $p_{\frac{3}{2}}$ state comprises about 93 ± 3 % of the total spectrum.

For comparison to the experimental spectra the theoretical distribution given by Eqn. 3.14 must be modified to take into account the finite resolution of the experiment. This was done by means of a convolution integral

$$h(x) = \int_{x_1}^{x_2} f(x, x')\, c(x')\, dx' \tag{3.16}$$

where $c(x')$ is the calculated spectrum (Eqn. 3.14) and $f(x, x')$ is the resolu-

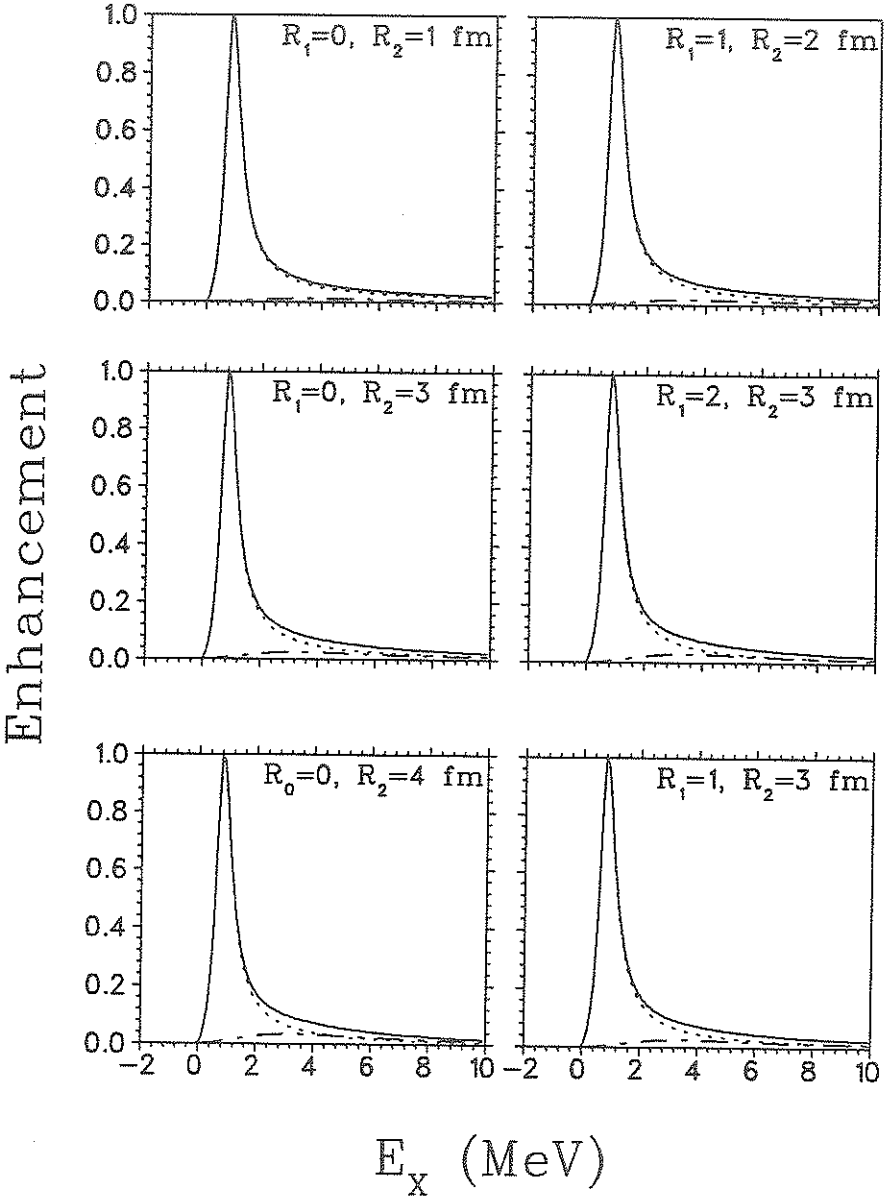

Figure 3.18: Dependence of enhancement, $|\zeta(k)|^2$, on r_1 and r_2. The dotted lines correspond to the $p_{\frac{3}{2}}$ state only and the dot-dash lines correspond to the $p_{\frac{1}{2}}$ state only.

Enhancement × Phase Space							
Integration Limits		Fraction		Integration Limits		Fraction	
r_1 (fm)	r_2 (fm)	$p_{\frac{3}{2}}$	$p_{\frac{1}{2}}$	r_1 (fm)	r_2 (fm)	$p_{\frac{3}{2}}$	$p_{\frac{1}{2}}$
0	1	0.95	0.05	0	2	0.93	0.07
0	3	0.90	0.10	0	4	0.87	0.13
1	2	0.93	0.07	2	3	0.88	0.12
1	3	0.90	0.10				

Table 3.3: Fraction of $p_{\frac{3}{2}}$ and $p_{\frac{1}{2}}$ states' contribution to final state interaction spectrum and its dependence on the integration limits r_1 and r_2. Calculations for $T_p = 500$ MeV and $\theta_{lab} = 18°$.

tion function of a Gaussian form,

$$f(x, x') = \exp\{-\frac{1}{2}(\frac{x' - x}{\sigma})^2\}. \tag{3.17}$$

Then $h(x)$ is the spectrum that is compared to experiment. The value of σ was chosen to obtain the best observed fit to the peak. Typically σ ranged from 0.4 to 0.7 MeV. By examining line shapes of the pion spectra corresponding to a bound state recoil nucleus (the deuteron for the pp $\rightarrow$ dπ^+ calibration spectra and ^{4}He for ^{3}He(p,π^+)^{4}He spectra in E413), and using the Monte Carlo, these values were found to be consistent.

Sample background-subtracted focal plane spectra observed for p ^{4}He $\rightarrow$ ^{5}He π^+ at 240 and 500 MeV at 18.4° are shown in Fig. 3.19. The solid line is the final calculated line shape from the final state interaction calculation, $h(x)$, up to 5 MeV in excitation. It is observed that the calculation does an excellent job in describing the peak shape for these spectra.

The FSI enhancement factor depends only on the excitation energy E_x. The other factor determining the spectrum shape of Eqn. 3.14 is the phase

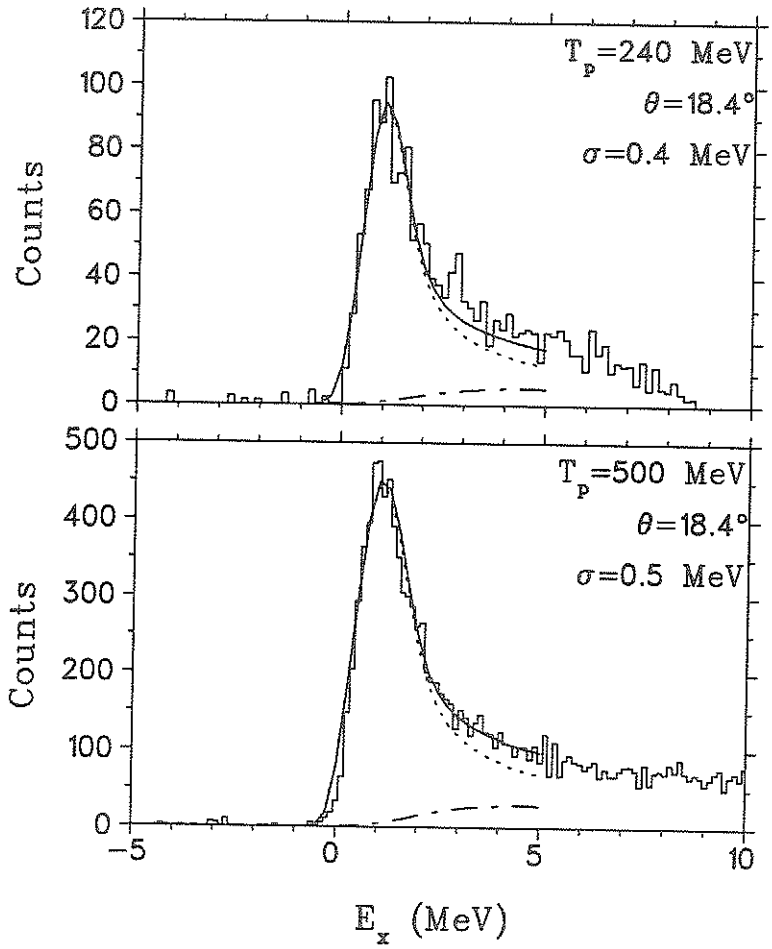

Figure 3.19: Final state interaction for $\alpha + n + \pi^+$ spectrum.

space factor given by Eqn. 3.7. For a given pion angle and incident proton energy the factor p_3^2/E_3 changes very little over a range of excitation energy E_x of a few MeV. Hence, for all intents and purposes the spectrum shape of Eqn. 3.14 becomes a function of the excitation energy E_x alone, i.e. a universal function independent of angle and bombarding energy.

In Fig. 3.19 the independence of the proton bombarding energy is observed to be indeed true. In Fig. 3.20 the spectra together with the FSI result for back angles are shown. Here the angle independence fails for excitation energies above $E_x \approx 3\,\mathrm{MeV}$. This general feature was observed in all the back angle spectra for all proton energies. It would therefore lead us to conclude that at these higher momentum transfers the FSI calculation is missing an essential ingredient to explain the additional cross section at the higher excitation.

The complete theory of final state interactions is discussed in more detail elsewhere (see Ref. [Wol68], Ref. [Gil64] and Ref. [Wat52]) and other much more sophisticated methods are also found in the literature (see for example Ref. [Ala+77] and Ref. [Wic+85]).

Peak Integration and Normalization

The integration limits were chosen from the lower edge of the pion peak up to 4.44 MeV in excitation (to be consistent with already published data). The pion momentum corresponding to the nominal ^{5}He ground state mass (excitation $\approx$0.9 MeV) was assumed to correspond to the XFK channel (focal plane coordinate) of the centroid, for very tight cuts around the pion peak. The cut at 4.44 MeV was then determined from the focal plane - momentum calibration (shown in Fig. 2.29). By integrating the peak with several

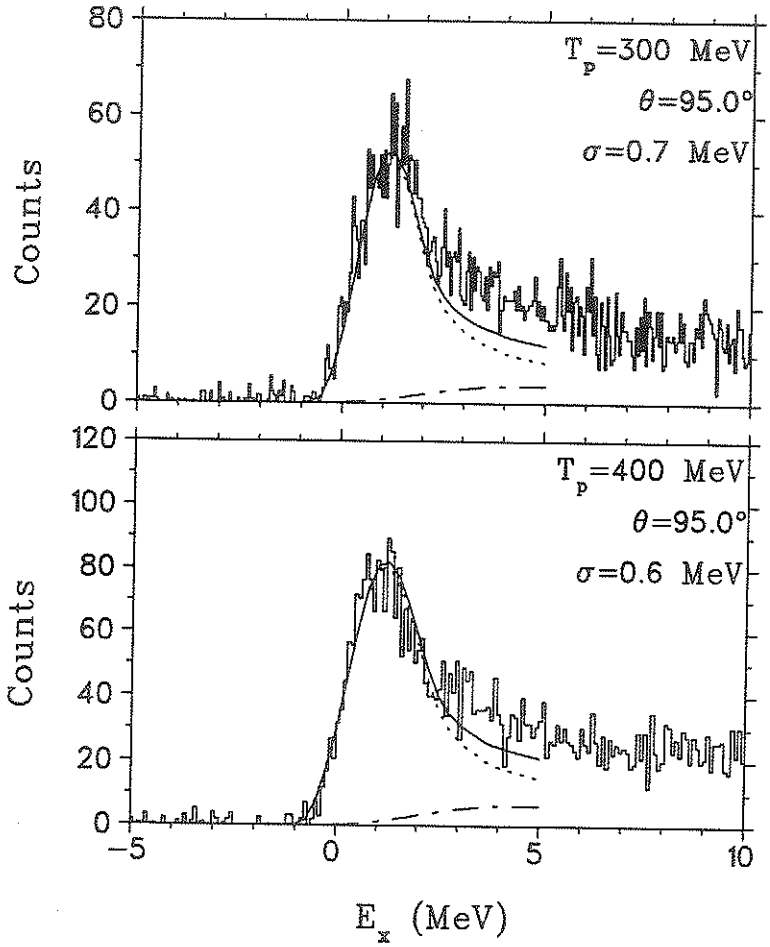

Figure 3.20: Final state interaction for back angles.

possible peak centroids (equivalent to 0.90±0.50 MeV) the error in the peak integration was estimated to be ≈3%. The error in establishing this cut was reasonably small since the number of counts per channel at 4.44 MeV excitation is quite small compared to the total area (arising mostly from the area under the peak for low excitation energy).

To determine the contribution of each of the $p_{\frac{1}{2}}$ and $p_{\frac{3}{2}}$ states, a cut at 4.44 MeV excitation was placed on the calculated line shapes and the fraction of each determined. Let $d\sigma/d\Omega_{4.44}$ be the cross section for the pion peak corresponding to integration from $0 \rightarrow 4.44$ MeV excitation in the recoil nucleus including both the $p_{\frac{1}{2}}$ and $p_{\frac{3}{2}}$ contribution. Let $d\sigma/d\Omega_{\frac{3}{2}}$ be the total $p_{\frac{3}{2}}$ cross section integrated between $0 \leq E_x \leq E_x^u$, determined from the calculated line shape. Define η_{fsi} to be

$$\eta_{fsi} = \frac{d\sigma/d\Omega_{4.44}}{d\sigma/d\Omega_{\frac{3}{2}}}. \tag{3.18}$$

In Fig. 3.21 the value of η_{fsi} versus upper integration limit E_x^u is shown for several sets of integration limits, r_1 and r_2, in Eqn. 3.13. The calculation for r_1=0 and r_2=2 fm (solid line) indicates that $\lim_{E_x \rightarrow \infty} \eta_{fsi} \approx 0.6$. With respect to angle and proton energy the calculation revealed that this ratio was nearly constant (i.e. independent as expected from previous discussion). Evidence from the analysis of the ^{4}He($\vec{p}$,π^+)^{5}He from [LeB+85] at 201 MeV supports the hypothesis of the angle independence. Their analysis was done assuming a parabolic background from $p_{\frac{1}{2}}$ state centred at 4.44 MeV. They also performed the integration without the parabolic background subtraction for comparison. The ratios of these was found to be nearly constant (≈ 0.6) as is shown in Table. 3.4. The constancy of this ratio indicates that the shape does not change significantly with angle which therefore supports the hypothesis of angle independence.

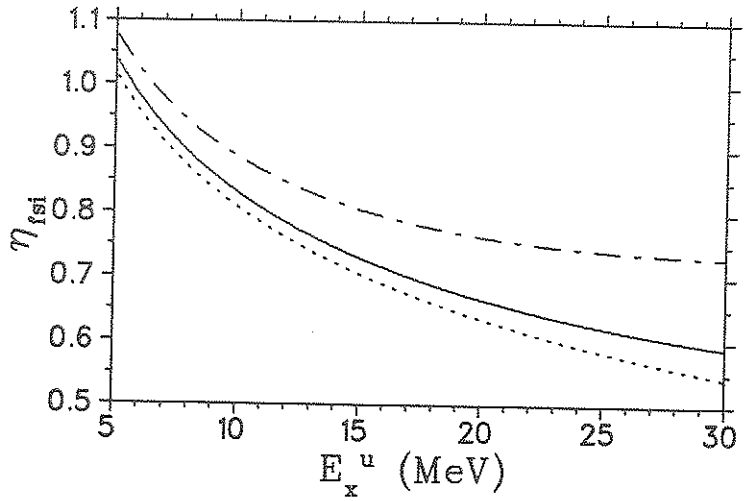

Figure 3.21: Sensitivity of the final state interaction correction factor, $\eta_{\rm fsi}$, on the integration limits, r_1 and r_2. The solid line is for r_1=0 and r_2=2 fm, the dotted line for r_1=0 and r_2=1 fm and the dashed-dotted line for r_1=0 and r_2=4 fm.

All this implies then that using a constant value for $\eta_{\rm fsi}$ for the cross section calculation is a good approximation. All the ^{5}He data were therefore renormalized by this constant factor of $\eta_{\rm fsi} = 0.6$.

$$\frac{\mathrm{d}\sigma}{\mathrm{d}\Omega}(\frac{3}{2}) = \frac{\mathrm{d}\sigma/\mathrm{d}\Omega_{4.44}}{\eta_{\rm fsi}} \tag{3.19}$$

$\mathrm{d}\sigma/\mathrm{d}\Omega(\frac{3}{2})$ is the cross section quoted in the data tables and shown in the figures. Note that this factor is a constant factor for *all angles* and *all proton energies.*

The error in $\eta_{\rm fsi}$ is difficult to determine. In Fig. 3.21 the sensitivity of the final state interaction calculation with the integration limits in Eqn. 3.13 would indicate that the error is quite large. Furthermore, since the calculation fails to reproduce the shape of the spectrum at back angles and at high excitation, a rather large error of 20 % was estimated.

^{4}He($\vec{p}$,π^+)^{5}He from LeBornec *et al.* (1985) T_p = 201 MeV			
θ_{lab}	$d\sigma/d\Omega_{cm}$† $\frac{nb}{sr}$	$d\sigma/d\Omega_{cm}$‡ $\frac{nb}{sr}$	Ratio
20	631 ± 45	1068 ± 11	0.59 ± 0.04
30	671 ± 45	1108 ± 12	0.60 ± 0.04
40	597 ± 63	1034 ± 45	0.58 ± 0.06
50	610 ± 63	1047 ± 46	0.58 ± 0.06

†*with parabolic background subtraction*

‡*without parabolic background subtraction*

Table 3.4: ^{4}He($\vec{p}$,π^+)^{5}He from LeBornec *et al.*

3.2 Proton Beam Normalization

For determination of the analyzing power and differential cross section the beam polarization P and the total number of beam protons N_p must be known. This was done by examining the output of the two beam line monitors, the SEM and IBP, and using results from previous calibration experiments.

3.2.1 Proton Beam Normalization from SEM

The SEM was calibrated using a Faraday Cup in a previous experiment [Abe+85] [Vet+90]. The scalar output of the SEM was evaluated in the offline analysis by using the following formula:

$$N_p = \frac{\text{SEM(scalar)}}{\text{RSEM}} \times \frac{1}{\frac{dE}{dx}(\text{Al})} \times \frac{10^{-10}}{1.602 \times 10^{-19}} \qquad (3.20)$$

RSEM Factor	
E413	0.307 ± 0.002
E564	0.235 ± 0.002

Table 3.5: Calibration constants for BL4B SEM for E413 and E564.

where RSEM is a constant which is related to the production of secondary electrons and is dependent on the density of the material. This constant was determined in the calibration experiment. The SEM was different for E413 and E564 so there were two values of RSEM, (see Table. 3.5). dE/dx(Al) is the energy loss of protons in Aluminum at the proton bombarding energy of interest (in units of MeV/g/cm^2).

3.2.2 Proton Beam Normalization from IBP

The absolute normalization of the IBP was also calibrated in a previous experiment using a Faraday Cup [Abe+85]. A schematic of the IBP electronics logic is shown in Fig. 2.2. The scalars for LEFT and RIGHT scattered events were first corrected for accidentals, for example for LEFT,

$$\mathrm{LEFT} = \mathrm{LEFT(scalar)} - \mathrm{LEFT(acc)} \tag{3.21}$$

and similarly for RIGHT. The number of beam protons was then obtained using the following formula

$$\mathrm{N_p} = \frac{(\mathrm{LEFT} + \mathrm{RIGHT})}{\mathrm{RIBP}} \times \frac{1}{\rho_{\mathrm{CH2}}} \times \frac{10^{-9}}{1.602 \times 10^{-19}}. \tag{3.22}$$

RIBP is related to the lab differential cross sections for pp elastic scattering and was determined from a polynomial fit to the data from the calibration experiment with the Faraday Cup.

$$\mathrm{RIBP} = 44.17 - \frac{\mathrm{T_p}}{100}(1.171 - \frac{\mathrm{T_p}}{100}1.250) \tag{3.23}$$

IBP Target Densities		
Expt	T_p (MeV)	$\rho^{\dagger}_{CH_2}$ ($\frac{mg}{cm^2}$)
E413	300,416 and 507	1.30
E564	240 and 300	1.17
	400 and 500	1.27

† errors are estimated at less than 1%

Table 3.6: IBP CH_2 areal target densities for E413 and E564.

The areal target densities, ρ_{CH_2}, used in the two experiments are tabulated in Table. 3.6.

3.2.3 Comparison of Proton Beam Normalization from IBP and SEM

The difference between the IBP and SEM normalization may determined by comparing the above formulae, 3.20 and 3.22. The expected ratio (R) of the IBP to SEM scalars was calculated as follows:

$$R = \frac{\text{IBP scalars}}{\text{SEM scalars}} = \frac{\text{RSEM}}{\rho_{CH_2}} \times \frac{\frac{dE}{dx}(Al)}{\text{RIBP}} \tag{3.24}$$

The first and second quotients contain the proton energy independent and dependent parameters respectively. The ratio obtained experimentally from the scalars themselves is plotted versus Run# in Fig. 3.22 for E413 and in Fig. 3.23 for E564. The dotted lines are the ratios obtained from Eq. 3.24. It was found that the experimental ratio differed from that expected. The discrepancy was between ≈1% and ≈5%, see Table. 3.7. For the cross section normalization the number of beam protons (N_p) from the IBP was used.

Suppose the ratio of IBP/SEM were less than that expected by 5%. If it

Ratio of $\frac{IBP}{SEM}$ Scalars			
E413			
T_p (MeV)	Expected	Average of Experimental	Difference
300	8.000	7.605 ± 0.042	−4.9%
416	10.884	10.542 ± 0.120	−3.1%
507	13.908	13.709 ± 0.197	−1.4%
E564			
T_p (MeV)	Expected	Average of Experimental	Difference
240	7.664	7.832 ± 0.097	+2.2%
300	9.346	9.319 ± 0.110	−0.3%
400	13.474	14.285 ± 0.141	+6.0%
500	17.435	18.609 ± 0.295	+6.7%

Table 3.7: Comparison of predicted and experimental R(IBP/SEM).

is assumed that the SEM was *absolute* then this would imply an underestimation of N_p by 5%, and therefore an overestimation of the cross section by 5%. The average error quoted for the number of beam protons is 5% which is the average deviation of Table. 3.7.

There are several possible reasons for the discrepancy between the SEM and the IBP normalization. Since the calibration constant RSEM is dependent on the secondary electron emission from the Aluminum foils in the SEM it is possible that, due to small leakages in the SEM vacuum, the Aluminum foils became oxidized and therefore changed the effective value of RSEM. It was also found that the RSEM factor is dependent on the position of the beam[2]. In Fig. 3.24 is shown the position scan (wire spacing approximately 3 mm) of the 4B SEM for E564 at $T_p = 350$ MeV. The value in the centre is

[2]discovered after running E564

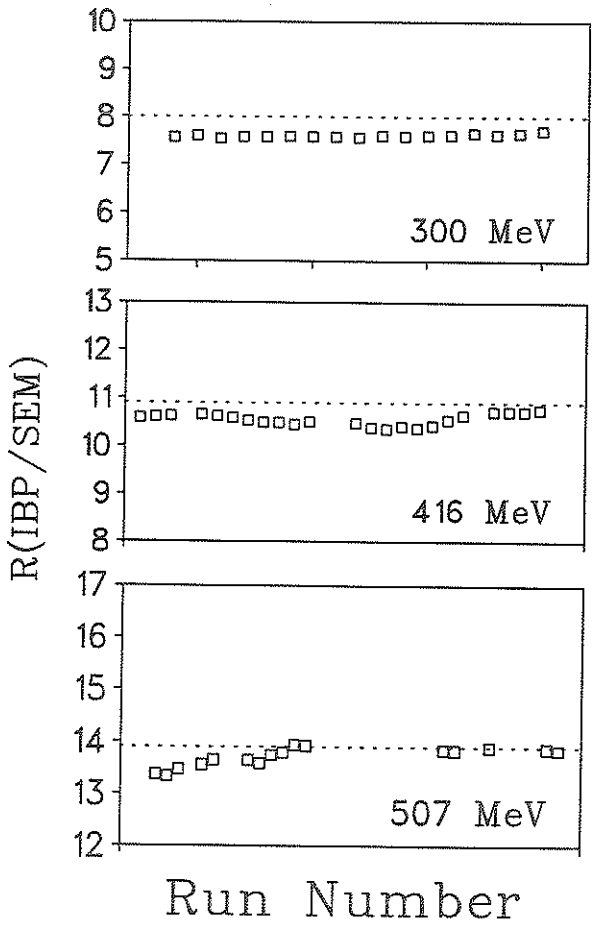

Figure 3.22: R(IBP/SEM) as a function of Run# for E413.

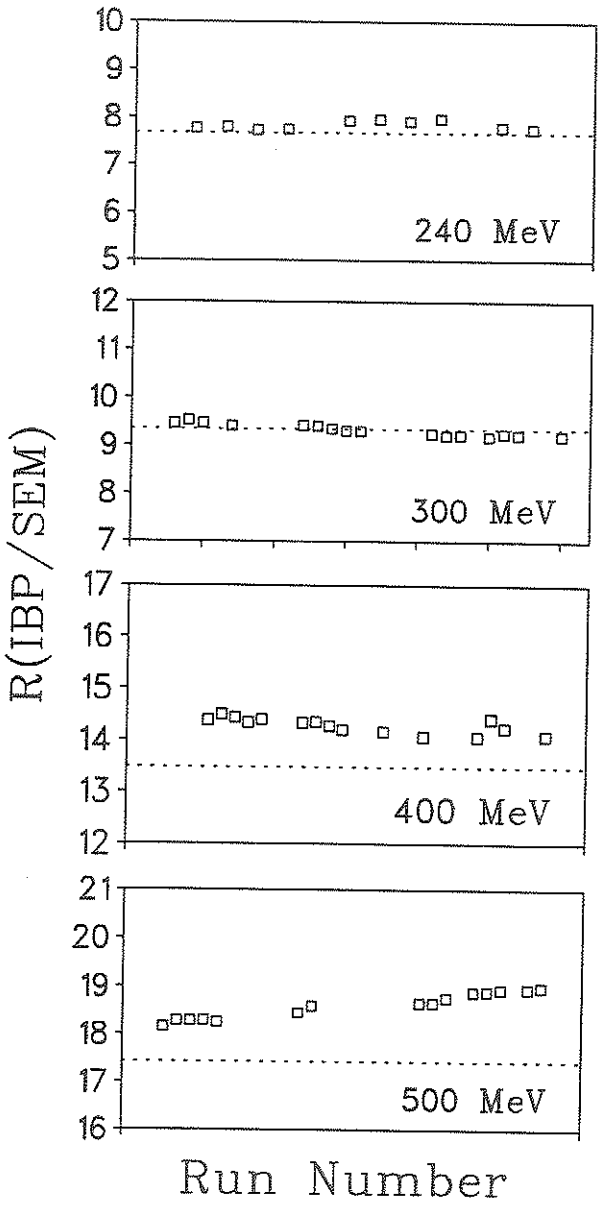

Figure 3.23: R(IBP/SEM) as a function of Run# for E564.

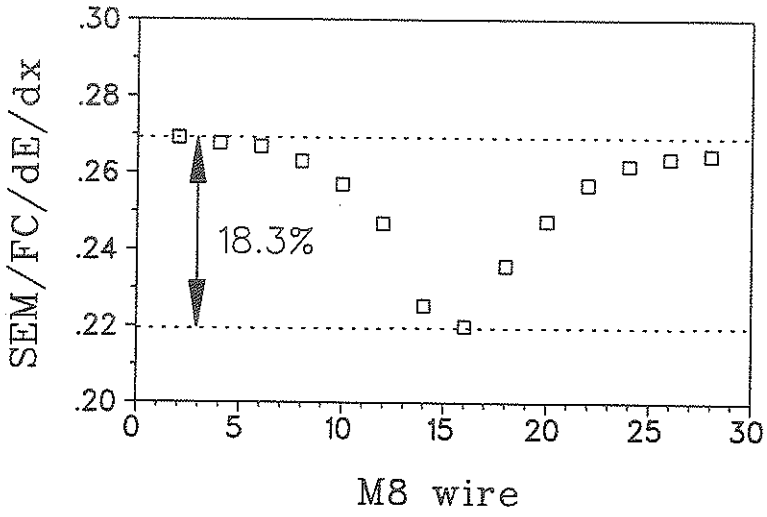

Figure 3.24: Position scan of 4B SEM at $T_p = 350$ MeV.

that used for the SEM normalization for all T_p. However one observes that the RSEM factor varies by about 18% from the centre to the outside regions of the SEM. It is possible therefore that this could give a variance in the IBP/SEM ratio. For example, a non-focussed beam at the SEM would give a larger value and so could account for the results observed at 400 and 500 MeV.

The IBP CH_2 effective target density has been noted to change, due to H_2 degradation, as an experiment progresses. However, from Fig. 3.22 and Fig. 3.23 this was not observed.

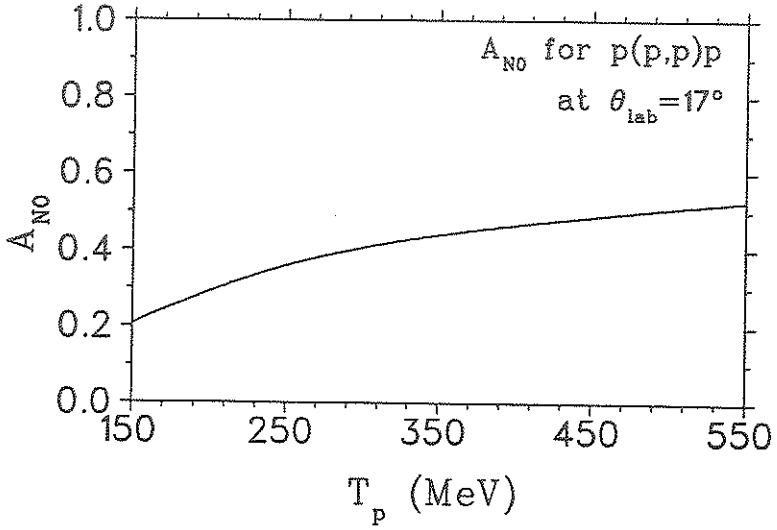

Figure 3.25: A_{N0} for pp elastic scattering.

3.2.4 Beam Polarization from IBP

To evaluate the proton beam polarization the IBP was used. First the asymmetry, ϵ, was determined.

$$\epsilon = \frac{\text{LEFT} - \text{RIGHT}}{\text{LEFT} + \text{RIGHT}} \tag{3.25}$$

From the asymmetry one may determine the polarization from the following formula.

$$\text{P} = \epsilon \times \frac{\text{A}_{\text{CH2}}}{\text{A}_{\text{H}}} \times \text{A}_{\text{H}} \tag{3.26}$$

A_H is the analyzing power for pp $\rightarrow$ pp from SAID [AR89] and this is shown in Fig. 3.25. A_{CH2}/A_H was determined in a previous calibration experiment and the results are shown in Fig. 3.26.

The uncertainty in this determination was dominated by the absolute error in the pp $\rightarrow$ pp analyzing power and the geometric asymmetry. The error in A_H was assigned to be 2% by considering the error of different phase shift

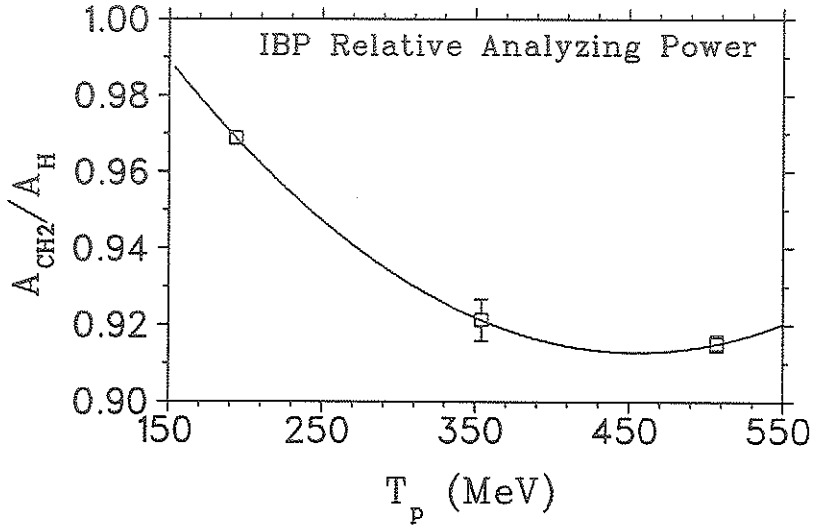

Figure 3.26: A_{CH2}/A_H for BL4B In-Beam-Polarimeter.

analyses using SAID. The geometric asymmetry error was determined from the polarization measured using unpolarized beam. The geometric asymmetry may be corrected for by adding (subtracting) the OFF polarization from that found for UP (DOWN). The residual error after this correction was found to be negligible.

3.3 Efficiencies

Here the determination of the rate-dependent efficiencies is discussed, those being the acquisition live time, and the wire chamber efficiencies.

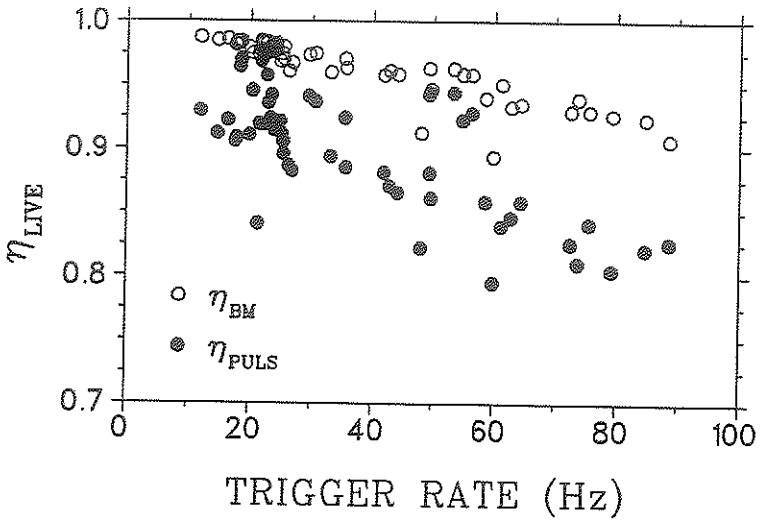

Figure 3.27: Live times from BUSY/MASTER and PULSERS versus trigger rate.

3.3.1 Acquisition Live Time

The live time of the acquisition system was determined in two ways. The first was that obtained from scalars. The number of computer BUSY signals and the number of MASTER triggers were recorded and the ratio of these gives a first order live time of the computer.

$$\eta_{\text{live}} = \frac{\text{BUSY}}{\text{MASTER}} \tag{3.27}$$

The error of the live time was estimated as,

$$\delta_{\text{live}} = \frac{\eta_{\text{live}}}{\sqrt{\text{MASTER}}}. \tag{3.28}$$

In Fig. 3.27 the computer live times are shown versus trigger rate for experiment E413.

The second method involves pulser events which were generated in coincidence with the IBP scalar to make them random. The rate was chosen

to approximately match the rate of the events. The number *generated* compared to the number actually *counted* by the master trigger gives a first order measure of the live time of the aquisition system.

$$\eta_{\text{live}} = \frac{\text{PULSER}_{\text{COUNTED}}}{\text{PULSER}_{\text{GENERATED}}} \tag{3.29}$$

The error determination is discussed in [Yen91] and is given by:

$$\delta_{\text{live}} = \sqrt{\frac{\eta_{\text{live}}(1-\eta_{\text{live}})}{\text{PULSER}_{\text{GENERATED}}}}. \tag{3.30}$$

The results are shown versus trigger rate for experiment E413 in Fig. 3.27. Commonly in proton scattering experiments the dead time of the system is dominated by the computer dead time. However, in the present case where pions are detected, the trigger rate is very low. In Fig. 3.28 the aquisition live time is plotted versus the FEC rate. It would appear that, at high rates, a significant fraction of the system dead time is dominated by the FEC dead time. The live time from the pulser events (i.e. Eqn. 3.29) was used in the analysis of the data.

3.3.2 Chamber Efficiencies

A hit in the X1 plane of the VDCs and in one of four planes in the FEC was required to produce a Master Trigger, however *all planes were recorded* even if there was not a hit in that particular plane. For the FEC, a good hit is a single hit in each of the planes such that there is no ambiguity in the track definition. A bad hit is when one of the planes registers a multiple hit or no hit at all. Each plane of the VDCs requires information from at least three contiguous wires to allow the track definition. Less than three implies a missing hit, and an event with non-adjacent tracks is a multiple hit.

Using this redundant information an estimate of the efficiency of each set of wire chambers was made. For example for the FEC efficiency deter-

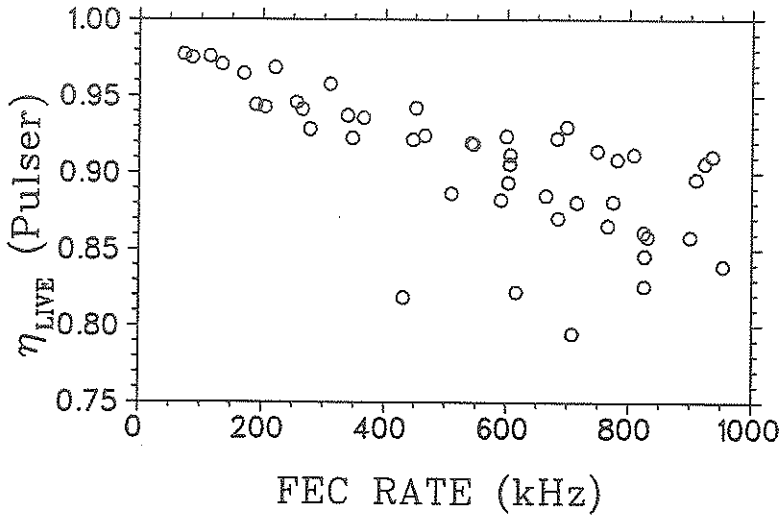

Figure 3.28: Live times from PULSERS versus FEC rate.

mination, the number of hits in the VDCs was compared to the number of coincident hits in all the chambers. This calculation is shown in the following equation where the + sign is for a logic AND.

$$\text{ALL} = \text{VDC1} + \text{VDC2} + \text{FEC} \tag{3.31}$$

where, for example, FEC means a good hit in the Front End Chamber.

$$\eta_{\text{FEC}} = \frac{\text{ALL}}{\text{VDC1} + \text{VDC2}} \tag{3.32}$$

A similar formula was used for the VDC's. The combination of each of the chamber efficiencies gave the total chamber efficiency.

$$\eta_{\text{chmb}} = \eta_{\text{FEC}} \times \eta_{\text{VDC1}} \times \eta_{\text{VDC2}} \tag{3.33}$$

The statistical uncertainty of this calculation was determined as follows, [Yen91].

$$\delta_{\text{chmb}} = \eta_{\text{chmb}} \sqrt{\frac{(1-\eta_{\text{FEC}})(1-\eta_{\text{VDC1}})(1-\eta_{\text{VDC2}})}{\text{N}_{\text{allgood}}}} \tag{3.34}$$

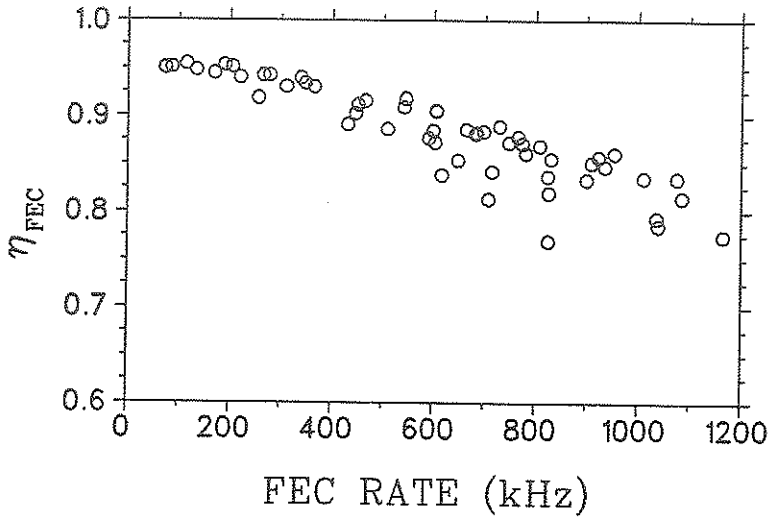

Figure 3.29: Front End Chamber efficiency dependence on chamber rate.

It was found from previous experience that the FEC efficiency drops dramatically when the FEC rate is higher than 1 MHz. For experiment E413 the FEC efficiency is plotted versus X0 FEC plane trigger rate in Fig. 3.29 and a correlation between FEC efficiency and rate is quite apparent. For this reason the beam current was kept at a point where the chamber rates were reasonable.

The efficiencies discussed here include only those which are rate dependent, and do not include possible overall rate-independent inefficiencies (for example, one which might result from a dead wire in the VDC's). However one has confidence that such inefficiencies must have been very small since calibration measurement with $pp \rightarrow d\pi^+$ were done which showed excellent agreement (see Section 3.6 below).

3.4 Acceptance

Here the determination of rate-independent acceptances of the MRS are discussed. These were measured using the pp $\rightarrow$ dπ^+ calibration reaction and compared with the Monte Carlo. The acceptances considered were the focal plane and the target acceptances.

3.4.1 Focal Plane Acceptance

The MRS focal plane acceptance was determined using the pp $\rightarrow$ dπ^+ reaction. For a chosen MRS angle the peak was swept across the focal plane by varying the Dipole field, yet keeping the Q/D ratio constant (and therefore the solid angle).

The edges of the focal plane tend to be rounded and this is due in part to the fact that some of the pions decay in flight to muons. Another reason is that the pion peak corresponding to the recoil deuteron used to measure the focal plane acceptance is of finite width. The peak width is related to the size of the kinematic correction and is smaller for for the ^{3,4}He($\vec{p}$,π^+)^{4,5}He reactions than the pp $\rightarrow$ dπ^+ reaction (see Section 2.3.4 and in particular Fig. 2.30). Since the peak width is smaller for the ^{3,4}He($\vec{p}$,π^+)^{4,5}He reactions, the roundedness is less for the ^{3,4}He($\vec{p}$,π^+)^{4,5}He reactions than for the pp $\rightarrow$ dπ^+ reaction.

In any event the peak should be kept sufficiently far away from the edges of the focal plane such that the focal plane acceptance is near unity. The acceptance determined from the pp $\rightarrow$ dπ^+ scan is shown in Fig. 2.36 along

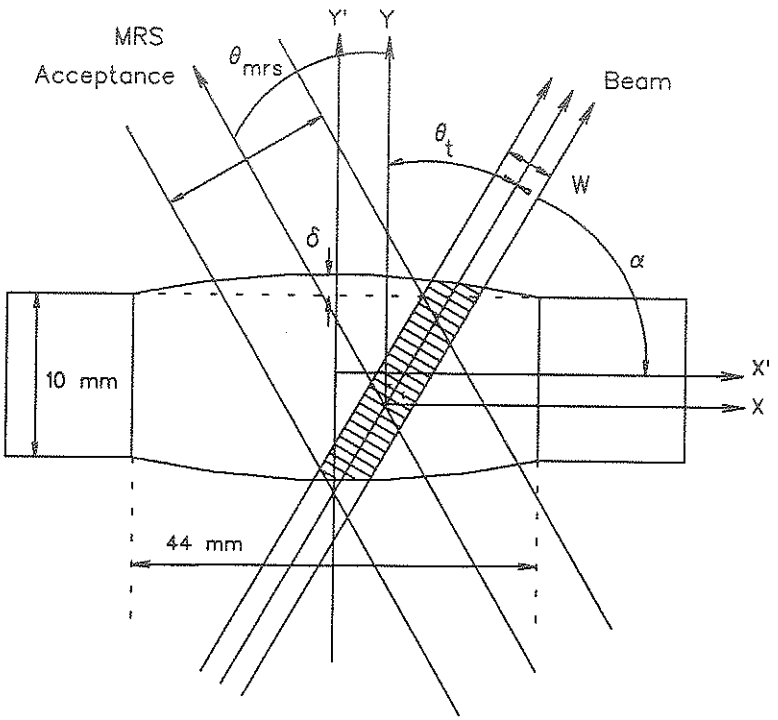

Figure 3.30: Schematic of projection of active target volume onto MRS acceptance.

with that determined from the Monte Carlo. In the actual experimental measurements the pions from the ^{3}He($\vec{p}$,π^+)^{4}He reaction were kept typically at XFK channel 5000 where the acceptance is indeed near unity.

3.4.2 Target Acceptance

Because of the thickness of the target cell the active volume extended beyond the acceptance of the MRS. Hence the effective active volume had to be carefully evaluated. Let F(y) be the distribution of the MRS acceptance. This is shown in Fig. 2.37.

The active volume of the target has a trapezoidal shape as shown in Fig. 3.30. (The vertical extent of the beam, approximately 5 mm, is not im-

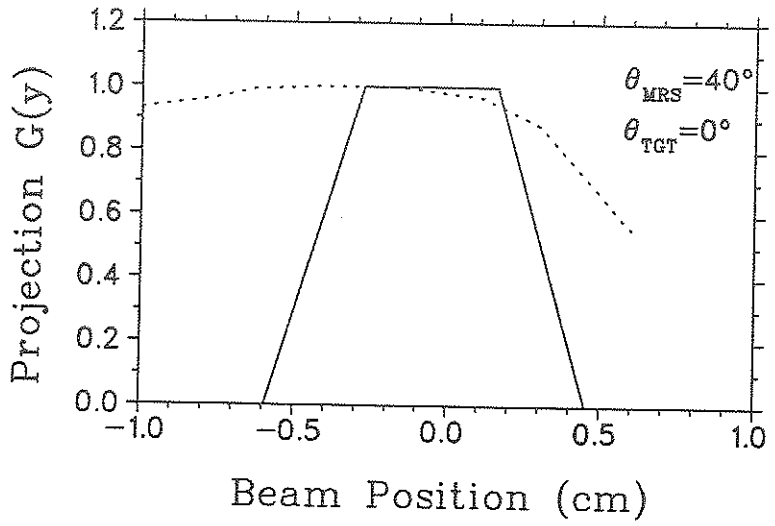

Figure 3.31: Projection of target profile onto MRS.

portant in these considerations). Projection of this trapezoidal shape onto a plane perpendicular to the central ray yields the function G(y). The details of the calculation of G(y) are contained in Appendix E. A typical projection G(y), is shown in Fig. 3.31 for θ_{mrs}=40° and θ_t=0°. The dotted line is the acceptance from the E564 pp $\rightarrow$ dπ^+ scan shown in Fig. 2.37, that is F(y).

The weighting of G(y) with F(y), defines the effective active target length.

$$\text{active target length} = \int G(y)\, F(y)\, dy \tag{3.35}$$

This equation may be rewritten as the product of the actual target length L_t, and a correction factor Q.

$$\text{active target length} = Q \times L_t \tag{3.36}$$

where

$$Q = \frac{\int G(y)\, F(y)\, dy}{\int G(y)\, dy}. \tag{3.37}$$

and

$$L_t = \int G(y)\,dy \tag{3.38}$$

The value of Q depends on the input used for the beam width and etc, and so the relative error was estimated to be about 3% due to the sensitivity to these parameters. The value of Q also depends on the which acceptance scan in Fig. 2.37 is used (i.e E413 or E564). The results differ by about 3% and therefore a systematic error for Q was estimated at 3%. Typically the value of Q ranged from 0.94 to unity depending on angle. The value of L_t does not depend on the beam width and position significantly and the error was found to negligible.

3.4.3 Test of Acceptance and Effective Length

To test the calculations performed above a series of measurements with the helium target were made where the MRS was fixed at one pion scattering angle and the cryostat set at several different target angles. In this way the possible values for Q and L_t were varied. The results are shown in Table. 3.8. Since the MRS angle is constant then the differential cross section is constant. The rate-independent corrections due to pion decay, losses and target density are all the same since these are only dependent on pion angle. Furthermore, to some extent the rate-dependent chamber efficiencies and live times are also the same (since the rates were held nearly constant). Any variance observed then would be due to the Q and L_t calculation but include those for extracting the peak area. The results in Table. 3.8 are for the $^3He(\vec{p},\pi^+)^4He$ reaction, so the error due to peak extraction was quite small. Within errors the agreement is excellent.

Acceptance Tests for $\theta_{mrs} = 40°$				
θ_t (deg)	Q	L_t(cm)	Yield (arb. units)	Difference from Mean
−20	0.96591	1.2236	512.1 ± 18.9	−3.2%
0	0.96548	1.1545	532.5 ± 17.0	+0.6%
+20	0.96179	1.2302	522.8 ± 17.2	−1.2%
+40	0.94226	1.5273	546.5 ± 17.5	+3.3%
Mean			529.1 ± 8.8	

Table 3.8: Acceptance tests with ^{3}He(p,π^+)^{4}He reaction.

3.5 Solid Angle

In past analyses of (p,π^+) experiments on the MRS, a constant value of the solid angle (determined from the pp → dπ^+ cross section) was used since it was assumed that the solid angle did not vary significantly if the Q/D ratio was kept fairly constant [Hub88]. Under this presumption, during experiment E413, the Q/D ratio was allowed to vary by several percent. However, it was found in the Monte Carlo study (performed after the running of E413) that the solid angle varies substantially with a small change in Q/D ratio (see Section 2.3.5). For E564 the Q/D ratio was kept constant to within ≈1%. The larger variation of Q/D ratio during experiment E413 implies a large systematic error when using a constant value for the solid angle. For the ^{3}He($\vec{p}$,π^+)^{4}He reaction of E413 and the pp → dπ^+ reaction of E413 and E564, a different method of extracting the solid angle was employed which decreased the systematic error in the solid angle significantly. For E564, where the Q/D ratio was kept relatively fixed, the analysis of the ^{4}He($\vec{p}$,π^+)^{5}He reaction spectra required maximum possible statistics and therefore a constant value for the solid angle was used.

The FEC is a distance R from the target (approximated to a point source). By placing cuts on the FEC coordinates X0 and Y0, the solid angle was determined from the following equation.

$$\Delta\Omega = \frac{X0 \times Y0}{R^2} \tag{3.39}$$

The error in the solid angle is then given by

$$\frac{d\Delta\Omega}{\Delta\Omega} = \sqrt{(\frac{dX0}{X0})^2 + (\frac{dY0}{Y0})^2 + 4(\frac{dR}{R})^2} \tag{3.40}$$

The uncertainty in the FEC cuts is estimated from the uncertainty in the FEC coordinate determination ($\pm$ 0.7 mm) and is about 3%. The combination of dX0 and dY0 then gives rise to an $\approx$4% relative uncertainty in the solid angle. The uncertainty in the distance of the FEC from the target is estimated at $\approx$1.5% and therefore the systematic error in the solid angle is about 3%. This geometric solid angle is the effective solid angle provided the cuts are placed tightly enough that the acceptance is not further restricted by the MRS.

For E564, the peak area extraction in the pion focal plane spectrum corresponding to the ^{5}He recoil required the maximum possible statistics. Therefore placing tight cuts on the FEC coordinates for the solid angle determination was not acceptable. In Appendix F the solid angle (corresponding to open FEC cuts) dependence on Q/D ratio is discussed and it was found that the Q/D ratio for E564 was kept sufficiently constant such that a constant value of solid angle for the data analysis could be used. The relative uncertainty was found to be about 2% and the absolute uncertainty was estimated at 6% (see Appendix F).

$$\Delta\Omega = 2.60 \pm 2\%(\pm 6\%)\,\text{msr.} \tag{3.41}$$

3.6 Results and Errors

Here the method of calculating differential cross section and analyzing power is discussed. Used in this calculation are all the different efficiencies and acceptances discussed above.

3.6.1 Differential Cross Section Calculation

The differential cross section for a given beam polarization is given by the following equation.

$$\frac{d\sigma}{d\Omega}|_{c.m.} = \frac{N_\pi}{\eta_{chmb}\eta_{live}\eta_\pi\eta_{foc}\eta_{loss}N_{prot}\rho Q L_t \Delta\Omega_{lab}} \times \frac{d\Omega_{lab}}{d\Omega_{cm}} \qquad (3.42)$$

where the parameters are explained in Table 3.9.

The errors are separated into statistical and relative with an overall systematic uncertainty. The typical statistical error was 3%. The statistical and relative errors were all combined in quadrature and that is the error quoted in the tables of Appendix G and shown in the figures of the data. The breakdown of these errors is shown in Table 3.10. Note the totals indicated are the errors added in quadrature.

A test of the reliability of the efficiency and acceptance information of the MRS was performed by using the $pp \rightarrow d\pi^+$ reaction. By using the cross section formula above the $pp \rightarrow d\pi^+$ cross section was determined at several angles for the highest proton bombarding energies for the two experiments, E413 at $T_p = 507$ MeV and E564 at $T_p = 500$ MeV. See Table. 3.11. The comparison values were determined from fits to the existing cross section data for the $pp \rightarrow d\pi^+$ reaction with Legendre polynomials and then a smooth line through the polynomial coefficients (data included in this fit are [Mat+83] [Gil85] [Hof+83] [Hof+84] [Sah+83] [May+85]). The results

Cross Section Parameters	
N_π	Peak area above background
η_{chmb}	Combined chamber efficiency
η_{live}	Acquisition live time
η_π	Pion survival fraction
η_{foc}	Focal Plane efficiency
η_{loss}	Losses due to absorption and multiple scattering
η_{fsi}	FSI renormalization factor (for ^{5}He calculation only)
N_{prot}	Number of protons on target
ρ	Number of target nuclei/volume
Q	Acceptance of MRS
L_t	Calculated actual target length
$\Delta\Omega_{lab}$	Solid angle
$d\Omega_{lab}/d\Omega_{cm}$	Jacobian

Table 3.9: Parameters used in cross section calculation.

Systematic Uncertainties	
Target Density for ^{3}He	± 3%
Target Density for ^{4}He	1%
Target Acceptance Q	3%
Solid Angle for ^{4}He peak	3%
Solid Angle for ^{5}He peak	6%
FSI for ^{5}He $\eta_{\rm fsi}$	20%
Pion Survival Factor η_π	<1%
Number of Beam Protons N_p	5%
Reaction Losses $\eta_{\rm loss}$	± 3%
Total Systematic Uncertainty	
^{3}He($\vec{p}$,π^+)^{4}He	± 8%
^{4}He($\vec{p}$,π^+)^{5}He	± 9% †
Relative Uncertainties	
Software Cuts	± 3%
Peak Integration to 4.44 MeV for ^{5}He	3%
Background Subtraction for ^{4}He	2%
Background Subtraction for ^{5}He	3%-6%
Solid Angle for ^{4}He	4%
Solid Angle for ^{5}He	2%
Focal Plane Acceptance $\eta_{\rm focal}$	2%
Target Acceptance Q	3%
Actual Target Length L_t	*negligible*
Wire Chamber Efficiency $\eta_{\rm chmb}$	± 2%
Total Relative Uncertainty	
^{3}He($\vec{p}$,π^+)^{4}He	± 6%
^{4}He($\vec{p}$,π^+)^{5}He	± 8%

† *not including* $\eta_{\rm fsi}$ *uncertainty.*

Table 3.10: Estimated or typical experimental errors.

$d\sigma/d\Omega_{lab}(\frac{\mu b}{sr})$ $pp \rightarrow d\pi^+$ Comparison				
E413				
Run#	θ_{lab}	This Work	Fit†	Difference
88	18.4	880 ± 56	913.5	−3.7%
171	28.0	589 ± 27	616.3	−4.4%
89	40.0	308 ± 14	290.2	+6.1%
E564				
Run#	θ_{lab}	This Work	Fit†	Difference
49	28.0	597 ± 25	585.8	+1.9%
42	39.8	279 ± 12	284.5	−1.9%
91	56.0	116 ± 5	128.5	−9.7%
90	72.9	109 ± 5	123.1	−11.4%
89	100.0	130 ± 5	139.5	−6.8%
64	122.0	113 ± 5	119.0	−5.0%

† *error in the cross sections from fit to previous data is estimated at 2%*

Table 3.11: Comparison of $pp \rightarrow d\pi^+$ cross sections with existing data.

are quite consistent with the fit to previous data. The average deviation is −0.6% and −5.0% for E413 and E564 respectively. This is well within the systematic errors of the measurements thus giving confidence in the methods of estimation of the efficiencies and acceptances used in this work.

3.6.2 Analyzing Power Calculation

The analyzing power was calculated from the polarized differential cross sections in the following way.

$$A_{N0} = \frac{d\sigma(\uparrow)/d\Omega - d\sigma(\downarrow)/d\Omega}{P(\downarrow)d\sigma(\uparrow)/d\Omega + P(\uparrow)d\sigma(\downarrow)/d\Omega} \tag{3.43}$$

The error in the polarization contributed to an overall systematic uncertainty in the analyzing power and was found to be approximately 2% (arising mostly from the uncertainty in pp $\rightarrow$ pp analyzing powers, see Section 3.2.4 above). The statistical and relative errors were calculated from the relative and statistical uncertainties in the polarized differential cross sections. These were added in quadrature and denoted $\delta_{N(\uparrow)}$ and $\delta_{N(\downarrow)}$ for the up and down polarizations respectively. The error for the analyzing power is given by:

$$\frac{(P(\uparrow) + P(\downarrow))}{(P(\downarrow)d\sigma(\uparrow)/d\Omega + P(\uparrow)d\sigma(\downarrow)/d\Omega)^2} \times \sqrt{(\delta_{N(\downarrow)}d\sigma(\uparrow)/d\Omega)^2 + (\delta_{N(\uparrow)}d\sigma(\downarrow)/d\Omega)^2} \tag{3.44}$$

The statistical uncertainties in the analyzing powers were typically ± 0.03, and the relative uncertainties were found to be comparable to the statistical.

Only one measurement of the analyzing power for a known reaction was performed, namely the ^{3}He($\vec{p}$,p)^{3}He reaction. The results obtained in the present work and those obtained by Hasell *et al.* [Has+86] are shown in Table. 3.12 and in Fig. 3.32. The point measured in the present experiment was certainly consistent with the existing measurements on either side. This gives one confidence then that the analyzing power determination and the estimation of the absolute polarization were reasonable.

3.7 Summary

The data analysis was performed in several stages, from online to the final pass, and with obvious intensive computer usage. Event processing was car-

^{3}He($\vec{p}$,p)^{3}He Analyzing Power Comparison		
θ_{cm}	A_{N0}	Reference
42.6	-0.426 ± 0.084	Hasell *et al.*
49.4	-0.704 ± 0.062	Hasell *et al.*
56.0	0.020 ± 0.072	Hasell *et al.*
59.9	0.353 ± 0.021	*present work*
62.5	0.386 ± 0.051	Hasell *et al.*
68.8	0.321 ± 0.055	Hasell *et al.*
75.0	0.287 ± 0.055	Hasell *et al.*

Table 3.12: Comparison of ^{3}He($\vec{p}$,p)^{3}He analyzing powers with existing data.

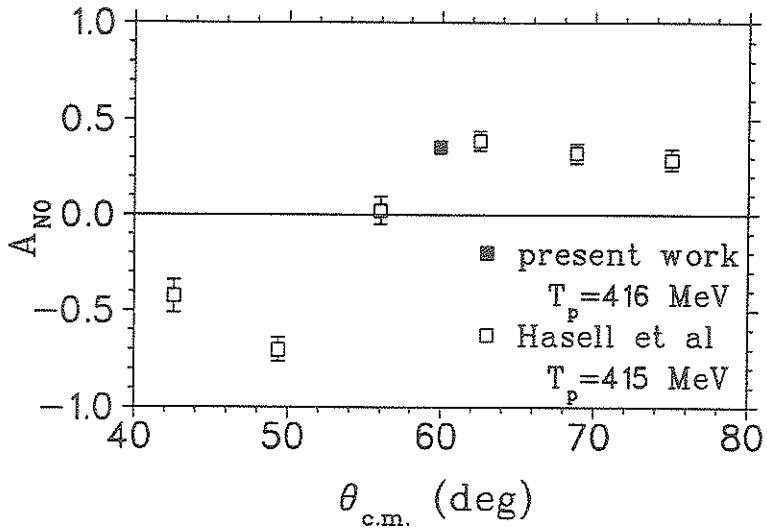

Figure 3.32: Comparison of ^{3}He($\vec{p}$,p)^{3}He analyzing powers with existing data.

ried out using the LISA data analysis program which would have never been completely understood without help from G.M. Huber and D. Frekers. Each run was comprised of approximately 2000 *good* events in the pion peak and the methods used to obtain the peak area have been discussed. In particular, to facilitate the extraction of the ^{5}He $p_{\frac{3}{2}}$ cross section, a final state interaction calculation based on the n + α low energy phase shifts was performed. The integrated area and number of beam protons (determined from the IBP) was then used to calculate the yield, correcting for the rate-dependent efficiencies due to the wire chambers and detector live time. Cross sections were obtained by normalizing the yield to the target density, the pion survival fraction and the rate-independent acceptances of the MRS. Measurements of the $pp \rightarrow d\pi^+$ reaction were carried out and the obtained cross sections were found to be consistent with existing measurements to within the systematic uncertainties. From the polarized cross sections, data for the analyzing powers were extracted using the beam polarization determined from the IBP. A measurement of the ^{3}He($\vec{p}$,p)^{3}He reaction was found to be consistent with a previous measurement.

The large effort expended in the analyses of these experiments is reflected in the size of the systematic uncertainties. In particular, the error in the solid angle, which in previous (p,π^+) experiments was quite large, was significantly reduced. The techniques employed here were a result of many fruitful discussions and experiences with the TRIUMF (p,π^+) group and specifically with P.L. Walden, G.M. Huber, and of course my advisor W.R. Falk.

Chapter 4

Results and Discussion

In this Chapter the data are presented and discussed. Comparisons with a previous measurement of the same reaction are made and, in particular, a difference in the normalization is noted. A comparison of the present data for the ^{3}He(p,π^+)^{4}He reaction with those of the charge symmetric ^{3}H(n,π^-)^{4}He reaction indicates substantial Coulomb effects. A fit to Legendre polynomials was also performed to investigate the contribution of the various underlying partial waves. Finally, the analyzing powers are compared with the elastic reactions for the same target and bombarding energy.

4.1 Data

The data were analyzed and the results for the two experiments are presented in detail in tables in Appendix G. The differential cross sections are also shown in Fig. 4.1 and the analyzing powers in Fig. 4.2. A measurement at $T_p = 198$ MeV from IUCF [Keh+86] is also included for comparison.

A general feature that is immediately apparent from Figures 4.1 and 4.2 is the overall similarity exhibited by the two reactions. The cross sections

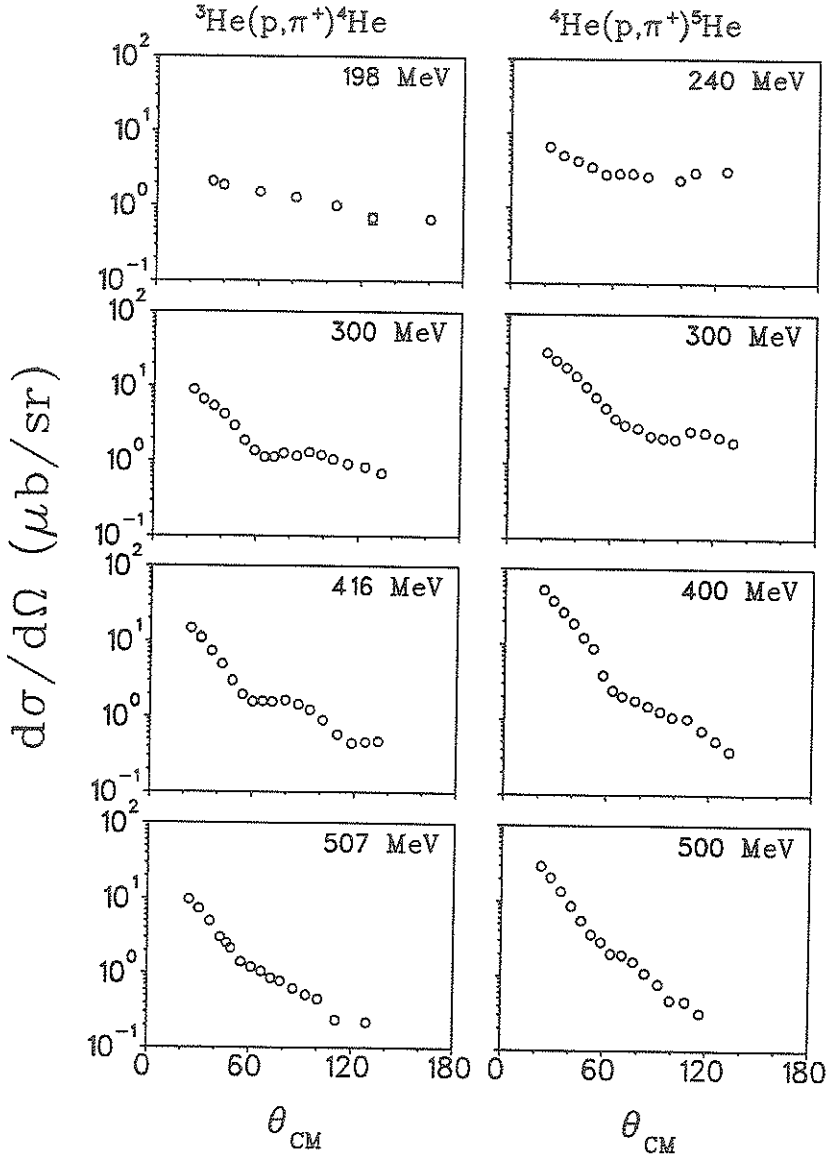

Figure 4.1: Differential Cross Sections for the ^{3,4}He($\vec{p}$,π^+)^{4,5}He reactions.

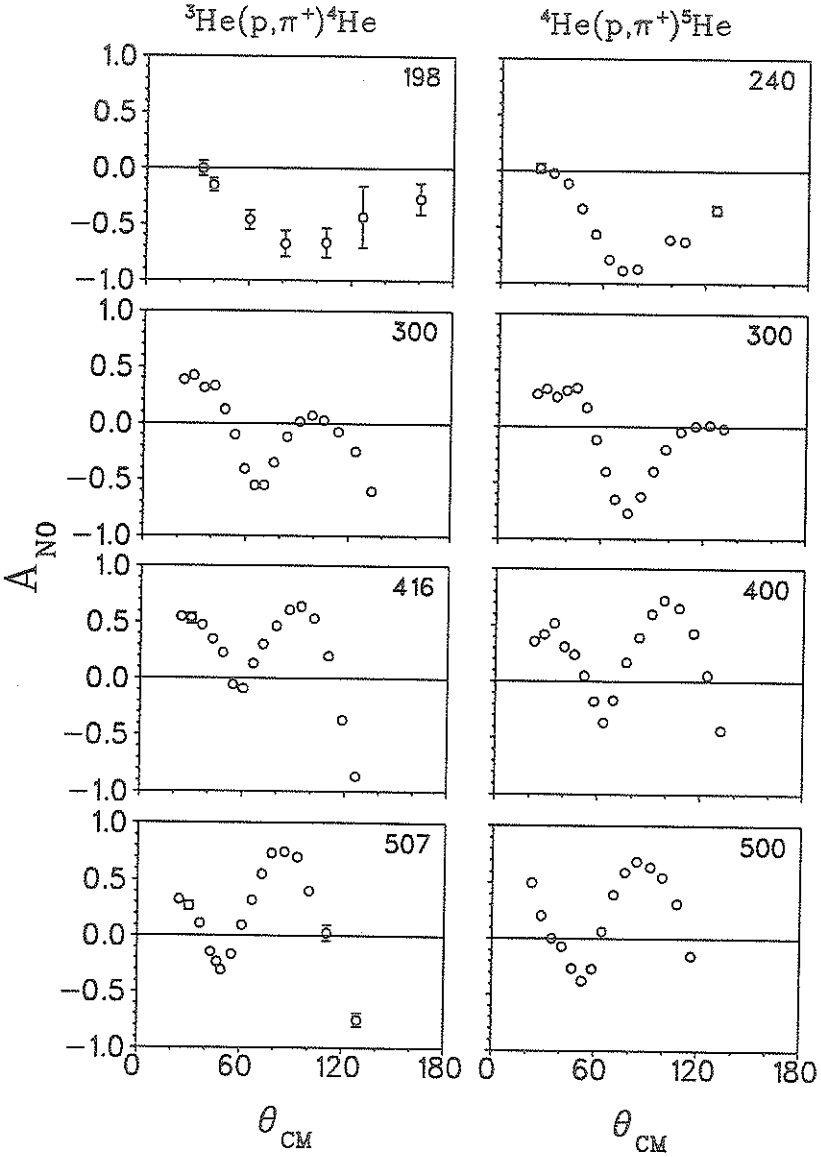

Figure 4.2: Analyzing powers for the ^{3,4}He($\vec{p}$,π^+)^{4,5}He reactions.

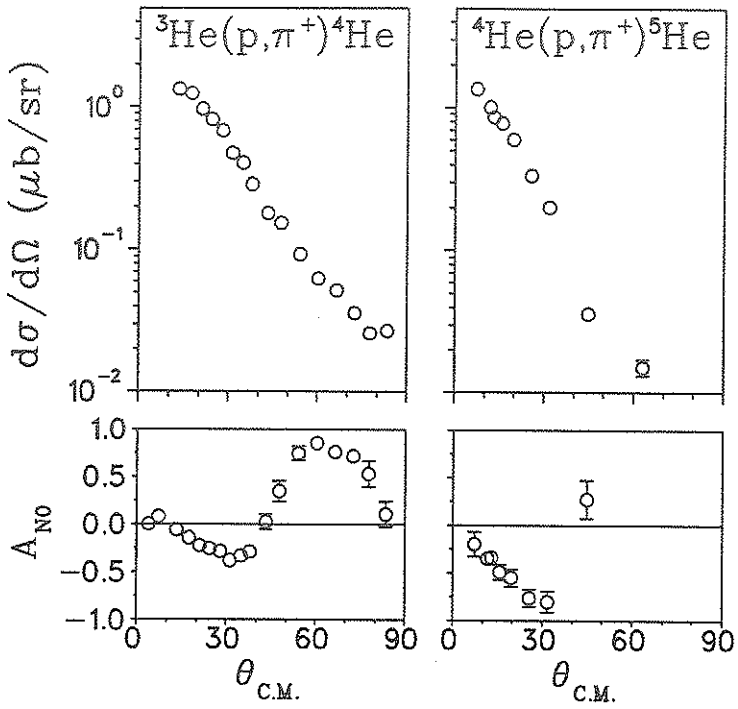

Figure 4.3: Differential cross sections and analyzing powers for the ^{3,4}He($\vec{p}$,π^+)^{4,5}He reactions at T_p = 800 MeV from Höistad *et al.* [Hoi+84].

are quite flat near threshold, and as the incident proton energy is increased the cross sections drop more rapidly with increasing angle. Near threshold the analyzing powers are qualitatively very much like those for low energy pp $\rightarrow$ dπ^+. However, a sharp transition in character between 200 and 300 MeV is observed. From 300 MeV to 800 MeV (data from Ref. [Hoi+84] shown in Fig. 4.3) the analyzing powers are large and oscillatory.

4.2 Systematics

It is possible that trends may be discovered in the data when plotted versus some appropriate kinematic variable, provided the reaction mechanism is not too complicated. Since the differential cross sections are relatively structure-

less, but a lot of structure is observed in the analyzing powers, only A_{N0} will be considered for the present.

In initial investigations of the (p,π^+) reaction the data were graphed versus the three momentum transfer (Q_{cm}) in light of the presumed ONM pionic stripping process. In Fig. 4.4 the analyzing powers for this work are shown versus Q_{cm}. Also shown are the $^3He(\vec{p},\pi^+)^4He$ reaction data of Kehayias *et al.* [Keh+86] at $T_p = 198$ MeV and the $^{3,4}He(\vec{p},\pi^+)^{4,5}He$ reactions data of Höistad *et al.* [Hoi+84] at $T_p = 800$ MeV. The first minimum for the three higher energies corresponds fairly closely to $Q_{cm} \approx 3.0\,fm^{-1}$ for $^3He(\vec{p},\pi^+)^4He$, and to $Q_{cm} \approx 3.3\,fm^{-1}$ for $^4He(\vec{p},\pi^+)^5He$. For the two lower energies ($\approx$ 200 and 300 MeV) however, this minimum occurs at smaller values for Q_{cm}.

Couvert [Cou83] and Huber [Hub88] have suggested that the four momentum transfer, t, might be a more suitable kinematic variable since it is a relativistically invariant quantity. In Fig. 4.5 the results for A_{N0} are shown versus $-t$.

Results from microscopic calculations show that the pion production process in nuclei is only reasonably well described when many competing contributions are taken into account [BAD90a]. Therefore, the lack of an observed systematic in the data, when plotted versus a simple kinematic variable like Q_{cm} or t, is possibly a result of this complexity.

4.3 Comparison to Previous Measurements

The $^{3,4}He(\vec{p},\pi^+)^{4,5}He$ reactions have also been studied earlier to some extent by other authors, in particular, investigations of the cross sections. In the

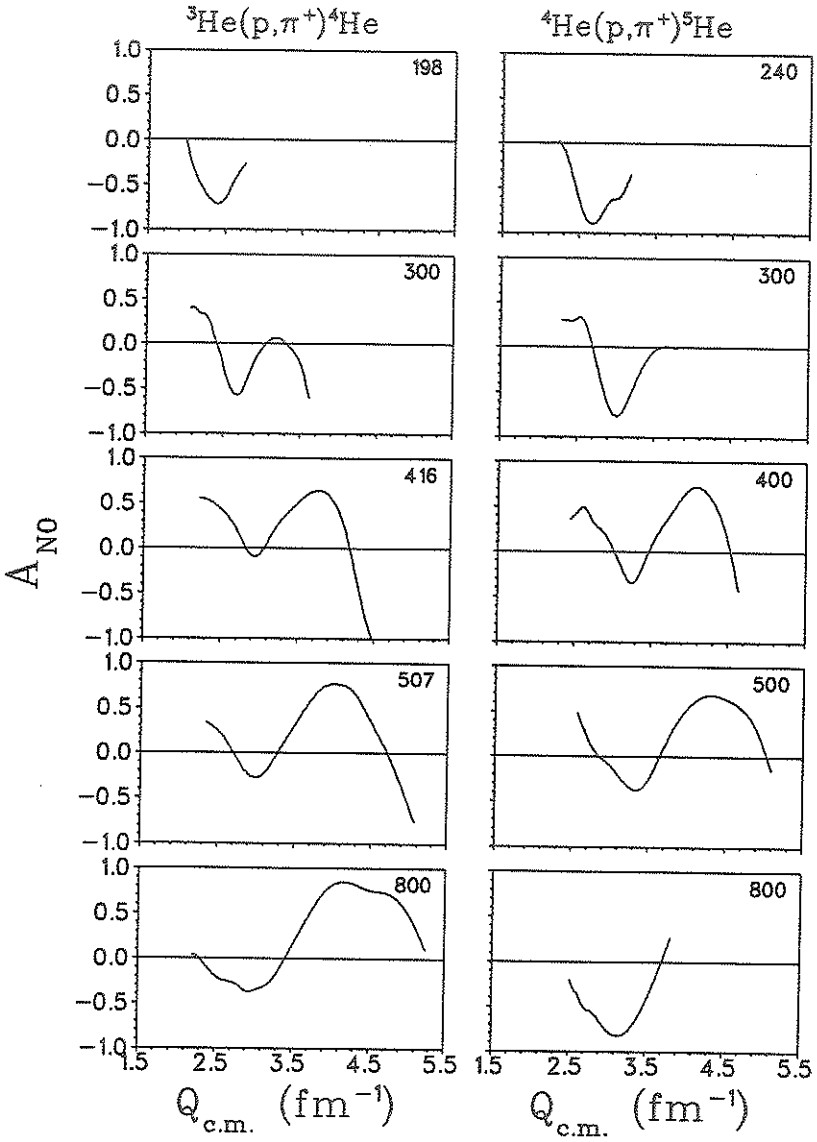

Figure 4.4: Analyzing powers for the ^{3,4}He($\vec{p}$,π^+)^{4,5}He reactions versus the three momentum transfer Q_{cm}. The data points of Figs. 4.2 and 4.3 have been joined by a smooth line in making this figure.

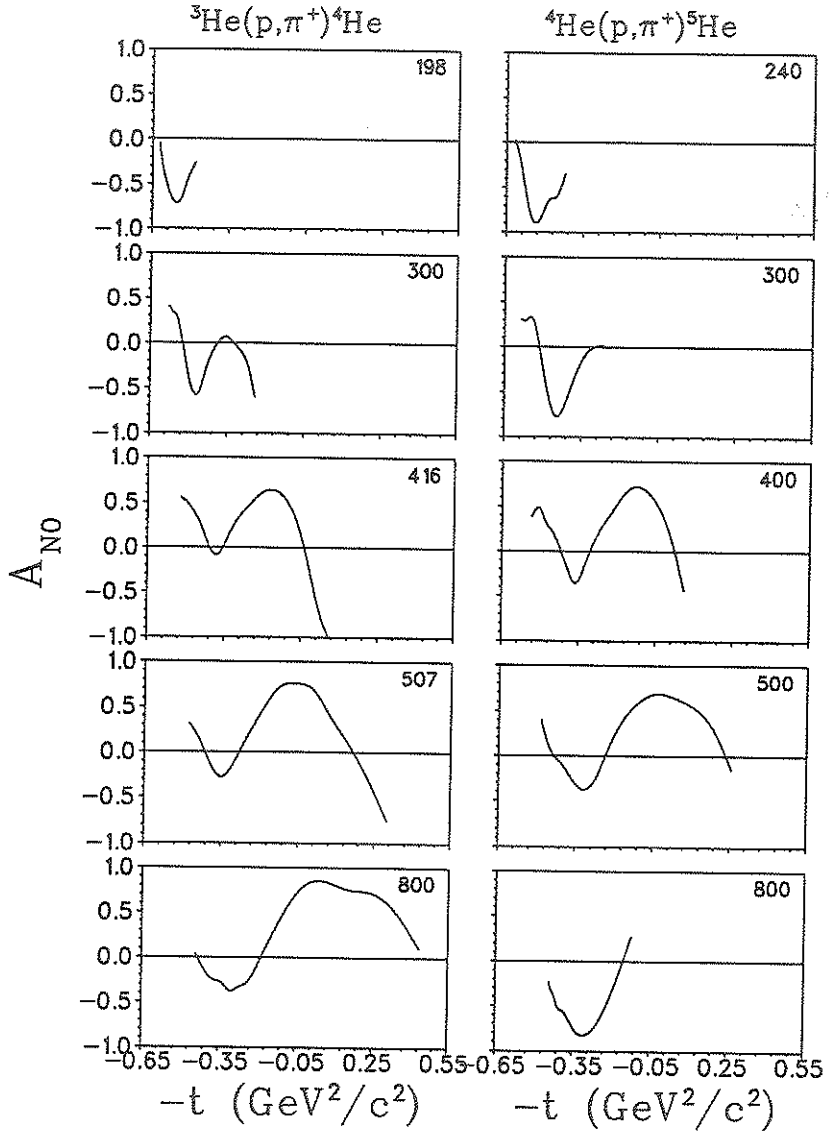

Figure 4.5: Analyzing powers for the ^{3,4}He($\vec{p}$,π^+)^{4,5}He reactions versus the four momentum transfer t. The data points of Figs. 4.2 and 4.3 have been joined by a smooth line in making this figure.

following sections the cross sections of this work are compared to measurements at similar energies and their discrepancies are discussed.

4.3.1 Comparison for ^{3}He($\vec{p}$,π^+)^{4}He

The data of Tatischeff *et al.* [Tat+76], measured at T_p = 415 MeV, are compared to the present measurements at T_p = 416 MeV in Fig. 4.6. The ratio R is calculated by fitting the present data to a Legendre polynomial series and then using the fit for interpolation to compare to the existing data.

$$R = \frac{\text{Present Experiment Result}}{\text{Previous Experiment Result}} \tag{4.1}$$

Also shown are the actual differential cross section results compared on a logarithmic plot. The systematic error is 20% for the data of Tatischeff *et al.* and the systematic error of the results of the present work was estimated to be 8%. The discrepancy between the two angular distributions averages about 86% (the dotted line in Fig. 4.6), with the data of the present work being higher. This disagreement is outside the range of the systematic errors of the two sets of data. Furthermore, the scatter of the ratio R is larger than the estimated relative uncertainty of the present measurements ($\approx$ 8%). Very little information is available on the errors of the Tatischeff data [Tat+76] and therefore little more may be inferred of this discrepancy from these measurements alone. The disagreement will be discussed in more detail with regards to comparison to another measurement below.

4.3.2 Comparison to ^{3}H(n,π^-)^{4}He

Källne *et al.* ([Kal+78], [Kal+81] and [Kal+83]) and Orphanos *et al.* ([Orp+81] and [Orp+82]) carried out experiments at LAMPF studying the ^{4}He(π^-,n)^{3}H reaction at many pion energies. These data may be transformed to the

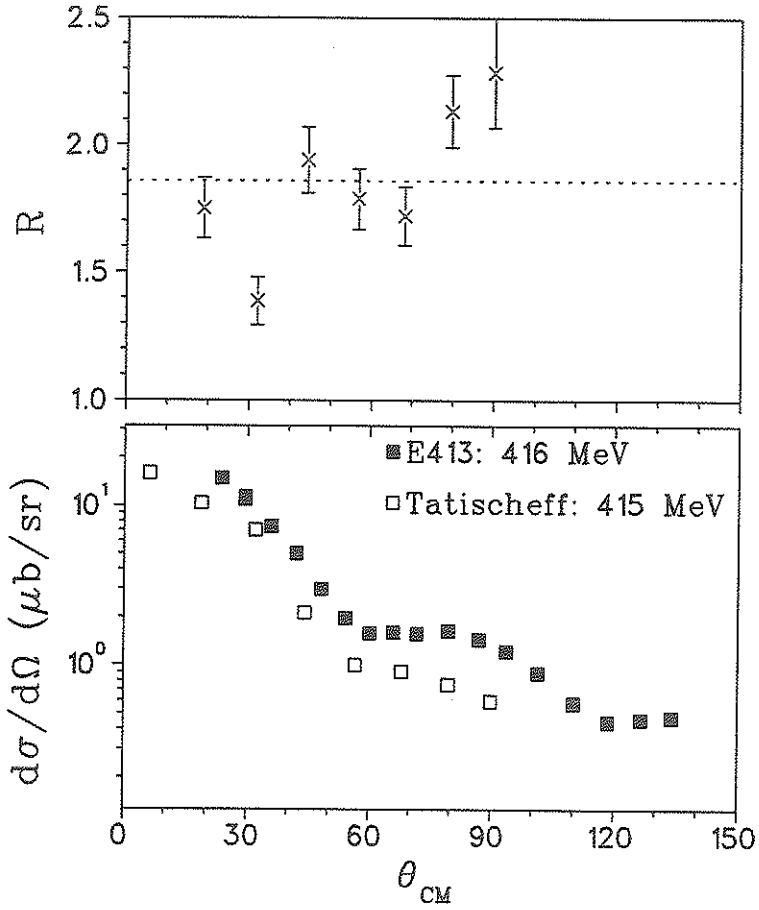

Figure 4.6: Comparison of present measurements at T_p = 416 MeV with data from Tatischeff *et al.* at T_p = 415 MeV for ^{3}He(p,π^+)^{4}He.

^{3}H(n,π^-)^{4}He reaction by using *Detailed Balance*. Detailed Balance relates the A(a,b)B cross section to the B(b,a)A cross section in the following way:

$$\frac{d\sigma}{d\Omega}|_{B(b,a)A} = \frac{(2J_a+1)(2J_A+1)}{(2J_b+1)(2J_B+1)} \times \frac{p_a^2}{p_b^2} \times \frac{d\sigma}{d\Omega}|_{A(a,b)B} \tag{4.2}$$

where p_a^2 and p_b^2 are the c.m. momentum of the particles for the A+a and B+b systems respectively. J denotes the spin of the particle. Upon substitution for the reaction in question one obtains:

$$\frac{d\sigma}{d\Omega}|_{^3H(n,\pi^-)^4He} = \frac{1}{4} \times \frac{k_\pi^2}{k_n^2} \times \frac{d\sigma}{d\Omega}|_{^4He(\pi^-,n)^3H}. \tag{4.3}$$

(Note that the spin factor is equal to 1/4). The ^{4}He(π^-,n)^{3}H data may then be interpreted as ^{3}H(n,π^-)^{4}He reaction results at equivalent neutron lab energies, T_n. The pion energies and their equivalent neutron energies for Detailed Balance are shown in Table 4.1. The *Factor* is that for the detailed balance relation.

$$\frac{d\sigma}{d\Omega}|_{^3H(n,\pi^-)^4He} = \text{Factor} \times \frac{d\sigma}{d\Omega}|_{^4He(\pi^-,n)^3H} \tag{4.4}$$

where

$$\text{Factor} = \frac{1}{4} \times \frac{p_\pi^2}{p_n^2} \tag{4.5}$$

The results for T_n = 227 MeV (T_π = 50 MeV) from Källne *et al.* were compared to the data at T_p = 198 MeV by Kehayias [Keh83]. For these energies it was found the ^{3}He(p,π^+)^{4}He data are higher by about a factor of three compared with the time reversed charge symmetric ^{3}H(n,π^-)^{4}He reaction. It should be also noted that results from Willis *et al.* [Wil+81] are in very good agreement with the Kehayias data.

The results of the present work for the ^{3}He(p,π^+)^{4}He reaction at proton bombarding energies of 300, 416 and 507 MeV are shown in comparison with the time reversed charge symmetric ^{3}H(n,π^-)^{4}He reaction from Källne *et al.*

Detailed Balance		
^{4}He(π^-,n)^{3}H	^{3}H(n,π^-)^{4}He	Factor†
T_π(lab) (MeV)	T_n(lab) (MeV)	$\frac{1}{4}p_\pi^2/p_n^2$
50	227	0.0152
75	260	0.0210
100	293	0.0262
125	326	0.0309
150	360	0.0352
175	393	0.0392
200	426	0.0430
225	459	0.0465
250	492	0.0499

† *Factor for the Detailed Balance.*

Table 4.1: Equivalent neutron energies for ^{4}He(π^-,n)^{3}H Detailed Balance.

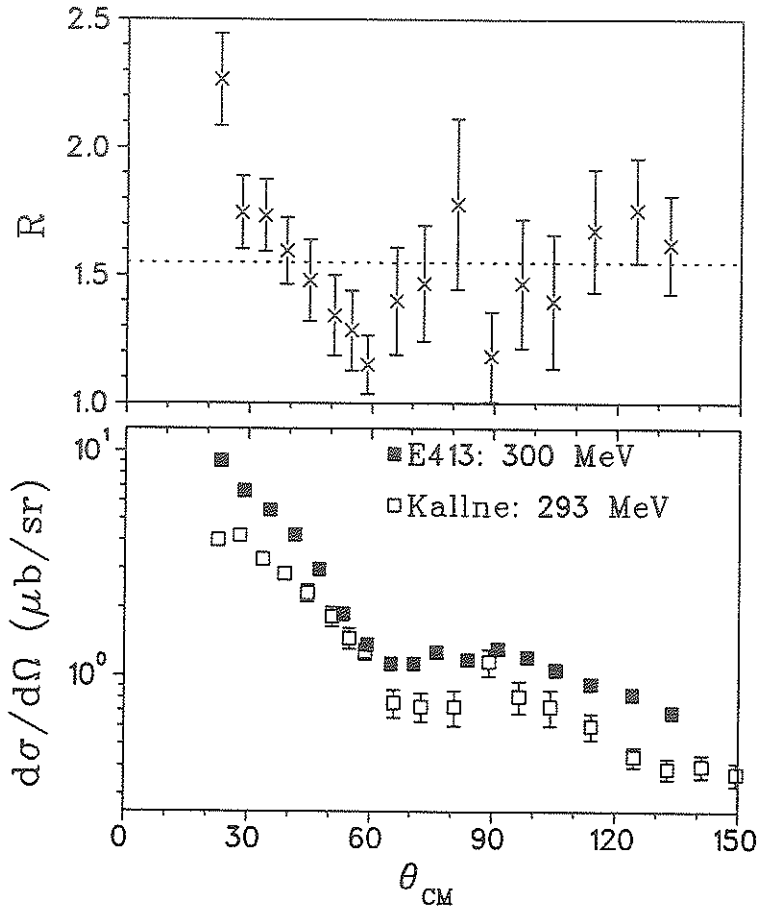

Figure 4.7: Comparison of 300 MeV ^{3}He(p,π^+)^{4}He reaction data with results for the ^{3}H(n,π^-)^{4}He reaction from Källne *et al.* from Detailed Balance.

[Kal+81] at T_n = 293 MeV (T_π = 100 MeV), T_n = 426 MeV (T_π = 200 MeV) and T_n = 492 MeV (T_π = 250 MeV) in Figures 4.7, 4.8 and 4.9 respectively. The ratio R is defined as

$$R = \frac{\sigma(^3\mathrm{He}(p,\pi^+)^4\mathrm{He})}{\sigma(^3\mathrm{H}(n,\pi^-)^4\mathrm{He})} \tag{4.6}$$

It is found that the ^{3}He(p,π^+)^{4}He reaction results are larger than those of the ^{3}H(n,π^-)^{4}He reaction by about 55%, 49% and 37% for the proton energies 300 and 416 and 507 MeV respectively.

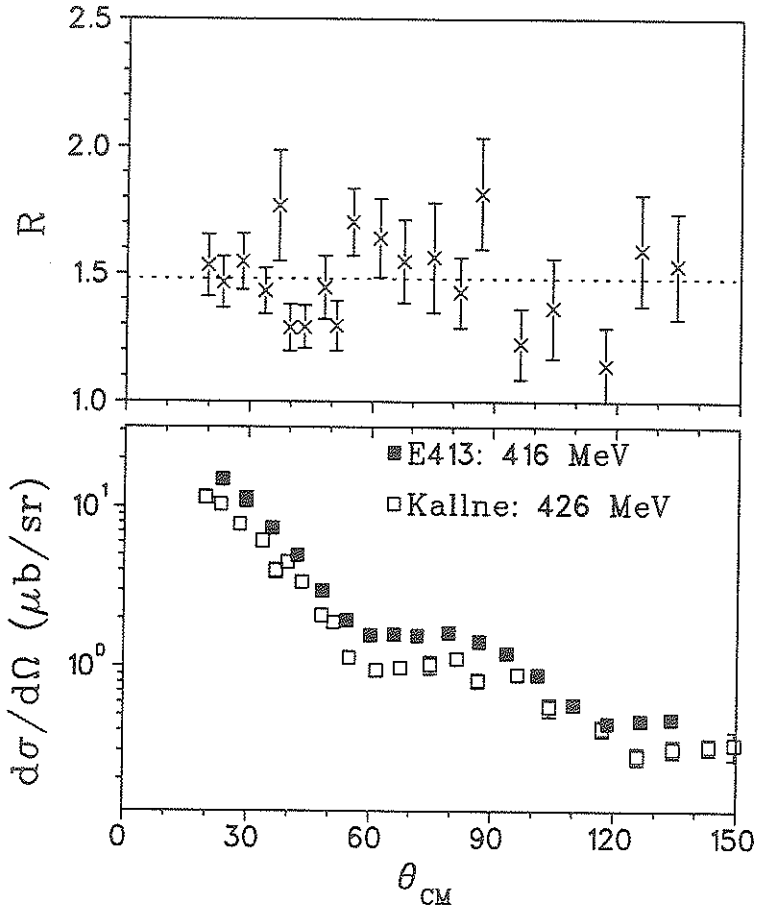

Figure 4.8: Comparison of 416 MeV ^{3}He(p,π^+)^{4}He reaction data with results for the ^{3}H(n,π^-)^{4}He reaction from Källne *et al.* from Detailed Balance.

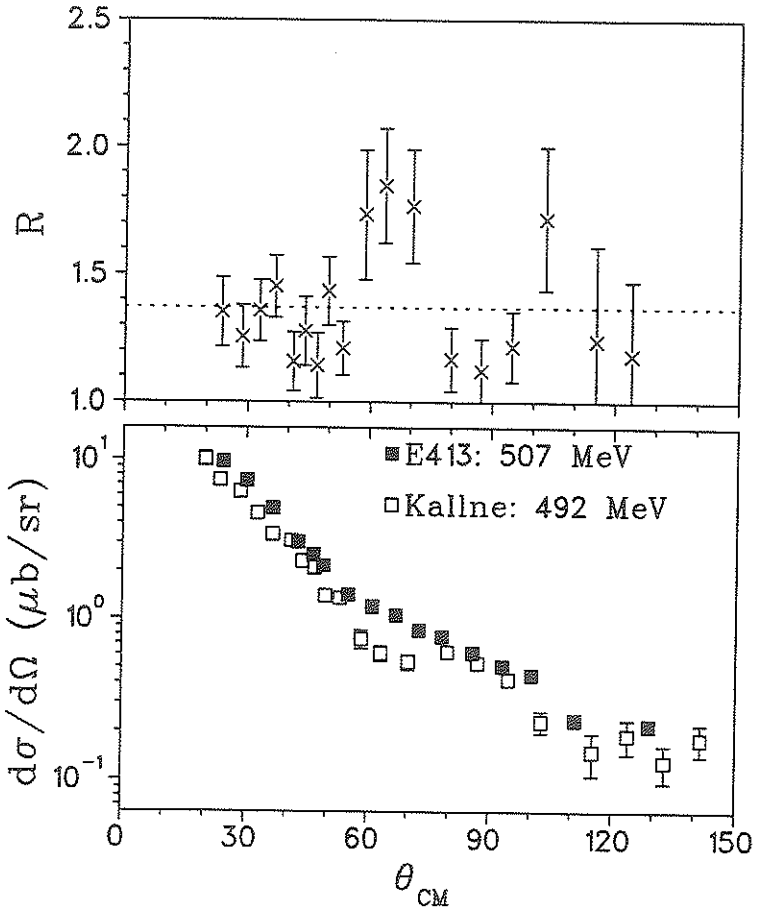

Figure 4.9: Comparison of 507 MeV ^{3}He(p,π^+)^{4}He reaction data with results for the ^{3}H(n,π^-)^{4}He reaction from Källne *et al.* from Detailed Balance.

Ratio of $\sigma(^3\mathrm{He}(\mathrm{p},\pi^+)^4\mathrm{He})$ / $\sigma(^3\mathrm{H}(\mathrm{n},\pi^-)^4\mathrm{He})$		
T_p (lab) (MeV)	Author	Ratio
227	Källne *et al.*	3.25
300	Present work	1.55
293	Källne *et al.*	1.70
360	Källne *et al.*	1.04
416	Present work	1.49
426	Källne *et al.*	1.21
492	Källne *et al.*	1.06
507	Present work	1.37

Table 4.2: Average RATIO of $\sigma(^3\mathrm{He}(\mathrm{p},\pi^+)^4\mathrm{He})$ / $\sigma(^3\mathrm{H}(\mathrm{n},\pi^-)^4\mathrm{He})$ for the present measurements and those of Källne *et al.*

Källne also performed a cross section measurement of the $^4\mathrm{He}(\pi^+,\mathrm{p})^3\mathrm{He}$ reaction [Kal+83] at several pion energies, T_π = 50, 100, 150, 200 and 250 MeV at a single angle, $\theta_p^{lab} = 20^o$ ($\theta_p^{cm} \approx 21^o$). These measurements were larger than those of the $^3\mathrm{H}(\mathrm{n},\pi^-)^4\mathrm{He}$ measurement [Kal+81] by a factor of 3.25, 1.70, 1.04, 1.21 and 1.06 for the pion energies, T_π = 50, 100, 150, 200 and 250 MeV respectively. It would appear unlikely that such a discrepancy is due to a systematic error and is more likely due to pronounced Coulomb effects. The average ratios between the present $^3\mathrm{He}(\mathrm{p},\pi^+)^4\mathrm{He}$ reaction measurements and $^3\mathrm{H}(\mathrm{n},\pi^-)^4\mathrm{He}$ reaction data are tabulated in Table 4.2 along with results found by Källne.

The Källne yields were normalized to the $pp \rightarrow d\pi^+$ reaction to obtain cross sections and the estimated systematic error was about 15%. Källne also performed a measurement of the $^4\mathrm{He}(\pi^+,\pi^+)^4\mathrm{He}$ reaction [Kal+81] and a disagreement of 25% with that expected from the assumed target density

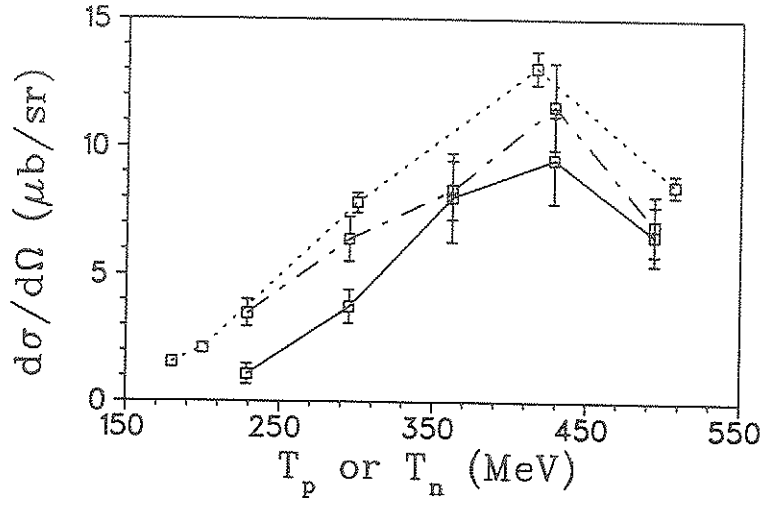

Figure 4.10: Comparison of ^{3}He(p,π^+)^{4}He measurement from Kehayias and present work (dotted line) and results from Källne *et al.* for ^{3}He(p,π^+)^{4}He (dot-dashed line) and ^{3}H(n,π^-)^{4}He from detailed balance (solid line) all at $\theta_{cm} \approx 21°$.

was found. The errors of the present work are considerably smaller and this is quite evident from Fig. 4.10 where the results of this work and that of Källne *et al.* are plotted for $\theta_{cm} \approx 21°$.

The data of Tatischeff *et al.* [Tat+76] for the ^{3}He(p,π^+)^{4}He reaction at 415 MeV were found to agree with the data of Källne *et al.* for the ^{3}H(n,π^-)^{4}He reaction to within the systematic uncertainties [Kal+81]. In Fig. 4.11 the data are shown to be comparable with an average deviation of 21%. There is evidence from microscopic calculations [BAD90a] that there are strong Coulomb effects in (N,$\pi^{+,-}$) reactions. This is observed in Fig. 4.12 where the result of the microscopic calculation ORCHID (to be discussed in the following Chapter) is shown for the ^{3}He(p,π^+)^{4}He and ^{3}H(n,π^-)^{4}He reactions. In light of this prediction and the supporting indication of Coulomb effects observed in Fig. 4.10, the disagreement with the Tatischeff data would seem to indicate an underestimation of the systematic uncertainties on their

part.

For the work in this thesis a measurement of proton elastic scattering was performed for ^{3}He (and ^{4}He) and indicated good agreement with the published data to within systematic error. Furthermore, measurements of $pp \rightarrow d\pi^+$ were also carried out which indicated that the estimation of the systematic uncertainties apart from those involving the ^{3,4}He target were reasonable. The present data are therefore internally self consistent.

4.3.3 Comparison for ^{4}He($\vec{p}$,π^+)^{5}He

The only published data for ^{4}He(p,π^+)^{5}He are at T_p = 200 and 800 MeV (Ref. [LeB+85] and Ref. [Hoi+84], respectively). The present data and the existing data cannot be directly compared because of the significant difference in proton bombarding energies. As is quite evident from Fig. 4.10, near threshold the cross section is rising rapidly and, therefore the 40 MeV difference between the data of LeBornec *et al.* at 200 MeV and the present measurements at 240 MeV implies a possible factor of two in the cross sections. The differential cross sections from the measurements at 200 MeV of LeBornec *et al.* [LeB+85] are shown in Fig. 4.13. The normalization of the LeBornec data are different from that of this work. Their cross section calculation assumed a parabolic background, and as was discussed in Section 3.1.3 in the Analysis Chapter, their cross section ratios with and without this parabolic background subtraction were approximately constant at 0.6. The data of this work was calculated assuming a constant factor of $\eta_{\rm fsi} \approx 0.6$. Therefore for direct comparison one must consider the following:

$$\begin{aligned} \frac{d\sigma}{d\Omega} &= \frac{d\sigma'}{d\Omega} \times \frac{1}{0.6} \times \frac{1}{\eta_{\rm fsi}} \\ &\approx \frac{d\sigma'}{d\Omega} \times \frac{1}{0.36} \end{aligned} \tag{4.7}$$

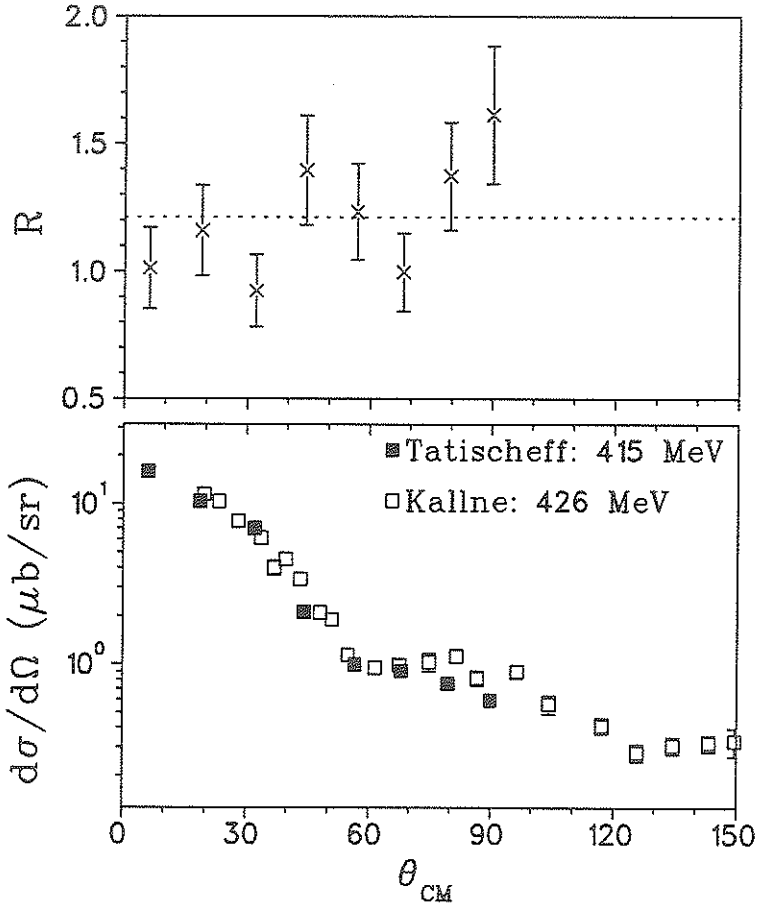

Figure 4.11: Comparison of 416 MeV data of Tatischeff *et al.* for the ^{3}He(p,π^+)^{4}He reaction with 426 MeV results from Källne *et al.* for the ^{3}H(n,π^-)^{4}He reaction from Detailed Balance.

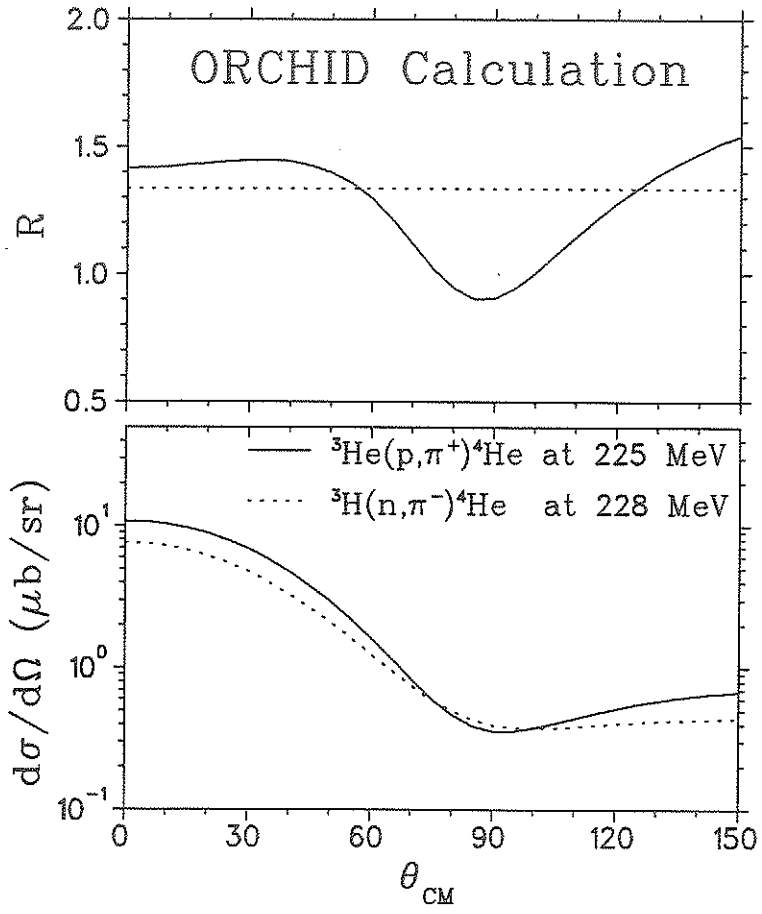

Figure 4.12: Comparison of ORCHID calculation for the ^{3}He(p,π^+)^{4}He reaction at 225 MeV and the ^{3}H(n,π^-)^{4}He reaction at 228 MeV. In the upper figure, R is the ratio of the cross sections of (p,π^+) to (n,π^-) where the dotted line is the average value. In the lower figure the calculations are compared explicitly.

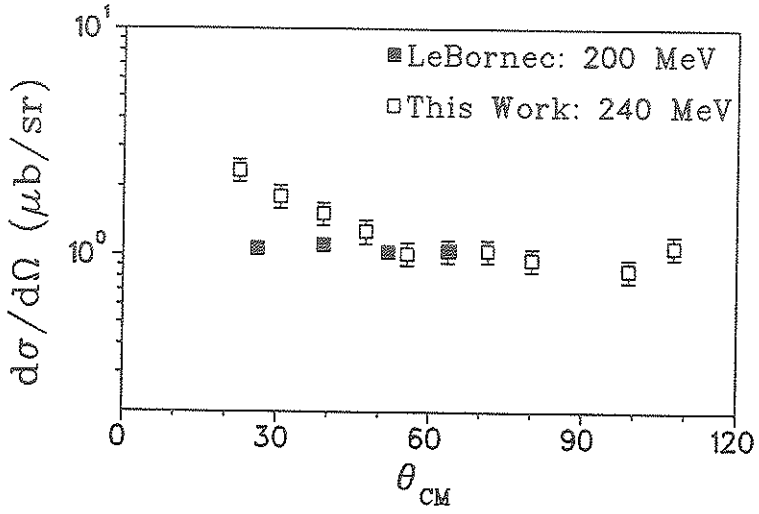

Figure 4.13: ^{4}He($\vec{p}$,π^+)^{5}He data at T_p = 200 MeV from LeBornec *et al.* compared to present measurements at 240 MeV renormalized by 0.36.

where $d\sigma/d\Omega$ is the cross section obtained using the normalization of this work and $d\sigma'/d\Omega$ is the cross section obtained using the normalization of Lebornec *et al.* (also used by Höistad *et al.* for the 800 MeV data shown in Fig. 4.3). For comparison, the data of this work shown in Fig. 4.13 was multiplied by 0.36.

The results are of comparable magnitude, with the 240 MeV cross sections being larger for angles less than about 45°. For the larger angles the cross sections are about the same. The systematic uncertainty of the LeBornec data was estimated at 20% and the systematic uncertainty of the present work is ≈9%.

4.4 Fit to Legendre Polynomials

In a further attempt to examine the role of underlying reaction mechanisms, partial wave expansions of the data were made. The unpolarized differential

cross section, $d\sigma_0/d\Omega$, may be written as a series of Legendre polynomials.

$$\frac{d\sigma_0}{d\Omega} = \sum_{l=0}^{\infty} a_l P_l(x), \tag{4.8}$$

where $P_l(x)$ are the Legendre polynomials. That is,

$$\begin{aligned} P_0(x) &= 1 \\ P_1(x) &= x \\ P_2(x) &= \frac{1}{2}(3x^2 - 1) \\ &\vdots \\ P_{l+1}(x) &= \frac{2l+1}{l+1} x P_l(x) - l P_{l-1}(x). \end{aligned}$$

The product of the unpolarized differential cross section and the analyzing power,

$$\frac{d\sigma_1}{d\Omega} = \frac{d\sigma_0}{d\Omega} \times A_{N0}, \tag{4.9}$$

may be parameterized as a series of partial waves.

$$\frac{d\sigma_1}{d\Omega} = \sum_{l=1}^{\infty} b_l P_l^{m=1}(x), \tag{4.10}$$

where $P_l^{m=1}(x)$ are the associated Legendre polynomials.

$$\begin{aligned} P_1^1(x) &= -y \\ P_2^1(x) &= -3xy \\ P_3^2(x) &= -\frac{3}{2} y(5x^2 - 1) \\ &\vdots \end{aligned}$$

where $x = \cos\theta$ and $y = \sin\theta$.

This implies then that one can write,

$$\begin{aligned} \frac{A_{N0} \times d\sigma_0/d\Omega}{\sin\theta} &= \frac{d\sigma_1/d\Omega}{\sin\theta} \\ &= -(b_1 + 3b_2\cos\theta + \frac{3}{2} b_3(5\cos^2\theta - 1) + \cdots), \end{aligned} \tag{4.11}$$

which shows that if only s and p (l=0,1) partial waves contribute $d\sigma_1/d\Omega / \sin\theta$ will be independent of θ, and as higher partial waves contribute dependence on $\cos\theta$ will be indicated.

The pp $\rightarrow$ dπ^+ reaction is well described by a few partial waves [Gil85]. Usually a prescription up to and including d-waves ($l = 2$) is sufficient for proton bombarding energies below 500 MeV. At $T_p = 178$ and 198 MeV for ^{3}He($\vec{p}$,π^+)^{4}He the parameter $d\sigma_1/d\Omega/\sin\theta$ is nearly flat with angle [Keh83] and is fit well using up to d ($l = 2$) partial waves. In Fig. 4.14 the data for ^{4}He($\vec{p}$,π^+)^{5}He are shown fit to Legendre polynomials up to f partial waves. The dotted line is the contribution up to the d wave, which is clearly not sufficient.

As the proton bombarding energy is increased, more and more partial waves are required. As more partial waves are required a forward angle peaking is observed in the $d\sigma_1/d\Omega/\sin\theta$ parameter, as is seen in Eqn. 4.11. For both the ^{3}He($\vec{p}$,π^+)^{4}He and the ^{4}He($\vec{p}$,π^+)^{5}He reactions at the energies of 300 MeV and above, many partial waves were required to fit the data. In Fig. 4.15 the fit to ^{3}He($\vec{p}$,π^+)^{4}He at $T_p = 300$ MeV is shown. The solid line is the fit up to the h ($l = 5$) partial wave and the dotted line is the contribution from *only* the s, p and d ($l = 0, 1, 2$) partial wave amplitudes. For the other energies above 300 MeV and for the ^{4}He($\vec{p}$,π^+)^{5}He reaction it was also found that many partial waves were required to fit the data.

Since the data do not cover the entire angular range from 0° to 180°, the coefficients are not unique and may vary considerably depending on the number of partial waves considered. However, one may conclude from this study that very many partial waves are indeed required to describe the (p,π^+) reaction observables, in particular, for proton bombarding energies above 300

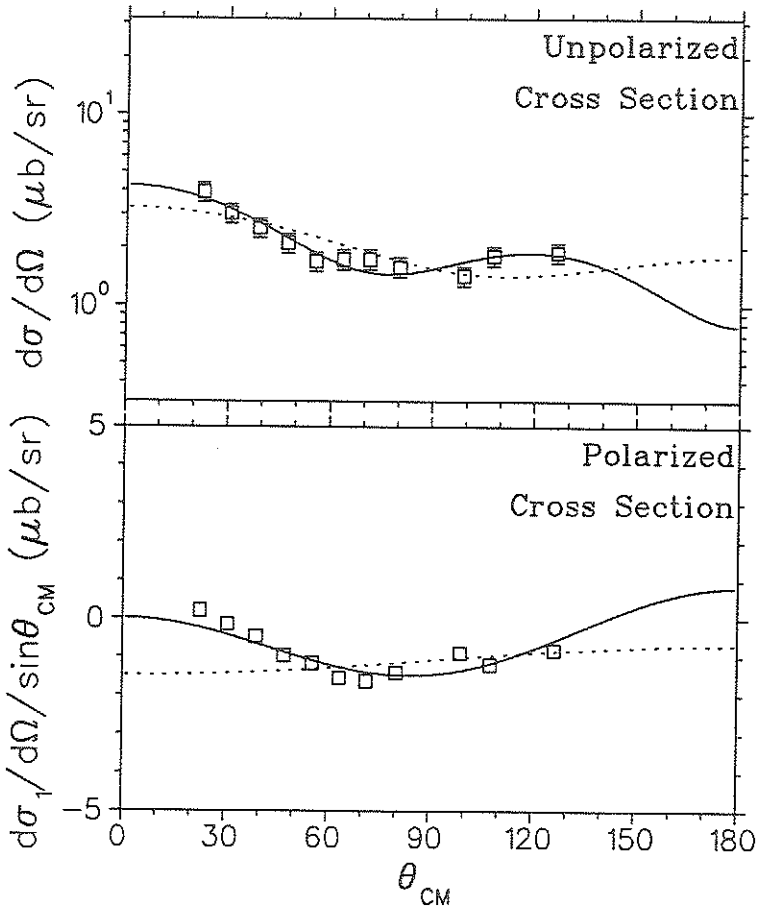

Figure 4.14: ^{4}He($\vec{p}$,π^+)^{5}He at T_p=240 MeV fit to Legendre polynomials for partial waves l=0-3 (solid line) and l=0-2 (dashed line).

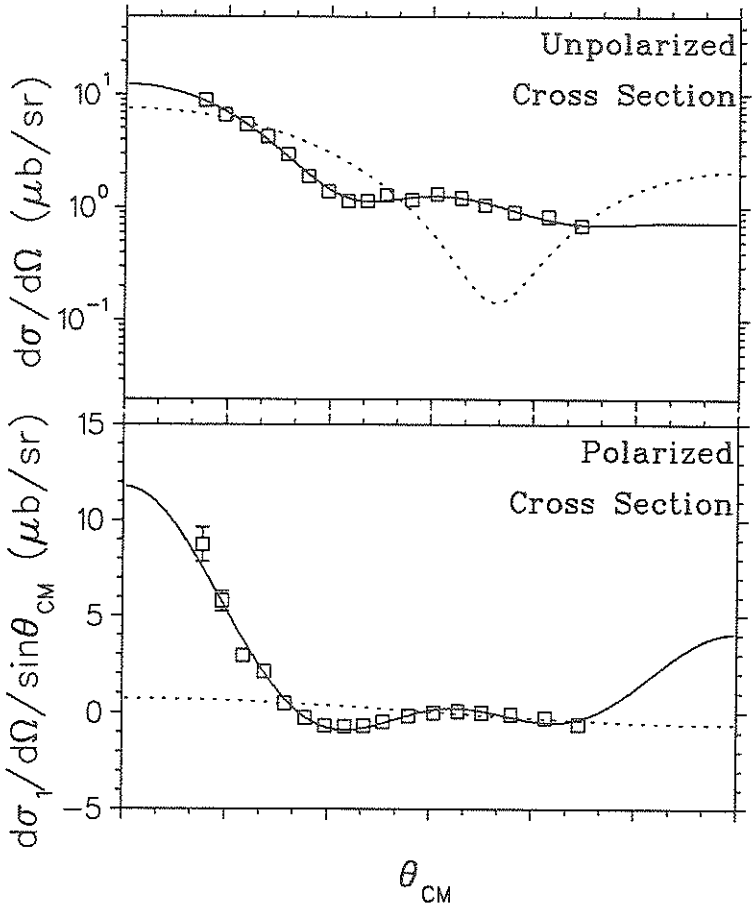

Figure 4.15: ^{3}He($\vec{p}$,π^+)^{4}He at T_p = 300 MeV fit to Legendre polynomials for partial waves l=0-5 (solid line) and l=0-2 (dashed line).

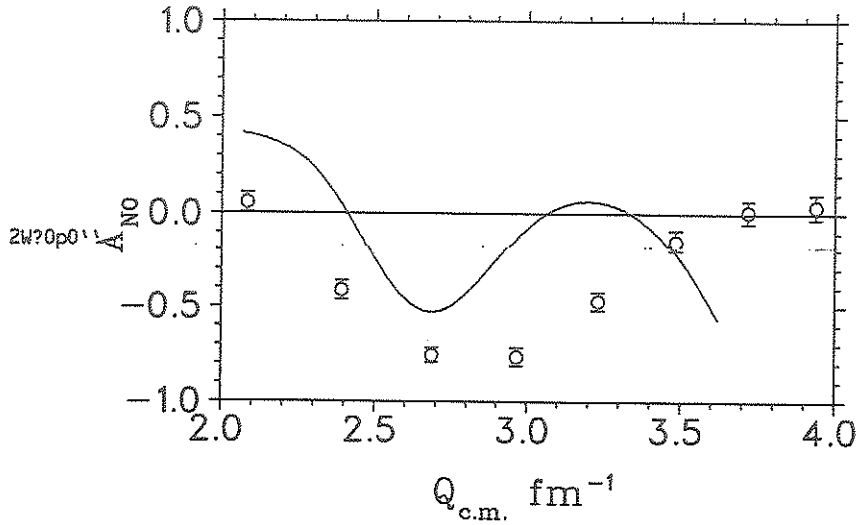

Figure 4.16: Comparison of A_{N0} for the ^{3}He($\vec{p}$,π^+)^{4}He reaction from present work (solid line) and the ^{3}He($\vec{p}$,p)^{3}He reaction from Ref. [Has+86] (points) at T_p = 300 MeV.

MeV.

4.5 Comparison to Elastic Data

The large oscillatory analyzing powers shown in Fig. 4.2 appear to be very similar to those for the corresponding proton elastic reaction at similar proton energies. As an example, the data at 300 MeV for ^{3}He($\vec{p}$,π^+)^{4}He and at 500 MeV for ^{4}He($\vec{p}$,π^+)^{5}He are plotted versus Q_{cm} and compared to the elastic reactions at the same proton energies (see Fig. 4.16 and Fig. 4.17). A striking similarity is observed in these figures. The minimum in the (p,π^+) reaction occurs at nearly the same momentum transfer as in the (p,p) reaction. This similarity could be a matter of coincidence or might possibly indicate that proton distortions play a strong role in the (p,π^+) reaction. However, one cannot reach more specific conclusions without a complete investigation in a microscopic calculation.

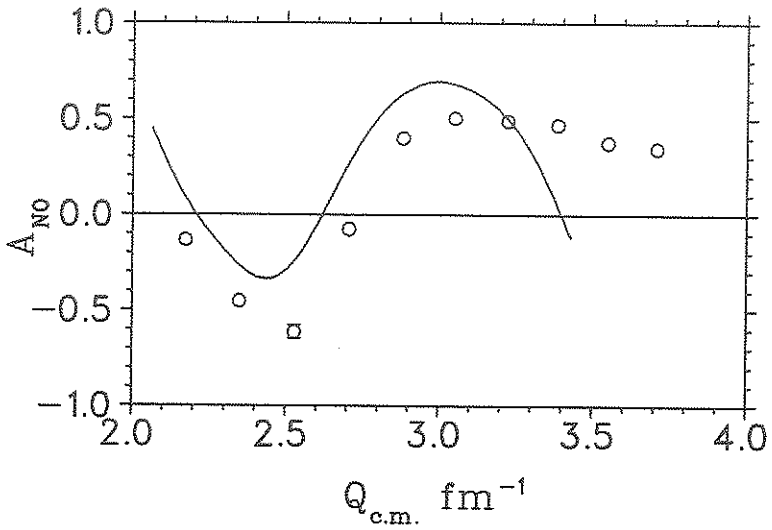

Figure 4.17: Comparison of A_{N0} for the ^{4}He($\vec{p}$,π^+)^{5}He reaction from present work (solid line) and the ^{4}He($\vec{p}$,p)^{4}He reaction from Ref. [Mos+80] (points) at T_p = 500 MeV.

4.6 Summary

High quality data for the differential cross sections and analyzing powers for the ^{3}He($\vec{p}$,π^+)^{4}He and ^{4}He($\vec{p}$,π^+)^{5}He reactions have been obtained at proton bombarding energies between 240 and 507 MeV. The data were compared to previous measurements and some notable discrepancies in the normalization of the differential cross sections are observed. The results were fitted to a series of Legendre polynomials and it was found that many partial waves are required to fit the data above 300 MeV. In combination with previous measurements near threshold for the ^{3}He(p,π^+)^{4}He reaction, and at 800 MeV for the ^{3,4}He($\vec{p}$,π^+)^{4,5}He reactions, one now has a comprehensive data set which spans the region of the Δ_{1232} resonance.

Chapter 5

Theory

In this Chapter the data are compared with theoretical calculations. Specifically, some of the early calculations for the reactions studied in this thesis will be discussed. The data are then compared with recent calculations, in particular, with a phenomenological pp $\rightarrow$ dπ^+ model calculation and with two microscopic model calculations.

5.1 Early Calculations

It was discovered quite quickly in studies of (p,π^+) reactions that a DWBA type of analysis was insufficient to explain the observed data. The initial One Nucleon Model (ONM) investigations (see Section 1.2.2) will not be explained in this thesis and may be found in the review articles of (p,π^+) research (see Refs. [Hoi79], [MM79] and [Fea81]). Since the ONM was found to be insufficient it was then assumed that the reaction mechanism proceeded dominantly via a Two Nucleon Mechanism (TNM). A microscopic TNM calculation is both complicated and time consuming. Furthermore, such calculations are found to be extremely sensitive to various wave function and distorting potential parameters. For these reasons, simpler approaches were

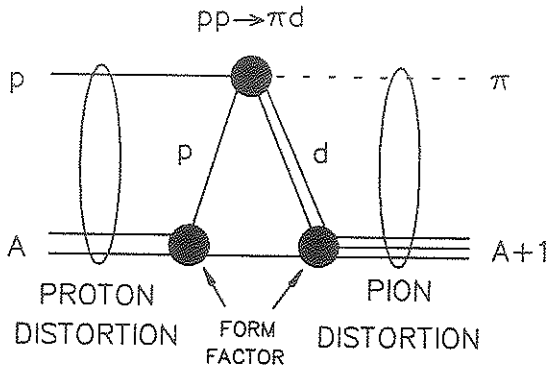

Figure 5.1: Basic physical picture for phenomenological DWIA.

considered which used the elementary reaction data as input. Two of these early Impulse type calculations will be discussed, one which assumed a reaction mechanism based upon the $pp \rightarrow d\pi^+$ reaction and the other based upon $p\pi \rightarrow p\pi$ elastic scattering. A cluster model calculation which uses the $^3He(p,\pi^+)^4He$ reaction data as input will also be briefly discussed.

5.1.1 Fearing DWIA Model

The model of Fearing ([Fea74], [Fea75a] and [Fea75b]) is based on the qualitative success of several earlier calculations which were done using the plane wave impulse approximation (PWIA) with the $pp \rightarrow d\pi^+$ cross sections as input (see for example Refs. [Rud52], [Blu54] and [Ing+71]). The model of Fearing improved upon these earlier calculations by including *distorted waves* (DWIA). It should be noted that both the PWIA and DWIA calculations used only the $pp \rightarrow d\pi^+$ cross section information as the input and therefore no spin observables (i.e. analyzing powers) could be calculated.

A schematic of the DWIA model is shown in Fig. 5.1. The basic physical assumption of the calculation is that the interaction responsible for nuclear

pion production can be treated as a sum of at most two nucleon interactions with the other nucleons acting as spectators. The cross section for the A(p,π^+)A+1 reaction is calculated from the pp $\rightarrow$ dπ^+ cross sections in the following way,

$$\frac{d\sigma}{d\Omega}|_{pA\rightarrow(A+1)\pi} = (KF) \times g \times |F(\Delta)|^2 \times \frac{d\sigma}{d\Omega}|_{pp\rightarrow d\pi} \qquad (5.1)$$

where (KF) are kinematic factors, g is a numerical factor arising from the proper inclusion of spin, isospin and antisymmetrization effects, and F(Δ) is the form factor. The form factor is from a loop integral over the nuclear wave functions which is a function of an effective momentum transfer. This effective momentum transfer is of the form,

$$\vec{\Delta} = (A-1)(\frac{\vec{p}_p}{A} - \frac{\vec{p}_\pi}{A+1}). \qquad (5.2)$$

The distortions were included in the eikonal approximation and the studies showed that while the distortions alter the shape of the angular distributions to some extent, their affect was primarily to the normalization.

The formalism of Fearing was quite general and set up for any A(p,π^+)A+1 reaction. The published studies were mostly carried out for the pd $\rightarrow$ tπ^+ reaction but investigations for other nuclei, including ^{3}He(p,π^+)^{4}He, were also done ([AF76] and [Kal+78]). The data from Ref. [Kal+78] for the ^{3}H(n,π^-)^{4}He reaction (obtained from detailed balance) are shown in Fig. 5.2 compared to the calculation for ^{3}He(p,π^+)^{4}He transformed to ^{3}H(n,π^-)^{4}He (assuming charge symmetry [Fea91]). The calculation fits the data well for forward angles but fails to reproduce the second maximum that is observed at about 80°. It was found that the DWIA calculation was quite sensitive to the nuclear wave functions used and, indeed, a calculation with a Gaussian wave function was found to drop off much more rapidly than one which used a Irving-Gunn wave function (used in the calculation of Fig. 5.2). While the presence of the high momentum components in the Irving-Gunn wave

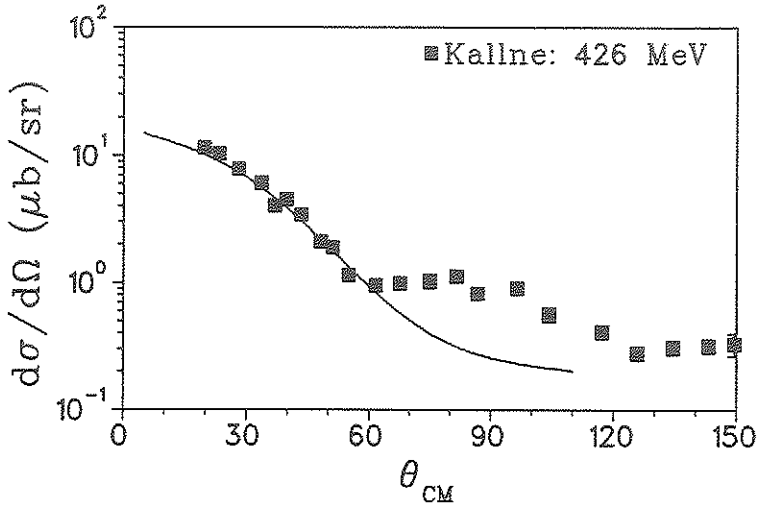

Figure 5.2: Calculation of ^{3}H(n,π^-)^{4}He by Alexander and Fearing.

function was seen to improve the fit to forward angles [AF76], it still fails to reproduce the observed cross section at back angles.

5.1.2 Gibbs and Hess Model

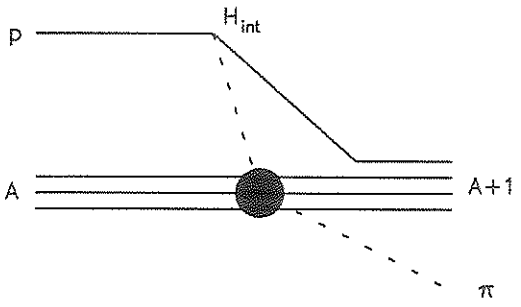

Figure 5.3: Diagram for pion production in the model of Gibbs and Hess.

Another phenomenological model calculation for the ^{3}He(p,π^+)^{4}He reaction is that of Gibbs and Hess [GH77]. Their model assumes that the (π^+,p) cross section is proportional to that for pion elastic scattering from the same target. The implication is that the cross section arises mostly from pion rescattering and so includes some of the TNM diagrams implicitly; however, the ONM is not included in this model in any way. From the (π^+,p) cross section, the (p,π^+) cross section is obtained by detailed balance. The model is shown schematically in Fig. 5.3. Note the incident pion is absorbed by the outgoing proton (or equivalently the outgoing pion is created from the incoming proton in the (p,π^+) reaction picture) and this is included using an operator from the non-relativistic reduction of the π-N interaction.

The calculation uses plane waves for the protons but these are attenuated according to the mean free path of the proton in nuclear matter. Since there is no dependence on the proton polarization, the analyzing powers would be zero and therefore in this respect the calculation fails miserably. In Fig. 5.4, the calculation for the differential cross section for the ^{3}H(n,π^-)^{4}He reaction is compared to the same data in Fig. 5.2. The calculation is quite reasonable for the forward angles but then falls off too quickly at back angles. From the results of this model it would seem that, indeed, a large part of the reaction mechanism is from pion rescattering, particularly at forward angles. From microscopic calculations this is seen to be true.

5.1.3 Cluster Model of Germond and Wilkin

The ^{1}H(^{3}He,π^+)^{4}He reaction may be considered the elementary process of the general A(^{3}He,π^+)A+3 reaction. These reactions have been studied in a series of survey experiments, and a model was formulated by Germond and Wilkin [GW84] which uses the ^{3}He(p,π^+)^{4}He data as input. The model

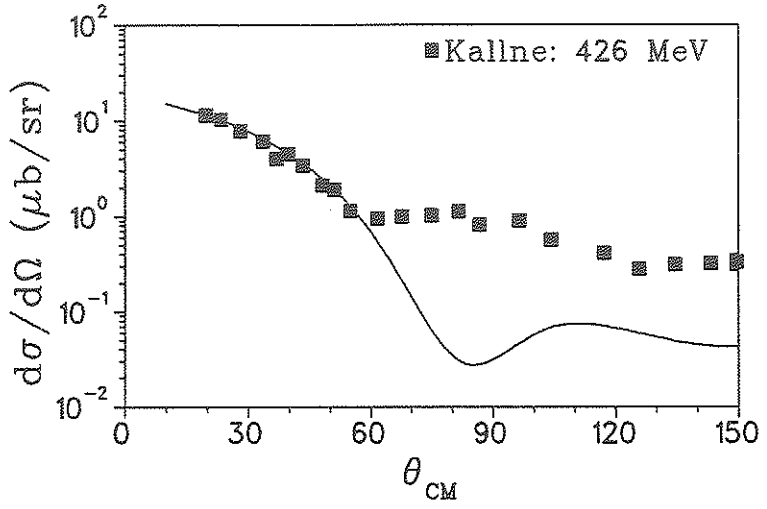

Figure 5.4: Calculation of ^{3}H(n,π^-)^{4}He by Gibbs and Hess.

is a cluster model and was modified for the calculation of the differential cross sections of the ^{4}He(p,π^+)^{5}He reaction from those of the ^{3}He(p,π^+)^{4}He reaction [GW85]. For the ^{4}He(p,π^+)^{5}He reaction calculation a final state interaction between the neutron and the alpha had to be assumed and this was discussed in Section 3.1.3.

A schematic of the dynamics of the model is shown in Fig. 5.5. The calculation was done for T_p= 200 and 800 MeV and, not surprisingly, the results showed that the ^{4}He(p,π^+)^{5}He and ^{3}He(p,π^+)^{4}He reactions have similar angular distributions. The model required, however, a multiplicative factor of $\approx$ 1.5 to obtain the correct normalization and no investigation of other incident proton energies was carried out. The authors did note however that their model would predict that the analyzing powers for the two reactions would be similar.

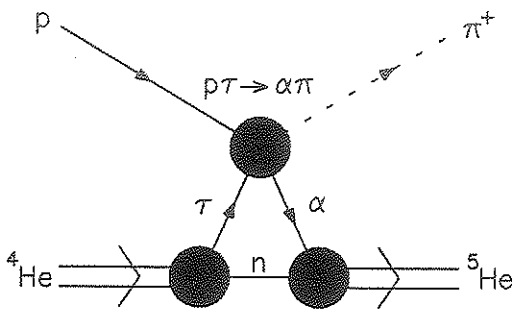

Figure 5.5: Dynamics of cluster model of Germond and Wilkin.

5.2 Impulse Model

The qualitative success of the older phenomenological pp $\rightarrow$ dπ^+ calculations imply that the pp $\rightarrow$ dπ^+ reaction plays a prominent role in the underlying mechanism of nuclear (p,π^+) reactions. Comparisons between the analyzing powers for light nuclei and those of the pp $\rightarrow$ dπ^+ reaction, kinematically transformed to the nuclear frame, exhibit strong similarities [Hub+87a]. Results from recent measurements provide convincing evidence that this is so in exclusive as well as inclusive nuclear pion production. It has been observed for 200 MeV proton bombarding energy, that the analyzing powers in the continuum corresponding to about 20 MeV in excitation energy, are very similar to those of the pp $\rightarrow$ dπ^+ reaction [Kor+89]. For inclusive reactions in the quasi-free region at 400 and 450 MeV it has been shown that the results observed are consistent with a model based on the elementary pp $\rightarrow$ dπ^+ and pN $\rightarrow$ NNπ^+ pion production processes [Fal+86]. All this would suggest that a phenomenological model based on the elementary processes might provide useful insights into exclusive nuclear pion production. Indeed there have been several calculations of this type incorporating details of the pp $\rightarrow$ dπ^+ reaction as input to model calculations. In addition to the Fearing model discussed above there have also been other similar calculations, ([Kur87] and

[Dil+80]), however, since all these earlier calculations used the cross section information only, they were unable to predict spin observables.

5.2.1 Description of Model

A phenomenological model of the A(p,π^+)A+1 reaction has been developed ([Fal91] and [Fur+91]) that incorporates the pp $\rightarrow$ dπ^+ reaction amplitudes [BAS88] and assumes this NN $\rightarrow$ NNπ reaction as the primary pion production mechanism. The formulation follows the general outline presented by Ingram *et al.* [Ing+71] with several important extensions. The model basically represents a plane wave calculation that incorporates the amplitudes of the pp $\rightarrow$ dπ^+ reaction in calculating the amplitudes for the A(p,π^+)A+1 reaction.

The pp $\rightarrow$ dπ^+ amplitudes may be obtained from the pp $\rightarrow$ dπ^+ reaction observables. Such an analysis has been done recently by several authors ([BAS88], [Bug85], [Bug84], [HWY84] and [KWY80]). The fit used for this model was that of Bugg [BAS88] and the definition of the amplitudes is shown in Table 5.1. The pp $\rightarrow$ dπ^+ reaction amplitudes were parameterized as a continuous function of the incident proton laboratory energy from threshold to 800 MeV. The dominant amplitudes in this energy region are A_2, A_4 and A_6.

Both the momentum distribution of the struck proton and the recaptured deuteron are contained in the formulation. Allowance can also be made for absorption of the proton and pion waves by attenuation factors in the plane waves. Simple shell model configurations, $(1s)^3$ and $(1s)^4$, were assumed for the target and residual nucleus respectively. These wave functions were expanded in the form (p + d) and (d + d) using one-particle and two-particle

Nomenclature for partial waves					
Amplitude	NN state $^{2s+1}L_j$	l_π	Amplitude	NN state $^{2s+1}L_j$	l_π
A_0	$^1S_0$	1	A_7	$^1D_2$	3
A_1	$^3P_1$	0	A_8	$^1G_4$	3
A_2	$^1D_2$	1	A_9	$^3F_3$	4
A_3	$^3P_1$	2	A_{10}	$^3F_4$	4
A_4	$^3P_2$	2	A_{12}	$^3H_5$	4
A_5	$^3F_2$	2	A_{13}	$^1G_4$	4
A_6	$^3F_3$	2	A_{14}	$^1I_6$	5

Table 5.1: Bugg convention for pp $\rightarrow$ dπ^+ partial wave amplitudes.

coefficients of fractional parentage.

In the model (see Fig. 5.6) the struck target proton has a laboratory momentum p_2 and is assigned an energy E_2=M_A-(M_R+p_2^2/2M_R), where M_A is the target mass and M_R is the mass of the $A-1$ recoil. This expression thus assumes an on-shell recoil nucleus. From the energies and momenta of the two protons, E_1, $\vec{p}_1$ and E_2, $\vec{p}_2$, all the requisite quantities in the pp cm frame are calculated, including the pion momentum at its kinematically mandated (laboratory) value. The deuteron and the struck proton are both off-shell. In order to determine the effective energy at which the pp $\rightarrow$ dπ^+ amplitudes are evaluated, one dynamical parameter must be specified. This dynamical parameter was taken to be the *pion momentum in the pp cm frame.* Justification for this choice, rather than the choice of the total energy in the pp cm frame for example, was based on the success of this procedure in interpreting the pp $\rightarrow$ pnπ^+analyzing powers [Fal+85]. The direction of the pion momentum with respect to the direction of the total momentum of the pp system was used to define the scattering angle of the pion in the pp cm frame.

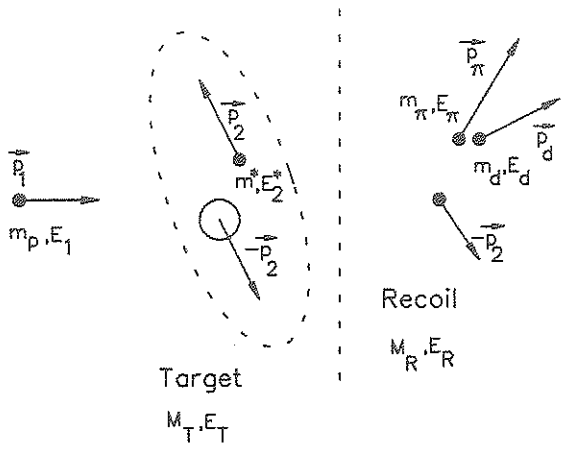

Figure 5.6: Impulse model pion production mechanism in nuclei.

5.2.2 Calculation for ^{3,4}He($\vec{p}$,π^+)^{4,5}He

The results of the calculation are shown in Fig. 5.7 and Fig. 5.8 at the energies of the experimental data. The shape of the calculated differential cross section angular distributions agree fairly well with the data at forward angles, but reveal increasing departures at the larger angles. Magnitudes of the calculated differential cross sections were found to be quite sensitive to the attenuation factors (mean free paths) of the proton and pion, as expected, although the shapes did not change significantly. The calculations shown in Fig. 5.7 are renormalized to fit the data at the forward angles.

The rapid changes in A_{N0} between $\approx$ 200 and 300 MeV observed in the experimental data are qualitatively reproduced by the calculation. At the two higher energies there remains some measure of qualitative agreement at the forward angles, but the calculation fails to reproduce the minimum observed. A feature of the predictions of this model is that the magnitude of the analyzing power can be much greater than that of the pp $\rightarrow$ dπ^+ reaction. The restrictions imposed by angular momentum coupling dictate that the

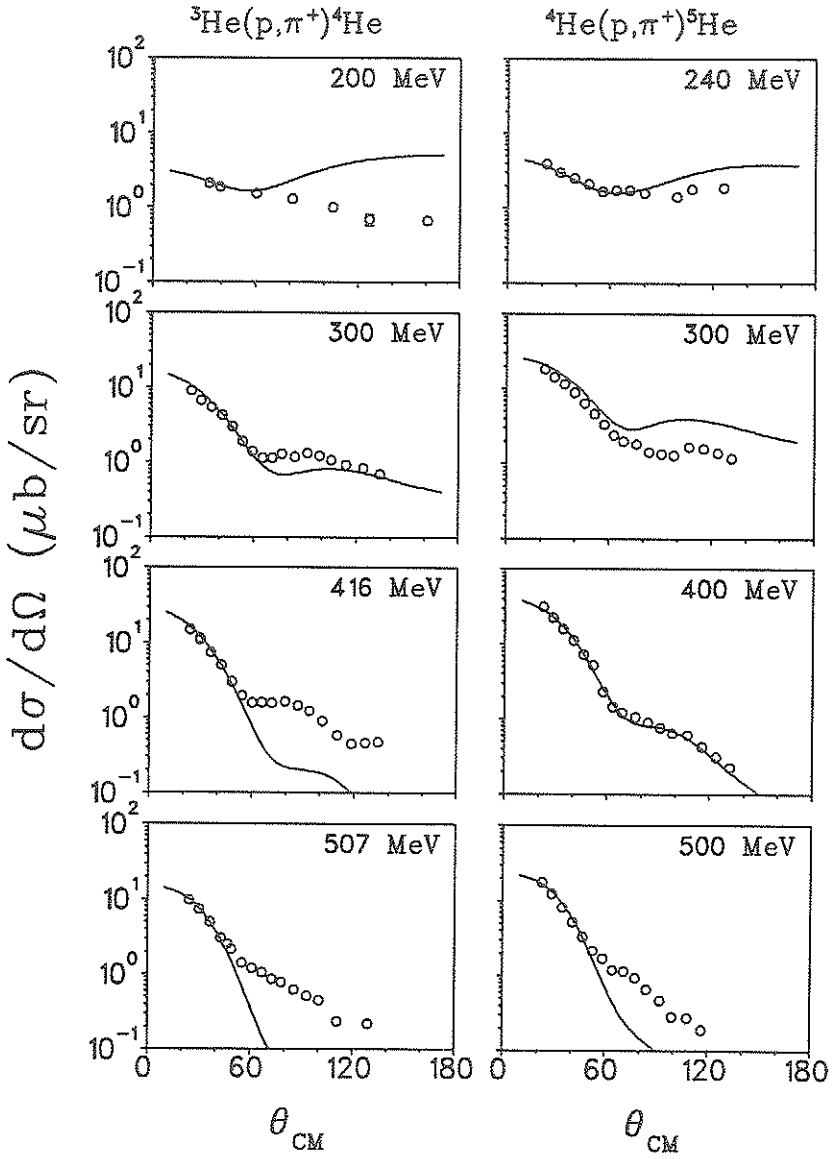

Figure 5.7: Impulse calculation for Differential Cross Sections.

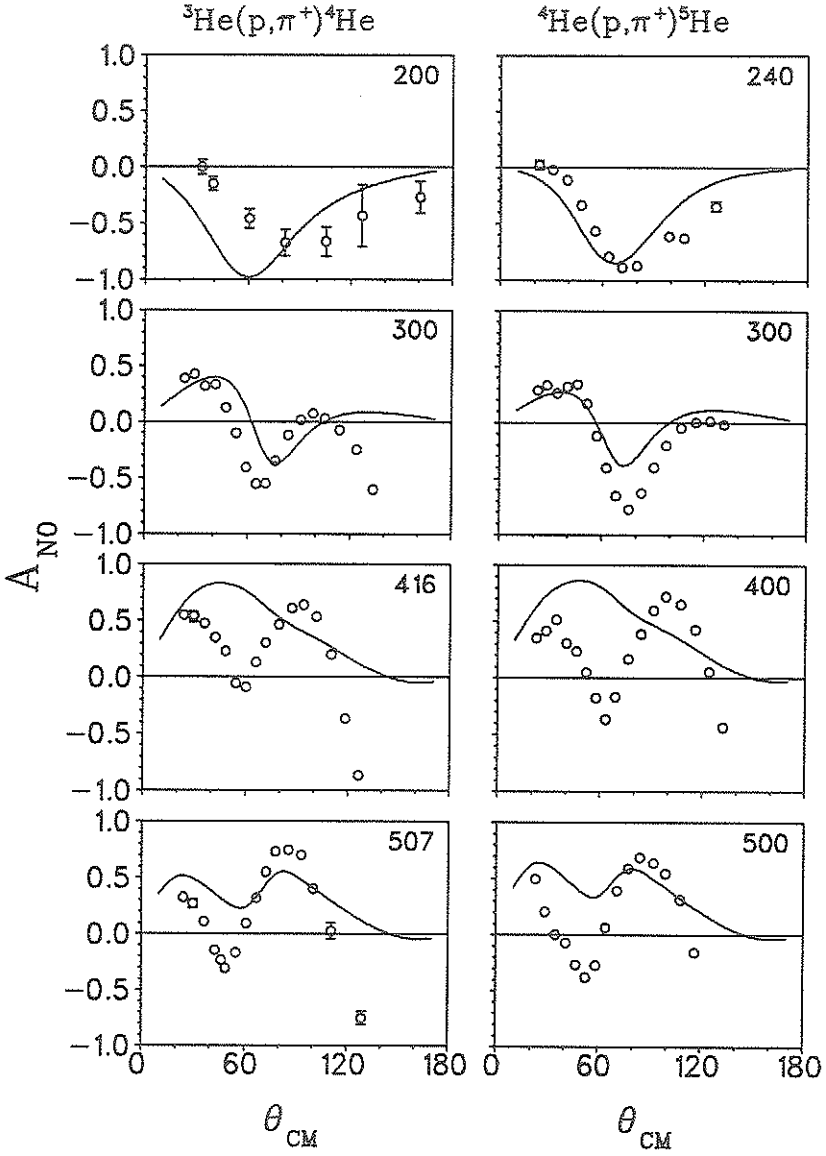

Figure 5.8: Impulse calculation for Analyzing powers.

amplitudes for the A(p,π^+)A+1 reaction combine with different weightings than in pp $\rightarrow$ dπ^+. Different final states should thus exhibit structure dependence of A_{N0}. The calculations of A_{N0} revealed only a weak dependence on the attenuation factors (mean free paths) of the proton and pion.

The model presented includes only the NN isospin channel ($T_i = 1, T_f = 0$), corresponding to the isospin cross sections σ_{10d} and σ_{10} [GW54]. However, the effective pp collision energies attain values where the ($T_i = 1, T_f = 1$) channel is far from negligible. Indeed for proton bombarding energies of 200, 300, 410, 500 MeV the effective pp collision energies are approximately 306, 462, 638, and 784 MeV respectively. At these energies the ratio σ_{11} / σ_{10d} is about 0.01, 0.16, 0.9 and 2.9 respectively [VA82]. Interference of amplitudes from the ($T_i = 1, T_f = 1$) transition with those of the ($T_i = 1, T_f = 0$) transition will thus become of increasing importance as the energy is raised. However, presently little information exists on these amplitudes and no further quantitative estimates can be made.

5.3 Δ-Hole Model

A Δ-hole model calculation has been performed for the angular distributions for the ^{3}H(n,π^-)^{4}He reaction by Sakamoto *et al.* [Sak+85]. The formulation of the model for (π^+,p) reactions was introduced by Hirata [Hir78]. In an earlier calculation [Hir+83] qualitative agreement with data was found. However, the later [Sak+85] calculation contains a better overlap function for the ^{3}He and ^{4}He wave functions. The results are shown in Fig. 5.9, where the calculation including only the background ONM is shown by the dotted line. The Δ-hole term contribution is shown by the dashed line and the contribution of both terms is indicated by the solid line. The authors concluded that, roughly speaking, the angular distribution is mainly determined by the

Δ-hole term (TNM) in the forward angle region up to the first dip or inflection, and the background term (ONM) dominates the reaction in the region of the second maximum or shoulder.

This calculation is one of the few full microscopic calculations for the ^{3}He(p,π^+)^{4}He reaction. However, no investigation of the analyzing powers was done.

5.4 ORCHID Model

The ORCHID model ([Alo+88], [ABD89] and [BAD90a]) was developed at IUCF and is used to investigate the various contributions to the (p,π^+) mechanism. The model initially used ^{3}He(p,π^+)^{4}He as a *test* reaction but has since been applied to other reactions as well [BAD90b]. Recently, the ORCHID model was used to calculate the differential cross section and analyzing power for the ^{3}He($\vec{p}$,π^+)^{4}He reaction up to T_p= 325 MeV [BAD90a].

5.4.1 Description of Model

The model includes microscopically both the one-nucleon mechanism and the resonant p-wave rescattering part of the two-nucleon mechanism, which is assumed to proceed through formation of the intermediate Δ_{1232} resonance induced by π and ρ meson exchange between the projectile and one target nucleon. Typical diagrams of the TNM resonant rescattering are shown in Fig. 5.10 where they are separated into *projectile emission* (PEM) and *target emission* (TEM). Higher order processes are included through proton-nucleus and pion-nucleus optical model distortions. The proton distortions are obtained from smooth interpolation of fits to the proton elastic data. The pion

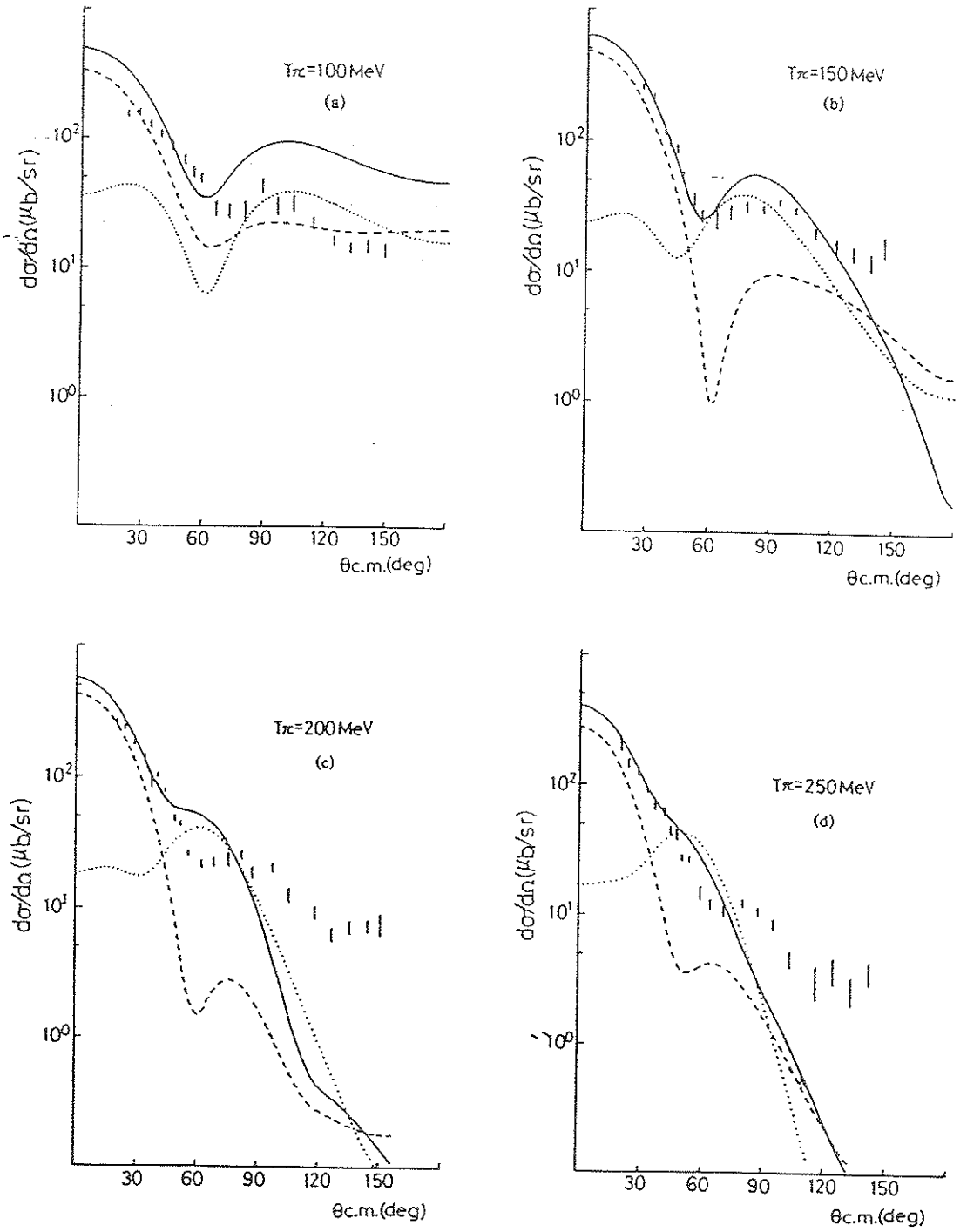

Figure 5.9: Δ-hole calculation by Sakamoto *et al.*

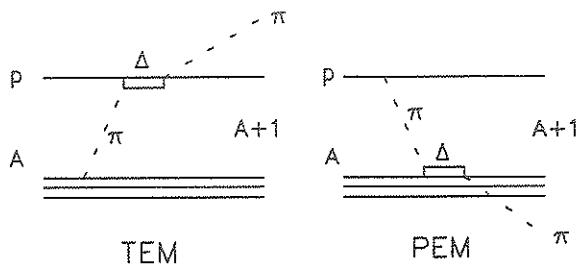

Figure 5.10: Two Nucleon mechanism of ORCHID involving intermediate Δ-isobar formation: projectile emission (PEM) and target emission (TEM).

distorted waves were generated from the configuration space pion-nucleus optical potential of Johnson and Siciliano ([JS83a], [JS83b] and [Sic+86]).

The calculation is similar to the Δ-hole model calculation by [Sak+85] except that Δ dynamics are treated differently. In the ORCHID model the medium corrections on the Δ is dealt with via a local Δ self energy in the propagator and in the Δ-hole model the Δ degree of freedom is treated dynamically [BAD90a].

5.4.2 Calculation for ^{3}He($\vec{p}$,π^+)^{4}He

The ORCHID model was *tested* with the ^{3}He($\vec{p}$,π^+)^{4}He data of Kehayias *et al.* [Keh+86] at T_p=178 MeV and T_p=198 MeV [BAD90a]. The calculation compares quite well with the data at forward angles but not so for the back angles at 198 MeV (these are shown in Fig. 5.11). A calculation was also performed for 300 MeV [Ben91] and this is compared with the data of this thesis in Fig. 5.12.

The full calculations do indeed produce the large and rapid oscillations

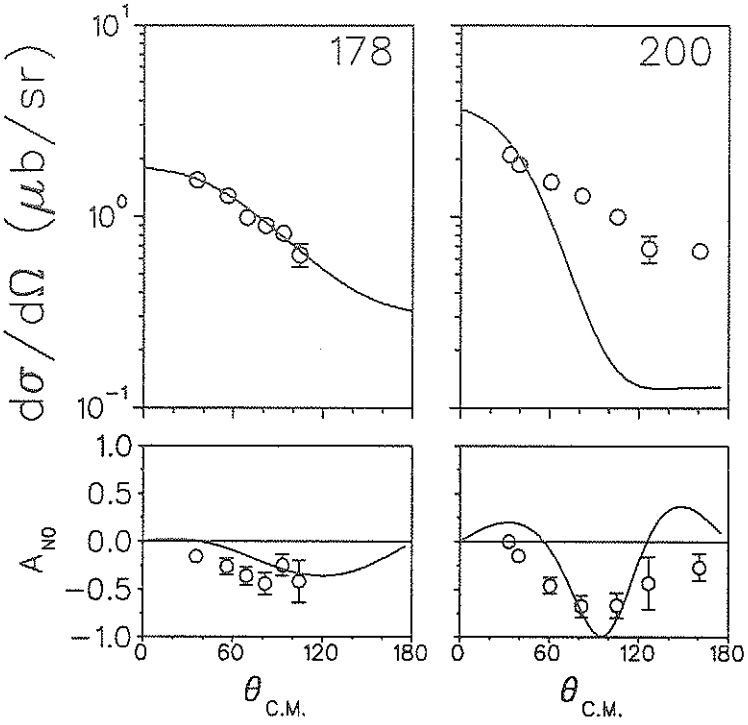

Figure 5.11: ORCHID calculation for ^{3}He($\vec{p}$,π^+)^{4}He at 178 and 198 MeV.

observed at 300 MeV (but not seen at 198 MeV shown in Fig. 5.11) but the agreement with the data is only qualitative. In Fig. 5.13 the decomposition of the full calculation into the contributions from various mechanisms is shown. It was found at 178 MeV that the ONM amplitude dominates and at 200 MeV the ONM and PEM term of the TNM are approximately equal. For both 178 and 200 MeV calculations the TEM piece was found to be small and this is also found to be true at 300 MeV.

In Fig. 5.14 the effects of the distortions are shown. The plane -wave (PW) calculations are those obtained with no distortions but still calculated in the manner of the ONM and TNM (as opposed to the plane wave ONM which gives a zero analyzing power). By including the higher order processes explicitly one would expect that the sensitivity to distortions would decrease. This was, indeed, found to be true near threshold, where the ONM is seen

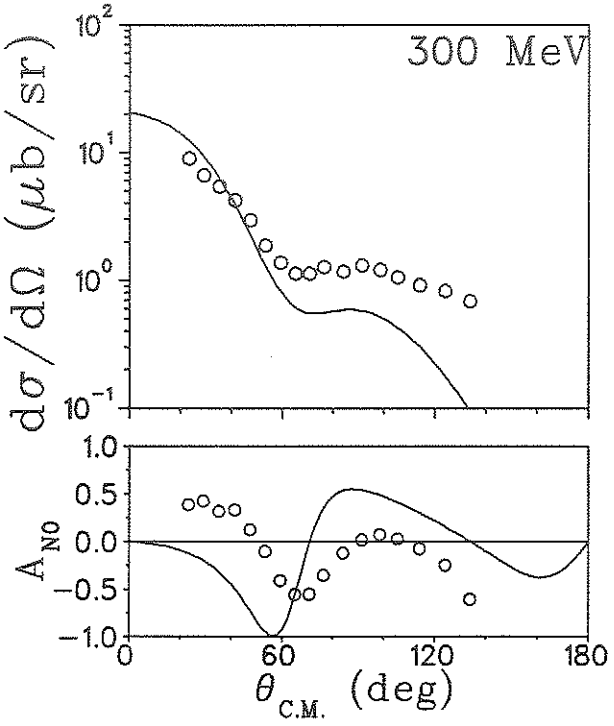

Figure 5.12: ORCHID calculation for ^{3}He($\vec{p}$,π^+)^{4}He at 300 MeV.

to dominate. As the energy increases, the cross sections are found to be somewhat insensitive to distortions. The analyzing powers however, are very sensitive at all energies. This is shown strikingly in Fig. 5.14 where different distortions are found to give rise to a different sign in A_{N0}.

The ORCHID model therefore provides an excellent starting point for studying (p,π^+) reactions but shows some marked discrepancies at this stage. Specifically, for ^{3}He($\vec{p}$,π^+)^{4}He at 300 MeV the cross section is quite well reproduced at forward angles but not so for back angles. For A_{N0} in the forward angles, it predicts the incorrect sign, however it does show the general trend for the back angle measurements.

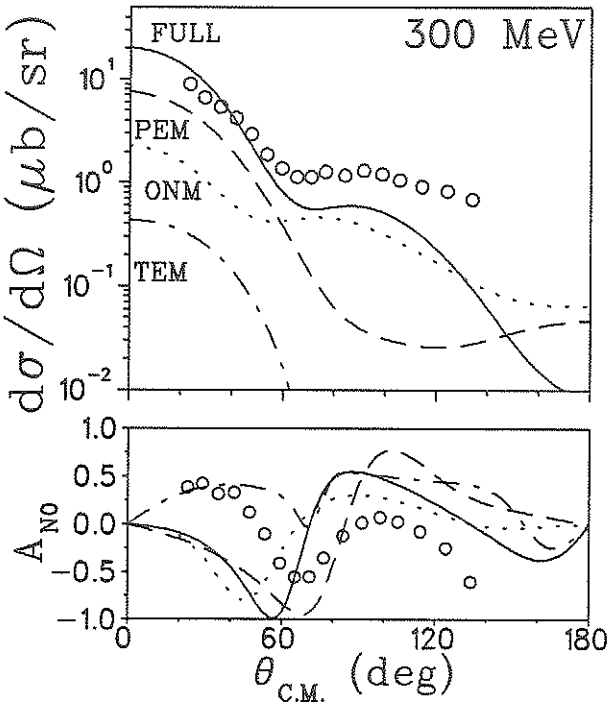

Figure 5.13: Decomposition of full ORCHID calculation (solid lines) into the one-nucleon mechanism (dotted lines), projectile-emission (dashed lines) and target emission (dot-dashed lines).

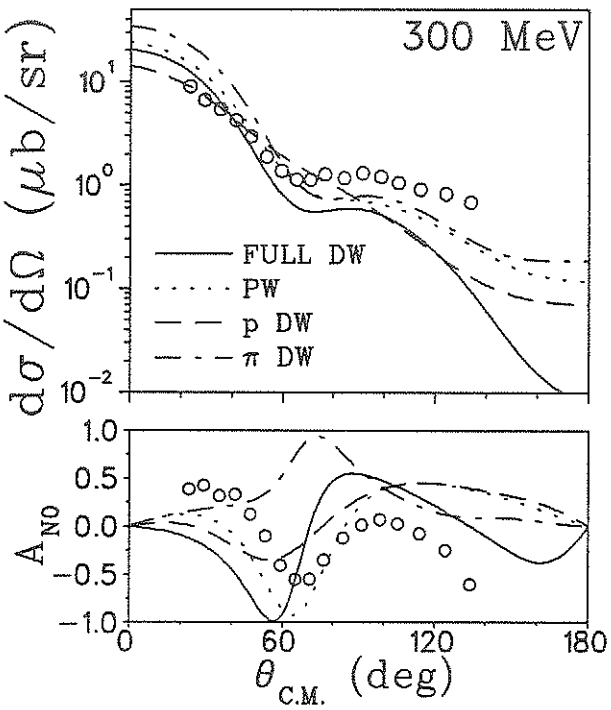

Figure 5.14: Effects of distortions in ORCHID calculation. Plane waves (dotted lines), proton distortions only (dashed lines), pion distortions only (dot-dashed lines) and full distortions (solid line).

5.5 Discussion

Both the Impulse and ORCHID models describe satisfactorily the analyzing powers at 200 MeV. At 300 MeV the microscopic model (ORCHID) fails most seriously at forward angles where it predicts the wrong sign of A_{N0}. On the other hand, the $pp \rightarrow d\pi^+$ model describes reasonably well the forward angle part of the A_{N0} distribution.

There are numerous reasons why the $pp \rightarrow d\pi^+$ model could fail. Among others, these include: neglect of distortions, inadequate treatment of off-shell effects and pion rescattering and inclusion of only the $(T_i = 1, T_f = 0)$ NN isospin channel, as discussed previously. All these factors may be significant in the failure of this model at the higher energies where the momentum transfer is correspondingly greater. It is less clear where the limitations of the microscopic model might occur. Incorporating the experimentally determined amplitudes of the dominant $pp \rightarrow d\pi^+$ reaction as in the former model ensures that this naturally includes the effects from resonant and non-resonant intermediate states. The ORCHID model however only includes resonant rescattering and the effects of this approximation remains to be determined.

5.6 Summary

In this chapter we have discussed various theoretical models used to investigate (p,π^+) reactions. Due to the complexity and limited predictive power of the microscopic calculations, one also studies these reactions within the considerations of other processes, for example the elementary $NN \rightarrow NN\pi$ processes. Here we summarize the results of the investigations of the $^3He(\vec{p},\pi^+)^4He$ and $^4He(\vec{p},\pi^+)^5He$ reactions.

At energies close to threshold, where the analyzing powers bear a striking resemblance to those for low energy pp $\rightarrow$ dπ^+ the ORCHID model predicts a dominant ONM term. As the energy is increased the ORCHID model and the Δ-hole model both indicate that the forward angle part is mostly from the TNM terms and the back angle part is mostly due to the ONM terms. It is important to note, however, that these contributions are quite sensitive to the optical model parameters. The phenomenological pp $\rightarrow$ dπ^+ model compares well with the forward angle data but in most cases, the observed back angle cross section does not fall off as quickly as the model prediction. Indeed, it is possible that the evident failure of the phenomenological pp $\rightarrow$ dπ^+ model at back angles is an indication that distortions must be included in the impulse calculation.

With respect to the analyzing powers, the sensitivity of this observable to the optical potential parameters is very significant. This could be an indication that an important ingredient of the reaction mechanism is missing in the microscopic calculations. Since the analyzing power is sensitive to interferences, it is possible that many higher order diagrams must be included for the calculation to be complete.

At the present stage, the theoretical calculations are insightful but limited in predictive power. One would hope that the high quality data of this thesis would inspire continued theoretical interest into this complex reaction.

Chapter 6

Conclusions.

In this chapter the results obtained in this work and the conclusions drawn from them are summarized.

Experiments were performed at TRIUMF to measure the differential cross sections and analyzing powers for the ^{3}He($\vec{p}$,π^+)^{4}He and ^{4}He($\vec{p}$,π^+)^{5}He reactions at energies spanning the region of the Δ_{1232} resonance. For this measurement a cryogenic Helium target was extensively refurbished and modified such that it provided stable and reliable operation for the two experiments. A Monte carlo study of the MRS as a pion spectrometer was performed to study the spectrometer's acceptance and to gain insight into its general performance. An effective pion survival length, L_π, for the MRS was found which parameterized the pion survival fraction over a large range of momenta.

A final state interaction calculation of the neutron and alpha particle for the low excitation energies of the ^{5}He recoil in the study of the ^{4}He(p,π^+)^{5}He reaction was performed. It was found that the pion spectrum as a function of excitation energy was nearly independent of pion angle and proton energy. In light of this result the ^{5}He data were renormalized by a constant value of $\eta_{\rm fsi} = 0.6$. The data obtained are of high quality and in combination with

existing data provide a data base from near threshold to 800 MeV.

The data were studied in terms of a fit to Legendre polynomials, a phenomenological pp $\rightarrow$ dπ^+ model and a microscopic calculation. The fit to Legendre polynomials indicate that many partial waves are required to fit the data for proton bombarding energies above 300 MeV. The phenomenological model calculation is based upon the pp $\rightarrow$ dπ^+ amplitudes and the cross sections are comparable to those obtained in previous calculations which used the pp $\rightarrow$ dπ^+ cross sections as input. The analyzing powers predicted by this model were found to be consistent with the data only in the forward angle region. In contrast, the microscopic calculation (ORCHID) predicts the wrong sign for the analyzing powers in the forward angle region but does indicate the general trend of the back angle data. The microscopic calculation was only performed for the ^{3}He($\vec{p}$,π^+)^{4}He reaction up to T_p = 325 MeV and further calculations for the other energies and the ^{4}He($\vec{p}$,π^+)^{5}He reaction would be very interesting.

Research in (p,π^+) has come a long way since the pioneering experiments at Uppsala over 20 years ago and the quality of the data presented in this thesis is certainly an indication of the progress that has been made. While the A(p,π^+)A+1 reaction analyzing power has proven to be an observable which is both theoretically interesting and difficult to understand, further experiments examining other spin observables of the A(p,π^+)A+1 reaction, for example

$$^3\vec{\mathrm{He}}(\vec{p},\pi^+)^4\mathrm{He}$$

$$^4\mathrm{He}(\vec{p},\pi^+)^5\vec{\mathrm{He}}$$

would certainly assist in the determination of the role of the underlying mechanisms. As well, experiments which look at possible three body final

states would also be of significant interest, for example the

$$^{3}\mathrm{He}(\mathrm{p},\pi^{+}\mathrm{n})^{3}\mathrm{He}$$

$$^{3}\mathrm{He}(\mathrm{p},\pi^{+}\mathrm{d})^{2}\mathrm{H}$$

reactions. Such programs of study are proposed for the DASS/SASP and MRS spectrometers at TRIUMF [Wal91].

The significant progress of the experiments has indeed been excellent and indicates exciting new possibilities. It is however most important that theoretical investigations at least attempt to keep pace with experiment. Calculations such as the pp $\rightarrow$ dπ^{+} Impulse model form an integral part of the study of pion production in nuclei. In light of the difficulties of a microscopic calculation such phenomenological models provide a foothold for our understanding of the (p,π^{+}) reaction mechanism. Still, more theoretical guidance is strongly encouraged to bring an understanding of these reactions to realization.

Bibliography

[Abe+85] R. Abegg, W.P. Alford, D. Frekers, K. Hicks, R. Schubank, P. Walden and S. Yen, TRIUMF Internal Report *New IBP Polarimeter Calibration Interim Report* (1985).

[Agu+90] M. Aguilar-Benitez *et al.*, *Review of Particle Properties*, Phys. Lett. **B239** (1990).

[ASS62] Yu.K. Akimov, O.V. Savchenko, and L.M. Soroko, JETP **14**, 512 (1962).

[Ala+77] B.S. Aladashvili, J.F. Germond, V.V. Glagolev, M.S. Nioradze, T. Siemiarczuk, J. Stepaniak, V.V. Streltsov, C. Wilkin and P. Zieliński, J. Phys. G: Nucl.Phys. **3** 7 (1977).

[AF76] J.A. Alexander and H.W. Fearing, *Meson Nuclear Conference-1976 Carnegie-Mellon*, AIP Conf. Proc. No. 33, edited by P.D. Barnes, R.A. Eisenstein and L.S. Kisslinger, AIP, New York, p.468 (1976).

[Alo+88] P.W.F. Alons, R.D. Bent, J.S. Conte, and M. Dillig, Nucl. Phys. **A480**, 413 (1988).

[ABD89] P.W.F. Alons, R.D. Bent and M. Dillig, Nucl. Phys. **A493**, 509 (1989).

[Ama+78] J.F. Amann, P.D. Barnes, K.G.R. Doss, S.A. Dytman, R.A. Eisenstein, J.D. Sherman and W.R. Wharton, Phys. Rev. Lett. **40**, 758 (1978).

[And+81] R.E. Anderson, B. Höistad, R.L. Boudrie, E.W. Hoffman, R.J. Macek, C.L. Morris, H.A. Thiessen, G.R. Smith and J. Källne, Phys. Rev. C **23**, 2616 (1981).

[Ani+86] K.A. Aniol, A. Altman, R.R. Johnson, H.W. Roser, R. Tacik, U. Wienands, D. Ashery, J. Alster, M.A. Moinster, E. Piasetzky, D.R. Gill and J. Vincent, Phys. Rev. C **33**, 1714 (1986).

[AR89] R.A. Arndt and D. Roper, VPI and SU Scattering Analysis Interactive Dial-In Program and Data Base, (1989).

[Asl76] E. Aslanides, *Meson Nuclear Physics Conference-1976 Carnegie-Mellon*, AIP Conf. Proc. No. 33, edited by P.D. Barnes, R.A. Eisenstein and L.S. Kisslinger, AIP, New York, p.204 (1976).

[Aul+78] E.G. Auld, A. Haynes, R.R. Johnson, G. Jones, T. Masterson, E.L. Mathie, D. Ottewell, P. Walden and B. Tatischeff, Phys. Rev. Lett. **41**, 462 (1978).

[Bac+85] G. Backenstoss, M. Izycki, P. Salvisberg, M. Steinacher, P. Weber, H.J. Weyer, S. Cierjacks, S. Ljungfelt, H. Ullrich, M. Furić and T. Petković, Phys. Rev. Lett **55**, 2782 (1985).

[Bal+91] M.J. Balbes, G. Feldman, L.H. Kramer, H.R. Weller and D.R. Tilley, Phys. Rev. C **43**, 343 (1991).

[Bar73] G.W. Barry, Phys. Rev. D **7**, 1141 (1973).

[BH71] *Proceedings of the 3rd International Symposium on Polarization Phenomena in Nuclear Reactions, Madison , Wisconsin, 1970*, edited by H.H. Barschall and W. Haeberli, University of Wisconsin Press, Madison, (1971).

[BAD90a] R.D. Bent, P.W.F. Alons and M. Dillig, Nucl. Phys. **A511**, 541 (1990).

[BAD90b] R.D. Bent, P.W.F. Alons and M. Dillig, *IUCF Scientific and Technical Report*, 56 (1990).

[BAS88] D.V. Bugg, A. Hasan and R.L. Shypit, Nucl Phys. **A477**, 546 (1988).

[Ben91] R.D. Bent, IUCF, private communication (1991).

[Ben82] *Pion Production and Absorption in Nuclei-1981 (Indiana University Cyclotron Facility)*, Proceedings of the Conference on Pion Production and Absorption in Nuclei, AIP Conf. Proc. No. 79, edited by R.D. Bent, AIP, New York, (1982).

[Beu+74] Data from experiment of R. Beurtey *et al.*, Saclay, from private communication with W.T.H. van Oers, University of Manitoba (1974).

[BF77] J.E. Bond and F.W.K. Firk, Nucl Phys. **A287**, 317 (1977).

[Blu54] S.A. Bludman, Phys. Rev. **94**, 1722 (1954).

[BMS82] P.F. Bosman, M. McDonald and P.W. Schmor, *Ninth International Conference on cyclotrons and their applications*, September 7-10th, 1981, Caen, edited by G. Gendreau, Les Ulis, France: Editions de physique, p. 225, (1982).

[Bou+81] A. Boudard, Y. Terrien, R. Beurtey, L. Bimbot, G. Bruge, A. Chaumeaux, P. Couvert, J.M. Fontaine, M. Garçon, Y. LeBornec, D. Legrand, L. Schecter, J.P. Tabet and M.Dillig, Phys. Rev. Lett. **46**, 218 (1981).

[Bro+77] K.L. Brown, F. Rothacker, D.C. Carey, and Ch. Iselin, *Transport, A Computer Program for Designing Charged Particle Beam Systems*, SLAC-91, (1977).

[Bug84] D.V. Bugg, J. Phys. G: Nucl.Phys. **10**, 717 (1984).

[Bug85] D.V. Bugg, Nucl Phys. **A437**, 534 (1985).

[Cam+81] J.M. Cameron, L.G. Greeniaus, D.A. Hutcheon, C.A. Miller, G.A. Moss, R.P. Liljestrand, H. Wilson, R. Abegg, W.T.H. van Oers, A.W. Stetz, M.P. Epstein and D.J. Margaziotis, Phys. Lett. **103B**, 317 (1981).

[Cam+87] J.M. Cameron, P. Kitching, J. Pasos, J. Thekkumthala, R. Abegg, D.A. Hutcheon, C.A. Miller, S.A. Elbakr and A.H. Hussein, Nucl Phys. **A472**, 718 (1987).

[Cao+87] Z-J. Cao, T.E. Ward, R.D. Bent, J.D. Brown, E. Korkmaz, H. Nann and T.G. Throwe, Phys. Rev. C **35**, 825 (1987).

[CES77] M.K. Craddock, K.L. Erdman and J.T. Sample, Nature **270**, 671 (1977).

[Cou83] P. Couvert, *Proceedings of the Workshop on Studying Nuclei with Medium Energy Protons*, Edmonton, Alberta, CANADA, 1983, edited by J.M. Greben, TRIUMF Proc. TRI-83-3, 287 (1983).

[Coy66] B. Coyler, *Cryogenic Properties of Helium-3 and Helium-4*, Central Engineering Group, Rutherford High Energy Laboratory, Chilton Didcot Berkshire (1966).

[CM86] E.D. Cooper and A. Matsuyama, Nucl. Phys. **A460**, 699 (1986).

[Cra+80] J.F. Crawford, M. Daum, G.H. Eaton, R. Frosch, H. Hirschmann, R. Horisberger, J.W. McCulloch, E. Steiner, R. Hausammann, R. Hess and D. Werren, Phys. Rev. C **22**, 1184 (1980).

[CS82] E.D. Cooper and H.S. Sherif, Phys. Rev. C **25**, 3024 (1982).

[Dah+73a] S. Dahlgren, P. Grafström, B. Höistad and A. Åsberg, Nucl. Phys. **A204**, 53 (1973).

[Dah+73b] S. Dahlgren, P. Grafström, B. Höistad and A. Åsberg, Nucl. Phys. **A211**, 243 (1973).

[Dah+73c] S. Dahlgren, P. Grafström, B. Höistad and A. Åsberg, Phys. Lett. **47B** 439 (1973).

[Deb+85] B. Debebe, C.F. Perdrisat, V. Raghunathan, J.M. Cameron, I.J. van Heerden, P. Kitching, R. MacDonald, W.J. MacDonald, W.C. Olsen, J. Soukup, H.S. Wilson, H.W. Fearing and C.A. Miller, Phys. Rev. C **31**, 1841 (1985).

[DHG71] S. Dahlgren, B. Höistad and P. Grafström, Phys. Lett. **35B** 219 (1971).

[DH77] M. Dillig and M.G. Huber, Phys. Lett. **69B**, 429 (1977).

[DiG+85] N.J. DiGiacomo, M.R. Clover, R.M. DeVries, J.C. Dousse, J.S. Kapustinsky, P.L. McGaughey, W.E. Sondheim, J.W. Sunier, M. Buenerd and D. Lebrun, Phys. Rev. C **31**, 292 (1985).

[Dil+80] M. Dillig, P. Couvert, Th.S. Bauer, R. Beurtey, A. Boudard, G. Bruge, H. Catz, A. Chaumeaux, H.H. Duhm, J.L. Escudie, M. Garcon, D. Garreta, G.J. Igo, J.C. Lugol, M. Matoba, L. Schecter, J.P. Tabet, Y. Terrien, E. Aslanides, R. Bertini, O. Bing, F. Brochard, F. Hibou, P. Gorodetzky, L. Bimbot, I.Brissaud, Y. LeBornec ad B. Tatischeff, Nucl. Phys. **A333**, 477 (1980).

[DKS87] J. Dubach, W.M. Kloet and R.R. Silbar, Nucl. Phys. **A466**, 573 (1987).

[Dom+70] J.J. Domingo, B.W. Allardyce, C.H.Q. Ingram, S. Rohlin, N.W. Tanner, J. Rohlin, E.M. Rimmer, G. Jones, and J.P. Girardeau-Montaut, Phys. Lett. **32B** 309 (1970).

[Doo91] J. Doornbos, TRIUMF, private communication (1991).

[EW88] T.E.O. Ericson and W. Weise, *Pions and Nuclei*, Oxford University Press, Oxford, England, (1988).

[Fal+85] W.R. Falk, E.G. Auld, G. Giles, G. Jones, G.J. Lolos, W. Ziegler and P.L. Walden, Phys. Rev. C **32**, 1972 (1985).

[Fal+86] W.R. Falk, E.G. Auld, G. Giles, G. Jones, G.J. Lolos, W. Ziegler,and P.L. Walden, Phys. Rev. C **33**, 988 (1986).

[Fal91] W.R. Falk, University of Manitoba, private communication (1991).

[Fea74] H.W. Fearing, Phys. Lett. **52B**, 407 (1974).

[Fea75a] H.W. Fearing, Phys. Rev. C **11**, 1210 (1975).

[Fea75b] H.W. Fearing, Phys. Rev. C **11**, 1493 (1975).

[Fea77] H.W. Fearing, Phys. Rev. C **16**, 313 (1977).

[Fea81] H.W. Fearing, Prog. Particle and Nuc Phys., **7**, 113 (1981).

[Fea91] H.W. Fearing, TRIUMF, private communication (1991).

[Fra+77] R. Frascaria, I. Brissaud, N. Marty, M. Morlet, F. Reide, A. Willis, R. Beurtey, A. Boudard, M. Garcon, G.A. Moss, Y. Terrien and W.T.H. van Oers, Phys. Lett. **66B**, 329 (1977).

[Fre88] D. Frekers, LISA program (1988).

[Fur+91] K.M. Furutani, W.R. Falk, F.A. Duncan, P.L. Walden, S. Yen, G.M. Huber, R.D. Bent, G.J. Lolos and E. Korkmaz, Phys. Rev. C 44, 1691 (1991).

[Gab+72] K. Gabathuler, J. Rohlin, J.J. Domingo, C.H.Q. Ingram, S. Rohlin, and N.W. Tanner, Nucl Phys. **B40**, 32 (1972).

[GH77] W.R. Gibbs and A.T. Hess, Phys. Lett. **68B**, 205 (1977).

[Gil85] G.L. Giles, Ph. D. thesis, University of British Columbia (1984).

[Gil64] J. Gillespie, *Final-State Interactions*, Holden-Day, Inc. San Francisco, USA (1964).

[Gre87] L.G. Greeniaus *TRIUMF Kinematics Handbook - 2nd Edition*, TRIUMF, Vancouver (1987).

[GW54] M. Gell-Mann and K.M. Watson, Ann. Rev. Nucl. Sci. 4, 219 (1954).

[GW84] J.F. Germond and C. Wilkin, J. Phys. G: Nucl.Phys. **10** 745 (1984).

[GW85] J.F. Germond and C. Wilkin, J. Phys. G: Nucl.Phys. **11** 1131 (1985).

[Hag63] R. Hagedorn, *Relativistic Kinematics*, W.A. Benjamin Inc., New York (1963).

[Has+81] D.K. Hasell, R. Abegg, B.T. Murdoch, W.T.H. van Oers, H. Postma, and J. Soukup, Nucl. Instr. Meth. **189**, 341 (1981).

[Has84] D.K. Hasell, Ph. D. thesis, University of Manitoba, (1984).

[Has+86] D.K. Hasell, A. Bracco, H.P. Gubler, W.P. Lee, W.T.H. van Oers, R. Abegg, D.A. Hutcheon, C.A. Miller, J.M. Cameron, L.G. Greeniaus, G.A. Moss, M.P. Epstein and D.J. Margaziotis, Phys. Rev. C **34**, 236 (1986).

[Hic88] K.H. Hicks, TRIUMF Internal Report *Medium Resolution Spectrometer Manual*, (1988).

[Hir78] M. Hirata, Phys. Rev. Lett., **40**, 704 (1978).

[Hir+83] M. Hirata, K. Masutani, A. Matsuyama and K. Yazaki, Phys. Lett., **128B**, 15 (1983).

[Hoi79] B. Höistad, Adv. Nucl. Phys., **11**, 135 (1979).

[Hoi+84] B. Höistad, M. Gazzaly, B. Aas, G. Igo, A. Rahbar, C. Whitten, G.S. Adams and R. Whitney, Phys. Rev. C **29**, 553 (1984).

[Hof+83] J. Hofteizer *et al*, Nucl. Phys. **A402** 429 (1983).

[Hof+84] J. Hofteizer *et al*, Nucl. Phys. **A412** 286 (1984).

[HRT58] E. Heer, A. Roberts and J. Tinlot, Phys. Rev. **111**, 640 (1958).

[Hub+87a] G.M. Huber, G.J. Lolos, E.L. Mathie, Z. Papandreou, K.H. Hicks, P.L. Walden, S. Yen, X. Aslanoglou, E.G. Auld, and W.R. Falk, Phys. Rev. C **36**, 1058 (1987).

[Hub+87b] G.M. Huber, G.J. Lolos, Z. Papandreou, K.H. Hicks, P.L. Walden, S. Yen, E.G. Auld, F.A. Duncan, R.D. Bent and W.R. Falk, Phys. Rev. C **36**, 2683 (1987).

[Hub+88] G.M. Huber, G.J. Lolos, K.M. Furutani, W.R. Falk, R.D. Bent, K.H. Hicks, P.L. Walden and S. Yen, Phys. Rev. C **38**, 1304 (1988).

[Hub88] G.M. Huber, Ph. D. thesis, University of Regina, (1988).

[Hum86] S. Humphries, Jr., *Principles of Charged Particle Acceleration*, John Wiley & Sons, New York, (1986).

[HWY84] N. Hiroshige, W. Watari and M. Yonezawa, Prog. Theo. Physics, **72**, 1146 (1984).

[Ing+71] C.H.Q. Ingram, N.W. Tanner, J.J. Domingo and J. Rohlin, Nucl. Phys. **B31**, 331 (1971).

[IW85] M.J. Iqbal and G.E. Walker, Phys. Rev. C **32**, 557 (1985).

[Jac+80] W.W. Jacobs, A.G. Drentje, P.H. Pile, P.P. Singh, T.P. Sjoreen and S.E. Vigdor, Phys. Lett. **94B**, 319 (1980).

[Jon79] G. Jones, in *Meson Nuclear Physics Conference-1979 Houston*, AIP Conf. Proc. No. 54, edited by E.V. Hungerford III, AIP, New York, p.116 (1976).

[JS83a] M.B. Johnson and E.R. Siciliano, Phys. Rev. C **27**, 730 (1983).

[JS83b] M.B. Johnson and E.R. Siciliano, Phys. Rev. C **27**, 1647 (1983).

[Kal+78] J. Källne, H.A. Thiessen, C.L. Morris, S.L. Verbeck, G.R. Burleson, M.J. Devereaux, J.S. McCarthy, J.E. Bolger, C.F. Moore and C.A. Goulding, Phys. Rev. Lett **40**, 378 (1978).

[Kal+81] J. Källne, J.E. Bolger, M.J. Devereaux, and S.L. Verbeck, Phys. Rev. C **24**, 1102 (1981).

[Kal+83] J. Källne, R.C. Minehart, R.R. Whitney, R.L. Boudrie, J.B. McClelland and A.W. Stetz, Phys. Rev. C **28**, 304 (1983).

[Keh83] J.J. Kehayias, Ph. D. thesis, Indiana University, (1983).

[Keh+86] J.J. Kehayias, R.D. Bent, M.C. Green, M.A. Pickar, and R.E. Pollock, Phys. Rev. C **33**, 725 (1986).

[Kei89] R. Keitel, *TICS Language Reference Manual v.3.4*, TRIUMF document, (1989).

[Kle+77] R. Klem, G. Igo, R. Talaga, A. Wriekat, H. Courant, K. Einsweiler, T. Joyce, H. Kagan, Y. Makdisi, M. Marshak, B. Mossberg, E. Peterson, K. Ruddock and T. Walsh, Phys. Rev. Lett **38**, 1272 (1977) and R. Klem, G. Igo, R. Talaga, A. Wriekat, H. Courant, K. Einsweiler, T. Joyce, H. Kagan, Y. Makdisi, M. Marshak, B. Mossberg, E. Peterson, K. Ruddock and T. Walsh, Phys. Lett **70B**, 155 (1977).

[KK84] B.D. Keister and L.S. Kisslinger, Nucl. Phys. **A412**, 301 (1984).

[Kor87] E.J. Korkmaz, Ph. D. thesis, Indiana University, (1987).

[Kor+87] E. Korkmaz, L.C. Bland, W.W. Jacobs, T.G. Throwe, S.E. Vigdor, M.C. Green, P.L. Jolivette, and J.D. Brown, Phys. Rev. Lett. **58**, 104 (1987).

[Kor+89] E. Korkmaz, S.E. Vigdor, W.W. Jacobs, T.G. Throwe, L.C. Bland, M.C. Green, P.L. Jolivette, and J.D. Brown,Phys. Rev. C **40**, 813 (1989).

[Kos88] C.J. Kost, INTRAN *A User Friendly Interface to Transport*, TRIUMF Computing Document, (1988).

[KR89] C.J. Kost and P. Reeve, REVMOC *A Monte Carlo Beam Tranport Program*, TRIUMF Computing Document, TRI-DN-82-28, (1989).

[Kra+82] V.A. Krasnov, A.B. Kurepin, A.I. Reshetin, K.O. Oganesjan and E.A. Pasyul, Phys. Lett. **108B** 11 (1982).

[KS78] *Proceedings of the Higher Energy Polarized Proton Beams-1977, Ann Arbor, Michigan*, AIP Conf. Proc. No. 42, edited by A.D. Krisch and A.J. Salthouse, AIP, New York, (1978).

[Kur87] D. Kurath, Phys. Rev. C **35**, 2247 (1987).

[KWY80] H. Kamo, W. Watari and M. Yonezawa, Prog. Theo. Physics, **64**, 2144 (1980).

[Lat+47] C.M.G. Lattes, M. Muirhead, C.F. Powell and G.P. Occhialini, Nature **159**, 694 (1947).

[LeB+85] Y. LeBornec, L. Bimbot, M.P. Combes-Comets, J.C. Jourdain, F. Reide, A. Willis and N. Willis, J. Phys. G: Nucl. Phys. **11** 1125 (1985).

[Lol+82] G.J. Lolos, E.L. Mathie, G. Jones, E.G. Auld, G. Giles, B.J. McParland, P.L. Walden, W. Zeigler and W.R. Falk, Nucl. Phys. **A386**, 477 (1982).

[Lol+84] G.J. Lolos, E.G. Auld, G. Giles, G. Jones, B.J. McParland, W. Zeigler, D. Ottewell and P.L. Walden, Nucl. Phys. **A422**, 582 (1984).

[Mac89] R. Machleidt, Adv. Nuc. Phys., **19**, 189 (1989).

[Mat+83] E.L. Mathie *et al*, Nucl. Phys. **A397** 469 (1983).

[May+85] B. Mayer *et al*, Nucl. Phys. **A437** 630 (1985).

[Mil83] C.A. Miller, *Proceedings of the Workshop on Studying Nuclei with Medium Energy Protons*, Edmonton, Alberta, CANADA, 1983, edited by J.M. Greben, TRIUMF Proc. TRI-83-3, 339 (1983).

[MM79] D.F. Measday and G.A. Miller, Ann. Rev. Nucl. Sci. **29**, 121 (1979).

[Mos+80] G.A. Moss, L.G. Greeniaus, J.M. Cameron, D.A. Hutcheon, R.L. Liljestrand, C.A. Miller, G. Roy, B.K.S. Koene, W.T.H. van Oers, A.W. Stetz, A. Willis and N. Willis, Phys. Rev. C **21**, 1932 (1980).

[Nob76] J.V. Noble, *Meson Nuclear Physics Conference-1976 Carnegie-Mellon*, AIP Conf. Proc. No. 33, edited by P.D. Barnes, R.A. Eisenstein and L.S. Kisslinger, AIP, New York, p.221 (1976).

[Orp+81] L. Orphanos, J. Källne, R. Altemus, P.C. Gugelot, J.S. McCarthy, R.C. Minehart, P.A.M. Gram, B. Höistad, C.L. Morris, E.A. Wadlinger and C. Perdrisat, Phys. Rev. Lett **46**, 1562 (1981).

[Orp+82] L. Orphanos, J.S. McCarthy, R.C. Minehart, P.A.M. Gram, B. Höistad, C. Perdrisat and J. Källne, Phys. Rev. C **26**, 2111 (1982).

[Rud52] M. Ruderman, Phys. Rev. **87**, 383 (1952).

[Sah+83] A. Saha *et al*, Phys. Rev. Lett. **51** 759 (1983).

[Sak+85] K. Sakamoto, M. Hirata, A. Matsuyama and K. Yazaki, Phys. Rev. C **31**, 1987 (1985).

[Sic+86] E.R. Siciliano, M.D. Cooper, M.B. Johnson and M.J. Leitch, Phys. Rev. C **34**, 267 (1986).

[Sjo+81] T.P. Sjoreen, P.H. Pile, R.E. Pollock, W.W. Jacobs, H.O. Meyer, R.D. Bent, M.C. Green and F. Soga, Phys. Rev. C **24**, 1135 (1981).

[Ste+77] A.W. Stetz, J.M. Cameron, D.A. Hutcheon, C.A. Miller, G.A. Moss, G. Roy, J.G. Rogers, C.A. Goulding and W.T.H. van Oers, Nucl. Phys. **A290**, 285 (1977).

[Tat+76] B. Tatischeff, L. Bimbot, R. Frascaria, Y. LeBornec, M. Morlet, N. Willis, R. Beurtey, G. Bruge, P. Couvert, D. Garreta, D. Legrand, G.A. Moss and Y. Terrien, Phys. Lett. **63B** 158 (1976).

[Thr84] T.G. Throwe, Ph. D. thesis, Indiana University, (1984).

[Tsa79] M.C. Tsangarides, Ph. D. thesis, Indiana University, (1979).

[VA82] B.J. VerWest and R.A. Arndt, Phys. Rev. C **25**, 1979 (1982).

[Vet+90] M. Vetterli *et al*, Calibration of the BL4B SEM, TRIUMF Internal Report, July (1990).

[Wal91] P.L. Walden, TRIUMF, private communication (1991).

[Wat52] K.M. Watson, Phys. Rev. **88**, 1163 (1952).

[Wic+85] K. Wick, U. Berghaus, H. Brückmann, P. Lara, W. Schütte, B. Anders and Y. Koike, Nucl. Phys. **A444**, 49 (1985).

[Wil+81] N. Willis, L. Bimbot, N. Koori, Y. LeBornec, F. Reide, A. Willis and C. Wilkin, J. Phys. G: Nucl.Phys. **7** L195 (1981).

[Wol68] G.F. Wolters, *Final State Interactions* in Kinematics and Multiparticle Systems edited by M. Nikolić for the Proceedings of the International School of Elementary Particle Physics, Gordon and Breach Science Publishers Ltd., New York, p267-313 (1968).

[Yen91] S. Yen, Nucl. Instr. Meth. **A302**, 493 (1991).

[Yuk35] H. Yukawa, Proceeding of the Phys. Math. Soc. of Japan, **17**, 48 (1935).

Appendix A

Data Acquisition Routine.

```
PROGRAM MRS_POLARIZED.TWO
! Twotran program for MRS polarized beam singles experiments.
! Adapted from MRS_NP.TWO by S. Yen, September 19, 1988
! with the addition of 2 extra scaler reads in the RSCAL subroutine.
!
!************************************************************
!
ON(%BEGINRUN,%TYPE=101,%MAXSIZE=0) CALL RSTART
ON(%PAUSE,%TYPE=102,%MAXSIZE=400) CALL RPAUSE
ON(%CONTINUE,%TYPE=103,%MAXSIZE=0) CALL RCONTIN
ON(%B=7,%GLAM=15,%TYPE=2,%MAXSIZE=350) CALL RLAM
ON(%PERIOD=50,%TYPE=1,%MAXSIZE=400) CALL RSCAL
ON(%ENDRUN, %TYPE=104,%MAXSIZE=400) CALL REND
END
!
!************************************************************
!
SUBROUTINE RSTART
! Subroutine to handle START of run
INTEGER*4 MASK /16384/
INTEGER*4 L60 /48/
INTEGER*4 L14 /12/
INTEGER*4 L40000 /16384/
INTEGER*4 L42000 /17408/
! Raise Inhibit (just for safety)
CSSA(%B=7,%C=3,%N=30,%A=9,%F=26) ! CLOSE crate 3
CSSA(%B=7,%C=2,%N=30,%A=9,%F=26) ! CLOSE crate 2
! Clear scalers
CSSA(%B=7,%C=2,%N=10,%A=0,%F=9) ! clear IBP scalers
CSSA(%B=7,%C=2,%N=9,%A=0,%F=9)
CSSA(%B=7,%C=2,%N=8,%A=0,%F=9)
CSSA(%B=7,%C=3,%N=4,%A=0,%F=9) ! clear Hex scalers
CSSA(%B=7,%C=3,%N=30,%A=10,%F=26) ! enable Crate Control demand
! Enable Demand in crate controller
CSSA(%B=7,%C=3,%N=28,%A=9,%F=26)
! write to LAM grader
CFSA (%B=7,%C=3,%N=28,%A=13,%F=17, %DATA=MASK)
! Initialize TDC, ADC; enable TDC LAM
CSSA (%B=7,%C=3,%N=15,%A=0,%F=9) ! clear TDC's
CSSA (%B=7,%C=3,%N=15,%A=0,%F=26) ! set LAM at TDC
CSSA (%B=7,%C=3,%N=19,%A=0,%F=9) ! clear 12 ADC's
CSSA (%B=7,%C=3,%N=17,%A=0,%F=9) ! clear ADC's for S1 and S2
```

```
CSSA (%B=7,%C=3,%N=16,%A=0,%F=9) ! clear additional ADC's
! Initialize and set up LeCroy 4290 system
CSSA (%B=7,%C=3,%N=22,%A=0,%F=9)
CFSA (%B=7,%C=3,%N=22,%A=0,%F=16,%DATA=L40000)
CFSA (%B=7,%C=3,%N=22,%A=0,%F=16,%DATA=L42000)
! Send clear pulse on output register
CFSA (%B=7,%C=3,%N=21,%A=0,%F=20,%DATA=L60)
CFSA (%B=7,%C=3,%N=21,%A=0,%F=22,%DATA=L60)
! Remove Inhibit from crates 3,2
CSSA(%B=7,%C=3,%N=30,%A=9,%F=24) ! OPEN crate 3
CSSA(%B=7,%C=2,%N=30,%A=9,%F=24) ! OPEN crate 2
! Send no inhibit on output register
CFSA (%B=7,%C=3,%N=21,%A=0,%F=22,%DATA=L14)
RETURN
END
!
!*************************************************************
!
SUBROUTINE RPAUSE
! Subroutine to handle PAUSE in run
! Inhibit crates 3,2
CSSA(%B=7,%C=3,%N=30,%A=9,%F=26)
CSSA(%B=7,%C=2,%N=30,%A=9,%F=26)
! read scalers
CALL RSCAL
FLUSH
RETURN
END
!
!*************************************************************
!
SUBROUTINE RCONTIN
! Subroutine to handle CONTINUE of run.
INTEGER*4 L60 /48/
! Clear TDC, ADC, 4290 system
CSSA(%B=7,%C=3,%N=15,%A=0,%F=9) ! TDC'S
CSSA(%B=7,%C=3,%N=19,%A=0,%F=9) ! ADC'S
CSSA(%B=7,%C=3,%N=22,%A=0,%F=9) ! 4290 DRIFT CHAMBER
CSSA(%B=7,%C=3,%N=16,%A=0,%F=9) ! ADDITIONAL ADC'S
CSSA(%B=7,%C=3,%N=17,%A=0,%F=9) ! S1, S2 ADC'S
! Send clear pulse on output register
CFSA (%B=7,%C=3,%N=21,%A=0,%F=22,%DATA=L60)
! Remove Inhibit from crates 3,2
CSSA (%B=7,%C=3,%N=30,%A=9,%F=24)
CSSA (%B=7,%C=2,%N=30,%A=9,%F=24)
! Send no inhibit on output register
CFSA (%B=7,%C=3,%N=21,%A=0,%F=22,%DATA=L14)
RETURN
END
!
!*************************************************************
!
SUBROUTINE RSCAL
! Subroutine for scaler events.
INTEGER*4 I17440 /7968/
!       Flags to keep track of whether there are things other
!       than scaler events happening.
!       SCALF is set .FALSE. by scalers, .TRUE. by LAM events.
!       If it is .FALSE. on entry to scaler events (indicating two
!       successive scaler events), the buffer is flushed.
!       This forces updating of scaler page.
LOGICAL SCALF
LOGICAL OLDSCF
COMMON /CEV12/ SCALF
```

```
!
OLDSCF = SCALF
SCALF = .FALSE.
! Set up scalers read
CFSA(%B=7,%C=3,%N=14,%A=0,%F=16,%DATA=I17440)
! Read C=3 scalers (BLOCK READ)
CFQIGNORE(%B=7,%C=3,%N=14,%A=0,%F=2,%R=32) ! read 32 scalers
! Now read scalers
CFSCAN(%B=7,%C=2,%N=8,%A=0,%F=0,%R=12) ! read 12 IBP scalers (UP)
CFSCAN(%B=7,%C=2,%N=9,%A=0,%F=0,%R=12) ! read 12 IBP scalers (DOWN)
CFSCAN(%B=7,%C=2,%N=10,%A=0,%F=0,%R=12) ! read 12 IBP scalers (OFF)
IF (OLDSCF) GOTO 10
FLUSH
10 RETURN
END
!
!************************************************************
!
SUBROUTINE RLAM
! Subroutine to handle LAM's.
INTEGER*4 L60 /48/
INTEGER*4 L6060 /3120/
INTEGER*4 L200 /128/
LOGICAL SCALF
COMMON /CEV12/ SCALF
SCALF = .TRUE.
! Response to LAM from TDC in slot 15
! Disable 4299 clear
CFSA (%B=7,%C=3,%N=21,%A=0,%F=22,%DATA=L200)
! Read DCR (24 bits)
CFSA(%B=7,%C=3,%N=18,%A=0,%F=2)
! Read TDC (TTB, TRF, TSLT, TDIP, TS1, TS2, TREC, TVET)
CSSCAN(%B=7,%C=3,%N=15,%A=0,%F=0,%R=8)
! Read ADC (ESLI, EDIP, EPD0, 1, 2, 3, 4, 5, 6, 7, 8, 9)
CSSCAN(%B=7,%C=3,%N=19,%A=0,%F=0,%R=12)
! Read ADC (ES1H, ES1L, ES2)
CSSCAN(%B=7,%C=3,%N=17,%A=0,%F=0,%R=3)
! Read additional ADC (EREC, EVET, SPARE)
CSSCAN(%B=7,%C=3,%N=16,%A=0,%F=0,%R=3)
! Clear TDC, ADC
CSSA(%B=7,%C=3,%N=15,%A=0,%F=9)
CSSA(%B=7,%C=3,%N=19,%A=0,%F=9)
CSSA(%B=7,%C=3,%N=17,%A=0,%F=9)
CSSA(%B=7,%C=3,%N=16,%A=0,%F=9)
! Send clear pulse on output register
CFSA (%B=7,%C=3,%N=21,%A=0,%F=20,%DATA=L60)
CFSA (%B=7,%C=3,%N=21,%A=0,%F=22,%DATA=L6060)
!
! Drift chamber readout via 4299
CSQSTOP(%B=7,%C=3,%N=22,%A=1,%F=2,%R=110)
!
! enable O/P REG 4299 clear, and clear it
CFSA (%B=7,%C=3,%N=21,%A=0,%F=20,%DATA=L200)
CSSA (%B=7,%C=3,%N=22,%A=0,%F=11)
RETURN
END
!
!************************************************************
!
SUBROUTINE REND
! Subroutine to handle END of run.
INTEGER*4 LCH1 /2/
! Disable LAM and Inhibit crates 3,2
CSSA(%B=7,%C=3,%N=15,%A=0,%F=24) ! disable LAM at TDC
```

```
CSSA(%B=7,%C=3,%N=30,%A=9,%F=26)
CSSA(%B=7,%C=2,%N=30,%A=9,%F=26)
! Read last scaler values
CALL RSCAL
! Clear TDC, ADC, 4290 system
CSSA(%B=7,%C=3,%N=15,%A=0,%F=9)
CSSA(%B=7,%C=3,%N=19,%A=0,%F=9)
CSSA(%B=7,%C=3,%N=22,%A=0,%F=9)
CSSA(%B=7,%C=3,%N=16,%A=0,%F=9)
CSSA(%B=7,%C=3,%N=17,%A=0,%F=9)
RETURN
END
```

Appendix B

Event Reconstruction Subroutine.

```
      SUBROUTINE INSERT (*)
C-------------------------------------------------------------------------
C                              PREAMBLE
C-------------------------------------------------------------------------
C
C     FILE INSERT_413.FOR
C
C-------------------------------------------------------------------------
C
C     Keith Furutani,          April 18, 1990
C
C                  Offline analysis routine for E413 3He(p,pi+)
C
C     E413 is a single arm MRS polarized beam experiment. The DATA is
C     acquired on the MRSVAX through a STARBURST preprocessor using
C     TWOTRAN as the definition of the datastream. The data is in
C     8032 byte records and was written using VDACS type Data Acquisition.
C     The experiment was run on October, 1988 at TRIUMF, Canada.
C
C-------------------------------------------------------------------------
C
C-------------------------------------------------------------------------
C              INCLUDE NECESSARY LISA COMMON BLOCKS
C-------------------------------------------------------------------------
C
      INCLUDE 'LISA$DIR:EVTCOM'
      INCLUDE 'LISA$DIR:DACCOM'
C
C-------------------------------------------------------------------------
C                          DEFINE CONSTANTS
C-------------------------------------------------------------------------
C
      PARAMETER (IVS = 34 )
      PARAMETER (VDCDIST= 5472.)
      PARAMETER (X1c0 = 5472.)
      PARAMETER (XUSEP = 525.)
      LOGICAL GOOD
C
```

```
C-------------------------------------------------------------------------
C                MAKE EQUIVALENCE TO KBUF INPUT COORDINATES
C-------------------------------------------------------------------------
C
      EQUIVALENCE ( KBUF(1) , KDCR) ,( KBUF(4) , KTTB)
      EQUIVALENCE ( KBUF(5) , KTRF) ,( KBUF(9) , KTS2)
      EQUIVALENCE ( KBUF(28) , KES2)
      EQUIVALENCE ( KBUF(IVS) , KU1) ,( KBUF(IVS + 1), KX2)
      EQUIVALENCE ( KBUF(IVS + 2), KU2) ,( KBUF(IVS + 3), KX1)
      EQUIVALENCE ( KBUF(IVS + 4), KX0) ,( KBUF(IVS + 5), KY0)
C
C-------------------------------------------------------------------------
C                MAKE EQUIVALENCE TO KBUF OUTPUT COORDINATES
C-------------------------------------------------------------------------
C
      EQUIVALENCE ( KBUF(45) , KY1) ,( KBUF(46) , KY2)
      EQUIVALENCE ( KBUF(50) , KESUM)
      EQUIVALENCE ( KBUF(60) , KTHETA),( KBUF(61) , KTHETAPC)
      EQUIVALENCE ( KBUF(63) , KPHI) ,( KBUF(64) , KPHID)
      EQUIVALENCE ( KBUF(70) , KXDIFF),( KBUF(71) , KUDIFF)
      EQUIVALENCE ( KBUF(80) , KXI) ,( KBUF(85) , KYI)
      EQUIVALENCE ( KBUF(81) , KXID) ,( KBUF(86) , KYID)
      EQUIVALENCE ( KBUF(90) , KXF) ,( KBUF(100) , KXFK)
      EQUIVALENCE ( KBUF(101) , KTTBC)
C
C-------------------------------------------------------------------------
C
      EQUIVALENCE ( KBUF(200) , KHIT) ,( KBUF(201) , KMISS)
      EQUIVALENCE ( KBUF(202) , KMULT) ,( KBUF(203) , MIMU)
C
C-------------------------------------------------------------------------
C
C                KBUF(271→275) USED FOR VDC AND FEC WIRE TDC TIMES
C
C-------------------------------------------------------------------------
C


C
C-------------------------------------------------------------------------
C                DEFINE ALL PARAMETERS NEEDED
C-------------------------------------------------------------------------
C
C                CALCULATION PARAMETERS
C
      EQUIVALENCE
     1 ( HIT_condition, PARA(1) )! Gating on GOOD chamber events
     1,( pick_wire_VDC, PARA(2) )! wire ADDR in VDC
     1,( pick_wire_FEC, PARA(3) )! wire NUMBER in FEC
     1,( CI_PLOW, PARA(4) )! scan ESUM from here
     1,( CI_PHIGH, PARA(5) )! scan ESUM to here
C
C                FIRST ORDER FOCAL PLANE PARAMETERS
C
      EQUIVALENCE
     1 ( TAN_DELTA, PARA(6) )! tangent of focal plane tilt angle delta
     1,( FOCAL_F, PARA(7) )! offset of focal plane at x=0 (try -1100)
C
C                CHAMBER AND TDC OFFSETS
C
      EQUIVALENCE
     1 ( TTB_CNTR, PARA(8) )! center for TTB
     1,( TTB_SCALE, PARA(9) )! scale for TTBC
     1,( TRF_OFFSET, PARA(10))! offset for TRF
     1,( Y_OFFSET, PARA(11))! offset for Y1, Y2 coordinates
```

```
     1,( X0_CNTR, PARA(12))! Center of X0, for calc of XI
     1,( Y0_CNTR, PARA(13))! Center of Y0, for calc of YI
     1,( Y1_CNTR, PARA(14))! Center of Y1, for calc of YI
C
CC                  TRANSPORT RECONSTRUCTION PARAMETERS
C
      EQUIVALENCE
     1 ( THETApcXF, PARA(20))! /-0.0062/ !=-.0070 FOR LAC
     1,( THETApc0, PARA(21))! /95./ 114 FOR LAC
     1,( THETAPC_OFFS, PARA(22))! offset to center THETAPC
     1,( THETA_DISP_FACT,PARA(23))! factor for boost theta display
     1,( THETA_DISP_OFFS,PARA(24))! offset to center display

     1,( PHI_OFFS, PARA(25))! offset to center PHI
     1,( PHI_DISP_FACT, PARA(26))! factor to boost PHI display
     1,( PHI_DISP_OFFS, PARA(27))! offset to center display

     1,( XDIFF_SCALE, PARA(30))! factor to scale XDIFF
     1,( XDIFF_OFFS, PARA(31))! offset to center display
     1,( UDIFF_SCALE, PARA(32))! factor to scale UDIFF
     1,( UDIFF_OFFS, PARA(33))! offset to center display
C
CC                  TARGET RECONSTRUCTION PARAMETERS
C
      EQUIVALENCE
     1 ( FACT_XIX0, PARA(40))! factor for XI that goes with X0
     1,( FACT_XITH, PARA(41))! fact. for XI goes with THETAPC
     1,( XI_OFFS, PARA(42))! offset for XI
     1,( XI_DISP_FACT, PARA(43))! factor to boost XI display
     1,( XI_DISP_OFFS, PARA(44))! offset to center display

     1,( FACT_YIY0, PARA(45))! fact. for YI that goes with Y0
     1,( FACT_YIY1, PARA(46))! factor for YI that goes with Y1
     1,( YI_OFFS, PARA(47))! offset for YI
     1,( YI_DISP_FACT, PARA(48))! factor to boost YI display
     1,( YI_DISP_OFFS, PARA(49))! offset to center display
C
CC                  FOCAL PLANE HIGHER ORDER PARAMETERS
C
      EQUIVALENCE
     1 ( FKIN, PARA(50))! kinematic correction factor
     1,( FACT_XFTHPC_SQ, PARA(51))! Aberration correction
     1,( XFTHPC_SQ_OFF, PARA(52))!
     1,( FP_DISP_FACT, PARA(53))! factor to boost Xf display
     1,( FP_DISP_OFFS, PARA(54))! offset for display of Xf
C
CC-------------------------------------------------------------------
C
CC                  PARAMETERS > 80 ARE RESERVED FOR EVENT TASK
C
CC-------------------------------------------------------------------
C
C
```

```
C
C
C-----------------------------------------------------------------------
C                          MAIN PROGRAM
C-----------------------------------------------------------------------
C
      GOOD = .TRUE.
C
C-----------------------------------------------------------------------
C     EXAMINE ONLY EVENTTYPE 2 EVENTS AND NOT PULSERS
C-----------------------------------------------------------------------
C
      IF(IEVENTTYPE.NE.2) GOOD = .FALSE.
C
      IPULSER = IAND(KDCR,4096) ! Mask on DCR word for Pulsers
      IF(IPULSER.NE.0) GOOD = .FALSE.
C
C-----------------------------------------------------------------------
C     MASKING HITPATTERN FOR MULTIPLES AND MISSING HITS
C-----------------------------------------------------------------------
C
      KHIT = HITPATTERN
      KMISS = IAND(HITPATTERN,255) ! MISSING WIRE CHAMBER.
      IMULC      = IAND(HITPATTERN,32512) ! MULTIPLE WIRE CHAMBER.
      KMULT = IMULC/256 ! SHIFT 8 RIGHT.
      MIMU = IOR(KMISS,KMULT) ! MISSING OR MULTIPLE
C
C-----------------------------------------------------------------------
C     PUTTING VDC AND FEC WIRE TDC TIMES INTO KBUF
C-----------------------------------------------------------------------
C
      IWIRE = pick_wire_VDC
      IWIREofFEC = pick_wire_FEC
C
      KBUF(271) = ITIMEofWIRE
      KBUF(272) = ITIMEofWIREplus1
      KBUF(273) = ITIMEofFECWIRE
      KBUF(274) = ITIMEofFECWIREplus1
      KBUF(275) = ITIMEofFECWIREminus1
C
C-----------------------------------------------------------------------
C     FOR A GATE ON ONLY GOOD CHAMBER EVENTS (HIT_COND = 0)
C-----------------------------------------------------------------------
C
      IHITBIT = HIT_condition + .5
      IRETURN = IAND(HITPATTERN,IHITBIT)
      IF (IRETURN.NE.0) GOOD = .FALSE. !be careful for efficiencies
C
      IF (.NOT.GOOD) THEN
      KTTB = -1000 ! Shift the values of the
      KESUM = -1000 ! coordinates out of the spectrum
      KTS2 = -1000 ! if it is a rejected event due to
      KES2 = -1000 ! PULSER or IEVENTTYPE or HIT_COND
      KTHETA = -1000
      KPHI = -1000
      KXI = -1000
      KYI = -1000
      KXF = -1000
      KXFK = -1000
      RETURN
      END IF
C
C
C
C
```

```
C
C-----------------------------------------------------------------------
C                  CALULATING ESUM FOR PADDLES
C-----------------------------------------------------------------------
C
      I_PLOW = CI_PLOW
      I_PHIGH = CI_PHIGH
      I_ESUM = KBUF(I_PLOW)
      DO I=I_PLOW+1,I_PHIGH
      IF(KBUF(I).GT.I_ESUM)I_ESUM = KBUF(I)
      ENDDO
      KESUM = I_ESUM
C
C-----------------------------------------------------------------------
C                        OFFSET FOR TTB
C-----------------------------------------------------------------------
C
      KTTBC    = TTB_SCALE*(KTTB - TTB_CNTR) + 500.5
C
C
C-----------------------------------------------------------------------
C                        OFFSET FOR TRF
C-----------------------------------------------------------------------
C
      KBUF(5) = KTRF + TRF_OFFSET
C
C-----------------------------------------------------------------------
C                        OFFSET FOR TS2
C-----------------------------------------------------------------------
C
      KBUF(9) = KTS2 + TS2_OFFSET
C
C-----------------------------------------------------------------------
C                  CALCULATE Y1 AND Y2 COORDINATES
C-----------------------------------------------------------------------
C
      X1C      = KX1 + X1c0
      DX12     = X1c - KX2
      XCORR    = XUSEP*DX12/VDCDIST
      Y1       = 1.732052*(KX1-XCORR)-2.*KU1+2829.54
      Y2       = 1.732052*(KX2-XCORR)-2.*KU2+2829.54
      KY1      = Y1 + Y_OFFSET
      KY2      = Y2 + Y_OFFSET
C

C-----------------------------------------------------------------------
C                  CALCULATE TRAJECTORY RECONTRUCTION
C-----------------------------------------------------------------------
C
      Q1       = VDCDIST*X1c - FOCAL_F*DX12
      Q2       = VDCDIST - DX12*TAN_DELTA
      IF ( Q2.EQ.0 ) RETURN
      IF ( DX12.EQ.0.) RETURN
      RATIO    = VDCDIST/DX12
      IF ( RATIO.EQ.-1.) RETURN
C
C-----------------------------------------------------------------------
C                  FIRST ORDER FOCAL PLANE
C-----------------------------------------------------------------------
C
      XF       = Q1/Q2
      KXF      = XF*FP_DISP_FACT + FP_DISP_OFFS
C
C
C
```

```
C
C-----------------------------------------------------------------------
C                    CALCULATE THETA AND THETAPC
C-----------------------------------------------------------------------
C
      THETA     = 1000. * (RATIO-1.) / (RATIO +1.)
      KTHETA    = THETA*THETA_DISP_FACT +THETA_DISP_OFFS !buffer value
      THETApc   = THETA + THETApcXF*XF*(1.+THETA/1000.)
      1                   + THETApc0 + THETAPC_OFFS
      KTHETAPC= THETAPC*THETA_DISP_FACT+THETA_DISP_OFFS !buffer value
C
C-----------------------------------------------------------------------
C                          CALCULATE PHI
C-----------------------------------------------------------------------
C
      PHI       = (Y2 - Y1)*1000./SQRT(VDCDIST**2 + DX12**2)
      KPHI      = PHI + PHI_OFFS !buffer value
      KPHID     = PHI*PHI_DISP_FACT + PHI_DISP_OFFS !buffer value
C
C-----------------------------------------------------------------------
C     CALCULATE INTRINSIC XPLANE ANGLE DIFFERENCE
C-----------------------------------------------------------------------
C
      INTR_XPLANE           = INTRINSICANGLE(4)-INTRINSICANGLE(6) ! X2 - X1
      KXDIFF                = INTR_XPLANE*XDIFF_SCALE + XDIFF_OFFSET
C
C-----------------------------------------------------------------------
C     CALCULATE INTRINSIC UPLANE ANGLE DIFFERENCE
C-----------------------------------------------------------------------
C
      INTR_UPLANE           = INTRINSICANGLE(3)-INTRINSICANGLE(5) ! U1 - U2
      KUDIFF                = INTR_UPLANE*UDIFF_SCALE + UDIFF_OFFSET
C
C
C-----------------------------------------------------------------------
C     CALCULATE TARGET COORDINATES XI AND YI
C-----------------------------------------------------------------------
C
      KXI       = (KX0-X0_CNTR)*FACT_XIX0
      1         + FACT_XITH*THETApc + XI_OFFS
      KXID      = KXI*XI_DISP_FACT + XI_DISP_OFFS !buffer value
      KYI       = FACT_YIY0*(KY0-Y0_CNTR)
      1         + FACT_YIY1*(KY1-Y1_CNTR) + YI_OFFS
      KYID      = KYI*YI_DISP_FACT + YI_DISP_OFFS !buffer value
C
C-----------------------------------------------------------------------
C     FOCAL PLANE TO HIGHER ORDERS
C-----------------------------------------------------------------------
C
      XFK       = XF ! First order
      1         + FKIN*(KY0 - Y0_CNTR) ! Kin Correction
      2         + FACT_XFTHPC_SQ*(THETAPC - XFTHPC_SQ_OFF) ! Aberrations
C
      KXFK      = XFK*FP_DISP_FACT + FP_DISP_OFFS !buffer value
C
C-----------------------------------------------------------------------
C                    THATS ALL FOLKS ...
C-----------------------------------------------------------------------
C
      RETURN
      END
C
C-----------------------------------------------------------------------
```

Appendix C

Monte Carlo

In this Appendix the details of the Monte Carlo are discussed. The program input was based on various sources of information, many of which were private communications. To summarize the input to the Monte Carlo, the elements are listed in Table. C.1 below. The column Z gives the distance from the target *source* neasured along the central trajectory.

Monte Carlo Elements					
Z (m)	Element	Material	Z (m)	Element	Material
0.08	Cu Can window	Al Mylar	10.82	VDC1	
0.11	Al Can window	Al Mylar	11.30	VDC2	
0.13	SS Can window	Kapton	11.31	FPP Scintillator	CH_2
0.63	FEC windows	Kapton	12.22	S1 Scintillator	CH_2
6.82	Dipole Exit window	Kapton	12.95	S2 Scintillator	CH_2

Table C.1: Monte Carlo elements.

A sample input used for REVMOC for the Monte Carlo is shown below. An explanation of the input form is found in [KR89].

```
1    MRS LAC for 352.008 MeV/c PIONS for E413 3He(p,pi)    RUN #101
!
!        MODELLING OF E413, 3He RUN at 416 MeV  THETA=18.41
!
!                                        Keith Furutani, March, 1991
!
TARGET 4BT2 0.00001 0.0001
! Copper Radiation Shield is 8.3 cm from target
DRIFT COPPER 0.082 3.0
DRIFT ALMYL2 * 0.0001 3.0
 1.0 1.14
 .578 6. .05 7. .105 8.
! Aluminum Radiation Shield is 11.2 cm from target
DRIFT ALUMIN 0.029 3.0
DRIFT ALMYL2 * 0.0001 3.0
 1.0 1.14
 .578 6. .05 7. .105 8.
! S.S. Can with Kapton Windows is 13.0 cm from target
DRIFT SSCAN 0.018 3.0
DRIFT KAPTON * 0.00013 3.0
 1.0 1.14
 .578 6. .05 7. .105 8.
! Chamber is 53 cm from 4BT2 target center
DRIFT CHAMBR 0.40 10.
! MRS Port Valve has Kapton Window
DRIFT PRTVLV * 0.0001 5.08
 1.0 1.14
 .578 6. .05 7. .105 8.
! MRS FEC is 63 cm from 4BT2 targer
DRIFT DFEC 0.0997 5.08
! FEC has Kapton Window
DRIFT FECWIN * 0.0001 5.08
 1.0 1.14
 .578 6. .05 7. .105 8.
! FEC has Anode and Cathode wires of effective density
DRIFT ANODE * 0.000012 4. -4. 4. -4.
 1.0 0.04632
 1.0 74.
DRIFT CATHOD * 0.000050 4. -4. 4. -4.
 1.0 0.896
 1.0 29.
! FEC0 is coordinate written to disk
DRIFT FEC0 0.0001 4. -4. 4. -4.
! QUAD distane can vary but typically 156 cm to center from 4BT2 target
DRIFT QENT 0.654 9.84
! Actual Quad length 40 cm, but effective typically 49.2 cm
!  must also use correct Quad field, not hall probe reading
QUAD 0.492 -2.000 10.0
DRIFT BMPIPE 0.383 9.84
DRIFT FLARED 1.842 18. -18. 5. -5.
DRIFT DIPENT 0.0001 27.94 -27.94 3.81 -3.81
FRIN 5. 0.17 3.8
ENTR 12.92 0.345
! Dipole has central mom approx p0=D*80.3 (in MeV)
BEND DIPOLE 2.82 4.2244 0. 0. 0.339219
EXIT -25.0 -0.20792
DRIFT DIPEXT * 0.0001 27.94 -27.94 3.81 -3.81
 1.0 1.14
 .578 6. .05 7. .105 8.
! Drift Coordinates written to disk
DRIFT VDC1 3.9999 37.3 -37.3 14.15 -14.15 0.
DRIFT VDC2 0.483 37.3 -37.3 14.15 -14.15 0.
! FPP Coordinates written to disk
DRIFT FPP * 0.005 71. -71. 150. -150.
```

```
 1.0 1.03
 0.857 6. 0.143 1.
DRIFT TOS1 * .909 100. -100. 100. -100. 0.
 1.0 0.0014
 .78 7. .21 8.
! S1 Coordinates (and energy deposit) written to disk
DRIFT S1 * 0.005 100. -100. 100. -100. 0
 1.0 1.03
 0.857 6. 0.143 1.
DRIFT TOS2 * .725 100. -100. 100. -100. 0.
 1.0 0.0014
 .78 7. .21 8.
! S2 Coordinates (energy deposit) written to disk
DRIFT S2 * 0.005 52. -52. 31. -31. 0.
 1.0 1.03
 0.857 6. 0.143 1.
X 0.864 14.81  0.00 0. 0. 1.
Y 0.864 14.81  0.00 0. 0. 1.
P 0.352008  0.003 0.339219 0. 0. 3. 0.
MASS * M 0.139567 37. 1. 26.03 1. 0. 0. 180.
1. 0.105658 0.
INIT 5525625
! Number of events., and must use 13 for MRSPI RAYIN subroutine
G 1. 50.000 0. 13.
! Write output to disk which is later decoded by REVVDACS
OUTPUT E413 7. 4BT2 FEC0 VDC1 VDC2 FPP S1 S2
END
FINI
```

Appendix D

Phase Space

In this Appendix the details of the three particle phase space calculation are discussed. Consider the case of:

$$1 + 2 \rightarrow 3 + 4 + 5 \tag{D.1}$$

and more specifically the reaction:

$$p + \alpha \rightarrow \pi + n + \alpha \tag{D.2}$$

First consider the two particle phase space for particles 4 and 5 (i.e. n+α). For any two particles in the zero-momentum frame with total energy E_{45} the momentum of each particle is given by

$$p = \frac{\sqrt{(E_{45}^2 - (m_4 + m_5)^2)(E_{45}^2 - (m_4 - m_5)^2)}}{2E_{45}}. \tag{D.3}$$

The two particle Lorentz-invariant phase space is then given by [Hag63],

$$R_2(0, E_{45}) = \frac{\pi p}{E_{45}}, \tag{D.4}$$

where the zero in the argument indicates zero total momentum of the two particles. Hence for $n + \alpha$,

$$R_2^{(n+\alpha)}(0, E_{45}) = \frac{\pi}{2E_{45}^2}\sqrt{(E_{45}^2 - (m_4 + m_5)^2)(E_{45}^2 - (m_4 - m_5)^2)}. \tag{D.5}$$

It very important to note that this is relativistically invariant!

Note also that E_{45} is the invariant mass of particles 4 and 5. Hence,

$$E_{45} = E_4 + E_5 = m_4 + m_5 + E_x, \tag{D.6}$$

where E_x is the internal excitation energy of 4 and 5. Since, in the present case, the excitation energy is only a few MeV, this may be written as

$$E_{45} = m_4 + m_5 + \frac{k^2}{2\mu}, \tag{D.7}$$

where k is the cm momentum of the $n + \alpha$ and μ is the reduced mass:

$$\frac{1}{\mu} = \frac{1}{m_4} + \frac{1}{m_5} \tag{D.8}$$

$$\mu = \frac{m_4 m_5}{m_4 + m_5} = 750.42\,\mathrm{MeV}. \tag{D.9}$$

The three particle phase space is given by the following expression [Hag63],

$$R_3(\vec{P}, E) = \int \frac{d^3\vec{p}_3}{2E_3}\frac{d^3\vec{p}_4}{2E_4}\frac{d^3\vec{p}_5}{2E_5}\delta(\vec{p}_3 + \vec{p}_4 + \vec{p}_5 - \vec{P})\delta(E_3 + E_4 + E_5 - E), \tag{D.10}$$

where $\vec{P}$ and E are the total momentum and energy of the three particles $(\pi^+ + n + \alpha)$ in the lab frame. This may rewritten in terms of the two particle phase space as follows,

$$R_3(\vec{P}, E) = \int \frac{d^3\vec{p}_3}{2E_3} \underbrace{\int \frac{d^3\vec{p}_4}{2E_4}\frac{d^3\vec{p}_5}{2E_5}\delta(\vec{p}_4 + \vec{p}_5 - (\vec{P} - \vec{p}_3))\delta(E_4 + E_5 - (E - E_3))}_{R_2(\vec{P}-\vec{p}_3, E-E_3)}. \tag{D.11}$$

But, since R_2 is Lorentz invariant,

$$R_2(\vec{P} - \vec{p}_3, E - E_3) = R_2(0, E_{45}), \tag{D.12}$$

where the invariant mass is

$$(E - E_3)^2 - |\vec{P} - \vec{p}_3|^2 = E_{45}^2, \tag{D.13}$$

and therefore

$$R_3(\vec{P}, E) = \int \frac{d^3\vec{p}_3}{2E_3} R_2(0, E_{45}), \tag{D.14}$$

$$R_3(\vec{P}, E) = \int \frac{p_3^2 dp_3 d\Omega_3}{2E_3} R_2(0, E_{45}). \tag{D.15}$$

Since the pion is detected within a certain momentum interval dp_3 in a solid angle $\Delta\Omega_3$, what is required is the differential phase space

$$\frac{dR_3(\vec{P}, E)}{d\Omega_3 dp_3} = \frac{p_3^2}{2E_3} R_2(0, E_{45}), \tag{D.16}$$

which from Eqn. D.5 is therefore given by

$$\frac{dR_3}{d\Omega_3 dp_3} = \frac{\pi p_3^2}{2E_3} \times \frac{\sqrt{(E_{45}^2 - (m_4 + m_5)^2)(E_{45}^2 - (m_4 - m_5)^2)}}{2E_{45}^2}. \tag{D.17}$$

E_{45} is given by Eqn. D.13 above and is related to the excitation energy of the $n + \alpha$ system by Eqn. D.6. A sample calculation of the phase space $(dR_3/dp_3 d\Omega_3)$ for a forward angle and $T_p = 500$ MeV and a back angle and $T_p = 240$ MeV is shown in Fig. D.1.

Note that in Eqn. D.17 if the phase space is graphed versus E_x (shown in Fig. D.2) then the pion angle and proton energy dependence of the phase space factor is contained in the first quotient (p_3^2/E_3). Since this is a slowly varying function with excitation energy for a given proton bombarding energy and pion scattering, the observed phase space spectra in Fig. D.2 will not change significantly for different angles or different proton energies.

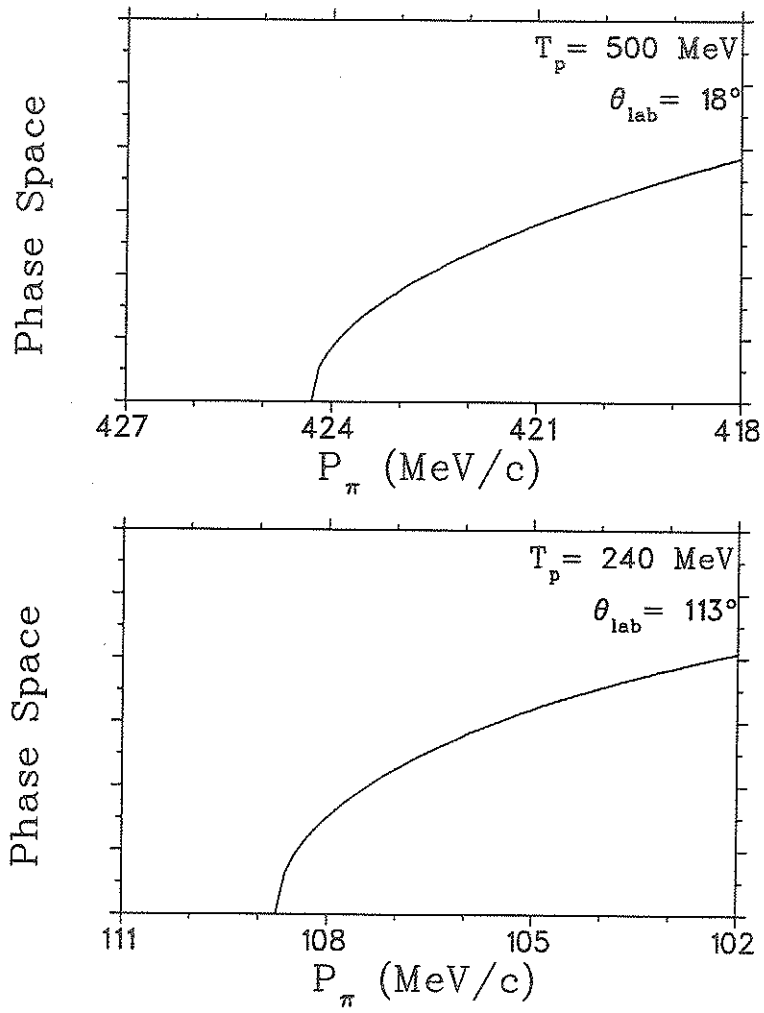

Figure D.1: Calculation of the three particle phase space for $p + \alpha \rightarrow \pi^+ + n + \alpha$ at $\theta_\pi = 18°$ and $T_p = 500$ MeV and at $\theta_\pi = 113°$ and $T_p = 240$ MeV.

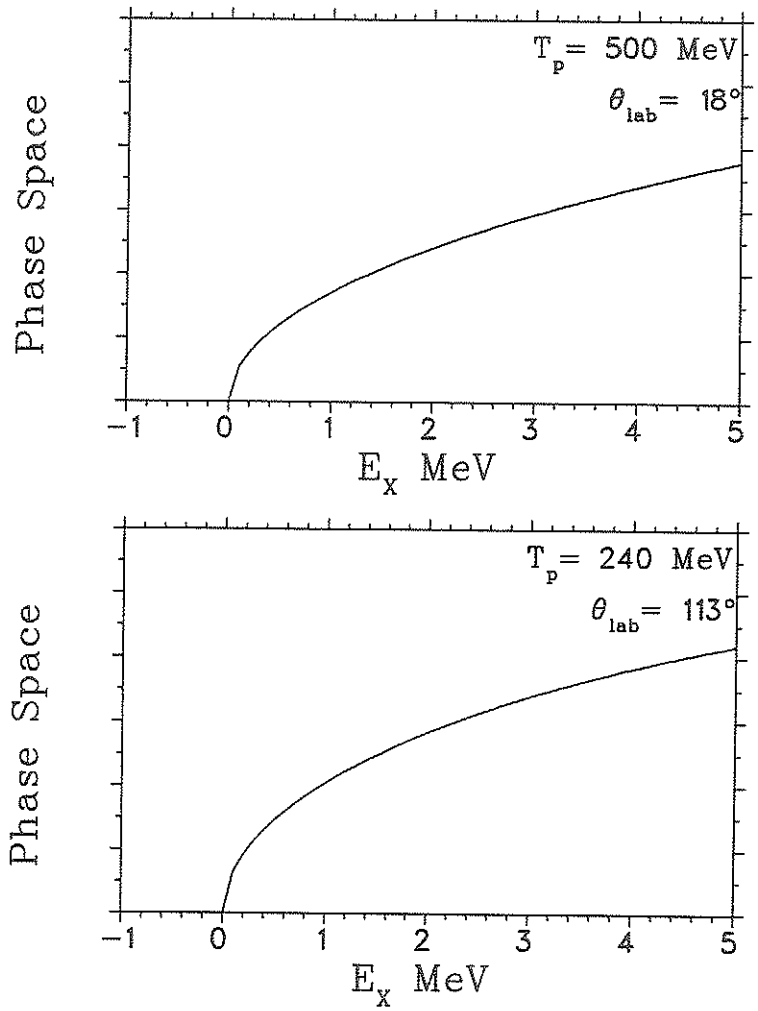

Figure D.2: Same as in Fig. D.1 but plotted versus E_x.

Appendix E

Target Projection Calculation

G(y) is the calculated target projection at a given target and pion scattering angle. This function is dependent on the angles of the MRS and target, and on the beam width and position. The determination of the position of the cell with respect to the scattering chamber was discussed in Section 2.2.6. In the X-Y frame shown in Fig. E.1 the windows are described by equations for a circle. For the the top window:

$$(X - X_t)^2 + (Y - Y_t)^2 = R^2 \tag{E.1}$$

where R is the radius of curvature and (X_t, Y_t) are the coordinates of the centre of the arc desribed by the top window. The may be rewritten in terms of the offsets as follows,

$$(X + X_0)^2 + (Y + (R - \delta - 5 + Y_0))^2 = R^2 \tag{E.2}$$

where δ is the *bulge* in the window shown in Fig. E.1. The bottom window given by:

$$(X - X_b)^2 + (Y - Y_b)^2 = R^2 \tag{E.3}$$

which may be rewritten as:

$$(X + X_0)^2 + (Y - (R - \delta - 5 - Y_0))^2 = R^2. \tag{E.4}$$

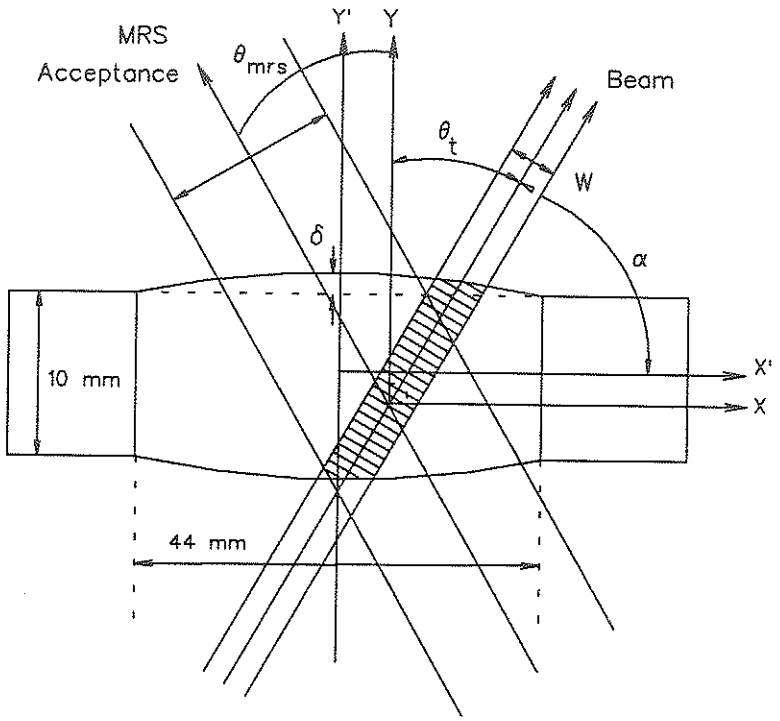

Figure E.1: Schematic of projection of active target volume onto MRS acceptance.

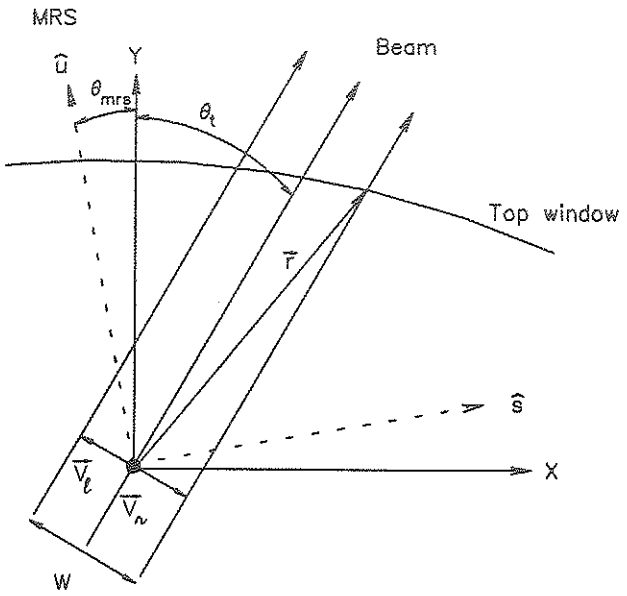

Figure E.2: Definition of vectors for projection calculation.

as in the top window case.

For the projection calculation the intersection of the beam edges with the cell windows must be determined. The proton beam was assumed to be a uniform distribution of width W for this calculation. The centre of the beam is given by:

$$\mathrm{Y} = \mathrm{X} \tan \alpha \tag{E.5}$$

where

$$\alpha = \frac{\pi}{2} - \theta_t \tag{E.6}$$

and so

$$\mathrm{X} = \mathrm{Y} \tan \theta_t. \tag{E.7}$$

Now let $\vec{v}_l$ and $\vec{v}_r$ be vectors perpendicular to the beam direction, left

and right respectively, (defined in Fig. E.2).

$$\vec{v}_r = \frac{W}{2}(\cos\theta_t\hat{\imath} - \sin\theta_t\hat{\jmath}) \tag{E.8}$$

$$\vec{v}_l = \frac{W}{2}(-\cos\theta_t\hat{\imath} + \sin\theta_t\hat{\jmath}) \tag{E.9}$$

From Fig. E.2 the equation for the right side of the beam is:

$$\vec{v}_r \cdot (\vec{r} - \vec{v}_r) = 0 \tag{E.10}$$

which simplifies to:

$$X = Y\tan\theta_t + \frac{W}{2\cos\theta_t}. \tag{E.11}$$

Similarly for the left side of the beam

$$\vec{v}_l \cdot (\vec{r} - \vec{v}_l) = 0 \tag{E.12}$$

which simplifies to:

$$X = Y\tan\theta_t - \frac{W}{2\cos\theta_t}. \tag{E.13}$$

The intersection of the beam edges with the target windows is found by combining the two equations of interest (i.e. top, bottom, left and right) and solving for X and Y. Defining

$$a = \tan\theta_t \tag{E.14}$$

and

$$b = \pm\frac{W}{2\cos\theta_t} \tag{E.15}$$

where $\pm$ is for the $\frac{\text{right}}{\text{left}}$ beam edge, then solving for Y a quadratic equation is obtained.

$$AY^2 + BY + C = 0 \tag{E.16}$$

The coefficients are:

$$A = a^2 + 1 \tag{E.17}$$

$$B = 2a(b + X_0) \pm 2(R - 6 \pm Y_0) \tag{E.18}$$

$$C = (b + X_0)^2 - 2R(6 \mp Y_0) + (6 \mp Y_0)^2 \tag{E.19}$$

where the $\pm$ and $\mp$ signs are for the $\frac{\text{top}}{\text{bottom}}$ window.

A unit vector $\hat{u}$ is defined which points in the direction of the MRS.

$$u_x = -\sin(\theta_{mrs} - \theta_t) \tag{E.20}$$

$$u_y = \cos(\theta_{mrs} - \theta_t) \tag{E.21}$$

Also a vector $\hat{s}$ is defined which is perpendicular to $\hat{u}$ so that

$$\hat{u} \cdot \hat{s} = 0 \tag{E.22}$$

and lies in the scattering plane. Solving:

$$s_x = u_y = \cos(\theta_{mrs} - \theta_t) \tag{E.23}$$

$$s_y = -u_x = \sin(\theta_{mrs} - \theta_t). \tag{E.24}$$

The projections of the intersections of the beam edges with the windows on the MRS acceptance direction are then given by,

$$P_i = \vec{r}_i \cdot \hat{s}. \tag{E.25}$$

where the subscript i is for: top-right, top-left, bottom-right and bottom-left. A typical projection G(y), calculation is shown in Fig. 3.31 for θ_{mrs}=40° and θ_t=0°.

Appendix F

Solid Angle

In this Appendix the dependence of the MRS solid angle corresponding to open Front End Chamber cuts (OFC) on the Q/D ratio is discussed and the solid angle used in the E564 analysis is obtained.

For E413 the solid angle was determined quite accurately by placing tight cuts on the FEC coordinate spectra (see Section 3.5) since it was found in the Monte Carlo study that the solid angle varied substantially with a small change in Q/D ratio (see Section 2.3.5). This dependence on Q/D ratio was investigated using experimental data. Open cuts on the FEC coordinates were used in previous analyses of (p,π^+) experiments by Huber [Hub88] to maximize the statistics. This was necessary to resolve structure in the focal plane spectrum. For experiment E413 the peak in the pion focal plane spectrum corresponding to the recoil ^{4}He nucleus in its ground state is cleanly resolved (similarly for the pp $\rightarrow$ dπ^+ calibration runs of both E413 and E564). For the study of the OFC solid angle dependence on Q/D ratio the OFC solid angle for the ^{3}He(p,π^+)^{4}He and the pp $\rightarrow$ dπ^+ reactions was obtained in the following way.

The FEC is a distance R from the target (approximated as a point source).

By placing tight cuts on the FEC coordinates X0 and Y0, a solid angle was determined from the following equation.

$$\Delta\Omega_1 = \frac{X0 \times Y0}{R^2} \tag{F.1}$$

This geometric solid angle is the effective solid angle provided the cuts are placed tightly enough that the acceptance is not further restricted by the MRS. The corresponding extracted peak area is denoted $PEAK_1$. The solid angle for different FEC cuts and their corresponding peak areas should be proportional.

$$\frac{PEAK_i}{\Delta\Omega_i} = \text{constant} \tag{F.2}$$

In Fig. F.1, where the solid angle from different FEC cuts and their corresponding peak areas are plotted, this is shown to be indeed true. The solid angle of interest here was determined by relaxing the FEC cuts completely, and then taking the ratio of the peak areas. That is

$$\Delta\Omega_0 = \Delta\Omega_1 \times \frac{PEAK_0}{PEAK_1} \tag{F.3}$$

where $PEAK_0$ is the peak area when the cuts are relaxed to their normal setting. The statistical error in this solid angle $\Delta\Omega_0$ is given by the statistics of $PEAK_1$ and is typically 5%. The relative uncertainty due to the uncertainty in $\Delta\Omega_1$ is about 4%. The errors in the solid angles shown in the tables and figures in this Appendix are statistical only.

A Q/D scan using the $pp \rightarrow d\pi^+$ reaction was performed during E564. The Q/D ratio was varied while keeping the peak position constant (that is keeping the Dipole field constant) and the results are shown in Table. F.1. The OFC solid angle ($\Delta\Omega_0$) is plotted versus Q/D ratio in Fig. F.2. The data are well described by a linear relationship with slope 7.69 msr and y-intercept -1.07 msr.

$$\Delta\Omega = 7.69 \times \frac{Q}{D} - 1.07 \tag{F.4}$$

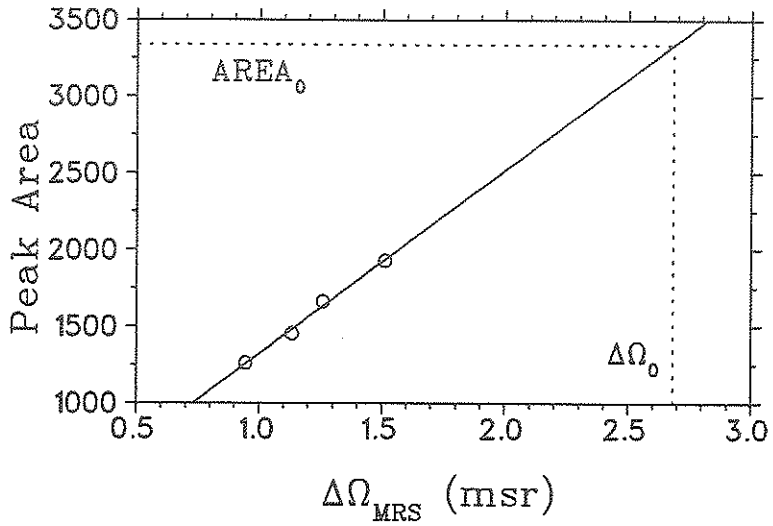

Figure F.1: The peak area, PEAK, versus solid angle for different FEC cuts.

$T_p = 500\,MeV$					
RUN#	Q/D	$\Delta\Omega_0^\dagger$ (msr)	RUN#	Q/D	$\Delta\Omega_0^\dagger$ (msr)
27	0.441	2.27	23	0.482	2.69
25	0.460	2.45	24	0.504	2.80
41	0.467	2.58	26	0.527	2.95

† statistical errors approximately 5%

Table F.1: Test of solid angle extraction with $pp \rightarrow d\pi^+$.

This dependence on Q/D ratio implies that (for the typical values of the Q/D ratios observed during the experiments) the fractional error in the solid angle is ≈1.4 times the fractional change of the Q/D ratio.

$$\frac{d\Delta\Omega}{\Delta\Omega} \approx 1.4 \times \frac{d(Q/D)}{Q/D} \tag{F.5}$$

This agrees well with that found by the Monte Carlo (see Section 2.3.5).

The range of Q/D ratios observed in E413 for the $^3He(\vec{p},\pi^+)^4He$ reaction was approximately 0.47 to 0.52 and is shown versus run number in

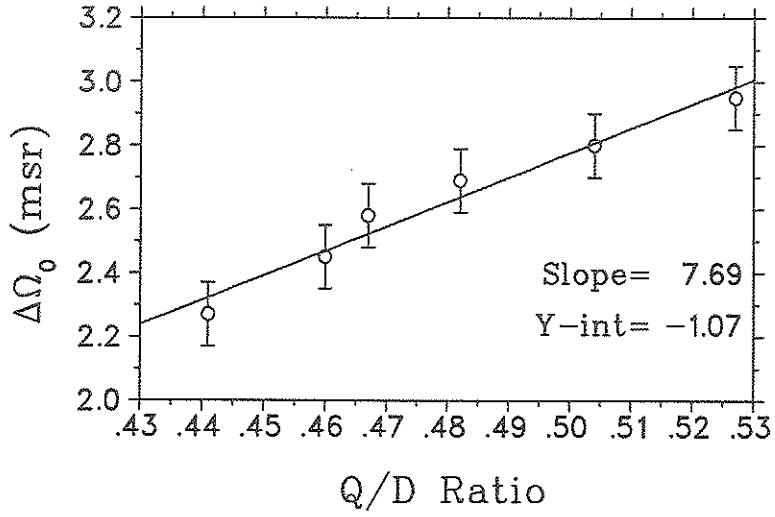

Figure F.2: Solid angle versus Q/D determined with $pp \rightarrow d\pi^+$.

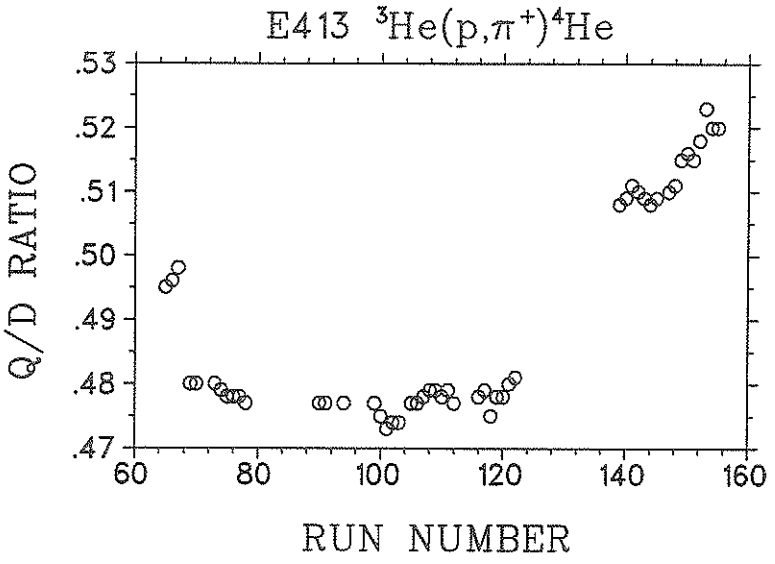

Figure F.3: Q/D ratio versus run number for the ^{3}He($\vec{p}$,π^+)^{4}He reaction.

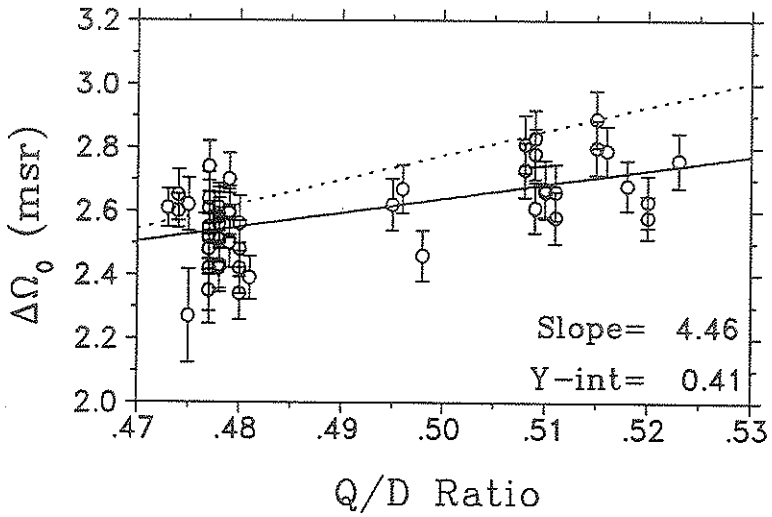

Figure F.4: Solid angle versus Q/D ratio for the ^{3}He(p,π^+)^{4}He reaction of E413 (solid line). The dotted line is the curve from the pp $\rightarrow$ dπ^+ scan of E564 in Fig. F.2.

Fig. F.3. The extracted OFC solid angle is shown versus Q/D ratio for the ^{3}He($\vec{p}$,π^+)^{4}He reaction in Fig. F.4. Note that the slope and intercept found is slightly different than that found for the Q/D scan using the pp $\rightarrow$ dπ^+ reaction in E564. This difference could be due to a different Quad position since this was not determined in E413.

For E564 the analysis of the ^{4}He($\vec{p}$,π^+)^{5}He reaction spectra required the maximum possible statistics and therefore a tight cut on the FEC coordinates was not acceptable. However, in Fig. F.5 the Q/D ratio is observed to be quite constant, about 0.490 to 0.500 or,

$$\frac{d(Q/D)}{Q/D} \approx 1\%. \qquad \text{(F.6)}$$

This is significantly smaller than that observed in E413 in Fig. F.3. The narrow range of Q/D ratios for E564 implies then (assuming $\lambda \approx 1.4$) that the

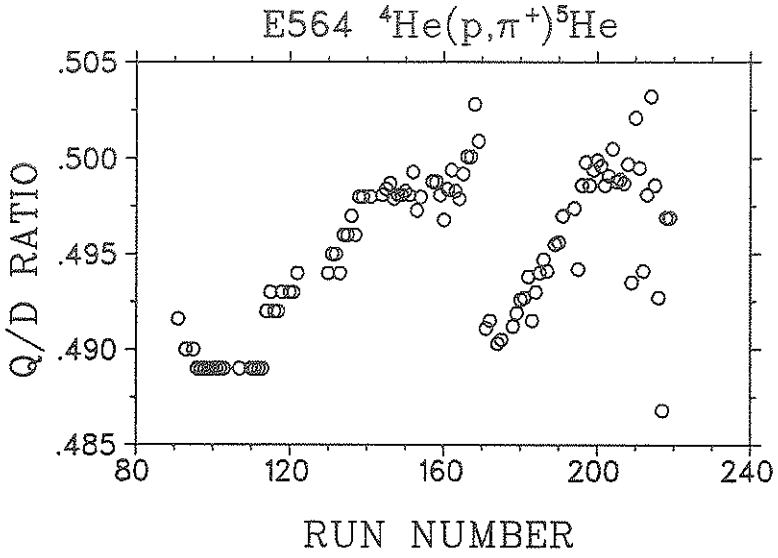

Figure F.5: Q/D ratio versus run number for the ^{4}He($\vec{p}$,π^+)^{5}He reaction.

solid angle varied by less than 2% which is therefore the relative uncertainty in the solid angle.

There still remains the question of the absolute solid angle. In Fig. F.5 the Q/D ratio is observed to be approximately 0.495 for E564. From the Q/D scan with the pp $\rightarrow$ dπ^+ reaction in E564 (shown in Fig. F.2) and from the ^{3}He($\vec{p}$,π^+)^{4}He reaction data of E413 (shown in Fig. F.4) a reasonable estimate of the solid angle for the E564 data would be 2.60 msr. Considering the observed variance of the solid angle in Fig. F.4, about 5%, and the systematic error in calculating the solid angle, about 3%, the error of this estimate is assumed to be about 6%.

$$\Delta\Omega = 2.60 \pm 2\%(\pm 6\%)\,\mathrm{msr} \tag{F.7}$$

Appendix G

Data

Following are the data tables for the ^{3}He($\vec{p}$,π^+)^{4}He and ^{4}He($\vec{p}$,π^+)^{5}He reactions. The uncertainties quoted are the statistical added in quadrature with the relative uncertainties. Not included are the systematic uncertainties estimated at approximately 8% for the ^{3}He($\vec{p}$,π^+)^{4}He reaction and 9% for ^{4}He($\vec{p}$,π^+)^{5}He reaction.

For the ^{4}He($\vec{p}$,π^+)^{5}He reaction, the ^{5}He peak was integrated from threshold to 4.44 MeV excitation. To obtain the ^{5}He ground state cross sections a renormalization factor was calculated from a final state interaction calculation (see Section 3.1.3). This calculation showed that the cross section contribution up to 4.44 MeV and the contribution from the ^{5}He ground state ($p_{\frac{3}{2}}$ only) up to very high excitation is a nearly constant ratio of about 0.6. The data in the tables include this factor of 0.6.

$$\frac{d\sigma}{d\Omega}(tables) = \frac{1}{0.6} \times \frac{d\sigma}{d\Omega}(0 \rightarrow 4.44\text{MeV})$$

$T_p = 300$ MeV		
θ_{CM}	$d\sigma/d\Omega$ μb/sr	A_{N0}
23.37	8.99 ± 0.46	0.389 ± 0.028
29.13	6.64 ± 0.34	0.432 ± 0.027
35.33	5.43 ± 0.28	0.317 ± 0.029
41.46	4.23 ± 0.22	0.331 ± 0.031
47.48	2.96 ± 0.15	0.124 ± 0.028
53.45	1.88 ± 0.10	−0.103 ± 0.030
59.35	1.38 ± 0.07	−0.405 ± 0.025
65.17	1.13 ± 0.06	−0.544 ± 0.026
70.79	1.13 ± 0.06	−0.543 ± 0.025
76.36	1.27 ± 0.06	−0.346 ± 0.028
83.96	1.17 ± 0.06	−0.119 ± 0.029
91.31	1.31 ± 0.06	0.015 ± 0.026
98.44	1.21 ± 0.06	0.071 ± 0.028
105.39	1.06 ± 0.05	0.027 ± 0.027
114.01	0.916 ± 0.046	−0.075 ± 0.028
124.12	0.828 ± 0.041	−0.246 ± 0.028
133.81	0.688 ± 0.034	−0.599 ± 0.021

Table G.1: ^{3}He(p,π^+)^{4}He 300 MeV data.

$T_p = 416$ MeV		
θ_{CM}	$d\sigma/d\Omega$ μb/sr	A_{N0}
23.79	14.83 ± 0.73	0.549 ± 0.025
29.63	11.38 ± 0.54	0.545 ± 0.024
29.64	10.90 ± 0.56	0.535 ± 0.048
35.96	7.37 ± 0.37	0.475 ± 0.031
42.18	5.00 ± 0.25	0.350 ± 0.027
48.30	2.99 ± 0.15	0.229 ± 0.029
54.31	1.95 ± 0.09	−0.055 ± 0.031
60.21	1.57 ± 0.08	−0.091 ± 0.031
66.04	1.59 ± 0.08	0.132 ± 0.031
71.71	1.56 ± 0.08	0.304 ± 0.031
79.45	1.64 ± 0.08	0.466 ± 0.032
86.97	1.44 ± 0.07	0.610 ± 0.029
93.74	1.22 ± 0.06	0.640 ± 0.027
101.39	0.893 ± 0.045	0.535 ± 0.030
110.12	0.579 ± 0.028	0.199 ± 0.026
118.48	0.444 ± 0.022	−0.368 ± 0.027
126.52	0.458 ± 0.023	−0.865 ± 0.026
133.81	0.470 ± 0.023	-1.040 ± 0.019

Table G.2: ^{3}He(p,π^+)^{4}He 416 MeV data.

$T_p = 507$ MeV		
θ_{CM}	$d\sigma/d\Omega$ μb/sr	A_{N0}
24.45	9.67 ± 0.47	0.325 ± 0.025
30.20	7.32 ± 0.39	0.270 ± 0.040
36.61	4.96 ± 0.25	0.111 ± 0.033
42.88	3.03 ± 0.15	−0.145 ± 0.035
46.64	2.53 ± 0.13	−0.234 ± 0.036
49.08	2.16 ± 0.11	−0.307 ± 0.035
55.19	1.41 ± 0.07	−0.168 ± 0.034
61.17	1.20 ± 0.06	0.093 ± 0.036
67.04	1.05 ± 0.05	0.319 ± 0.035
72.74	0.854 ± 0.045	0.552 ± 0.036
78.32	0.777 ± 0.040	0.734 ± 0.031
85.82	0.617 ± 0.031	0.748 ± 0.026
93.26	0.510 ± 0.025	0.701 ± 0.026
100.34	0.447 ± 0.023	0.400 ± 0.035
111.00	0.235 ± 0.015	0.026 ± 0.070
129.02	0.218 ± 0.015	−0.754 ± 0.060

Table G.3: ^{3}He(p,π^+)^{4}He 507 MeV data.

$T_p = 240$ MeV		
θ_{CM}	$d\sigma/d\Omega$ μb/sr	A_{N0}
22.66	6.54 ± 0.59	0.021 ± 0.040
30.70	5.03 ± 0.45	-0.023 ± 0.034
39.11	4.23 ± 0.37	-0.114 ± 0.036
47.39	3.52 ± 0.33	-0.336 ± 0.039
55.58	2.82 ± 0.25	-0.564 ± 0.037
63.56	2.90 ± 0.27	-0.791 ± 0.034
71.40	2.90 ± 0.27	-0.886 ± 0.035
80.12	2.64 ± 0.24	-0.872 ± 0.037
98.93	2.39 ± 0.21	-0.610 ± 0.036
107.77	3.03 ± 0.28	-0.627 ± 0.038
126.40	3.16 ± 0.29	-0.347 ± 0.042

Table G.4: ^{4}He(p,π^+)^{5}He ($\frac{3}{2}^-$) 240 MeV data.

$T_p = 300$ MeV		
θ_{CM}	$d\sigma/d\Omega$ μb/sr	A_{N0}
22.38	30.4 ± 2.2	0.287 ± 0.028
27.95	23.9 ± 1.7	0.331 ± 0.035
33.92	19.2 ± 1.5	0.260 ± 0.031
39.83	14.7 ± 1.0	0.318 ± 0.030
45.69	10.7 ± 0.77	0.341 ± 0.027
51.50	7.68 ± 0.56	0.168 ± 0.024
57.22	5.53 ± 0.39	−0.119 ± 0.025
62.87	3.98 ± 0.28	−0.403 ± 0.024
68.41	3.28 ± 0.23	−0.651 ± 0.025
76.01	3.01 ± 0.21	−0.774 ± 0.020
83.51	2.36 ± 0.18	−0.626 ± 0.023
90.74	2.21 ± 0.17	−0.399 ± 0.023
97.88	2.13 ± 0.15	−0.203 ± 0.029
106.72	2.76 ± 0.21	−0.048 ± 0.027
115.32	2.61 ± 0.20	0.003 ± 0.029
123.64	2.29 ± 0.16	0.013 ± 0.026
131.75	1.96 ± 0.14	−0.016 ± 0.029

Table G.5: ^{4}He(p,π^+)^{5}He ($\frac{3}{2}^-$) 300 MeV data.

$T_p = 400$ MeV		
θ_{CM}	$d\sigma/d\Omega$ μb/sr	A_{N0}
22.60	52.4 ± 3.7	0.356 ± 0.018
28.27	37.5 ± 2.6	0.418 ± 0.029
34.25	26.4 ± 2.0	0.517 ± 0.029
40.24	18.8 ± 1.3	0.310 ± 0.024
46.08	12.1 ± 0.9	0.240 ± 0.029
51.93	8.71 ± 0.63	0.052 ± 0.027
57.67	3.87 ± 0.29	−0.177 ± 0.029
63.33	2.44 ± 0.17	−0.365 ± 0.029
68.92	2.04 ± 0.14	−0.167 ± 0.026
76.51	1.78 ± 0.14	0.172 ± 0.025
83.99	1.50 ± 0.11	0.392 ± 0.026
91.25	1.28 ± 0.09	0.602 ± 0.026
98.34	1.08 ± 0.08	0.723 ± 0.023
107.15	1.03 ± 0.07	0.654 ± 0.027
115.69	0.715 ± 0.052	0.431 ± 0.029
123.95	0.523 ± 0.038	0.057 ± 0.031
132.02	0.378 ± 0.028	−0.433 ± 0.030

Table G.6: ^{4}He(p,π^+)^{5}He ($\frac{3}{2}^-$) 400 MeV data.

$T_p = 500$ MeV		
θ_{CM}	$d\sigma/d\Omega$ μb/sr	A_{N0}
23.02	29.2 ± 2.0	0.498 ± 0.017
28.66	20.5 ± 1.4	0.206 ± 0.021
34.82	13.5 ± 0.9	0.003 ± 0.021
40.86	8.59 ± 0.62	−0.070 ± 0.025
46.79	5.46 ± 0.40	−0.266 ± 0.022
52.67	3.59 ± 0.25	−0.378 ± 0.022
58.48	2.84 ± 0.20	−0.271 ± 0.029
64.20	1.99 ± 0.14	0.065 ± 0.028
70.80	1.91 ± 0.13	0.394 ± 0.024
77.50	1.56 ± 0.11	0.593 ± 0.031
84.20	1.09 ± 0.08	0.691 ± 0.031
92.19	0.780 ± 0.058	0.643 ± 0.030
99.25	0.473 ± 0.037	0.549 ± 0.037
108.02	0.455 ± 0.033	0.316 ± 0.035
116.50	0.318 ± 0.023	−0.153 ± 0.036

Table G.7: ^{4}He(p,π^+)^{5}He ($\frac{3}{2}^-$) 500 MeV data.